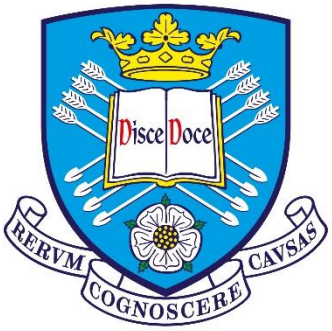

The University Of Sheffield.

A study of the Dissolution of UK Nuclear Waste Glass in Cement Waters

Colleen Mann

A thesis submitted in partial fulfilment for the degree of Doctor of Philosophy

Immobilisation Science Laboratory/NucleUS
Department of Materials Science and Engineering
The University of Sheffield

Sponsored by EPSRC as part of the Nuclear FiRST DTC

August 2018

Abstract

Within the United Kingdom (UK), it is proposed that nuclear waste will be disposed of in a geological facility, utilising an engineered barrier system that will be optimised to physically and chemically impede the transport of radionuclides to the biosphere. Understanding glass dissolution in environmental conditions designed to mimic geological disposal is paramount to the safety case of the UK's radioactive waste disposal programme.

Interaction of groundwater with the cementitious components of the facility will lead to the presence of high pH conditions within a disposal facility. The effect of such cement leachates on the durability of vitrified wasteforms is not well understood. The following body of work aims to address the concerns of nuclear waste glass in contact with cementitious materials. Here we present results from glass durability studies using simulated cement leachates and equilibrated cement water to elucidate the mechanisms that govern glass corrosion under these complex geochemical conditions. The normalised mass loss and normalised leaching rate as a function of cement leachate composition was determined by effluent solution analysis. Additionally, we present characterisation results collected on alteration layers by conducting x-ray diffraction and electron microscopy measurements on glass powders and monolith samples. Collectively, these data provide new insights into the mechanisms that govern glass dissolution in the complex geochemical conditions expected for vitrified UK waste if water breaches the engineered barrier system in a geological disposal facility.

The work demonstrated in this thesis indicates that glass dissolution is less severe in cementitious leachates compared to pure water and young synthetic cement waters are more corrosive than evolved solutions with a lower concentration of alkali/alkaline earth ions.


SCIENCE MAKES AMERICA GREAT
SCIENCE BUILDS THE FUTURE

Acknowledgements

Firstly I would like to thank Dr Claire Corkhill for her outstanding academic supervision, without her unwavering support and encouragement this thesis would have been an enormous challenge for me.

I am grateful for being part of the Immobilisation Science Laboratory/NucleUS family, it has offered me friendship both inside and outside of the office, being a member of the Nuclear FiRST DTC Cohort 5 lead to the development of close friendships that will continue to flourish beyond our PhD's.

I would like to thank Dr Daniel Backhouse and Mr Adam Fisher for continued glass discussions and Dale Prentice for sharing his knowledge of cement and geochemical modelling. Dr Clare Thorpe dedicated a significant amount of her time to assist me whilst I was recovering from injury and many ISL members moved heavy 'bean tins' for me time and time again. Without the assistance of technical staff experimental work would have been hindered, special thanks to Dr Lisa Hollands (MAT), Robin Markwell (CIV), Robert Ashurst (Geography), and Dr Cheryl Shaw (MAT).

I am grateful for the fantastic opportunities I have had throughout my PhD, numerous international conferences, training courses, social trips (including a visit to Chernobyl) and a secondment at Oak Ridge National Laboratory working with Dr Eric Pierce. My time with Eric was invaluable, as a mentor he ensured I left his lab with new skills and much greater knowledge of microscopy. Eric also encouraged me to make memories of my time in Tennessee. Thanks also to Dr Jeremy R Eskelsen who spent many hours helping me refine my microscopy skills, which have been invaluable to this thesis. A special thanks goes to Dr Anthony Walker, for welcoming me into his home and friendship circle. Many of my memories where made in the company of my good friends Anthony, Dr Bobby Bridges and April Morton, thanks for staying in touch!

An extra special thank you goes to Drew M^{c}Laughlin who made the decision to move with me and to build a home in the city of Sheffield. Drew's love and support never faltered, his rich inner strength, understanding, kindness and patience have been invaluable, especially in the last 6 months when my focus has been dedicated to this thesis and not our love for one another. I thank you for your constant encouragement, boxes of kisses and mini bubbles, they have all helped me get to the end goal… \o/

Publications

The author has contributed to the following peer reviewed publications during the production of this thesis;

1. C Mann, C.L. Thorpe, A.E Milodowski, L.P Field, R.P Shaw, L Boast, R.J Hand, N.C Hyatt, J.L Provis and C.L. Corkhill *Interactions between Simulant Vitrified Nuclear Wastes and High pH Solutions: A Natural Analogue Approach*, MRS Advances, 2017, **2**,1147-1154
2. C Mann, T.L Hoh, C.L Thorpe, C.L Corkhill, *Dissolution of glass in cementitious solutions: An analogue study for vitrified waste disposal*, MRS Advances, 2018, **3**, 669-674
3. C.L Thorpe, C. Mann, A. Fisher, R.J. Hand, N.C Hyatt, B.J Riley, M.J Schweiger, J Mayer, C Arendt, A.A Kruger, D Kosson and C.L Corkhill *Evaluation of Novel Leaching Assessment for Nuclear Waste Glasses*, Waste Management, 2018
4. C Mann, K Ferrand, S Liu, J.R Eskelsen, E Pierce, K Lemmens and C.L Corkhill *Influence of Young Cement Water on the Dissolution Mechanism and Kinetics of the International Simple Glass*, NPJ Materials Degradation, 2019

The following have been accepted for publication;

5. T.C. Kaspar, J Ryan, C.G. Pantano, J Rice, N.C. Hyatt, C.L. Corkhill, C Mann, R.J. Hand, M.A. Kirkham, C.L. Crawford, C Jantzen, R.J. Workman, Jincheng Du, Xiaonan Lu, M.T Harrison, C Cushman, M.R. Linford and N Smith *Invited review: Physical and optical properties of the International Simple Glass*, NPJ Materials Degradation, due 2019

The work included in this thesis has also been disseminated at a number of conferences and meetings during this time which are listed below;

Oral Presentations

- Dec 2017: Nuclear Research Frontiers Conf., *UK*
- May 2017: GOMD Pacific Rim 12, *Hawaii*
- Apr 2016: Winner IOM3 Young Persons' Lecture, *London*
- Nov 2016: Material Research Symposium, *Boston*
- Sep 2016: Society of Glass Technology Conf., *Sheffield*
- Jun 2016: UK Project on Nuclear Issues, *London*
- Aug 2015: Goldschmidt, *Prague*

Poster Presentations

- May 2017: GOMD Pacific Rim 12, *Hawaii*
- May 2015: Environmental Mineralogy Group, *Leeds*
- Jan 2015: Thermal Treatment of Radioactive Wastes Symposium, *UK*
- Nov 2014: Decommissioning & Radioactive Waste Management, *BGS Nottingham*

Awards and Bursaries

- May 2017:Armourers & Brasiers Travel Grant £800
- Nov 2016: Andrew Carnegie Research Fund £250
- Apr 2016: Winner IOM3 Young Person' Lecture Competition
- Aug 2015: Student Ambassador at Goldschmidt
- Mar 2015: Sheffield Metallurgical and Engineering Association Travel Award £500
- Feb 2015: Mineralogical Society Student Bursary £400

Contents

Chapter 1. Introduction

Geological disposal is a solution proposed by the UK Government for the long term management of higher activity radioactive wastes. The key principle is to isolate the waste from the surface environment to allow the radioactivity to safely reduce naturally to background levels without intrusion from future populations. This will be achieved by surrounding the waste with a number of engineered and natural barriers to restrict the transport of radionuclides to the biosphere[1]. It is internationally recognised that a geological disposal facility (GDF) is the safest solution for permanent disposal, many countries including Belgium, France, Sweden, Finland and the USA are implementing such a strategy[2].

Within the UK, it is envisaged that such a facility will be built at depths between 200 m to 1 km; the facility is expected to house high level waste (HLW) and intermediate level waste (ILW) in two distinct regions of the disposal facility. Each region will be made up of vaults and galleries to allow emplacement of waste containers. In the 2016 UK radioactive waste inventory[3], it was stated that 1500 m^3 of HLW was packaged or due to be packaged; much of this waste has been vitrified. The volume of ILW is significantly more, currently at 99,000 m^3 but increasing to an estimated 191,000 m^3 by 2125. There are many ILW waste streams that require different processing techniques to condition the waste into a safe wasteform that meets the industrial standards, these include; encapsulation in cement in stainless steel or concrete containers, wastes immobilised in polymer in a mild steel container which will later require an over pack, in addition to vacuum drying methods. The 2016 inventory does not contain vitrified ILW, however, several organisations have identified vitrification of ILW as a viable alternative to the methods listed above[4] and there have been several full scale ILW melt trials in the UK in collaboration with Veolia (formally Kurion) using the GeoMelt® system.

[1]The safety case for the geological disposal of nuclear waste is dependent on the behaviour of multiple engineered barriers. The wasteform is the first barrier to radionuclide release (last to groundwater access), followed by the waste container. Once the waste packages are placed inside the designated vaults within a GDF, they will be backfilled. It is likely that different backfill

[1] The reader is directed to NDA report no. DSSC/402/01[6] for further information on the illustrative disposal concepts in the UK for three types of host rock.

materials will be used in the HLW and ILW regions of the disposal facility; the HLW deposition tunnels will be backfilled with a clay material similar to bentonite. A specially formulated cement called Nirex Reference Vault Backfill was proposed in the 1990's as a backfill[5] for cementitious waste packages in the ILW vaults in a hardrock (e.g. granite) GDF.

It is essential to demonstrate that the multiple barriers can provide the necessary long-term safety[1] before a GDF can be operated. The research presented in this thesis provides underpinning scientific understanding of the mechanisms that control glass dissolution in an evolving geo-disposal environment and quantifies the rates of dissolution, that may be used as input to so-called source-term models.

The thesis is structured as follows:

Chapter 2 is a review of the relevant literature on glass dissolution in high pH solutions with a focus on cementitious leachates. It is evident that there are gaps in the literature regarding complex high pH solutions, hence the desire to conduct the experiments outlined in Chapters 4 to 7. The experimental methods for all of the results chapters are outlined in Chapter 3; the reader is directed to the pull-out page in Appendix II, which tabulates the compositions of the glasses and solutions used in the research in an easy-access format.

Synthetic cement waters representative of an aging Portland cement were utilised in Chapter 4 which outlines the results from dissolution tests on HLW and ILW glasses over a three month period. Chapter 5 investigates the impact of synthetic young cement water with added Ca on the International Simple Glass (ISG), a 6-component reference glass widely investigated by other researchers in glass dissolution. This chapter has been published in the Nature Materials Degradation journal and has been a collaborative study with the Belgian nuclear waste research organisation, SCK.CEN, and the Oak Ridge National Laboratory, where the author visited on a three-month placement. Chapter 6 considers the implications of an evolving geochemical environment on glass dissolution behaviour, and details the results of experiments were the solution was replaced with synthetic cement waters or ground water mimicking an aging leachate.

The final results chapter (Chapter 7) addresses the requirement for understanding how potential engineered barrier cement materials, namely NRVB and BFS:PC, will interact with glass wasteforms (MW, LBS and ISG glasses). These hardened cement pastes were dissolved in water to generate cement equilibrated waters used as leachates for the dissolution experiments.

Chapter 8 details a final discussion, which compares synthetic cement waters to the cement equilibrated water. It also highlights the implications of this work for the developing safety case for nuclear waste disposal in a cementitious geological disposal facility.

Finally, Appendix I. provides information on a natural analogue study at the Peak Dale Cave in Buxton, conducted in collaboration with the British Geological Survey. It contains two peer reviewed MRS Advances proceedings papers that pave the way for future work at the site.

Chapter 2. Corrosion of Nuclear Waste Glass in High pH, alkali and alkali-earth solutions: A Review

2.1. Introduction

This Chapter summarises the existing literature relating to glass dissolution in high pH, alkali and alkali-earth solutions, with the aim of facilitating the understanding and critical analysis of this PhD thesis.

In recent years the implications for glass dissolution in high pH, cement-rich environments have been considered; the majority of research in this field is being conducted in the UK, Belgium and France. Within the UK, one of the possible scenarios for the disposal of waste in a hard rock geology (e.g. granite) includes the co-disposal of HLW and ILW within a single GDF[1] (Figure 2.1); a large proportion of the existing ILW inventory comprises cemented wasteforms. When emplaced within a hard-rock disposal concept, the ILW vaults will be backfilled using a specialised high pH cement grout known as the Nirex Reference Vault Backfill (NRVB), which has been specially formulated to promote chemical retardation of radionuclide species (in addition to some other key functions; the reader is directed to a recent review by Vasconcelos et al.[7] for further information). In recent years, much attention has been focused on alternative immobilisation strategies for ILW[8]; the application of thermal treatment using vitrification technologies, such as Geomelt®, is currently undergoing 'cold' testing with simulant nuclear wastes and it is anticipated that the resulting vitrified product, which has a radiogenic heat output similar to cementitious ILW, will be co-disposed with cement. Safety assessments are being conducted to determine the compatibility of vitrified ILW with a cementitious disposal environment. Additionally, since vitrified HLW will be co-disposed within the same facility, albeit not in the same vaults, the proximity of a large volume of cementitious materials may result in the generation of a high-pH, alkaline plume that may contact the HLW glass, should it be transported by groundwater.

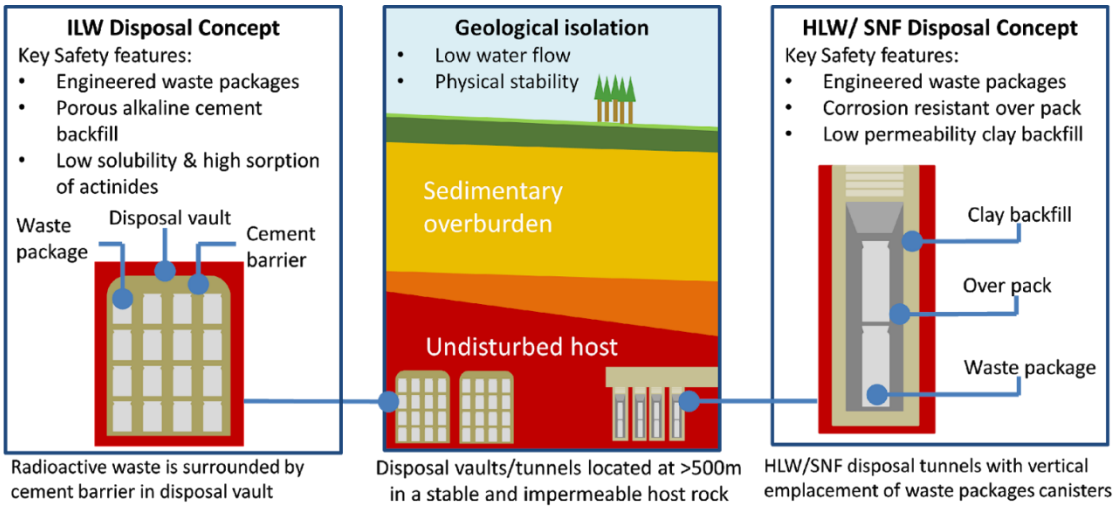

Figure 2.1 UK generic geological disposal concept for nuclear waste in high-strength crystalline rock, including separate but co-located disposal concepts for ILW and HLW/spent nuclear fuel. Adapted from Corkhill et al.[9]

The Belgian disposal concept for spent nuclear fuel and vitrified HLW, in the Boom Clay formation near Mol, is known as the Supercontainer design[10]. The design utilises a watertight carbon steel overpack, which houses two waste canisters[11]. This is surrounded by a protective (~70 cm thick) Portland cement buffer with limestone aggregates to generate a highly alkaline environment to inhibit the corrosion of the carbon steel overpack through passivation of the carbon steel surface. The buffer is encased with a 309 grade stainless steel[12] envelope a few millimeters thick. Following emplacement within the horizontal galleries in the Boom clay, any remaining voids will be backfilled with a cement based material (Figure 2.2).

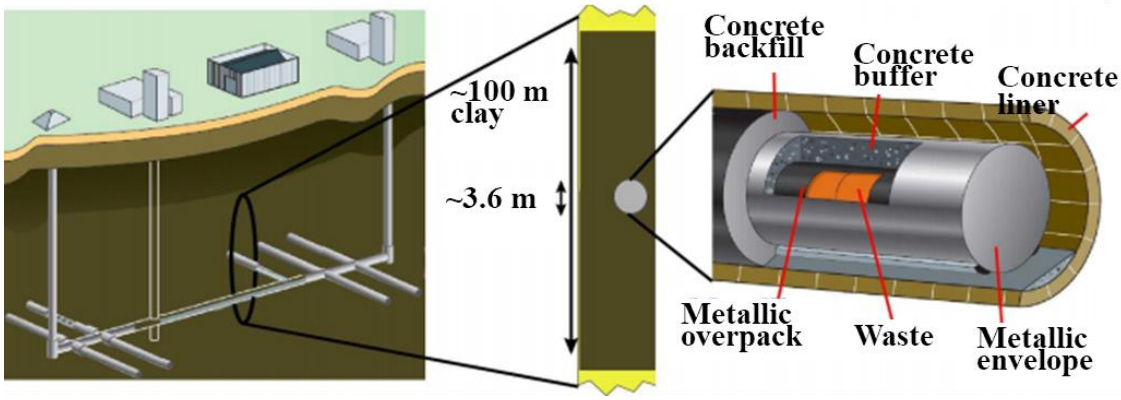

Figure 2.2 Taken from Geet et al[13]*. Schematic view of the Supercontainer design, and the current reference layout of a geological repository in plastic clay like the Boom clay.*

The main drivers for selecting the Supercontainer design are long term safety and operational handling. First, the engineered buffer around the overpack will have predictable chemical

conditions and will ensure the corrosion rate is slow due to the formation of a passive oxidation layer that is expected to form on the surface of the overpack under high pH conditions, aiding both the containment and chemical retardation of radionuclide release from the waste[14]. Second, the thick concrete buffer layer provides permanent shielding, protecting the workforce and eliminating the need for remote handling[13].

Most other disposal concepts avoid direct contact of the clay and cementitious material, however, due to the limited strength of the Boom clay, concrete liners are required in the galleries[15]. Glass wasteforms will not be in contact with cementitious pore water during the thermal phase, although the overpack will eventually fail and high pH cementitious pore water will initiate the dissolution of the glass and radionuclide migration into the buffer[14].

The major component of most cement formulations utilised in the immobilisation or disposal of nuclear waste is Portland cement, which is composed of Ca-silicates (Ca_3SiO_5 and Ca_2SiO_4), Ca-aluminate ($Ca_3Al_2O_6$) and Ca-ferrite ($Ca_4(Al_xFe_{1-x})_4O_{10}$), in addition to other minerals such as Ca-sulphates (gypsum, anhydrite and/or hemihydrate), calcite ($CaCO_3$), Ca-oxide (CaO), Mg-hydroxide ($Mg(OH)_2$), and Na and K-sulphates[16]. When Portland cement comes in contact with water, for example groundwater within a geological disposal facility, K and Na hydroxides are the first elements to leach, resulting in a solution with a very high pH > 13. Hydration products, including C-S-H ($CaO\text{-}SiO_2\text{-}H_2O$), portlandite ($Ca(OH)_2$), ettringite ($Ca_6Al_2(SO_4)_3(OH)_{12}.6H_2O$), calcium monosulphoaluminate ($Ca_4Al_2O_6(SO_4)\cdot 12H_2O$) or calcium monocarboaluminate ($3CaO\cdot Al_2O_3\cdot CaCO_3\cdot xH_2O$ (x =8 or 11)) form. With continual replenishment of groundwater, and ongoing dissolution of these phases, $Ca(OH)_2$ will slowly dissolve (buffering the pH of the pore water to ~pH 12). Once the Ca has been depleted from portlandite, C-S-H phases will begin to dissolve, buffering the pH of the pore water to values in the range of ~ pH 10 to pH 11[17] as demonstrated in Figure 2.3 (adapted from Cau-dit-Coumes et al[18]).

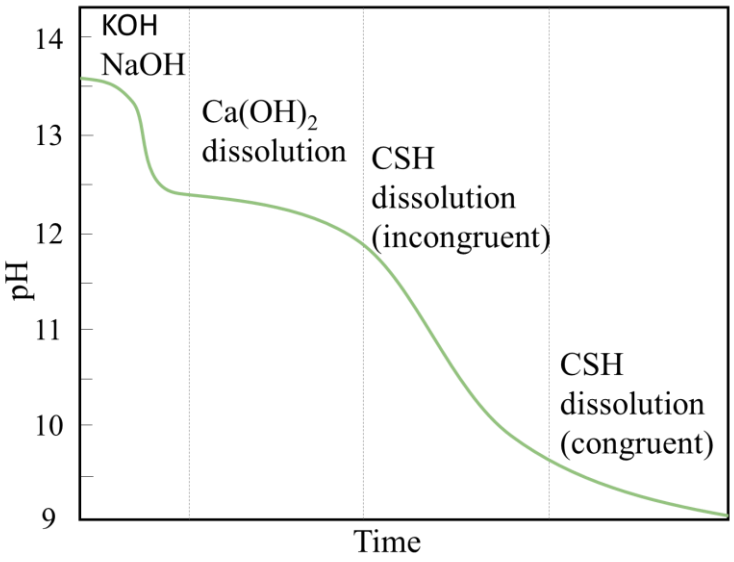

Figure 2.3 Adapted from Cau-dit-Coumes 2006; evolution of Portland cement pore water as a function of time.

While the mechanisms of glass dissolution at near neutral pH have been extensively described by several authors (e.g. Grambow[19], Frugier[20], Gin[21,22], Mercado-Depierre[23] and Geisler[24,25]), the dissolution of glass in high pH, alkali- or alkali earth-rich solutions are less well understood. An increase in the solubility of elements like Si, Al and Zr in the glass network occurs at high pH, and the precipitation of minerals, like calcium silicate hydrates (C-S-H), calcium aluminium silicate hydrates (C-A-S-H), zeolites, clays and layered double hydroxides occurs; some of these phases are normally not observed at near neutral pH[14]. For these reasons, high pH conditions are reported to have a significant influence on the mechanisms and kinetics of each of the dissolution rate regimes (described in detail below). However, the specific role of high pH and alkali / alkali earth content of the leachate medium in the dissolution of borosilicate glass remains poorly constrained; this should be resolved so that models of glass performance in cementitous conditions can be developed.

To this end, a number of studies have attempted to investigate the effect of solution chemistry at high pH on the dissolution of nuclear waste glasses. A major focus has been the effect of high pH alkali or alkali earth solutions on dissolution mechanisms and kinetics, utilising KOH, NaOH or $Ca(OH)_2$ solutions as a simplified version of cement pore waters (described in detail in Section 2.3 of this Chapter). These solutions have been shown to drastically influence dissolution rates and the morphology and composition of alteration layers when compared to dissolution in pure water, due to both pH and the chemical reactivity of Na, K and Ca with silicate in solution or at the glass surface. A review of the current knowledge pertaining to how these factors influence glass dissolution will be discussed herein.

2.2. Influence of high-pH alkaline solutions on the initial rate

It has been well documented that high pH solutions can result in increased dissolution rates[26]. This is a result of the increased solubility of silica above pH 9 which drives dissolution of the glass[27] (Figure 2.4). Above this pH value, dissociation of H_4SiO_4 into $H_3SiO_4^-$ and $H_2SiO_4^{2-}$ occurs, promoting the glass dissolution by silica network hydrolysis[14,27,28]. Conversely, below pH 9, diffusion or ion exchange is the prevalent dissolution mechanism of glass.

Figure 2.4[29] highlights the greater solubility of amorphous silica (v-SiO_2) over crystalline silica (quartz) at high pH[27]. This is important to note because the majority of silica present in glass wasteforms is amorphous and in high pH solution there is a greater abundance of hydroxyl ions that attack Si-O bonds, leaving hydrolysed ≡Si-OH groups[30]. Elements from a cementitious pore water are likely to react with dissolved glass species, in particular silicon[27], and cations like Na, K and Ca (amongst others) act to charge balance the repulsive silicates[31]. With time, amorphous species will slowly crystallise into more stable phases[32], as discussed in (Section 2.3).

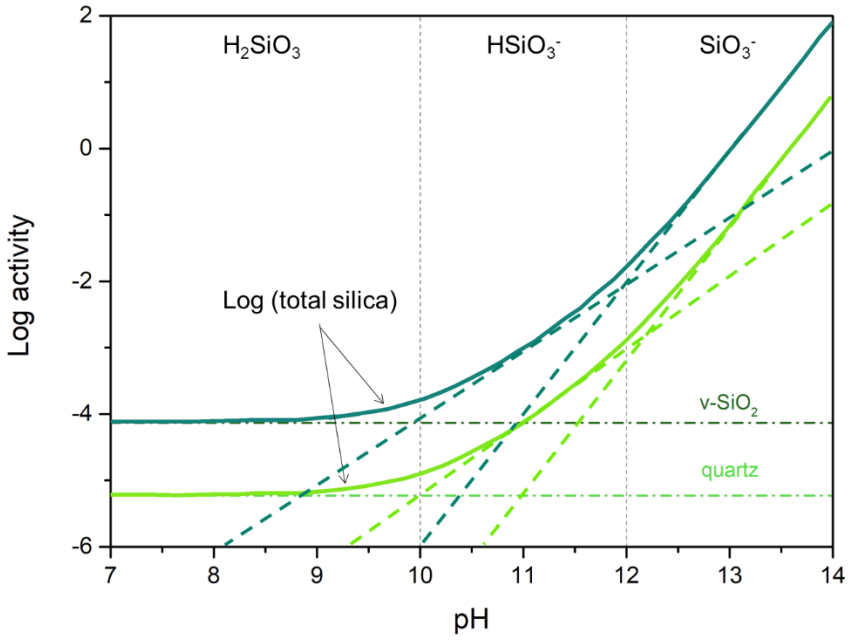

Figure 2.4 Adapted from Paul 1990; change in solubility of silica with pH at 25 °C

Glass dissolved in highly alkaline solutions follows all of the regimes used to describe the dissolution of glass[33], beginning with a linear initial rate followed by a rate drop and a residual

regime. However, in high pH solutions the forward rate is accelerated, and the rate drop is often observed sooner[27] due to the increase in silica solubility above pH 9.

Transition state theory (TST) typically models the kinetics of glass dissolution[28] in under saturated conditions (i.e. in the initial rate). It has been used for waste glasses by Grambow et al.[34], the TST-based rate law has since been modified to account for the intrinsic rate constant being independent of pH as shown in Equation 1, where r is the rate of dissolution, mol/(m^2 s^{-1}), k_i is the intrinsic rate constant, mol m^{-2} s^{-1}, a is the activity of H^+, H_2O, or OH^- (unit less), η_{H^+} is the coefficient for hydronium ions and η_{OH^-} the OH^-, E is the activation energy associated with the acid, water, or hydroxide activated reactions, kJ mol^{-1}; R is the gas constant, kJ mol^{-1} K^{-1} and T is the temperature, Kelvin[35]. The Single Pass Flow Through (SPFT) methodology is the most commonly applied to ascertain the forward (or initial) dissolution rate, which can be achieved when the solution flow rate is high enough to avoid the accumulation of soluble species in solution.

$$r = k_i \left[a_{H^+}^{\eta_{H^+}} + a_{OH^-}^{\eta_{OH^-}}\right]\left[\exp\left(\frac{-E_a}{RT}\right)\right] \qquad \textbf{Eq. 1}$$

To predict the corrosion behaviour of nuclear waste glass in a disposal environment it is necessary to accumulate dissolution rate data and determine rate model parameters and uncertainties[36]. While the initial dissolution rates can be used to extrapolate the glass wasteform lifetime in a disposal facility, there is uncertainty associated with how the repository environment, and specifically the chemistry of the over pack and backfill materials[37], influences such rates.

Generally, the forward rate of glass dissolution increases with an increase in pH from approximately pH 7 to 13 as reported by the authors listed in Table 2.1. Data shown by Cassingham et al.[28] indicated a 5 fold increase in the forward rate of MT-25 glass when the leachate pH was increased from 8 to12. Inagaki et al.[38] observed a ~10 fold increase in the forward rate of the International Simple Glass (ISG) after the pH rose from 8 to10, while Neeway et al.[36] observed the dissolution rate of the same glass to be 23 times faster at pH 12 compared to pH 9 (it was 30 times faster for SON68 at the same pH values). Elia et al.[39] noted that the forward rate of ISG was lower than SON68 in artificial cement waters at pH 13.5, suggesting that Ca had a positive effect in reducing the rate in alkaline solutions. In their study of the dissolution of SON68 in a clay equilibrated ground water, which imposed a higher pH than de-ionised water, Jollivet et al.[40] found that an increase in the forward rate was not due to the pH, but rather the high ionic strength of the clay ground water. The latter investigation is the only SPFT study in the literature

that attempts to understand the effects of Na, K, Mg and Ca in solution on the forward rate; it was found that reduced dissolution rates were concurrent with the removal of Mg, Ca and SO_4 from the clay ground water.

Table 2.1 Summary of forward rates, obtained from the literature, derived from SPFT experiments conducted in high pH solutions. The studies listed here kept the chemical affinity term Q/k near zero so that the inherent forward rate of dissolution was sustained.

Author	Glass	pH	Temp, °C	Rate, g m^{-2} d^{-1}	Solution
Cassingham[28]	MT-25	8	40	R_B 0.051 ± 0.015	THAM +HNO3
		10	40	R_B 0.106 ± 0.032	THAM +HNO3
		12	40	R_B 2.55 ± 0.651	LiOH+ LiCl
Abraitis[41]	MW	10	40	R_B 0.139 ± 0.034	KOH+KCl + x
Inagaki[38]	ISG	5.6	50	Rs_i 0.027 ± 0.002	KCl
		8	50	R_{Si} 0.041 ± 0.003	KCl
		10	50	R_{Si} 0.378 ± 0.030	KCl
Elia[39]	ISG	11.5	30	R_{Si} 0.068 ± 0.018	KOH
		13	30	R_{Si} 0.112 ± 0.040	KOH
		14	30	R_{Si} 0.204 ± 0.126	KOH
		13.5	30	R_{Si} 0.041 ± 0.030	YCWCa
Neeway[36]	ISG	9	40	R_B 0.017	TRIS +LiCl
		10	40	R_B 0.087	TRIS +LiCl
		11	40	R_B 0.100	TRIS +LiCl
		12	40	R_B 0.389	TRIS +LiCl
Neeway[36]	SON68	9	40	R_B 0.021	TRIS +LiCl
		10	40	R_B 0.019	TRIS +LiCl
		11	40	R_B 0.183	TRIS +LiCl
		12	40	R_B 0.651	TRIS +LiCl
Elia[39]	SON68	13.5	30	R_{Si} 0.424 ± 0.246	YCWCa
Jollivet[40]	SON68	6	50	R_{Si} 0.017	DW
		7	50	R_{Si} 0.093	Clay GW

x = additional chemicals were added to the buffer

DW = de-ionised water, GW = ground water, YCWCa = young concrete water+ Ca

2.3. The influence of high-pH alkali and alkaline earth solutions on the transition rate

Increased silica solubility at high pH significantly influences the transition/rate drop regime, which, at near-neutral pH values, is characterised by the formation of a gel through silicon recondensation. This process results in incongruent dissolution due to some of the glass constituent elements being retained in the gel[42] and reduced dissolution rates in comparison to the initial rate. At near-neutral pH, silica gel is formed through hydrolysis and condensation reactions; a $Si(OH)_4$ monomer, formed from monosilic acid polymerises such that there is a maximum number of Si-O-Si bonds and a minimum number of SiOH groups. This behaviour leads to the formation of ring structures that undergo further condensation reactions compacting the Si

particles. This results in the organisation of SiOH groups on the outer surface of the glass, which readily dissolve and re-precipitate onto larger particles in a process known as Ostwald ripening[32].

The pH of the solution, and the presence of "salts" (like alkali and alkaline earth ions), alter the polymerisation mechanisms as outlined in Figure 2.5. Above pH 7, the rate of dissolution and precipitation of SiOH groups is high, which promotes continual Ostwald ripening, resulting in the accumulation of large particles of silica (and large particles give rise to large pores); the growth rate slows as the particle diameter exceeds 10 nm. Under high pH (>pH 10) conditions, $[Si(OH)_3]^-$ and $[Si(OH)_2]^{2-}$ experience repulsion due to their negative charge, which prevents aggregation (therefore not forming a gel). However, in the presence of salts, Si species react with the cations available in solution to compensate for the negative charge (i.e. $[Si(OH)_3] + M^+$). This allows for aggregation to occur which, in turn, leads to gel formation.

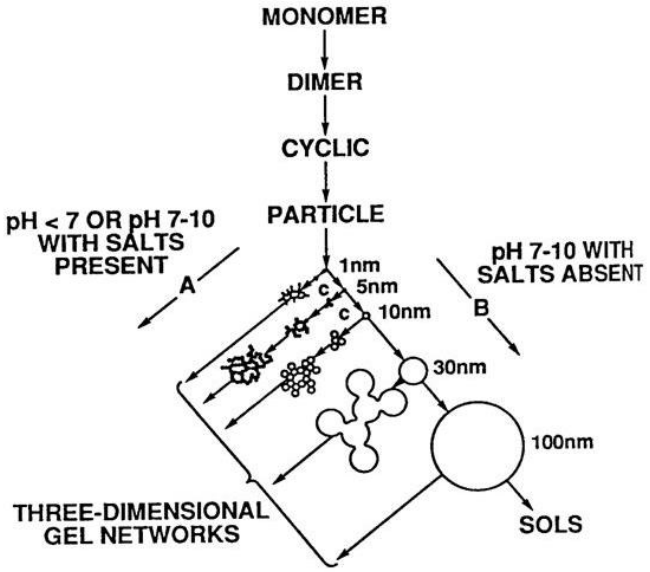

Figure 2.5 Polymerisation behaviour of silica, in basic solutions (B) particles in solution grow in size with decrease in numbers: in acid solution or in the presence of flocculating salts (A), particles aggregate into three-dimensional networks and form gels. Taken from Iler[32]

The diffusion model that is widely accepted for glass corrosion does not adequately describe glass dissolution at extreme values of pH. Geisler et al.[24] provided significant evidence that, at acidic pH, gel layer formation is not the result of diffusion-controlled ion exchange and hydrolysis. Tracer elements in alkali solutions showed chemical oscillations in the alteration layer, enrichment of the tracer elements ^{18}O and ^{26}Mg in the silica rim without observable diffusion profiles, high porosity in precipitated amorphous silica, and silica spherules present at the surface. None of these observations are compatible with a diffusion model; rather, evidence for direct precipitation of amorphous silica from solution fits better with a model described as an interface-coupled dissolution-reprecipitation reaction (Figure 2.6), which considers congruent glass

dissolution in parallel with precipitation and growth of an amorphous silica layer at an inwardly moving reaction interface[24]. The solubility difference between glass and amorphous silica controls the thermodynamics of such a process; the glass dissolution reactions control the kinetics, which in turn is regulated by the transport of soluble elements and water through the developing corrosion zone[14].

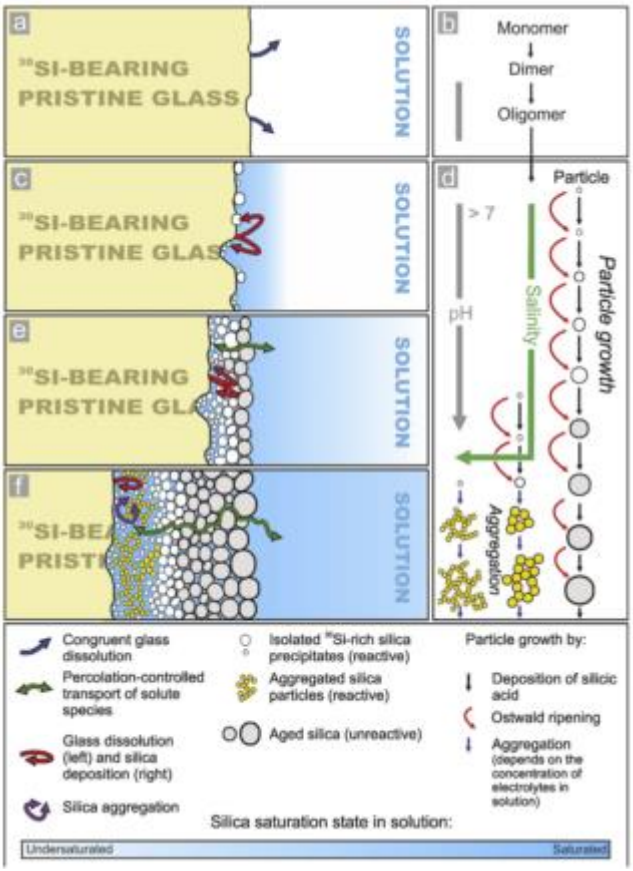

Figure 2.6 Dissolution-re-precipitation model suggested by Geisler 2010; a) congruent glass dissolution; b) Si polymerisation through condensation reactions at the same time as glass network modifiers (Na) are released increasing the pH; c) glass surface is supersaturated, nucleation of amorphous silica starts, and grow to large silica spherules; d) at high pH larger polymeric species become stable, pH and salinity determine growth by direct deposition of silicic acid or by aggregation of colloidal particles, forming a surface layer of spherical silica aggregates of different sizes leading to porosity; e)increased thickness of corrosion rim leads to a decrease in the release in the elements from bulk solution, driving the interfacial pore solution away from equilibrium with the bulk; f) the silica rim reaches critical thickness, restricting transport of water and other soluble species, potentially trapping them.

Under alkaline conditions, the glass experiences nucleophilic attack from the OH^- in solution and the highly degraded silica structure acts as a hygroscopic silica gel. In the presence of alkali ions it is postulated that cross linking can occur, leading to coagulation and the formation of alkali-silica gels[43] as outlined in Figure 2.5. The effect of Na, K, Mg and Ca on gel layer formation at high pH is largely neglected in the literature, although several authors including Gin[44], Collin[45], Rebiscoul[46] and Rajmohan[47] postulated that alkali/alkali earth cations act as charge compensators

for Al and Zr species in the gel. Collin et al.[45] demonstrated that at pH 7 the passivation layer that formed on ISG exhibited selectivity for K > Cs > Na >> Li from solution, replacing the Ca in the pristine glass to charge compensate the Al; the incorporation of cations from solution effected the amount of water in the gel, which impacted the dissolution rates. Silica gel reorganisation is a slow process; soluble elements, such as alkali or alkali-earth cations, are not efficiently transported from the glass (or from the solution to the glass) so they can become trapped in pores. Once trapped, silica gel has the ability to absorb metal cations and alkali elements into its structure[48]; Al^{+3}, Fe^{+3}, and Mg^{+2} have been reported to substitute into the gel causing morphological changes in the gel structure[49], and there is ample evidence that Ca^{2+} can do the same (see below). The combined effects of high pH and element substitution have been shown to interrupt the recondensation process, resulting in greater porosity and elevated surface area of the gel, thereby promoting more diffusion through the gel[50]. Rajmohan et al.[47] showed that once dissolved Si reached a steady state in solution, Al and Zr readily interacted with the gel, and alkaline earth (Ca) or alkali metals (Na) were retained in the gel to charge compensate Al and Zr[47]. Furthermore, Kaspar et al.[51] demonstrated that as the solution pH increased, the porosity of the silica gel alteration layer increased.

In a comparison of the effects of Na and K on the dissolution of SON68 glass at pH 11.4 and 90°C, Ribet et al.[52] observed a reduction in the initial rate when compared to that observed at pH 7 to 10. They attributed this to the formation of a Si-gel layer, but did not specify its composition or porosity. The dissolution rate was greater in NaOH solution than in KOH, as evidenced by the normalised mass loss of B, depicted in Figure 2.7. The glass entered the rate drop regime more rapidly in NaOH (at day 14) compared to KOH (at day 28), indicating that the type of alkali species plays a role in the gel layer formation.

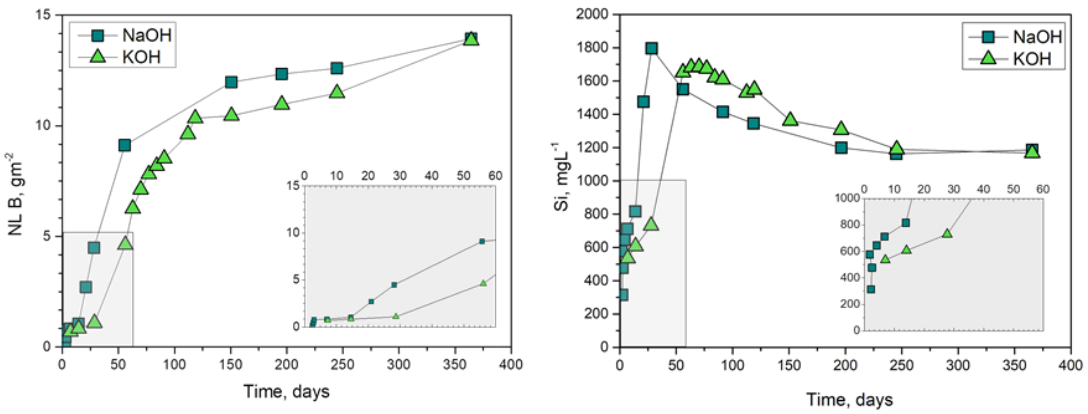

Figure 2.7 a) LHS Normalised mass loss of B (gm^{-2}) from SON68 in NaOH and KOH solution b) RHS dissolved Si concentration (mgL^{-1}) in NaOH and KOH at pH 11.4. Taken from Ribet 2004.

Another example of a study that aimed to identify the influence of high pH and alkali elements in solution on glass dissolution was that performed by Andriambololona et al.[53], who investigated the dissolution of the French glass, R7T7, in Volvic water containing crushed hardened cement paste compositions (pH 9 – 10.5), and a synthetic cement effluent known as 'Lawrence solution' (pH 12.6). Full compositions of each solution are listed in Table 2.2.

Two monoliths of glass were placed in each test vessel. Figure 2.8 shows the concentration values obtained in the 6 different test conditions. R7T7 exposed to the Lawrence solution exhibited the greatest accumulation of elements in solution, concurrent with the very high pH and high alkali and alkaline earth composition of this solution. When hardened cement paste was present in the water, the corrosion rates of the glass were at least 10 times lower than in pure Volvic water and also lower than the Lawrence solution.

Despite the high pH (12.5), and overall elevated dissolution in the Lawrence solution, there was an "incubation" period where the initial (0 to 14 day) rate of release of elements from R7T7 to solution was lower than in Volvic mineral water (pH 9.1) (Table 2.2). The authors attributed this behaviour to the formation of a protective gel on the glass surface (Figure 2.9) that was composed of Si-Al-Na from the glass and Ca and K released from the solution. Figure 2.9 demonstrates the variation in alteration layer thickness under the 6 different test conditions; dissolution in the presence of Portland cement (M1) led to the formation of a thick alteration layer (~ 26 µm) when compared to Volvic water (~2.1 µm) and Lawrence solution (~ 11.3 µm). The gel layer was described as acting as a diffusion barrier, inhibiting further corrosion of glass elements. Multiple alteration zones were observed, which were depleted in Si when exposed to Portland cement. Andriambololona attributed this to the Ca reaction front restricting Si extraction from the glass[53].

Table 2.2 Solution pH and composition taken from Andriambololona[53], units for elements in solution are mg L^{-1}.

	pH	mg L^{-1}					
		Si	Na	Li	Al	Ca	K
Volvic water	9.1	10.7	9.2	-	-	9.8	5.5
Lawrence solution	12.6	0.75	434	0.2	0.4	112.7	1788
PC (M1) + Volvic	10.5	3.6	104	2.7	1	82	305
PC + 20% pozzolana (M2) + Volvic	9.0	10.6	74	2.1	2.7	590	51
PC + 5% amorphous Silica (M3) +Volvic	9.5	2.6	51	3.2	2.4	576	35
BFS (M4) + Lawrence sol.	10.5	2.6	956	0.8	5	350	1815

The values listed are for blank solution after 91 days

PC = Portland cement, BFS = Blast furnace slag

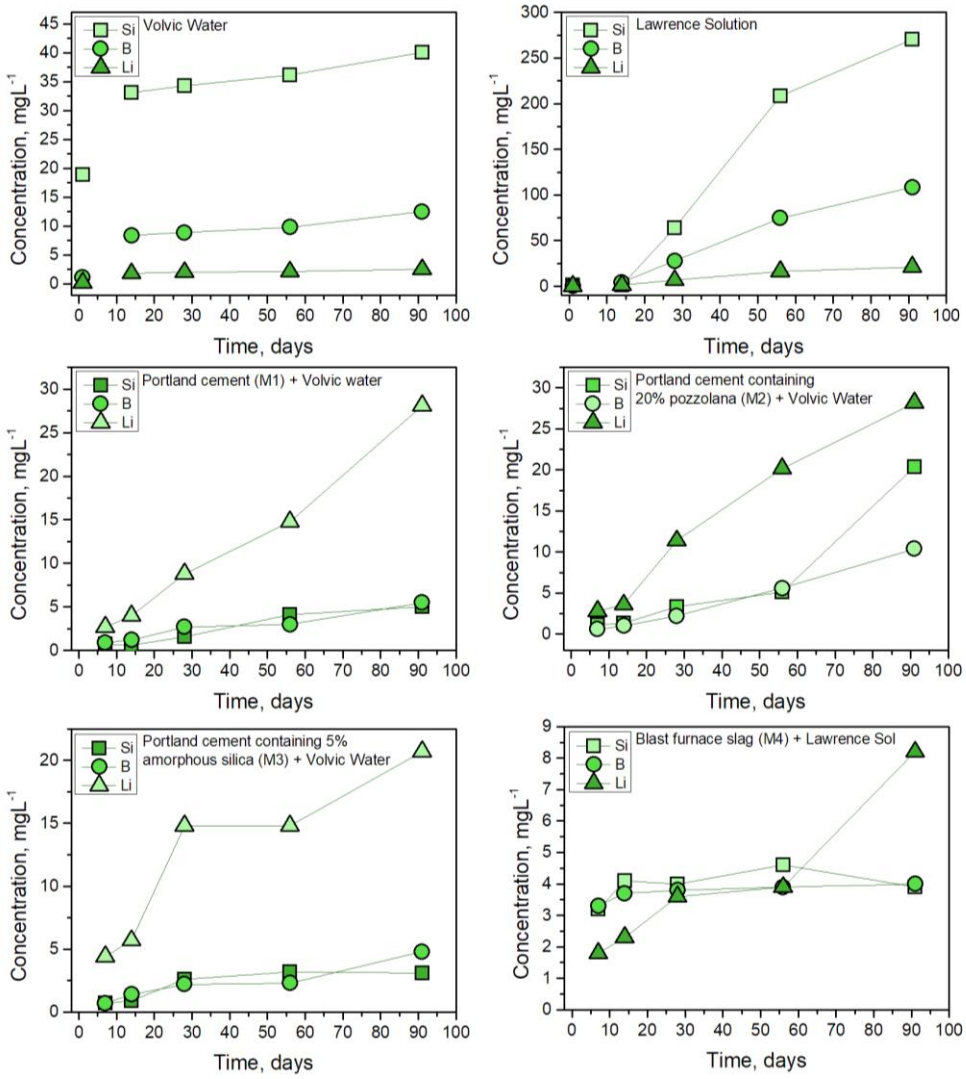

Figure 2.8 Adapted from Andriambololona, glass corrosion in Volvic mineral water, Lawrence solution and leachates containing mortars M1-M4: Si, B and Li concentration in the leachate versus time.

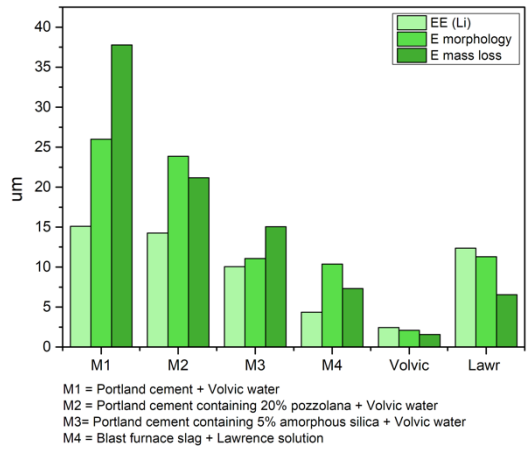

Figure 2.9 Equivalent leached glass thickness calculated from Li concentration in solution, measured on polished cross sections and calculated from mass losses after 91 days. Adapted from Andriambololona,

A number of recent publications have highlighted the significant role that Ca can play in the dissolution of glass materials[23,54–57]. Despite this, there is ambiguity over the terminology used to describe phases and gel layers that are composed of Ca. In the literature, the term "C-S-H, or calcium silicate hydrate" has been used to describe *both* the Ca-containing amorphous gel layer that forms during the condensation of dissolved silica and also the (semi)crystalline precipitates containing Ca and Si that are formed *on top* of the initial gel layer. Since these are formed by different mechanisms, we have distinguished these as two distinct phases: 1) Ca-silica gel, which is a layer formed at the onset of the rate-drop regime by recondensation of Si to form a gel, into which Ca is incorporated (sometimes with Al) as a charge compensator. This typically has a low Ca:Si ratio and is not crystalline in nature; and 2) C-S-H precipitates, which are phases formed via precipitation from solution on top of the gel layer. These phases may be nano- or micro-crystalline and typically have a higher Ca:Si ratio than the gel layer (0.5 to 3.0 [58]), although over time, and as Ca is consumed from solution, the Ca:Si ratio can decrease.

The importance of Ca as a charge-compensating cation within the silica gel layer has been shown by a number of authors. For example, the presence of Ca was found to initially mitigate the effects of high pH, and Ca was found to react with the glass during alteration layer formation, slowing the dissolution rate of the glass[59]. Maraghechi et al.[30] reported that dissolution of silicate glass was slower in the presence of Ca due to the formation of a strongly adhered, "*protective C-S-H layer, formed by in-situ transformation of the glass as opposed to precipitation from solution*" [30], with high density (and low porosity); Note that the suggestion of in-situ transformation indicates this is a Ca-silica gel rather than C-S-H precipitate. Furthermore, it has been observed that when the concentration of Ca in solution is restricted, an apparently passivating Ca-silica layer can be formed[60], lowering the dissolution rate either by limiting the Si-O bond hydrolysis or through the inclusion of Ca in the gel layer to compensate the non-bridging O of Si species[54,56]. Corkhill et al.[61] and Utton et al.[59] observed a delay in the release of Si from the glass in saturated $Ca(OH)_2$ solutions, which was termed the "incubation regime", explained by the removal of Ca from solution and subsequent incorporation into the hydrated surface as a Ca-silica gel, although Utton et al. postulated the cause may have been due to the formation of a Ca-borate phase. As such, the dissolution rate was found to be an order of magnitude lower than observed for the same glass dissolving in water. Conversely, Ferrand[54] observed that when an unlimited supply of Ca is present, the dissolution of glass is accelerated due to the formation of both Ca-silica gel and C-S-H precipitates, which continually drive Si dissolution through dissolution / re-precipitation reactions.

Figure 2.10[62] shows that the initial reaction of Ca with dissolved Si is highly pH dependent[60]. Below pH 7 at 90 °C, Ca is not expected to react with amorphous silica; however at pH values of > pH 10, Ca, Si-bearing phases have been observed experimentally by Atkinson[63], Greenberg[64]and Fujii[65], and modelled by Sugiyama et al.[62]. The data shown in Figure 2.10 illustrates the relationship between pH and Ca:Si ratio; as the pH increases, so too does the Ca:Si ratio of the phase.

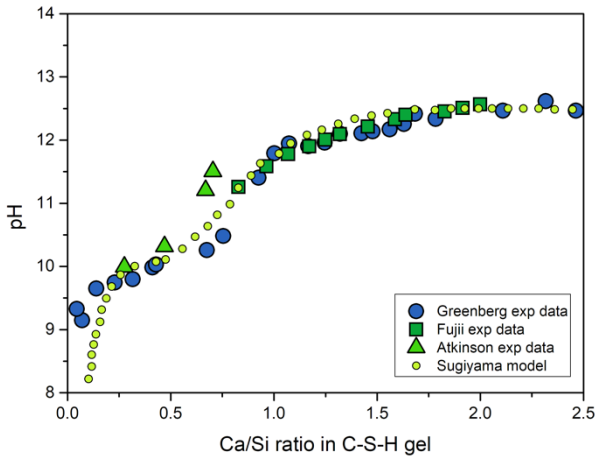

Figure 2.10 Adapted from Sugiyama 2006, Ca:Si ratio in C-S-H gel with pH

Nieto et al.[66] demonstrated that once Ca is incorporated into a Ca-Si gel it could not be removed except by acid attack since the Ca is chemically incorporated into the solid structure. In agreement with the scheme proposed by Iler[32], the authors hypothesised that the presence of Ca encourages condensation of polysilicate anions and links silicate species together to form a solid by modifying the equilibrium of Ca–Si–H_2O[66].

The CaO-SiO_2-H_2O phase diagram taken from Jennings[67] shown in Figure 2.11 demonstrates how a change in the solution concentration of Ca and Si determines the composition of Ca, Si-bearing phases; line A is the metastable solubility curve for noncrystalline C-S-H phases with a Ca:Si ratio > 1.5, and line B corresponds to crystalline C-S-H phases with a Ca:Si ratio between 0.5 and 1. In glass dissolution, it has been shown that the Ca:Si ratio of C-S-H phases (i.e. Ca,Si-bearing precipitates) evolves as a function of leaching time, towards more crystalline products[61].

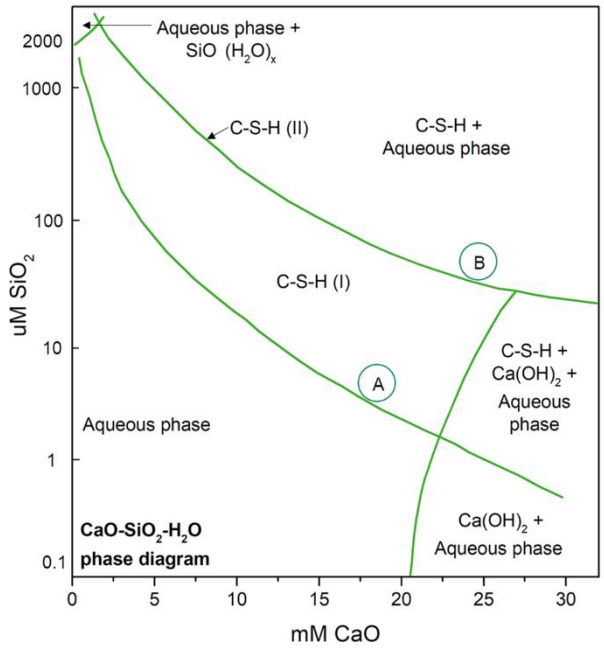

Figure 2.11 Concentration of SiO_2 components vs CaO in an aqueous phase. A CaO-SiO_2- H_2O phase diagram. The logarithmic scale is used to help separate the points at high CaO concentrations. Adapted from Jennings[67]

Mercado-Depierre[23] studied the impact of Ca in solution on SON68 when compared to a solution of KOH. Below pH 10.5, the addition of Ca to solution was shown to increase the initial dissolution rate by a factor of 4 when compared to KOH. Above pH 11, Ca was seen to reduce the initial rate by a factor of 6. At the higher pH value, it was proposed that Ca sorption to the gel layer could result in pore closure, thus limiting diffusion and lowering the dissolution rate. Ca did not incorporate into the alteration layer at pH 8 and, as such, the initial rate increased with an increase in the Ca concentration up to 0.125 $mmolL^{-1}$. At low concentrations of Ca, it was further proposed that metal surface complexes are formed between Ca and Si, and that above a certain threshold concentration, all sites are occupied at the glass surface. Above this concentration, Ca can no longer be incorporated into a Ca-silica gel layer, and instead precipitates with Si dissolved from the glass to form C-S-H or other precipitates[23]. This aligns with the work of Corkhill et al.[61], Chave et al.[57], and Utton et al.[59], who found that once the Ca concentration in a saturated Ca solution dropped to below ~150 – 200 mg L^{-1}, there was no further removal of Ca from solution.

The studies of Corkhill et al.[61] and Utton et al.[55] also indicated that aluminium and other alkali elements (Na, K) may co-precipitate in the Ca- silica gel layer[61]. Utton et al.[59] hypothesised that calcium borate hydrates could be responsible for an incubation period; boron has been shown to retard cement hydration by complexing with Ca in solution[68,69].

2.4. Influence of high-pH alkali and alkali-earth solutions on the residual rate

The residual rate is characterised by the formation of precipitates and secondary phases, including C-S-H as mentioned in the previous section. The secondary phases formed are dependent on the glass composition and leachate solution[27]. Common precipitates identified in high pH alkali and alkaline-earth solutions include variations of C-S-H like C-A-S-H observed by Ferrand[54] in the presence of an Al-rich glass, M-S-H, as reported by Corkhill[61] when Mg-rich glass is dissolved, meixnerite $(Mg_6Al_2(OH)_{18}\bullet 4(H_2O))$ [70] and clay phases, predominantly smectite clay (e.g. saponite $(M^{+}_{x-y}nH_2O)\,(Mg_{3-y}(AlFe)_y)\,(Si_{4-x}Al_x)\,O_{10}OH_2)$ [59, 70–74]. The precipitation of these phases, controlled by the composition of the solution, the solution pH and the composition of the glass, can exert a significant influence on the dissolution behaviour.

Table 2.3 summarises the available literature pertaining to studies that have attempted to elucidate the influence of varying the pH and the alkali / alkaline-earth composition of the solution on the residual rate. When compared to dissolution in water, the rate of dissolution for SON68[52] at 90 °C is higher in NaOH and KOH (where NaOH > KOH). The same observation is true for Magnox waste glass (MW) [70,75] at 40 °C (Table 2.3). Compared to a study of SON68 dissolution conducted in DI water by Curti et al.[72], Ferrand et al.[54] found that the average rate of dissolution of the same glass was a factor of 10 lower when dissolution was performed in a synthetic cement water (YCWCa). Thus, the common assumption that the presence of cement has a negative impact on glass dissolution is not necessarily supported by the available residual rate data shown in Table 2.3. However, it is true that cementitious solutions generate complex dissolution media that are currently not fully understood.

Table 2.3 Summary of residual rates obtained from the literature from authors who conducted leaching tests in high pH, alkali or alkali-earth bearing solutions.

Author	Glass	SA/V, m^{-1}	Solution	pH @ 25ºC	Initial rate, g m^{-2} d^{-1}
Utton et al. [59]	LBS	1200	$Ca(OH)_2$	12.37	NL_{Na} 0.023 @ 50 ºC
	Clino	1300	$Ca(OH)_2$	12.29	NL_{Na} 0.041 @ 50 ºC
	PCM	1200	$Ca(OH)_2$	12.42	NL_{Na} 0.041 @ 50 ºC
Utton et al. [75]	MW	1200	NaOH	12.0	NL_B 0.156 @ 40 ºC
	MW	1200	$Ca(OH)_2$	12.0	NL_B 0.029 @ 40 ºC
	LBS	1200	$Ca(OH)_2$	12.0	NL_B 0.024 @ 40 ºC
Utton et al. [55]	LBS	10	$Ca(OH)_2$	12.5	NL_B 0.122 @ 50 ºC
	LBS	9750	$Ca(OH)_2$	12.5	NL_B 0.012 @ 50 ºC
Corkhill et al.[61]	MW	10,000	Water	9.8	NL_B 0.00003 @ 50 ºC
		10,000	$Ca(OH)_2$	12.4	NL_B 0.00006 @ 50 ºC
Curti et al.[72]	MW	1200	DI water	9.6	NL_B ~0.0149 @ 90 ºC
	SON68	1200	DI water	9.6	NL_B ~0.0133@ 90 ºC
AMEC report[76]	MW25	1200	DI water	9.7	NL_B 0.015 @ 40 ºC
		1200	$Ca(OH)_2$	12	NL_B 0.0329 @ 40 ºC
Backhouse thesis [70]	ISG	10	$Ca(OH)_2$	13.5	NL_B 0.146 @ 50 ºC
		1200	$Ca(OH)_2$		NL_B 0.051 @ 50 ºC
	MW	10	$Ca(OH)_2$	13.5	NL_B 0.087 @ 50 ºC
		1200	$Ca(OH)_2$		NL_B 0.062 @ 50 ºC
Mercado-Depierre et al. [23]	ILW (7oxide)	1000	PW + lime	11.7	NL_{Na} 0.082 @ 50 ºC
		1000	KOH (no lime)	11.7	NL_{Na} 0.056 @ 50 ºC
Ribet et al.[22]	SON68	65	NaOH	11.4	NL_B 0.0517 @ 90 ºC
		65	KOH	11.4	NL_B 0.0183 @ 90 ºC
Ferrand et al. [54]	SON68		Synthetic YCWCa	13.5	NL_{Li} 0.006 @ 30 ºC
	SM539		YCWCa + 2.14 g PC		NL_{Li} 0.007 @ 30 ºC
			YCWCa + 7.5 g PC		NL_{Li} 0.018 @ 30 ºC
			YCWCa + 22.5 g PC		NL_{Li} 0.007 @ 30 ºC
Andriambololona et al. [53]	R7T7	36.25	CPA	10.5	NL_{Li} 0.19 @ 90 ºC
		36.25	CPA + pozzolana	9	NL_{Li} 0.19 @ 90 ºC
		36.25	CPA + amorphous Si	9.5	NL_{Li} 0.30 @ 90 ºC
		36.25	BFS cement	10.5	NL_{Li} 0.10 @ 90 ºC
		36.25	Volvic mineral water	9.1	NL_{Li} 0.30 @ 90 ºC
		36.25	Lawrence solution	12.5	NL_{Li} 0.09 @ 90 ºC

YCWCa= Young concrete water with added Ca
PC= Portland cement
PW= Portlandite saturated water
CPA = Portland cement
BFS = Blast furnace slag

Utton et al.[75] showed that MW dissolved five times faster in NaOH compared to $Ca(OH)_2$ as shown in Figure 2.12 and Table 2.3. The lower dissolution rate observed in $Ca(OH)_2$ solution was attributed to the removal of Ca from solution (Figure 2.12) and its subsequent reaction with the glass to form Ca-rich precipitates, which reduced the dissolution rate through the passivating effects of the precipitate layer.

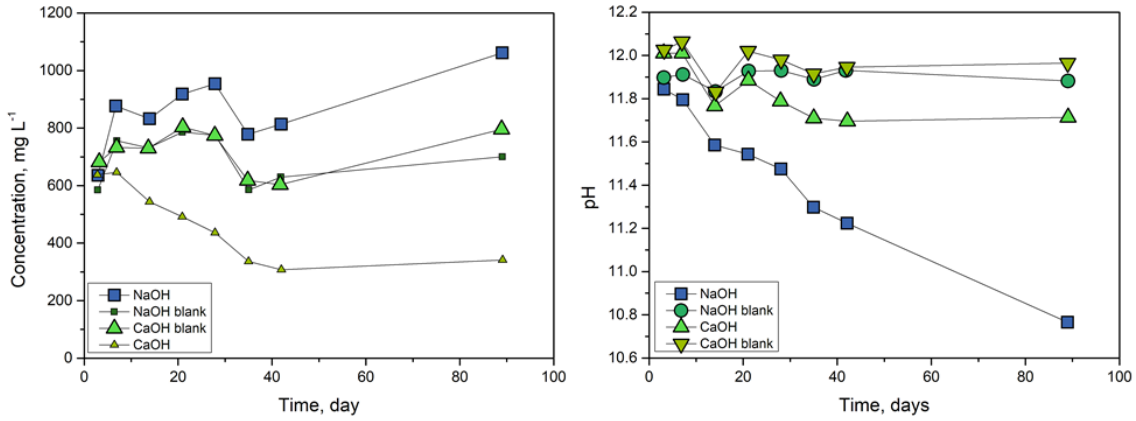

Figure 2.12 LHS: Ca and Na concentrations in $Ca(OH)_2$ and NaOH solutions as a function of HLW glass leaching at 40 °C as compared with blank solutions; RHS: variation of pH under the same conditions. Adapted from Utton[75]

Ferrand et al.[54] designed an experiment to study the dissolution behaviour of SON68, the inactive reference of R7T7 and SM539 HLW glasses, in the presence of Portland cement. Four glass monoliths were mounted above crushed hardened cement paste in a solution of synthetic cement water (YCWCa) at pH 13.5; glass powder was then placed at the bottom of the test vessels to mix with the crushed cement, which was stirred for the duration of the experiment. The concentrations of Na, K and Ca in the initial solution were 3300 mg L^{-1}, 12900 mg L^{-1} and 16 mg L^{-1} respectively. The authors concluded that the cement acted as a sink for the matrix elements of the glass, since the concentration of these elements in solution was far from saturation. This resulted in relatively high dissolution rates compared to solutions that had a restricted Ca concentration; for example, in a solution of YCWCa with no added cement, the Ca concentration was 1.38 mg L^{-1} (compared with 55.99 mg L^{-1} in the presence of cement), and the dissolution rate was a factor of three lower. This led the authors to suggest that alteration layers on the surface of the glass did not act in a protective manner. A Si-gel layer was observed in these samples and was found to contain Ca or Ca and Al in the Al-rich SM539 glass. The pore size of the gel, as measured by high resolution TEM, was found to be ~ 10 nm in diameter, which is large enough for water molecules (>0.28 nm[77]) to pass through, to which the authors attribute the elevated dissolution rates. In support of this hypothesis, recent experiments by Kaspar et al.[51] correlated alteration layer porosity and pH when studying ISG; it was found that as the pH of the leachate increased, the number of voids/pores increased at the surface of the alteration layer. This concurs with Iler's model (Figure 2.5) for polymerisation at high pH; larger particles form leading to greater porosity.

UK HLW glasses have a significant concentration of Mg, resulting from reprocessing of spent fuel clad in Magnox alloy (comprised of Mg and Al). Magnesium, as a divalent cation similar in chemistry and hydrated ionic radius to Ca^{2+} [Mg_{hyd} 4.28 Å, Ca_{hyd} 4.12 Å[45,78]], should also be

considered as a species that may play an important role in gel layer and secondary phase formation at high pH, although above pH 12, the solubility limit for brucite ($Mg(OH)_2$) is reached. Below this pH however, $Mg^{2+}_{(aq)}$ is a stable chemical species in solution. Schofield et al.[79] suggested that there was a correlation between the amount of Mg in the glass (and a concurrent reduction in Ca) and the extent of leaching. Harrison et al.[80] concluded that with a greater ratio of oxide to Magnox waste (which thus lowered the Mg content), the durability of the glass improved. Magnesium has been reported to have dual effects on glass dissolution[55]; for example, it could act as a charge compensator in the gel alteration products, that can protect the glass in much the same way as Ca (the affinity for the gel is highest for Ca >Mg > Na)[81]. However, if Mg-containing secondary phases form, such as aluminous hectorites ($Na_{0.52}(Mg_{2.47}Li_{0.12}Al_{0.11}Fe_{0.01}M_{0.29})(Si_{3.45}Al_{0.55})O_{10}(OH)_{2,}$ M = trace cation)[82], the dissolution rate has been shown to accelerate due to the consumption of Si to form these phases. Curti et al.[72] concluded that Mg-free SON68 glass had better resistance to corrosion and radionuclide retention properties than Magnox glass as a result of the slow formation of clay phases[72]. It should also be noted that Magnox glass is sensitive to Li concentration; increased Li content leads to an increase in elemental losses from the glass during aqueous corrosion[80].

Ribet et al.[52] observed cation incorporation into the alteration products; the concentration of K decreased in solution, suggesting that alteration products consumed a large proportion of hydroxide ions and K^+ cations, leading to an initially K-rich protective layer. The Na concentration continued to increase, indicating that no passivating layer had formed[52]. Liu et al.[83] complemented an experimental study with geochemical modelling to aid determination of secondary phases that formed on the surface of SON68 after more than 300 days in a synthetic cement water (YCWCa). At 30 ^oC no crystalline phases were observed and geochemical modelling indicated that K-phillipsite ($KAlSi_3O_8{:}3H_2O$) was close to saturation. At 70 ^oC, Lui observed Al, Ca, and Si in addition to alkali cations from the solution (namely K) were involved in the formation of secondary phases; phillipsite and foshagite ($Ca_4Si_3O_9(OH)_2{:}0.5H_2O$) (which represents C-S-H in the database) were supersaturated. This agrees with observations by authors Ribet et al[52], Frugier et al.[20], and Ferrand et al.[54] who reported C-(A)-S-H and Na- and K-containing zeolite precipitates on the surface of SON68 after dissolution under high pH conditions and/ or at high temperatures[83].

2.5. Influence of high-pH alkali and alkali-earth solutions on the rate resumption regime

Resumption of the alteration rate, otherwise known as Stage III, is possible at any point during the residual rate, where the solution is close to saturation with Si and a passivating layer has formed. It is generally agreed that resumption of alteration is driven by the precipitation of secondary phases, and zeolites in particular, which develop at the expense of the gel by depleting the Al content in the alteration layer [84]. This phenomenon has also been associated, to a lesser extent, with the precipitation of C-S-H phases[42]. As shown in Table 2.4, one of the key conditions necessary to initiate a resumption of glass dissolution is high pH. A comprehensive review of the role of secondary phases thought to contribute to the resumption of alteration in a selection of glasses was recently published by Fournier et al.[42]; some of the studies featured in this review will be briefly discussed below.

Table 2.4 Occurrence of resumption of alteration of SON68 glass as a function of the temperature and pH, (N: no resumption of alteration observed; Y: resumption of alteration detected. Adapted from Fournier[42]

Author	Temp	pH 8.4- 9.5	pH 10.5	pH 11	pH 11.5
Ferrand[54]	30 °C				N, remained in initial rate (700 d at 4.78 m^{-1})
Frugier[20]	90 °C	N (even at 20000 m^{-1} and > 3000 days			
Gin[85]	90 °C		N (600 days at 6500 m^{-1})	Y (after 200 days at 6500 m^{-1})	Y (14- 28 days at 6500 m^{-1})
Caurel[86]	150 °C	Y (after 30 days at 50 m^{-1})	No data		
Caurel[86]	250 °C	Y (after 21 days at 50 m^{-1})			

(N: no resumption of alteration observed; Y: resumption of alteration detected)

Under alkaline conditions (pH 8-14), Ca-Si gel or Alkali-Si gel (the alkali is often a cation removed from solution and incorporated into the Si-gel), cover the glass surface uniformly prior to zeolite formation. While the mechanisms and kinetics of zeolite formation are not yet fully understood, zeolites that have been observed on glasses dissolved in high pH solutions include phillipsite ($AlSi_3O_8{:}3H_2O$)[87], chabazite ($(Ca,Na2,K_2,Mg)Al_2Si_4O$ and, at high temperatures (150-250 °C), analcime[85] ($NaAlSi_2O_6{\cdot}H_2O$). Glasses with a high alkali metal content, temperatures of > 90 °C or pH > 10.5 and high surface area to volume ratios have been attributed to the formation of zeolitic phases. Other crystalline alteration products observed include C-S-H phases, anhydrite ($CaSO_4$), molybdates, phosphates haiweetie[88] $Ca((UO_2)2Si_5O_{12}(OH)_2){:}3(H_2O)$

and layered double oxides like hydrotalcite[70] ($Mg_6Al_2CO_3(OH)_{16}$:4(H_2O)). Smectite clays[89] ($(Al_{2-y}Mg^{2+}_y)(Si_{4-x}Al_x)O_{10}(OH)_2M^+_{x+y}$: nH_2O, M= interlayer cation) have also been known to form under highly alkaline conditions.

Immediately before the glass dissolution rate accelerates (i.e., resumption) the Al concentration in solution has been shown to decrease [90]. Gin et al.[85] examined the dissolution of SON68 between pH 7-11.5 and determined that alteration resumption could be attributed to secondary phase formation at pH 11 at 90 °C, reporting the precipitation of analcime ($NaAlSi_2O_6.H_2O$). This phase was also observed by Ribet et al.[52] when at pH > 9.6 at 90 °C for SON68. The solution data from this study showed that Si from solution was being incorporated into the analcime phases in solution of NaOH, or the phase merlinoite ($K_5Ca_2(Al_9Si_{23}O_{64}).24H_2O$) in KOH solution, despite the concentration of B continuing to increase[52,14].

Table 2.4 confirms that for SON68, the pH threshold for secondary phase precipitation is pH 11 at 90 °C. Ferrand et al.[14] observed a similar threshold for SON68, of pH 11.5 at 30 °C using old cement water (OCW), of pH 12.5 for evolved cement water (ECW), and of pH 12.5 for young cement water with added Ca (YCWCa). The zeolite phase, phillipsite-K ($Na_4KAl_5Si_{11}O_{32}.10H_2O$), was identified in YCWCa at 30 °C and 70 °C[87]. Despite the low temperatures of these experiments, the Al concentrations in solution reached ~ 70 mg L^{-1} [14] Gin et al.[85] made a similar observation. This suggests that high pH dissolution media promote zeolitic formation, even at the low temperatures. Further evidence for this can be found in the PhD thesis of Depierre[91]; at temperatures of 30 °C the formation of merlinoite ($(K,Ca_{0.5},Ba_{0.5},Na)_{10}(H_2O)_{22}[Al_{10}Si_{22}O_{64}]$) was observed on CSD-B glass (French glass formulated for decommissioning effluents from UP2-400 facility in France[92]) at 50 °C.

Inagaki et al.[89] observed the formation of smectite clay ($Na_{0.33}Al_2Si_{3.67}Al_{0.33}O_{10}(OH)_2$) on Japanese simulant waste glass P0789, (which is similar in composition to SON68) at $pH_{(25\ oC)}$ 9.5-12, and analcime formed when the pH exceeded $pH_{(25\ oC)}$ 11. The formation of these secondary phases was dependent on the presence and concentration of alkali metals in solution; smectite formed under all test conditions in NaOH, however analcime was sensitive to the amount of Na in solution and only formed with 0.03 M and 0.1 M NaOH. In KOH Inagaki didn't observe any crystalline phases, indicating that alteration layer formation and rate of formation is influenced by the cation in solution[89].

Ribet et al.[52] indicated that gels formed during resumption of alteration in NaOH and KOH solution (pH 11.4) were not as protective as gels formed at lower pH (8-9), likely due to Si being

used for secondary phase formation rather than silica gel recondensation. This was evidenced by a difference in the Si content calculated from a mass balance; the Si quantity in the gel was 0.32 $g_{Si}\,cm^{-3}$ in a KOH solution and 0.34 $g_{Si}\,cm^{-3}$ in NaOH, compared to 0.57 $g_{Si}\,cm^{-3}$ in R7T7 glass formed during the rate drop regime. In the same study (Ribet[52]), Si was also observed to behave differently in NaOH as compared to KOH; after the initial release of Si to solution, the consumption by a silica gel (as exemplified by the removal of Si from solution) occurred more quickly in the NaOH solution, than in the KOH solution (see Figure 2.7b, Section 2.3). Resumption of alteration, demonstrated by a sharp increase in alteration after a plateau (see grey shaded areas in Figure 2.7b), occurred after 14 to 28 days. This was proposed to be due to the formation of zeolite phases that consumed Al, initially from solution, and then from the gel layer forming minerals such as analcime ($Na\,AlSi_2O_6.H_2O$) (formed at 90 ^oC in 0.25M NaOH for 218 days) or merlinoite ($K_5Ca_2(Si_{23}Al_9O_{64}).24H_2O$) (formed at 90 ^oC in 0.25M KOH for 30 days) at the gel surface. Potassium was removed from KOH solution while Na was continually released into solution in both KOH and NaOH solutions during the rate resumption stage. Alteration products incorporated a large proportion of the hydroxide ions, and the K^+ cations, but less Na^+ leached from the glass. It is likely that the differences in alteration rates are due to K being consumed by the gel to form an initially protective layer.

Ribet demonstrated that it is possible to slow dissolution by controlling the pH; an artificial reduction to pH 9.5 during the rate resumption stage led to an immediate and significant drop in the alteration rate, and a reduction in the Si concentration concurrent with reduced silica solubility at lower pH. SEM images indicated that zeolites were gradually dissolving under these reduced pH conditions, most likely due to the high sensitivity of these phases to the solution chemistry[52].

A greater number of glass dissolution studies at high pH are required to develop a well parameterised model to describe the rate resumption. Evidence suggests that resumption only occurs in high pH solutions; therefore, cement repositories could be determined as a high risk for inducing stage III corrosion, thus making it challenging to predict the long-term durability of the vitrified wasteform required for the disposal safety case.

2.6. Concluding remarks

High pH alkali and alkaline-earth solutions impact the rate of dissolution at each stage of glass corrosion. The dissolution rates increase with a rise in pH, which is due to the higher solubility of silica and, at high pH, the glass dissolution is promoted by silica network hydrolysis. The initial rate is controlled by pH, temperature, glass composition and solution chemistry.

The rate drop can be explained by two theories[93,94]; first, when the solution becomes saturated with dissolved species, the chemical affinity for dissolution decreases. Second, ionic exchange between the glass and solution is restricted due to a protective gel layer on the surface of the glass[95]. Research by Mercado-Depierre[23], Ferrand[54], Corkhill[61], Utton[59], Cailleteau[96], Chave[57] and Andriambololona[53] in the presence of Ca showed that this species had a positive effect on glass dissolution by reducing the initial or final dissolution rates compared to experiments in pure water, through the formation of a passivating gel layer on the surface of the glass. Mercado-Depierre postulated that Ca acts as a charge compensator for non-bridging oxygen of silicon species in a Ca-Si gel or precipitates as C-S-H[23]. Early age cement waters with little or no Ca present still result in reduced dissolution rates when compared to pure water, but these are often higher than when Ca is present. The solution chemistry of such early age cement waters is dominated by NaOH and KOH from Portland cement dissolution, which keeps the pH high, and promotes the formation of alkali-silica gel that protects the glass[87].

High pH and alkali / alkali-earth containing solutions have been linked with zeolite formation, which is considered a pre-requisite for rate resumption. This is thought to occur when zeolites consume Al and Si from the gel, reducing its protective capabilities and leading to a rate resumption regime which in some cases exceeded the initial rates. It is not yet clear how other phases formed at high pH in the presence of Na, K, Ca and Mg. For example, C-S-H and Mg-bearing smectite clays might influence rate resumption behaviour; these phases are all capable of consuming Al and Si from solution, so in theory, could lead to resumption.

Determining the long-term durability of nuclear waste glass in a cementitious environment is complex. In scenarios where vitrified wastes come into contact with a highly alkaline plume from the cement used in construction or the engineered barrier materials, the glass will be exposed to a high pH mixed alkali / alkaline-earth solution, which evolves as a function of time. The majority of research conducted to understand glass-cement interactions has focused on simplified solutions that represent early age Portland cement pore water, focusing on glass dissolution in K, Na and

Ca hydroxide solution. Our understanding of dissolution under these conditions is relatively general; it is widely thought that at pH values of 11.5 and above, the dissolution-precipitation model for glass dissolution adequately describes the behaviour observed. However, limited investigations using high spatial resolution techniques has hindered the proof of this hypothesis.

This thesis sets out to enhance our understanding of how glass behaves during dissolution in high pH, alkali- and alkaline-earth conditions, how the dissolution kinetics are influenced by these solutions, and to elucidate which mechanisms control this behaviour. Furthermore, since the chemistry of cements will constantly evolve within a GDF, the role of the evolving, complex cementitious pore waters on the long term durability of nuclear waste glass within a GDF in the UK will be explored.

Chapter 3. Experimental Methods

3.1.Materials

3.1.1. Vitrification

MW-25% is a sodium lithium aluminoborosilicate glass, loaded with 25 wt % HLW calcine from the reprocessing of UK nuclear waste. The calcine typically consists of HLW from the reprocessing of Magnox fuel (U-metal) blended with HLW from the reprocessing of oxide fuel (UO_2) from ThORP, at a ratio of 75:25 o:m. Significantly, the Magnox portion of the HLW calcine is rich in Mg from the Mg-Al alloy used to clad Magnox fuel rods. For the purpose of this thesis, an inactive surrogate for MW25 was prepared using glass frit (H0023/1 Ca/Zn ½ Li) and calcine (WRW17, contains Ru & Li)) kindly provided by Dr Mike Harrison at the National Nuclear Laboratory. The synthesis parameters are listed in Table 3.1 and the analysed (by HF digest and ICP-OES analysis) composition is detailed in Table 3.2 and the pull-out reference in Appendix II.

The **Laboratory BoroSilicate glass (LBS)** was developed at the University of Sheffield as a demonstration of the feasibility to immobilise ILW Magnox waste stream. The composition was developed by Utton et al.[59] and used in a previous Radioactive Waste Management Ltd. funded study on the geological disposal behaviour of vitrified ILW by Utton et al.[97]. The alkali borosilicate glass contained a 30 wt% loading of a simulant ILW waste stream, comprising; 20 wt% $Mg(OH)_2$, 30 wt% clinoptilolite, 30 wt% sulphonic ion exchange resin and 20 wt% radionuclide surrogates (Cs_2O, SrO, CeO_2, La_2O_3) in addition to metallic corrosion products (Fe_2O_3, Al_2O_3, ZrO_2)[59,97].

The oxide precursors for LBS were weighed and mixed prior to the melt according to Table 3.1. The melting glass rose and bubbled significantly and the melt was fluid at 1000 ^oC. The analysed composition is detailed in Table 3.2 and the pull-out reference in Appendix II. The oxide precursors were; $Al(OH)_3$ (>99.9 % Acros), H_3BO_3 (>99.9 % Merck), $BaCO_3$ (99 % Alfa Aeser), $CaCO_3$ (96 % Fluka), CeO_2 (99.5% Alfa Aesar), $CsCO_3$ (99 % FluroChem), Fe_2O_3 (98 % Alfa Aesar), K_2CO_3 (99 % Sigma), La_2CO_3 (99 % Testbourne), $LiCO_3$ (99.5 % Analar), MgO (99.9 % Acros), MoO_3 (99 % Sigma), Na_2CO_3 (98 % Alfa Aesar), SiO_2 (95 %), $SrCO_3$ (99.9 % Sigma) and ZrO_2 (99 % Aldrich).

Table 3. 1 Melt conditions for vitrified glasses

Glass	MW-25%	LBS
Melt Temp, ^{o}C	1050	1200
Melt Duration, hrs	4	4
Cooling Rate, ^{o}C min^{-1}	1	1
Anneal. Temp, ^{o}C	500	450
Anneal. Duration, h	1	1
Furnace Type	Electric	Electric
Stirred	Yes	Yes
Crucible Material	Alumina	Alumina

The **International Simple Glass (ISG)** was produced by MoSci Corporation (Rolla, MO, USA) as part of an international effort to understand the mechanisms and kinetics of the dissolution of nuclear waste glass[98]. It is a simplified, 6-component oxide glass based on the inactive surrogate for French HLW glass, R7T7 with the following composition (mol%): 60.2SiO_2, 16.0B_2O_3, 12.6Na_2O, 3.8Al_2O_3, 5.7CaO, 1.7ZrO_2[33]. The composition is detailed in Table 3.2 and the pull-out reference in Appendix II. In this thesis, two batch numbers of ISG were used: L12012601-M12050803 (Chapters 6 and 7) and L12012601-M12042403 (Chapter 5).

Table 3.2 Glass compositions wt% values taken from ICP-OES analysis of original samples

	MW25		LBS		ISG	
	wt%	mol%	wt%	mol%	wt%	mol%
SiO_2	39.12	43.08	47.92	52.14	56.20	60.10
B_2O_3	19.40	18.43	9.62	9.03	17.30	15.97
Na_2O	6.84	7.31	12.94	13.65	12.20	12.65
Li_2O	3.20	7.08	3.90	8.54	-	-
ZrO_2	1.02	0.55	0.67	0.35	3.30	1.72
MoO_3	0.90	0.41	0.52	0.24	-	-
Al_2O_3	8.13	5.28	6.85	4.39	6.10	3.84
Fe_2O_3	2.38	0.99	10.25	4.20	-	-
Nd_2O_3	1.38	0.27	-	-	-	-
Cs_2O	0.88	0.21	0.69	0.16	-	-
MgO	3.57	5.86	3.71	6.02	-	-
CeO_2	1.01	0.20	0.36	0.07	-	-
BaO	0.27	0.12	0.11	0.05	-	-
La_2O_3	0.52	0.11	1.53	0.31	-	-
RuO_2	0.63	0.36	0.00	0.00	-	-
Pr_2O_3	0.24	0.05	-	-	-	-
SrO	0.23	0.15	0.13	0.08	-	-
NiO	0.40	0.36	0.05	0.05	-	-
Sm_2O_3	0.25	0.05	-	-	-	-
Y_2O_3	0.14	0.04	-	-	-	-
CaO	4.52	5.33	0.45	0.52	5.00	5.73
K_2O	0.01	0.00	0.15	0.10	-	-
Cr_2O_3	0.41	0.18	0.01	0.01	-	-
SO_3	0.08	0.07	0.02	0.02	-	-
TiO_2	0.01	0.01	0.01	0.01	-	-
Cu_2O	0.02	0.02	0.02	0.01	-	-
ZnO	4.20	3.42	0.01	0.01	-	-
Total	99.74	99.89	99.95	99.96	100.10	100.00

3.1.2. Synthetic Cement Waters

Four synthetic cement waters were prepared for use in experiments outlined in Chapters 4, 5 and 6. These solutions were developed by SCK.CEN to aid understanding of glass dissolution in the supercontainer concept and were designed according to thermodynamic modelling of Portland cement in equilibrium with Boom Clay groundwater. Full details of the modelling can be found in SCK.CEN report ER-17 by Wang (2009)[15], a brief description is given below.

Hydration products were selected based on literature values for Portland cement (Table 3.3 and 3.4) taken from Atkins and Glasser[99]. The volume percentage of concrete aggregates and hydration phases were determined through equilibrium calculations with a thermodynamic database by Wang[15] at SCK.CEN. A water to cement ratio of 0.43 was used to calculate the water content and porosity. The alkali concentration in the concrete pore water was established based on literature values and the total alkali content of the cement. The Portland cement composition, a CEM I type cement, used in the model by SCK.CEN is outlined in Table 3.. Pore water with dissolved alkalis were assumed to be in chemical equilibrium with the selected mineral assemblage of concrete to derive concrete pore water compositions for three stages; young cement water, evolved cement water, and C-S-H water.

Table 3.3 Hydration products selected to model synthetic cement waters by Wang[15]

Hydration Products	Formula
portlandite	$Ca(OH)_2$
afwillite	$Ca_3Si_2O_4(OH)_6$
C-S-H_1.8	$Ca_{1.8}SiO_{4.6}H_{3.6}$
ettringite	$Ca_6Al_2(SO_4)_3(OH)_{12}\cdot 26H_2O$
hydrogarnet	$Ca_3Al_2(OH)_{12}$
hydrotalcite	$Mg_4Al_2(OH)_{14}:3H_2O$
hematite	Fe_2O_3

Table 3.4 Chemical composition of Portland cement used in the model by SCK

Oxide	wt%
CaO	63
SiO_2	20
Al_2O_3	5
Fe_2O_3	3
MgO	2
SO_3	3

Hydration products of the Portland cement were defined as; afwillite ($Ca_3Si_2O_4(OH)_6$ or C-S-H_1.8($Ca_{1.8}SiO_4.6H_{3.6}$), ettringite ($Ca_6Al_2(SO_4)_3(OH)_{12}.26H_2O$), hematite ($Fe_2O_3$), hydrogarnet ($Ca_3Al_2(OH)_{12}$), hydrotalcite ($Mg_4Al_2(OH)_{14}.3H_2O$) and portlandite ($Ca(OH)_2$) according to models outlined by Berner[100], Reardon[101] and Nielsen[102]. Afwillite was used to represent C-S-H in hydrated cement since it is stable in the presence of portlandite at high Ca/Si ratios[15]. An incongruent dissolution model would be required to consider amorphous C-S-H which may be more realistic in a real system.

Liquid phases in a hardened Portland cement paste are located in the pores, and the chemistry of pore water is controlled by the solubility of solid phases like portlandite, calcium silicate hydrates and hydrated aluminate. The theoretical evolution of pore water as a function of geological disposal time is schematically described in Figure 3.1 (adapted from Coumes et al.[103]).

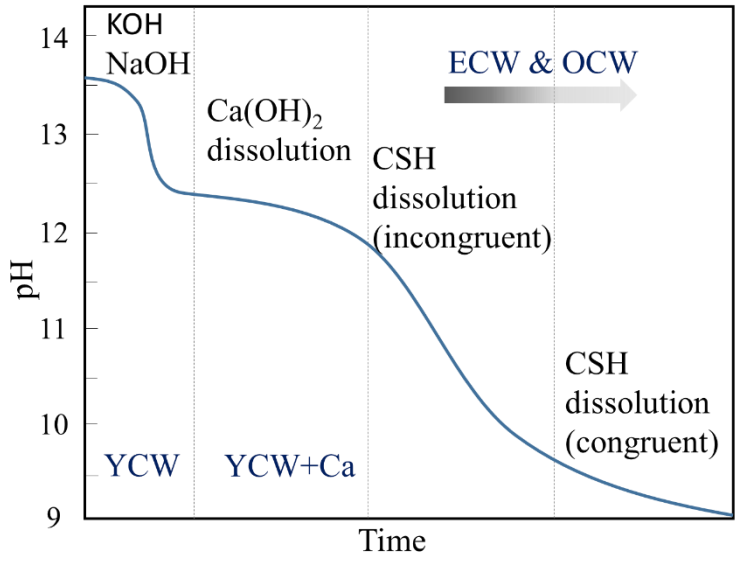

Figure 3.1 Schematic of Portland cement paste pore solution pH during leaching in pure water adapted from Cau Dit Coumes et al (2006)

The initial stage of cement hydration results in a high pH pore fluid due to the high solubility of Na and K sulphate salts. Due to high concentrations of free Na and K, equivalent hydroxyl ions are produced to charge balance the system. This results in a high pH (pH >13) during the initial stage of hydration, giving rise to "Young Cement Water", YCW). In the synthetic version of this solution, Na and K are added in their hydroxide form. As the dissolved alkalis leach into groundwater, the pH is reduced to 12.5 and becomes controlled by portlandite dissolution, giving rise to "Evolved Cement Water" (ECW). With an increasing number of cement pore water volume replacements by groundwater, portlandite dissolves completely and the pH reduces to pH <12, giving rise to "Old Cement Water", OCW. Table 3.6 details the target composition of the cement waters used in this study.

These synthetic cement leachate solutions were prepared in an anaerobic chamber to ensure a CO_2-free environment (O_2 and CO_2 are eliminated using a H_2 and N_2 gas mix), to prevent carbonation (and thus a deviation from the desired solution pH). Degassed ultra high quality water (UHQ, 18 ΩM) was utilised to make solutions of 0.1 M KOH, 1 M KOH and 1 M NaOH. These stock solutions were used in conjunction with chemicals listed in Table 3.5 to create 1 litre of each synthetic cement water solution. Powders were weighed at the bench and transferred to the

anaerobic chamber immediately and left for 1 day before being used to make solutions. The reagents used were; NaOH, KOH, $Ca(OH)_2$ (99 %, 85 % and 96 % respectively, supplied by Merck), Na_2SO_4 (99 % Alfa Aesar) and $CaCO_3$ (99% Sigma).

Table 3.5 Chemicals used to prepare 1 L of each synthetic cement water

	NaOH (l) 1M	KOH (l) 0.1M	KOH (l) 1M	$Ca(OH)_2$ (s)	Na_2SO_4 (s)	$CaCO_3$ (s)
	Mass, g					
YCWCa	136	-	370	0.0296	0.284	0.03
YCW	136	-	370	-	0.284	-
ECW	16	2	-	1.11	-	-
OCW	3.45	-	-	0.0577	0.0057	0.002

Glass volumetric flasks were used in the preparation of solutions; once prepared, the solutions were transferred to polyethylene plastic bottles as quickly as possible and allowed to equilibrate within the anaerobic chamber for 3 months. During this time, the storage bottles where shaken on a weekly basis. Table 3.6 outlines the target composition of each of the synthetic cement waters and Table 3.7 provides the composition of synthetic cement waters as determined by ICP-OES. This information is also available in the pull-out section in Appendix II, for ease of reference while reading the results Chapters.

Table 3.6 Target composition of synthetic cement waters

Element	Concentration							
	Young Cement Water pH(RT) 13.5		Young Cement Water plus Ca pH(RT) 13.5		Evolved Cement Water pH(RT) 12.5		Old Cement Water * pH(RT) 11.7/11.8	
	mg L^{-1}	mol L^{-1}	mg L^{-1}	mol L^{-1}	mg L^{-1}	mol L^{-1}	mg L^{-1}	mol L^{-1}
Ca	-	-	28	7×10^{-4}	601.5	1.5×10^{-2}	32.06	0.08/0.13
Na	3220	1.4×10^{-1}	3220	1.4×10^{-1}	368	1.6×10^{-2}	347	1.51
K	14467	3.7×10^{-1}	14467	3.7×10^{-1}	7.8	2×10^{-4}	7.82	0.02
Al	1.62	6×10^{-5}	1.62	6×10^{-5}	0.13	5×10^{-6}	253	0.94/0.29
Si*	8.43	3×10^{-4}	8.43	3×10^{-4}	0.08	3×10^{-6}	22.46	0.08/0.63
Mg	2.4×10^{-7}	9×10^{-12}	2.4×10^{-7}	9×10^{-12}	9.7×10^{-5}	4×10^{-4}	2.4×10^{-5}	10^{-7}
Fe	5.6×10^{-5}	1×10^{-9}	5.6×10^{-5}	1×10^{-9}	5.6×10^{-5}	1×10^{-6}	5.5×10^{-6}	10^{-8}
SO_4^{2-}	192	2×10^{-3}	192	2×10^{-3}	0.67	7×10^{-6}	4.80	5×10^{-3}
CO_3^{2-}	18	3×10^{-4}	3.60	3×10^{-4}	0.48	8×10^{-6}		
C	3.6	3×10^{-4}	18	3×10^{-4}	0.1	8×10^{-6}	0.24	2×10^{-3}

*controlled by afwillite and CSH_1.8 if two values are given

Table 3.7 Composition of synthetic cement waters as determined by ICP-OES, errors calculated based on the standard deviation of 6 blank samples.

Element	Concentration, mg L^{-1} as determined by ICP-OES			
	Young Cement Water pH(RT) 13.50 ± 0.43	Young Cement Water + Ca pH(RT) 13.01 ± 0.48	Evolved Cement Water pH(RT) 12.30 ± 0.50	Old Cement Water pH(RT) 11.56± 0.26
Ca	-	1.81 ± 1.11	290 ± 37	3.66 ± 0.18
Na	2900 ± 850	2900 ± 500	212 ± 22	65 ± 14
K	9000 ± 3000	9000± 600	-	-
Al	-	-	0.60 ± 0.48	0.24 ± 0.01
Si	-	-	4.35 ± 2.63	-
Mg	-	-	0.15 ± 0.05	-
Fe	-	3.26 ± 1.36	-	-
S	63 ± 12	67.19 ± 6.17	4.34 ± 1.10	5.28 ± 1.40

3.1.3. Granitic Ground Water

One of the conceptual scenarios for the geological disposal of nuclear waste in the UK is disposal within a hardrock (e.g. granite) geology. This particular concept may utlilise a high-pH cement backfill for ILW, thus it is of interest to this thesis. For sequential dissolution experiments performed in Chapter 6, where the final solution in the sequence is a groundwater, a granitic composition was therefore chosen. The composition of the synthetic granitic groundwater utilised is based on the groundwater samples taken between 100-500 m in Swedish bedrock[104,105]. The composition is detailed in Table 3.8 and the Appendix II pull-out. The components were weighed at the bench and dissolved in 1L of de-gassed UHQ water (N_2 was bubbled into the water overnight to de-gas) and transferred to the anaerobic chamber to equilibrate for 1 month prior to use. The container was shaken once a week, to ensure components had fully equilibrated. Table 3.9 outlines the measured composition of the ground water solution used in this study, as determined by ICP-OES. The reagents used were; KCl, $MgCl_2$, $NaHCO_3$ (supplied by Sigma ≥ 98 %), Na_2SO_4 (99% Alfa Aesar), $CaCl_2$ (99+ % Acros) and NaCl (≥99% VWR).

Table 3.8 Granitic ground water composition, components listed in mg to make 1 L of solution.

Granitic Ground Water, 1 L	
	mg
KCl	7.45
Na_2SO_4	14.20
$MgCl_2.6H_2O$	40.66
$CaCl_2$	55.49
NaCl	35.06
$NaHCO_3$	168.00

Table 3.9 Granitic ground water composition as analysed by ICP-OES, mg L^{-1}.

Granitic Ground Water	
Element	Concentration, mg L^{-1}
	pH(RT) 8.83 ± 0.34
Ca	24.12 ± 0 .08
Na	63.67 ± 2.56
K	12.90 ± 0.54
Al	-
Si	5.17 ± 0.94
Mg	6.00 ± 0.19
Fe	1.14 ± 0.05
S	3.90 ± 0.05

3.1.4. Nirex Reference Vault Backfill Cement

Specific requirements for a cementitious backfill within a UK geological disposal facility led to the development of a high-pH cement material known as the Nirex Reference Vault Backfill (NRVB). The functionalities required included: a low strength to allow for possible re-excavation, high porosity and permeability to allow the escape of gases and to provide a high surface area for sorption of radionuclides, and a highly alkaline buffered environment to suppress dissolved radionuclides[7,106]. In Chapter 7, the effects of NRVB-leachate on glass dissolution are investigated.

NRVB is composed of Portland cement, limestone flour and hydrated lime (see Table 3.10) and has a water:solid (w/s) ratio of 0.55. CEM I 52.5R (Sellafield grade) Portland cement was utilised in this study. For comparison with previous[107] and recently published work[7], reagent grade $CaCO_3$ ($\geq$ 99.0 % sourced from Sigma-Aldrich) was used instead of limestone flour, and reagent grade $Ca(OH)_2$ ($\geq$ 95.0 % sourced from Sigma-Aldrich) was used in place of hydrated lime. A recent study by Vasconcelos et al.[7], compared the hydration of NRVB prepared using reagent grade chemicals and industrial materials (i.e., limestone flour and hydrated lime); they found that the cement hydrate phases formed are the same no matter which source materials are used, only the hydration occurs slightly more rapidly when using reagent grade materials (due to higher surface area of $CaCO_3$ than limestone flour). Table 3.11 lists the composition of Portland cement used to make the NRVB in this study.

Table 3.10 NRVB composition

NRVB	Mass, g
Portland Cement	78
Calcium Carbonate	85.8
Calcium Hydroxide	30
Water	106.5
water/solid ratio (w/s) 0.55	

Table 3.11 Composition of Portland cement (raw materials), as determined by XRF.

	Portland cement, %
Na_2O	0.31
MgO	2.09
Al_2O_3	4.55
SiO_2	19.99
P_2O_5	0.17
K_2O	3.23
CaO	0.67
TiO_2	65.37
Mn_3O_4	0.09
V_2O_5	0.01
Cr_2O_3	0.01
Fe_2O_3	3.12
BaO	0.03
ZrO_2	0.00
ZnO	0.15
SrO	0.11

Dry components, according to Table 3.10, were mixed by hand prior to the addition of water, after which time the wet cement pastes were mixed in excess of 20 mins. NRVB remains quite fluid

and was easily packed into centrifuge tubes for curing. Cement pastes were cured at room temperature for a minimum of 28 days; the cement utilised to make NRVB-leachate for Chapter 7, was cured for 826 days, The XRD patterns and TG-MS analysis of NRVB cured for 28 d and 826 d are shown in Figure 3.2. With age the phase assemblage of the NRVB samples change slightly, more calcite is present in the 826 day cured sample as shown by the increased peak intensity at 23.09 °2θ and 29.43 °2θ, in addition to the disappearance of the peak assigned to hemicarboaluminate at 11.6 °2θ. The TG data (depicted by the black line) in Figure 3.2 follows the same trends samples cured for 28 and 826 days the peaks between 100-200 °C can be attributed to ettringite and monocarboaluminate, while the peaks observed between 400-500 °C and 650-800 °C correspond to portlandite and calcite respectively[7,16].

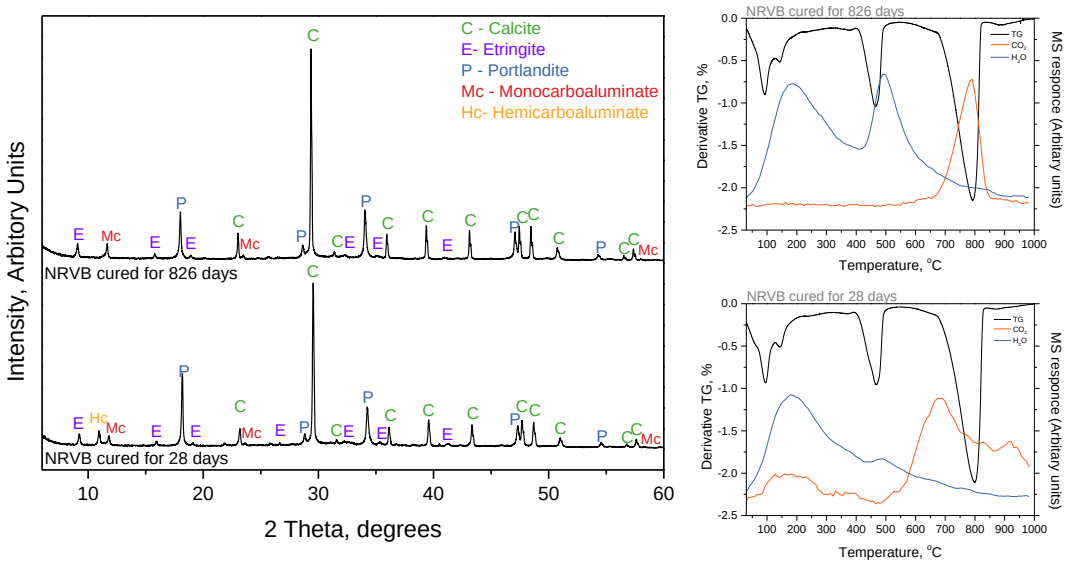

Figure 3.2 Diffraction patterns (LHS) and TG-MS of NRVB cured for 28 or 826 days

3.1.5. Blast Furnace Slag Portland Cement (BFS:PC)

Blast furnace slag (BFS) is produced as a by-product in the manufacture of iron and steel. It is mostly an amorphous material containing silicates and aluminosilicates of calcium. To hydrate and exhibit cementitious properties, it requires activation, usually from alkali hydroxide, lime, gypsum or Portland cement. BFS is blended with Portland cement (to lower the heat of hydration and enhance compressive strength) and used to grout intermediate level wastes in the UK. It is also commonly used in the construction industry[108,109]. Table 3.12 outlines the ratio of starting materials required to make BFS:PC, Table 3.13 lists the composition of the raw materials used; CEM I 52.5 N and BFS sourced from Hanson Cement Ltd, Ribblesdale works (i.e. Sellafield specification; BS EN 197-1:2011).

Table 3.12 BFS:PC composition (5.67:1)

BFS:PC	Mass, g
Portland Cement	33.26
Blast Furnace Slag	188.96
Water	77.79
water/solid ratio (w/s) 0.35	

Table 3.13 Composition of Portland cement and BFS % (raw materials), as determined by XRF.

	PC, %	BFS, %
Na_2O	0.31	0.39
MgO	2.09	8.35
Al_2O_3	4.55	12.15
SiO_2	19.99	36
P_2O_5	0.17	<0.05
K_2O	3.23	0.65
CaO	0.67	39.68
TiO_2	65.37	0.84
Mn_3O_4	0.09	0.5
V_2O_5	0.01	<0.05
Cr_2O_3	0.01	<0.05
Fe_2O_3	3.12	0.43
BaO	0.03	0.07
ZrO_2	0.00	0.06
ZnO	0.15	<0.05
SrO	0.11	0.09

Dry components were mixed by hand prior to the addition of water and wet cement pastes were mixed in excess of 20 minutes prior to packing into centrifuge tubes for curing. Cement pastes were cured at room temperature for a minimum of 28 days; the cement utilised in the glass dissolution experiments in Chapter 7 was cured for 826 days. The XRD patterns are shown in Figure 3.3, as the BFS:PC sample ages it becomes slightly more amorphous in nature, as determined by a reduction peak height and a broadening of peaks. The enhanced amorphosity can be attributed to C-S-H/C-A-S-H formation. The phases identified in the BFS:PC sample cured for 826 days include; calcite, ettringite, portlandite, monocarboaluminate, monosulfoaluminate, hemicarboaluminate, hydrotalcite and C-S-H. The peaks identified in the TG data have been attributed to ettringite between 100-200 °C, while the peaks observed between 400-500 °C and 650-800 °C correspond to portlandite and calcite respectively[7,16].

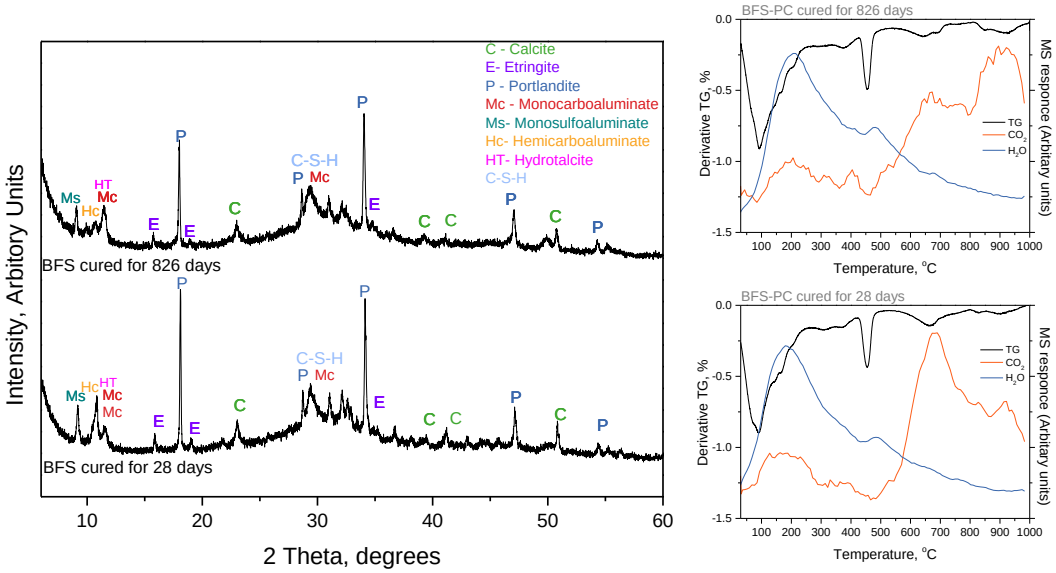

Figure 3.3 XRD patterns (LHS) and TG-MS (RHS) of BFS:PC cement cured 28 days and 826 days.

3.1.6. Synthesis of NRVB and BFS:PC Equilibrated Cement Waters

Hardened cement pastes of NRVB and BFS:PC were cured at room temperature for more than 2 years (826 days) and were transferred into the anaerobic chamber for crushing and sieving. Fifty grams of powder less than 150 µm was added to 2 litres of de-gassed UHQ water (N_2 was bubbled into the water overnight to de-gas). The PE bottles were shaken on a daily basis for 1 month to allow the solutions to equilibrate. After 1 month, the solutions were filtered to reduce the likelihood of cement particles being present in the dissolution media and used in PCT-B and MCC1 tests outlined in Chapter 7. The measured composition of the equilibrated cement waters are listed in Table 3.14.

Table 3.14 Compositions of NRVB and BFS-PC equilibrated water, mg L^{-1}, as determined by ICP-OES. The values listed below are the average of all the blank samples throughout the 112 day experiment, errors calculated from the standard deviation of triplicate blank samples. Carbonate content was calculated from TG-MS data Figure 3.2 and 3.3.

Element	Concentration, mg L^{-1}	
	NRVB pH(RT) 12.65 ± 0.2	BFS:PC pH(RT) 12.59 ± 0.2
Ca	766 ± 59	487 ± 28
Na	13 ± 10	43 ± 6
K	36 ± 5	74 ± 7
Al	0.08 ± 0.2	1.96 ± 0.7
Si	1.79 ± 1.4	0.34 ± 1.4
*Mg	16 ± 9. *	0.30 ± 0.2
Fe	1.57 ± 0.7	1.67 ± 1.4
S	10 ± 7	13.5 ± 1.5
*$CaCO_3$	0.88	0.88

*Mg conc = 0 day 1-42, day 56 onwards ~ 20 mg L^{-1}
*$CaCO_3$ conc= calculated based on the dissolution of calcite in the hardened cement pastes using PHREEQC

3.2. Methodology to Determine the Chemical Durability of Simulant Nuclear Waste Glass

A measure of the chemical durability of waste glasses can be obtained by measuring the chemical concentration of elements released from the glass into solution under carefully controlled conditions.

Figure 3.4 demonstrates the methodology applied in this thesis: glass was contacted with a leachate and placed in an inert (CO_2-free) atmosphere at 50 ^oC for a given time period; solutions were analysed by Inductively Coupled Plasma-Optical Emission Spectroscopy (ICP-OES) and; the glass was characterised by Scanning Electron Microscopy (SEM) coupled with Energy Dispersive Spectroscopy (EDS), Tranmission Electron Microscopy (TEM), coupled with EDS and Selective Area Electron Diffraction (SAED) and X-ray Diffraction (XRD). Three dissolution methodologies were utilised, as described below.

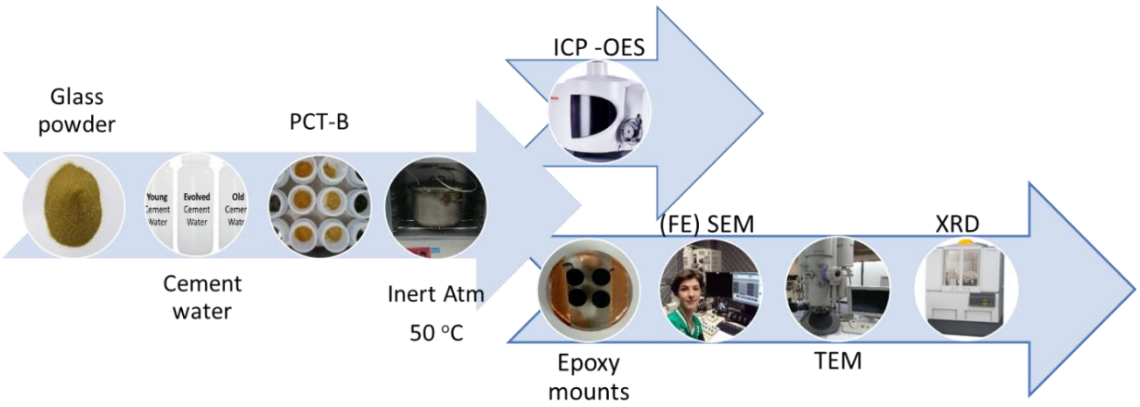

Figure 3.4 Flow chart of experimental processes for chemical durability tests

3.2.1. Product Consistency Test B (PCT-B)

Static tests were conducted in 15 ml Teflon vessels, glass powder was prepared according to the ASTM standard C1285-14 [110] (The Product Consistency Test, PCT-B). Glass fragments were crushed using a percussion motor or Tema mill and sieved to obtain the size fraction between 75-150 μm. The powder was subsequently washed using Type 2 water in an ultrasonic bath until the waste water was clear (minimum of 3 washes) followed by 3 washes with isopropanol alcohol to ensure the removal of fines. The glass powder was dried in an oven overnight prior to use.

Leachates used included synthetic cement waters outlined in Section 3.1.2, cement waters prepared from NRVB and BFS/PC in Section 3.1.6 and ground water, as outlined in Section 3.1.6.

The initial surface area to volume ratio of 1200 m^{-1} and a temperature of 50 ^{o}C (as recommended by the UK geological disposal implementer, Radioactive Waste Management Ltd, 50 ^{o}C is the long-term target temperature within a cementitious backfill (ILW)[111]) was used for all PCT-B experiments. Test vessels were cleaned according to an in-house modified version of the cleaning procedure in ASTM C1285. Glass was weighed into vessels and solution added within the anaerobic chamber to prevent carbonation of the leachate solutions. All test vessels were sealed and transferred to a stainless steel "bean tin" that, once sealed was purged continuously with nitrogen gas, remained CO_2-free for the duration of the experiment. The bean-tin was housed within an oven at 50 ± 2 °C.

At specific time points, triplicate samples and duplicate blanks were removed from the oven and transferred to the anaerobic chamber. The mass of the vessel was recorded and the pH measured. Aliquots were taken for elemental analysis by ICP-OES. The normalised mass loss of elements in solution was calculated according to Equation 3.1:

$$NL_i = \left(C_i - C_{i,b}\right) / \left(f_i \times \frac{SA}{V}\right) \qquad \textbf{Eqn. 3.1}$$

where NL_i is the normalised mass loss for element i in gm^{-2}; C_i is the average concentration of i in solution in the triplicate tests, in g m^{-3}; $C_{i,b}$ the average concentration of i in the blank tests in g m^{-3}; f_i is the mass fraction of i in the glass; SA is the surface area of the glass powder in m^{-2}; and V is the volume of leachate in m^3.

In sequential dissolution tests performed in Chapter 6, the leachate solutions were replaced to simulate the evolution of cement solution composition as a function of time. Glass powders and monoliths were exposed to the ECW solution for 1 month, at which time 3 vessels were sacrificed, aliquots of solution from these sacrificed vessels were removed for analysis (pH, ICP-OES) and the powder samples were analysed by XRD and SEM/EDS. For vessels that were not sacrificed, the ECW solution was removed and replaced by OCW solution before being returned to the oven for 1 month. At this time, the same process was followed (some vessels were sacrificed for analysis) and non-sacrificed vessels were emptied and filled with a replacement solution of granitic groundwater. Dissolution continued for a further month before all remaining samples were analysed.

3.2.2. Monolithic (MCC-1)

Low SA/V ratio ($10m^{-1}$) experiments were conducted in parallel with PCT-B tests to study the reaction of monolithic waste forms and allow investigation of the alteration layers formed under static conditions[112]. Monolith tests performed in this thesis used the ASTM C1220-98 standard, known as the MCC-1 test. Samples of known volume and geometric surface area of 400 mm^2 were immersed in a leachate for the duration of the experiment. Glass monoliths were prepared using a slow saw with a diamond blade to achieve the desired sample size and were ground and polished using 600, 800, 1200 grit paper followed by 6, 3, 1µm diamond suspension to ensure a uniform surface finish. The leachates used in the MCC-1 experiments were identical to those used in the corresponding PCT-B experiments; the samples were treated and analysed in the same way post dissolution.

3.2.3. pH Measurements

The pH of the solutions were measured at room temperature (~ 25 ^oC) inside the anaerobic chamber to prevent the solution from carbonating. The pH probe was calibrated at pH 4, 7 and 10 prior to use and rinsed with UHQ water between samples. It should be noted that the pH measurements were not corrected for the high ionic strength of the leachates, therefore the values stated throughout this thesis are indicative and not absolute[61].

It is well known that temperature impacts the pH of a solution; as the temperature rises, the pH decreases due to the dissociation of water. It is possible to calculate the pH for solution above room temperature using the Nernst equation (Eqn. 3.2). Table 3.15 lists the measured pH(RT) and calculated pH at temperature (30/50/70 ^oC) of all the solutions used in this study.

$$pH\ (at\ Temp) = pH(RT) - \frac{Faraday\ Constant,\ 96485.33\ Cmol^{-1} \times Gas\ Constant, 8.31\ Jmol^{-1}}{measured\ potential\ E,\ 0.092\ JC^{-1}\ \times Temp\ of\ sol,\ K} \times Ln10 \qquad \textbf{Eqn 3.2}$$

Table 3.15 pH values measured at room temperature (pH(RT)) and the calculated value for the leachate in the test vessel at temperatures greater than room temperature.

Relevant Chapters	Solution	pH(RT)	pH @ 50°C	pH @ 30°C	pH @ 70°C
Chapter 4 and 6	YCWCa	13.50	12.07		
Chapter 4 and 6	YCW	13.01	11.58		
Chapter 4 and 6	ECW	12.30	10.87		
Chapter 4 and 6	OCW	11.56	10.13		
Chapter 5	YCWCa	13.50	-	11.97	12.15
Chapter 6	Granitic Ground Water	8.83	7.40		
Chapter 7	NRVB	12.65	11.22		
Chapter 7	BFS:PC	12.59	11.16		

3.2.4. Glass Density Measurements

The density of the glasses was determined using helium pycnometry AccuPycII. The inert gas, is used as the displacement medium, a known mass of glass powder (<1 g) was sealed in the instrument compartment. The sample solid phase volume is computated based on pressure changes observed when the sample chamber is filled and discharged. The displacement density is calculated by dividing the volume into the sample weight. The measured density of the MW25, LBS and ISG was 2.76 ± 0.14 g cm^{-3}, 2.67 ± 0.14 g cm^{-3} and 2.53 ± 0.13 g cm^{-3} respectively.

The glass density is essential to calculating the amount of glass required to work at a specific surface area to volume ratio, it is generally assumed that glass particles are spherical. Given the particle size is distributed between 75 – 150 µm the median is used in addition to the mass of glass to determine the amount of glass required.

3.2.5. Dissolution Methodology used in Chapter 5

Chapter 5 details the results of static dissolution tests that were performed at SCK.CEN. Experiments were conducted at 30 °C and 70 °C in YCWCa solution with a composition as reported by Ferrand et al[54], shown in Table 3.16. The YCWCa solution was prepared in an inert atmosphere glove box to prevent carbonation, at room temperature, and had a pH measured at 23 ± 1 °C (pH(RT)) of 13.5 ± 0.2. Experiments were conducted using 9 g of glass powder and two monoliths, in contact with 50 mL of solution that had been equilibrated at either 30 °C or 70 °C; the surface area to volume ratio was 8280 m^{-1}.

Table 3.17 Target composition of synthetic young cement water with added calcium (YCWCa), in mmol L^{-1}, after Ferrand et al.[54]

	Element concentration, mmol L^{-1}						
	Ca	Na	K	Al	Si	S	C
YCWCa	0.70	141.00	367.00	0.06	0.05	2.00	0.30

Experiments were performed in duplicate using a bespoke reactor (shown in Figure 3.5), where the monoliths were located on a Teflon holder above glass powder settled on the bottom of the vessel; the powder and monoliths were not in contact. Blank tests without glass were also performed. Solutions were manually stirred a few hours before removal of 1 mL aliquots at regular time points. The aliquots were acidified prior to analysis (HNO_3) and diluted with 2 mL ultra-high quality water and the chemical composition determined by ICP-AES or MS (X series II Thermo Fisher). The monoliths were removed from solution after 200 days and 721 days.

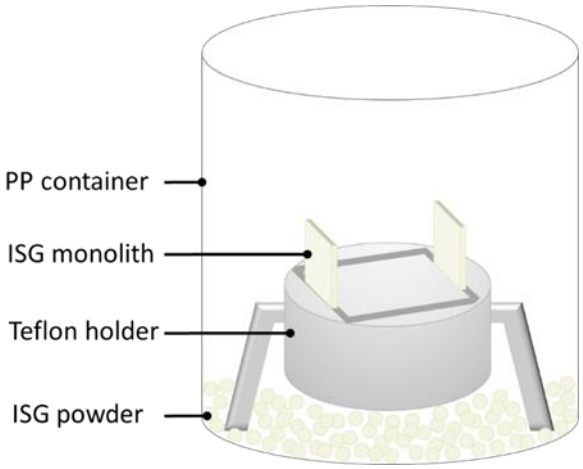

Figure 3.5 Bespoke sample holder used in experiments with ISG glass monoliths mounted on a Teflon holder. ISG powder was placed at the bottom of the test vessel, which was made from polypropylene.

The normalised mass loss NL_i (g m^{-2}) was calculated according to Eqn. 3.3:

$$NL_i = \frac{(C_i \cdot V \cdot F_i)}{f_i \cdot SA} = \frac{(m_i \cdot f_i)}{\left(F_i \cdot \frac{SA}{V}\right)} \qquad \textbf{Eqn. 3.3}$$

where C_i is the concentration of element i in the aliquot of solution (mg L^{-1}), V is the total volume of solution (m^3), F_i is the factor to convert the atomic weight of element i to the atomic weight of the oxide containing element i, f_i is the weight % of the oxide containing element i in the pristine glass, SA is the total surface area of the exposed glass (m^2) and m_i is the mass of element i (g). The NL_i values were further corrected by taking into account the volume decrease due to periodic

sampling of solution aliquots and evaporation and the amount of glass components (e.g., B, Si, etc.) that were discarded with the previous sampling, by adding the cumulative amounts of B, Si, etc. in the discarded sample to the amount still present in the leachate at a given time point.

3.2.6. Calculating Alteration Layer Thickness using Mass Loss Data

Equivalent Boron Calculation

Equivalent boron thickness calculations are used in addition to measurements made on micrographs to determine the thickness of the alteration layer based on the amount of boron leached from the glass, using Equation 3.4.

$$Calculated\ thickness\ (\mu m) = \frac{Concentration\ of\ Boron\ in\ solution\ (mg\ L^{-1})}{Concentration\ of\ Boron\ in\ the\ glass\ (mg\ L^{-1})} \times Time\ (days) \quad \textbf{Eqn. 3.4}$$

Alteration Layer Thickness Calculated using the Initial Rate

The thickness of the alteration layer can be calculated using the initial rate, as shown in Equation 3.5. It is assumed that the gel layer has the same density as the glass (which may not be the case since the density of the gel is dependent on the water content).

$$Calculated\ thickness\ (\mu m) = \frac{Initial\ dissolution\ rate\ (g\ m^{-2} day^{-1})}{Density\ of\ the\ glass\ (g\ m^{-3})} \times Time\ (days) \quad \textbf{Eqn. 3.5}$$

3.3. Analytical Methods

3.3.1. X-Ray Diffraction

X-ray diffraction (XRD) is a non-destructive analytical technique that utilises X-rays to determine the arrangement of atoms in a materials crystal structure. X-rays are generated by bombarding a focused electron beam at a metal target (e.g. Cu). Two forms of scattering occur (see Figure 3.6); coherent scatter, an elastic event whereby the wavelength of the incoming photon does not change upon collision with inner shell electrons and incoherent scattering which increases the wavelength of the incoming photon, as a result, the energy of the photon decreases; Compton scatter occurs when an electron is excited into a higher energy level or forced out of its orbital, the incoming x-ray photon loses energy though this interaction therefore is overlooked in XRD. Fluorescence occurs when an incoming photon ejects an inner orbital electron from the atom and the vacancy is filled by an electron that was residing in a higher energy orbital this results in excess energy that is released as an x-ray photon with an energy difference of 2 orbitals, the energy is dependent on the atomic number and is characteristic of the atom itself. X-ray fluorescence (XRF) relays upon this interaction aiding identification of elements in a material[113,114].

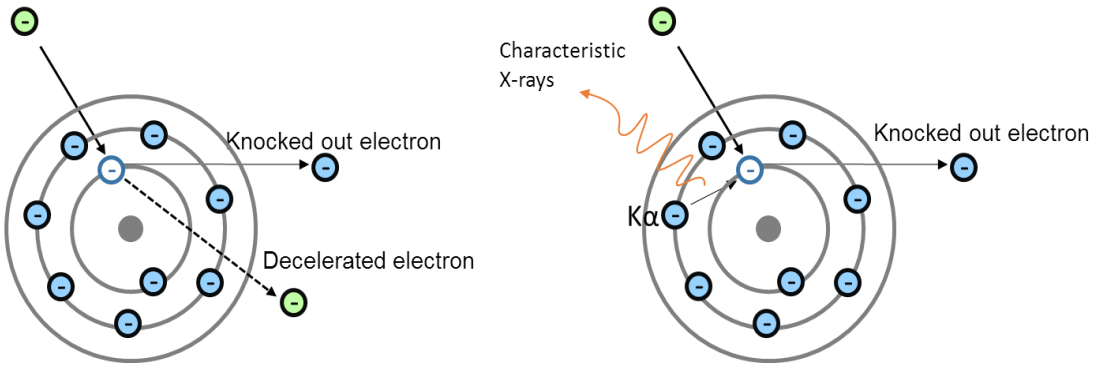

Figure 3.7 Generation characteristic x-rays

The incident x-rays of known wavelength (λ) interact with the atoms of a crystal structure, the interplanar spacing (d spacing) is used for characterisation (see Figure 3.7). The angle of incident (θ) is measured when constructive inference occurs generating diffracted x-rays that leave the sample at an angle equal to the incident beam.

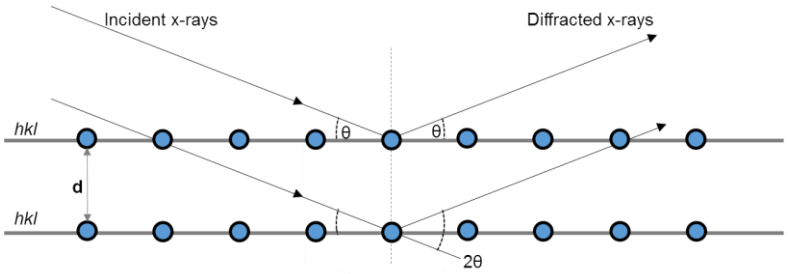

Figure 3.7 Derivation of Bragg's Law, ηλ= 2d sin ϑ

Bragg's equation[115] allows the d spacing value to be calculated; a diffraction pattern is generated through the accumulation of diffracted x-rays (reflections) from all the planes in the crystal. Peaks indicate reflections and are characterised by their position, intensities and profile. The peaks and backgrounds are the source of information and allow compositional identification of unknown samples.

Experimental XRD Parameters used in this Thesis:

Chapters 4 to 8: X-ray diffraction was performed on hardened cement paste samples cured for a minimum of 28 days. Samples were crushed and subsequently ground using an pestle and mortar and passed through a 63 µm brass sieve prior to powder XRD analysis.

Unaltered glass fragments were crushed to powder and passed through a 75 µm sieve. These powders were ultrasonically cleaned in isopropanol to remove fines. Altered glass (i.e. removed from dissolution test vessels) was dried in air and ground prior to XRD. In both cases, material was front loaded into a zero background sample holder and the sample surface made flush with the container by pressing with a glass slide.

All diffraction patterns were analysed using the PDF4+ database from the International Centre for Diffraction Data (ICDD).[116]

X-ray diffraction data were acquired in theta two theta reflection mode on a Bruker D2 Phaser X-ray Diffractometer, with Cu Ka radiation, using a Ni filter and Lynx-Eye Position Sensitive Detector. Diffraction data were acquired with an incident beam divergence slit of 0.6 mm and a knife edge (1 mm) to eliminate stray scatter; these are normal settings for this diffractometer system. The data acquisition parameters were: Start 2θ = 5 °, End 2θ = 70 °, Step Size = 0.02 °, effective total scan time = 3 hours (for glass and cement samples), Sample rotation = 60 Hz. LynxEye Detector settings were: Lower discriminator = 0.110, Upper discriminator = 0.250. The X-ray tube settings were 30 kV and 10 mA.

X-ray diffraction data acquired for Chapter 5 was analysed using Philips X'Pert Pro System (SCK.CEN) with the following settings: two theta range 5-60°, step size 0.02° 2θ, 30s per step, Cu Kα radiation and X'Celerator detector. Monoliths were examined using a Bruker D2 Phaser x-ray diffractometer (University of Sheffield) in theta two theta mode with Cu Kα radiation, using a Ni filter and a LynxEye position sensitive detector, as described above. The resulting patterns were evaluated with the aid of X'Pert High Score Plus software and PDF 2 mineral database.

3.3.2. Scanning Electron Microscopy and Energy Dispersive Spectroscopy

A focused beam of electrons can be scanned/rastered across the surface of a sample to gain characteristic information. The electrons are generated in the tip of the electron gun, and a potential difference is generated between the tip and the first anode. This pulls the electron from the tip and the potential difference between the 1st and 2nd anodes accelerates the electrons through the gun column. Apertures and lenses focus the beam of electrons to ensure convergence of the beam on the sample, and by changing the current that passes through the deflector coils, the user is able to raster the beam across the sample[117,118]. A schematic of a field emission SEM is shown in Figure 3.8.

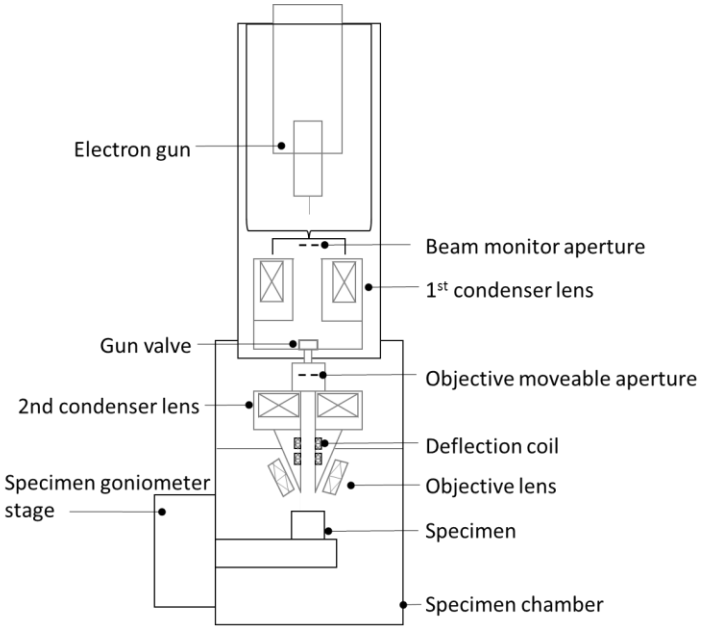

Figure 3.8 Schematic of S4800 Field Emission SEM used at ORNL

The beam sample interactions are detected to gain grey scale images. There are 3 main interactions (Figure 3.9): (1) secondary electrons are generated through inelastic scattering of electrons in the sample, these low energy electrons provide topographical information; (2) back scattered electrons are high energy electrons (elastic events) where the coulomb force of the nuclei drives the incident electron back in the direction of travel. The size of the atom determines

the coulombforce, therefore heavier elements will appear brighter on a grey scale image; and (3) X-rays are emitted when a vacancy is generated in an electron orbital and a higher energy electron drops down an energy level to fill the vacancy. This releases the excess energy in the form of X-ray radiation. As an electron drops to lower orbital the energy released is unique for each element therefore elemental composition can be acquired[119]. This is known as Energy Dispersive Spectroscopy (EDS).

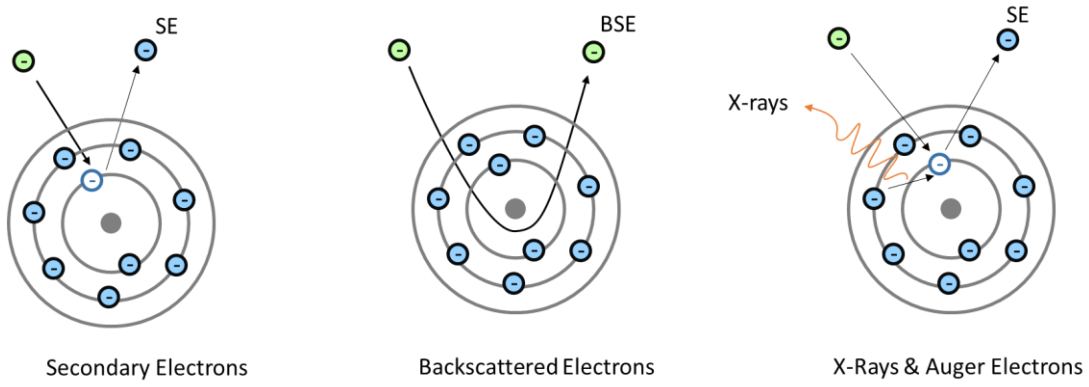

Figure 3.9 Electron beam/ sample interactions

Experimental SEM Parameters used in this Thesis:

In Chapters 4 to 8 the sample preparation was executed using the following procedure: Epoxy resin was used to encapsulate samples for SEM and TEM. Dried glass powders were mixed with epoxy to form a slurry that was poured into small circular sample holders ~0.5mm in diameter. The mould was topped up with epoxy to ensure the sample was tall enough for the polishing steps. Monolith samples were placed into the resin mould in cross section and filled with epoxy. Once removed from the mould, samples were ground using 600 grit to break through the epoxy to expose the glass and then 800 and 1200 grit were used, isopropanol alcohol was used as the lubricant. Samples were polished to a 1 µm finish, in three stages, to 6, 3, 1 µm using diamond suspension or paste. They were subsequently carbon coated and had the addition of silver dag or copper strips to reduce charging.

Three different SEM instruments were utilised: (1) A Hitachi TM3030 Plus was used for imaging (BSE and SE) and obtaining elemental composition (EDS) of glass and cement samples. Images were acquired at 5kV using the charge reduction observation mode; (2) A Hitachi S4800 a FE-SEM was used for analysis of glass samples after dissolution. For the majority of images the accelerating voltage was 5 kV and the current 7uA, with a spot size of 2 (unknown beam diameter) on the condenser lenses and a working distance of 7mm (unless collecting EDS during which the working distance was increased to 14mm); and (3) an Inspect F50 FE-SEM was also used for

analysis of glass samples after dissolution, in addition to selected cement samples. The accelerating voltage was 15kV, the spot size was 3 (unknown beam diameter) and the working distance did not require adjustment for EDS measurements.

Micrographs were post-processed, to obtain quantitative data. The thickness of alteration layers on top of the pristine glass were measured using Image J as follows: monoliths were imaged lengthwise along the cross section on both sides of the monoliths. At least 15 images were taken along each long edge of the sample, and the alteration layer was measured 40 times in each of those images. Forty line measurements were selected based on the results from basic statistical analysis as outline in Figure 3.10 which shows the number of line measurements and the average measured thickness. It can be seen that the error was not minimised with more than 40 measurements. For Glass powders mounted in epoxy, 7 grains were randomly selected from the sample for analysis, based on Figure 3.11, which indicated no significant reduction in the error associated with measuring more than 7 grains.

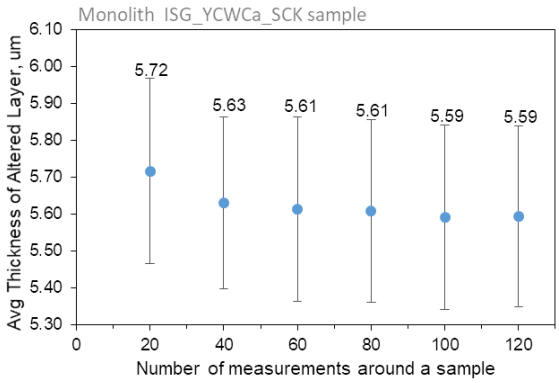

Figure 3.10 Statistical analysis to determine the number of line measurements in each micrograph

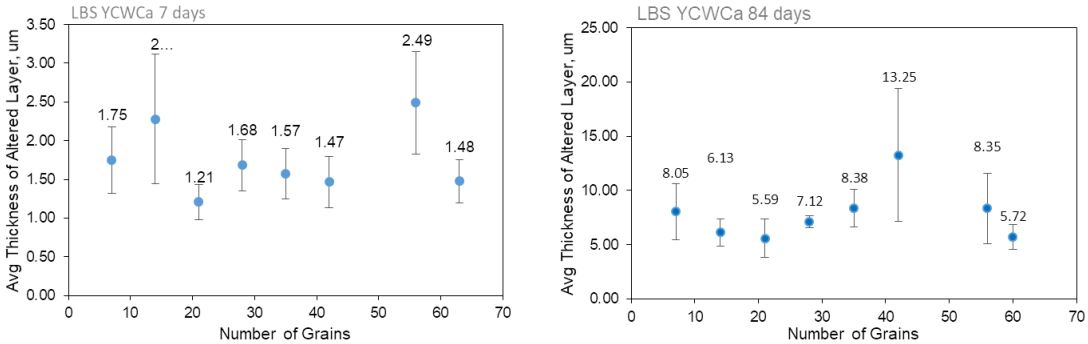

Figure 3.11 Statistical analysis to determine the number of grains that should be measured to ensure a representative sample spread

In Chapter 5 the following procedure was used; the altered glass was characterised as follows: the glass alteration layers were examined using a Field emission Scanning electron microscope

(SEM) (powders were analysed on a JEOL JSM 6610 and monoliths on a Hitachi S-4800). Energy Dispersive X-ray spectroscopy (EDX) was utilised to determine the chemical composition of altered layers and the total layer thickness was determined by line measurements around glass grains and in the cross sectional images of the monolith (~440 measurements per sample, as above).

3.3.3. Transmission Electron Microscopy

In Transmission Electron Microscopy (TEM), an electron beam passes through an electromagnetic condenser system, the sample, then the objective system and onto a phosphor screen or CCD camera (projector system). The condenser system is a series of lenses, stigmator coils and beam deflector lenses; the intention is to place the beam on the sample by controlling the probe size, convergence angle and the intensity. The objective lenses can be considered as the imaging system; the relationship between the sample and object plane is required for the optimum position of the sample to be determined (where it does not translate when you tilt).

Sample preparation was completed by Donovan Leonard at ORNL, on the SEM samples polished to 1µm. SEM samples were coated in ~ 20 nm of carbon, prior using the FIB-SEM Hitachi NB5000, the dual beam FIB-SEM combines a high resolution FE-SEM with a 40 kV FIB column to prepare a lift-out sample (see below).

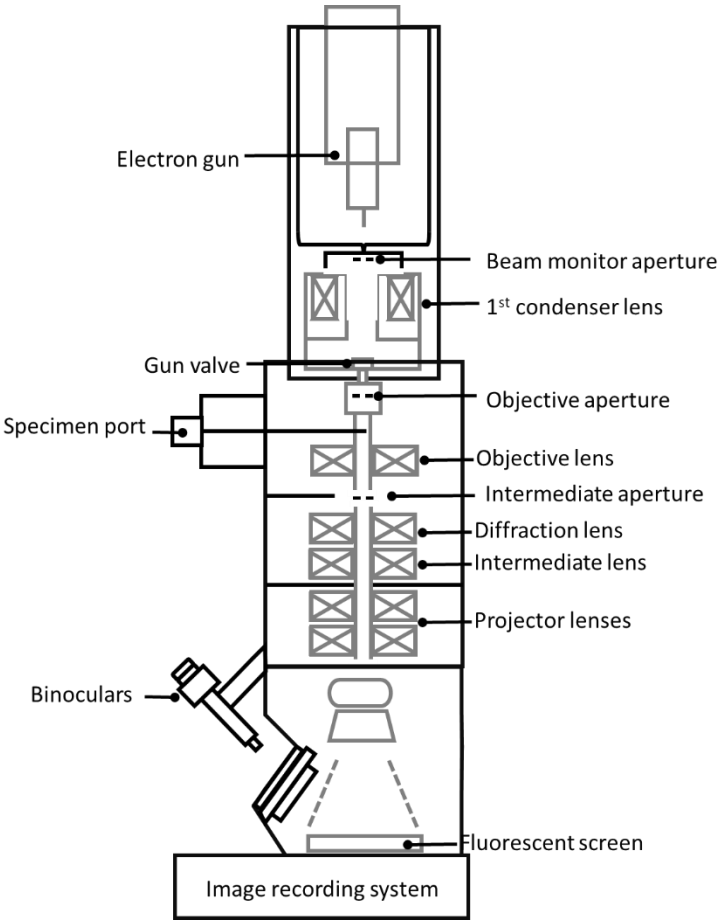

Figure 3.12 Schematic of a transmission electron microscope

The underlying physics for TEM is related to electron scattering. Examples of possible scattering interactions are detailed in Figure 3.13. Diffraction analysis requires elastic scattering, imaging analysis utilises both elastic and inelastic scattering, and analysis by spectroscopy requires inelastic scattering.

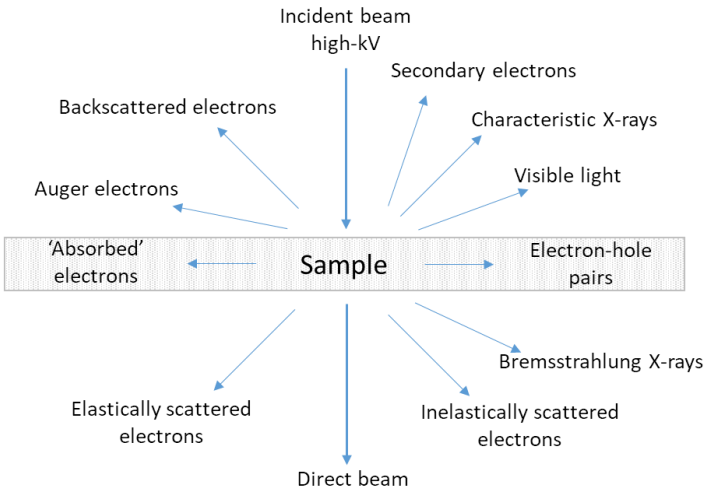

Figure 3.13 Multiple electron scattering processes associated with electron interactions

Elastic and inelastic events are the same as those outlined for the SEM in Figure 3.9. It is worth noting that the high voltage, high current electron beam can do significant damage to the samples, particularly regions of hydrated altered glass.

Diffraction patterns, known as Selective Area Electron Diffraction (SAED), are generated in the back focal plane of the objective lens. When coupled with TEM, diffraction can determine the orientation of single crystals, provide measurements of the average spacing between layers of atoms and find the crystal structure of an unknown material. All of these methods are most successful when crystalline materials are investigated; glass samples are more likely to generate diffuse rings indicating their amorphous nature.

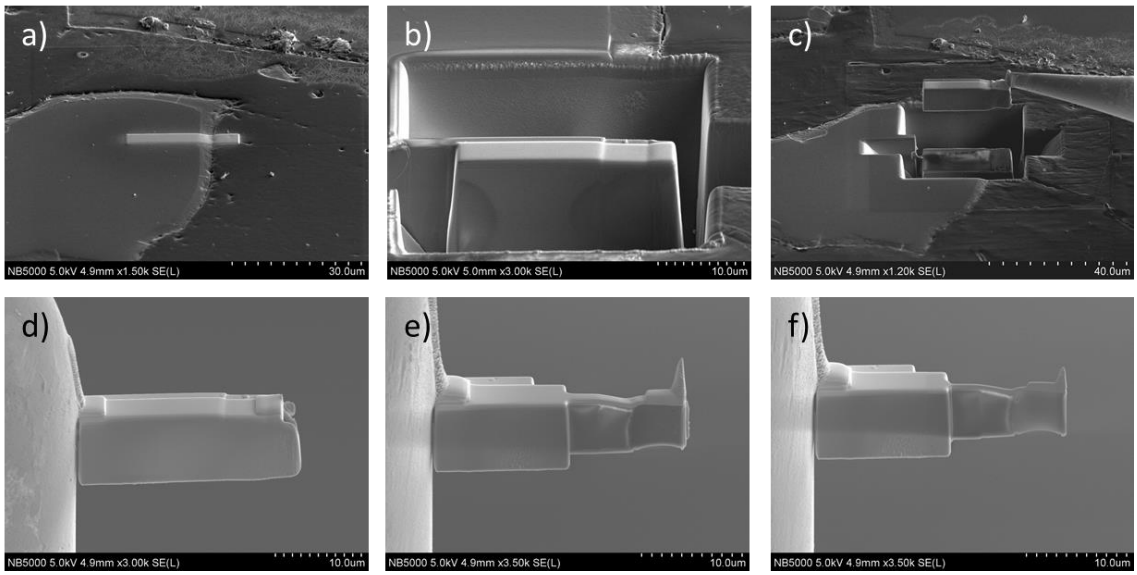

Figure 3.14 FIB sample preparation

The region of the FIB lift out was selected based on the presence of an alteration layer, confirmed previously by SEM/EDS analysis. The region was milled using a Hitachi NB5000 dual focused ion beam scanning electron microscope (FIB-SEM) at ORNL. Firstly, a tungsten strip was laid on top of the region (Figure 3.14a) and the ion beam rastered across the regions around the tungsten strip (Figure 3.14b), leaving the area to be lifted out. The sample was subsequently tilted to 58 o and horizontally milled. Figure 3.14c demonstrates how the FIB section was fused to the tungsten needle tip to allow it to be moved to the TEM grid, where it was secured with a further application of tungsten (Figure 3.14d). Figure 3.14e and f demonstrate that the FIB section was methodically thinned.

FIB lift out samples were examined using a cold field emission Hitachi HF-3300 high-resolution transmission electron microscope TEM/STEM/SEM with an accelerating voltage of 300 keV at Oak Ridge National Laboratory, which has the capability to generate simultaneous secondary electron and STEM images. EDX was performed using a Bruker XFlash silicon drift detector (SDD) attached to the HF3300 TEM/STEM/SEM for elemental mapping of the thin FIB section. This was utilised to determine the composition and structure of the altered layers. The SAED patterns require post process analysis using Image J and a "Radial Profile Angle" plug in. Radial profiles can be plotted by measuring the distance from the centre pixel to each ring in the diffraction pattern. The values are converted from pixel to nm and the intensity normalised prior to applying a fifth order polynomial.

3.3.4. Pore diameter determination, TEM image processing

Image J[2] was used to measure the average pore diameter using TEM images obtained as described above. The TEM images were processed with a fast Fourier transform (FFT) bandpass filter to exclude features larger than 100 pixels and smaller than 3 pixels; the aim of this step was to achieve an even brightness across the image and to reduce noise to ensure better results when thresholding. Black and white inversion highlighted pores in white for size analysis against the image scale. The images in Figure 3.15 and Figure 3.16 depict the image processing steps used to collate the pore size diameter of the gel listed Chapter 4.

[2] Image J is an open source image processing program, utalised for the analysis of scientific images

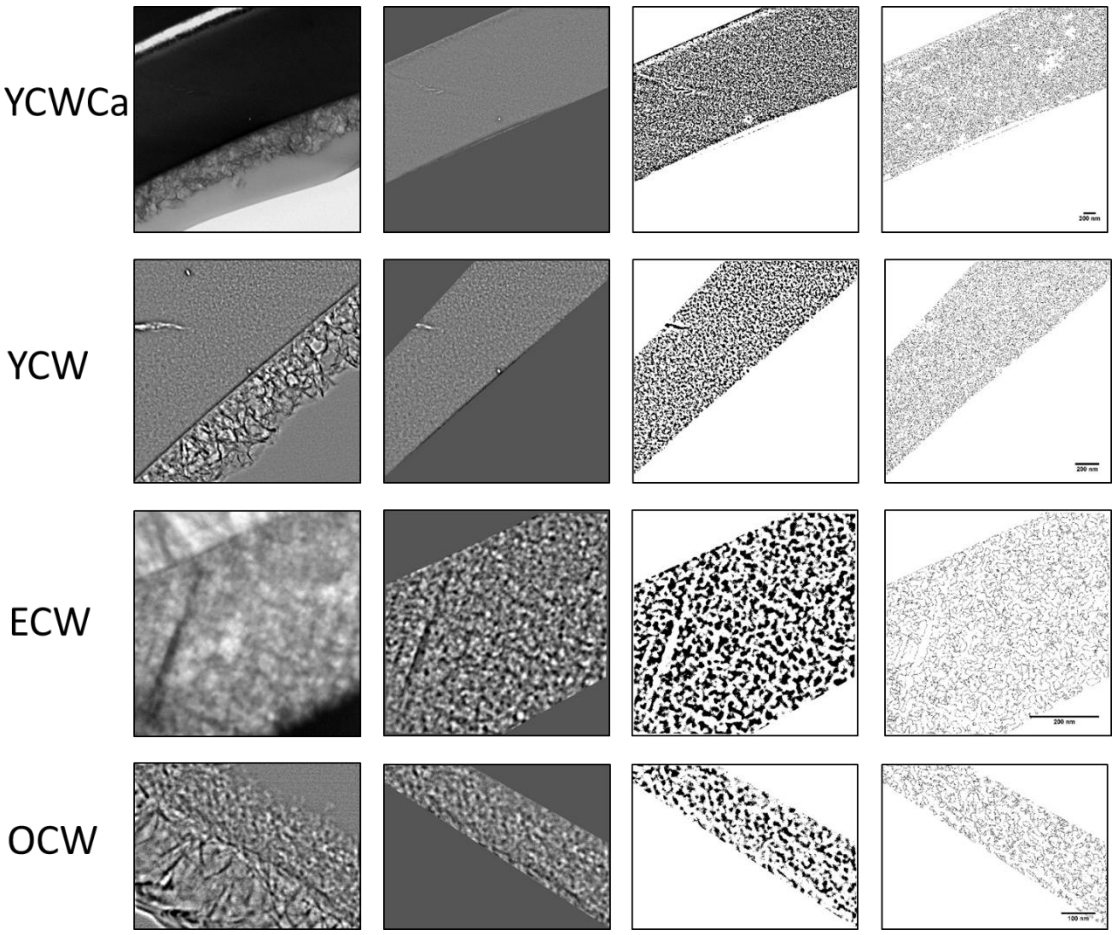

Figure 3.15 Image processing steps to acquire average pore diameter measurements of MW25 glasses from TEM image; the scale bar is first removed from the image, a FFT bandpass applied, threshold applied and the final step is particle size analyser.

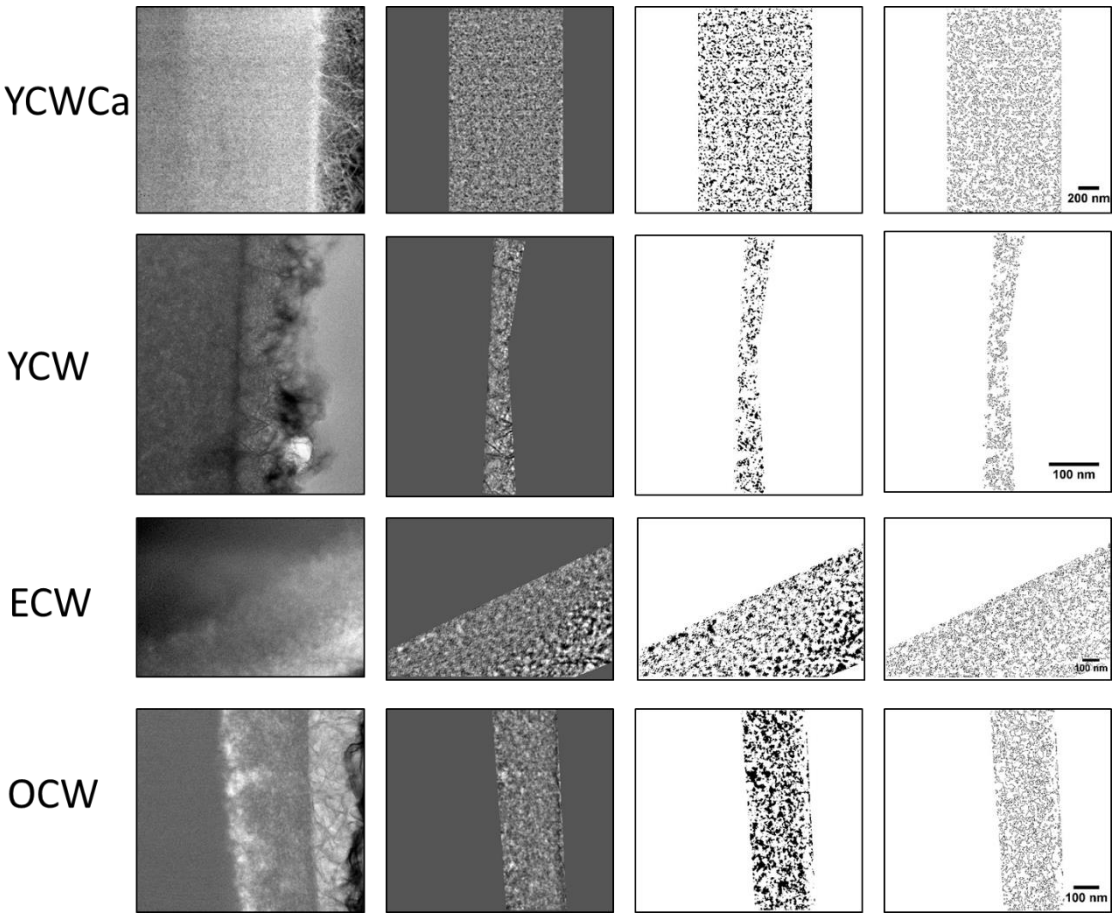

Figure 3.16 Image processing steps to acquire average pore diameter measurements of LBS glasses from TEM image; the scale bar is first removed from the image, a FFT bandpass applied, threshold applied and the final step is particle size analyser.

3.3.5. Thermal Analysis: Thermo-Gravimeter Analysis (TGA)

Thermogravimetric analysis (TGA) is an analytical technique applied to measure the mass loss of a sample as a function of temperature. A small quantity, ~40 mg, of the finely ground sample is placed inside the instrument under a controlled atmosphere (usually N_2), the temperature is gradually ramped up and thermal events associated with mass loss are recorded; for example, dehydration which is observed over a distinct temperature range.

For TG-MS analysis, a PerkinElmer Pyris 1 thermogravimetric analyser was used for cured cement samples of NRVB and BFS:PC (Figure 3.2 and 3.17). The temperature ranged from 20 °C to 1000 °C with a heating rate of 10 °C/minute under nitrogen atmosphere. A Hiden Analytical mass spectrometer (HPR-20GIC EGA) was used to record the mass spectrometric signals for H_2O and CO_2.

The amount of carbonate in the cured samples was determined by calculating the difference in the derivative TG % for the calcite peak and using that to determine the wt % of $CaCO_3$ present in the sample. The amount of carbonate is determine by the precipitation of calcite[120] in the system using geochemical modelling.

3.3.6. Inductively Coupled Plasma Spectroscopy

Inductively coupled plasma spectroscopy (ICP) is an elemental analysis technique that allows for identification and quantification of elements present in a liquid sample by measuring the emission spectra. Figure 3.17 is a schematic diagrm of the process described below; atoms are excited by plasma that is generated when argon gas is ionized due to high frequency electricity creating an electromagnetic field at the end of the torch where argon gas was expelled. The liquid sample is vaporised by a nebuliser before it is passed through the plasma torch and becomes atomized and ionised. Atoms are excited through two main processes: by inelastic scattering of an electron from an atom (M), according to Equation 3.6; and by the radiative-recombination of an ion (M^+) with an electron, which leads to the emission of photons (hv), according to Equation 3.7 [121].

$$e + M \rightarrow M^* + e \qquad \textbf{Eqn. 3.6}$$

$$M^+ + e \rightarrow M^{+*} + hv \qquad \textbf{Eqn. 3.7}$$

Optical and radial windows allow for a broad spectrum of wavelengths to be collated for each element. The signal passes through the optics to the spectrometer, where it is passes through charge-coupled devices (CCDs) and the identification of elements utilises the characteristic

emission peaks for each element. The intensity of the emission peaks is related to the quantity of element present. It is at the user's discretion to select an appropriate wave length to analysis the solution data.

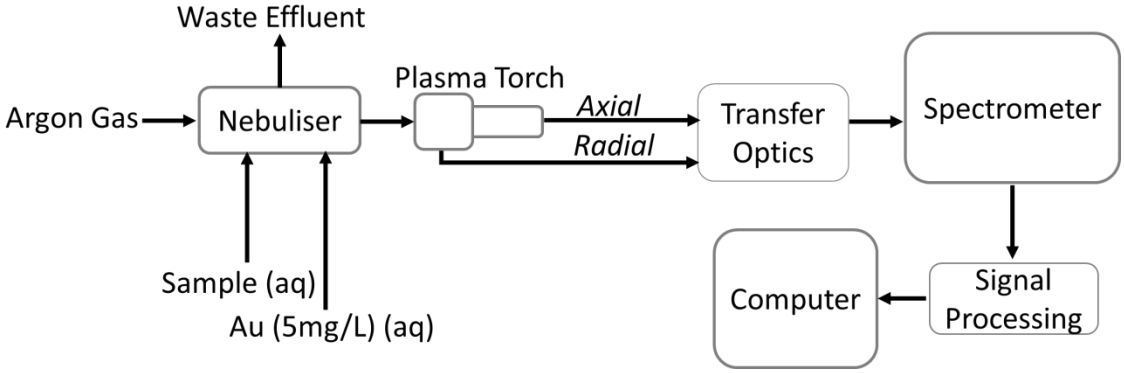

Figure 3.17 Schematic diagram of ICP-OES processes[122]

Experimental ICP-OES Parameters used in this Thesis:

Chapters 4 to 8:

An ICP-OES must be calibrated to obtain reliable results. Multi-element calibration standards were prepared using high quality Fluka elemental standards of known concentration (10,000 mg L^{-1}) diluted in a nitric acid solution where appropriate (note high concentrations of Si will precipitate out in nitric acid, so an alternative acid is required).

Two sets of standards were made: (1) the first contained Al, B, Ca, Ce, K, Li, Mg, Na, Zn, S, diluted with 1% ultra-pure nitric acid at a concentration of 250, 100, 10, and 1 mg L^{-1}. The second set of standards contained Fe, Si, Zr and Ru, which were diluted using UHQ water. The final concentrations were 25, 10, and 1 mg L^{-1} for Fe, Zr and Ru, and 250, 100, and 10 mg L^{-1} for Si. The analytical samples were acidified using ultrapure HNO_3 prior to analysis to prevent precipitation in the ICP-OES tubing and to stabilise the elements in solution.

For solutions of such high ionic strength, two further steps were required in the ICP-OES set-up to improve the reliability of the measurements: firstly, a ceramic torch must be used to extend the lifetime of the equipment (a standard silica glass torch would corrode quickly with cement waters); secondly an internal standard of 5 mg L^{-1} Au solution was analysed concurrently with all samples and standards. Internal standards improve the accuracy and precision of the results obtained, the 5 mg L^{-1} Au standard is introduced into the nebuliser with samples and blanks, the Au emission intensities are measured and ratioed to the initial internal standard reading. The values obtained for the samples can then be corrected by this ratio, therefore compensating for introduction efficiencies and sample matrix effects[123].

3.3.7. Geochemical Modelling

In Chapters 6 and 7, geochemical modelling was performed using the geochemical modelling software, PHREEQC version 3, utilising the Hatches database. Thermodynamic data for brucite ($Mg(OH)_2$) was manually added to the database (data was obtained from the LLNL database). The concentration of elements measured by ICP-OES was input into the PHREEQC software to calculate the saturation indices of phases present in the database. The information obtained through geochemical modelling was complementary to SEM, EDS and XRD to identify alteration products.

In Chapter 5 the geochemical modelling was performed by Sanheng Liu at SCK.CEN. Two different models were applied to simulate the experimental dissolution results: (1) an affinity-based model where congruent dissolution is driven by the undersaturation of the solution with

respect to silica; and (2) a diffusion model that describes "diffusion-through-alteration-layer-dissolution", i.e. when the alteration products (gel and precipitates) cover the glass surface and limit solute transport, decreasing the dissolution rate.

The affinity model is given in Eqn 3.8, where dm/dt is the rate of the glass dissolution in g d^{-1}, A_0 (m^2) is the initial glass surface area, m (g) and m_0 (g) are the current and initial mass of glass, [Si] is the silica concentration in the solution in mmol L^{-1} and $[Si_{sat}]$ is the saturation concentration of silica with respect to a silica-containing phase in mmol L^{-1}.

$$\frac{dm}{dt} = -A_0 \left(\frac{m}{m_0}\right)^{\frac{2}{3}} r_0(T, pH) \left(1 - \frac{[Si]}{[Si_{sat}]}\right) \qquad \textbf{Eqn. 3.8}$$

The "diffusion-through-alteration-layer-dissolution" model is given in Eqn. 3.9 and is accompanied by Eqn. 3.10, which describes the evolution of elemental concentration under diffusion-limited dissolution. In these equations, C_i (mmol L^{-1}) is the concentration of an element i, A_0 (m^2) is the initial surface area of the glass, V (L) is the solution volume, x_i (dimensionless) is the weight percent of element i in the glass, ρ (mg m^{-3}) is the density of the glass, D_i (m^2 d^{-1}) and M_i (mg $mmol^{-1}$) are the diffusion coefficient and the atomic weight of an element, and t (d) is the time.

$$\frac{dm}{dt} = -A_0 \left(\frac{m}{m_0}\right)^{\frac{2}{3}} \rho \sqrt{\frac{D}{\pi t}} \qquad \textbf{Eqn. 3.9}$$

$$C_i = \frac{2A_0\rho}{VM_i} \left(\frac{m}{m_0}\right)^{\frac{2}{3}} x_i \sqrt{\frac{D_i t}{\pi}} \qquad \textbf{Eqn. 3.10}$$

In applying Eqns. 3.9 and 3.10 to model glass dissolution it is necessary to assume that a dissolution front progressed proportionately to the square root of time into the pristine glass and that the region behind the dissolution front was completely dissolved into solution (assuming congruent dissolution). It is further assumed that precipitation (or re-condensation in the case of amorphous silica) of secondary phases back onto the glass surface compensated for the retreat of the glass surface, leading to the formation of an alteration layer with a thickness that increased with the square root of time. Thus the size of the glass sample did not change with time, only the size of the inner unreacted core (the glass) decreases (i.e., isovolumetric substitution). This is similar to pseudomorphic replacement processes that commonly occur in geochemical

reactions[14,30] additionally, it was assumed that when the solution became over-saturated with respect to certain secondary species, they were precipitated out of solution.

Eqns. 3.8 and 3.9 were implemented into the PHREEQC geochemical code as a kinetic reaction, however, to ensure a good fit to the experimental data, it was necessary to impose specific equilibrium controls on the reaction. Firstly, to ensure a good fit for Ca concentrations, the solution was considered to be in equilibrium with C-S-H (in an ideal solid solution with end member Ca/Si ratios of 0.8 and 1.6). Secondly, phillipsite-K, a K-containing zeolite, was assumed to be in equilibrium with the solution; this ensured a good fit for the Al solution data and helped to improve fits for K. To accurately model the Si data, it was also necessary to assume equilibrium with a K-bearing alkali-silica gel.

The solution data were modelled according to Eqns. 3.8 – 3.10, by implementation in Phreeqc using the Thermochimie database at SCK.CEN.

Chapter 4. Dissolution of Vitrified Simulant Nuclear Waste in Synthetic Cement Waters

4.1. Introduction

To better understand the long-term behaviour of nuclear waste glass in a cement-rich disposal environment, synthetic cement waters have been utilised. As described in Chapter 2, many previous studies have examined the effect of highly alkaline solutions on glass dissolution mechanisms using simplified solutions of NaOH, KOH and $Ca(OH)_2$. However, few studies have investigated the role of cementitious leachates, which have a complex chemistry, containing multiple elements other than Na, K or Ca. A hardened paste of Portland cement is a porous medium; the pore water chemistry is dependent upon the solubility of the solid phases within the cement matrix. The evolution of pore water during cement leaching is well known; the first stage will be dominated by highly soluble alkali hydroxides (NaOH and KOH) creating a pH of > 13. In the second stage the pore solution chemistry will be controlled by the dissolution of $Ca(OH)_2$; and in the third stage C-S-H gel, in particular, the Ca:Si ratio of that gel, will determine the pore solution chemistry. The pH is expected to reduce to around pH 10.8[103]. These values are also dependent on the type of groundwater in which the cement will leach; both UK and Belgian disposal concepts, where cement pore waters will come into contact with vitrified waste, are considering disposal in a clay geology, which is the focus of this Chapter. Within the UK a clay geology is one of a possible three options for the host rock in a geological disposal facility.

The synthetic cement waters used as leaching media in this study have compositions that assume that a bulk cement specimen, upon contact with a clay groundwater, would generate solutions similar to those expected for Portland cement at three stages in time; young cement water, evolved cement water and C-S-H fluid (old cement water)[15]. The Belgian nuclear research organisation, SCK.CEN, developed a flow-through local equilibrium model, to define the near field porewater compositions for the Belgian supercontainer concept in a boom clay repository[120,15]. It was assumed that the pore water and the selected hydration products of cement (see Chapter 3) were in chemical equilibrium. As a function of time, effective components of the concrete were gradually eluted by the incoming Boom Clay pore water, which resulted in the evolution of the pore fluid composition. The resulting compositions, given previously in Chapter 3 (Table 3.4), were applied in this study. While these are representative specifically of the Belgian Boom clay, the groundwater composition is also relevant to other clay geologies, including those in the UK, as outlined in Table 4.1.

Table 4.1 Clay ground water compositions from the UK published by the British geological survey (BGS) and from Belgium by SCK.CEN.

Clay ground water composition			
	BGS	**SCK**	
Species	Concentration		Units
Na^+	1.87	15.6	
K^+	0.33	0.2	
Ca^{2+}	2.11	0.06	
Mg^{2+}	0.84	0.06	
Si	0.35	0.1	
HCO_3^-	2.80	14.4	mmol L^{-1}
Cl^-	1.55	0.7	
SO_4	1.92	0.02	
Al	3×10^{-3}	2×10^{-5}	
Fe	0.10	3×10^{-3}	
pH	6.7	8.5	
Eh	237	-274	
Temp	12.4	16	^oC

BGS[124] Clay ground water chemistry from the Palaeogene of the Thames Basin UK
SCK[120] Boom Clay pore water

This Chapter describes the dissolution mechanisms and kinetics of HLW and ILW UK simulant nuclear waste glasses, Magnox waste glass (MW25) and laboratory borosilicate simulant (LBS), respectively, in four cement leachates: Young Cement Water; Young Cement Water with added Ca; Evolved Cement Water and; Old Cement Water. The reader is directed to Appendix II for the detailed solution compositions. Data are shown for a three month leaching period, from experiments utilising glass powder and monoliths at 50 ^oC (RWM, *per. Comm.*). Aqueous geochemical analysis and concurrent surface investigation of altered layer formation are described.

4.2. Results (MW25 and LBS in synthetic cement water systems)

4.2.1. pH

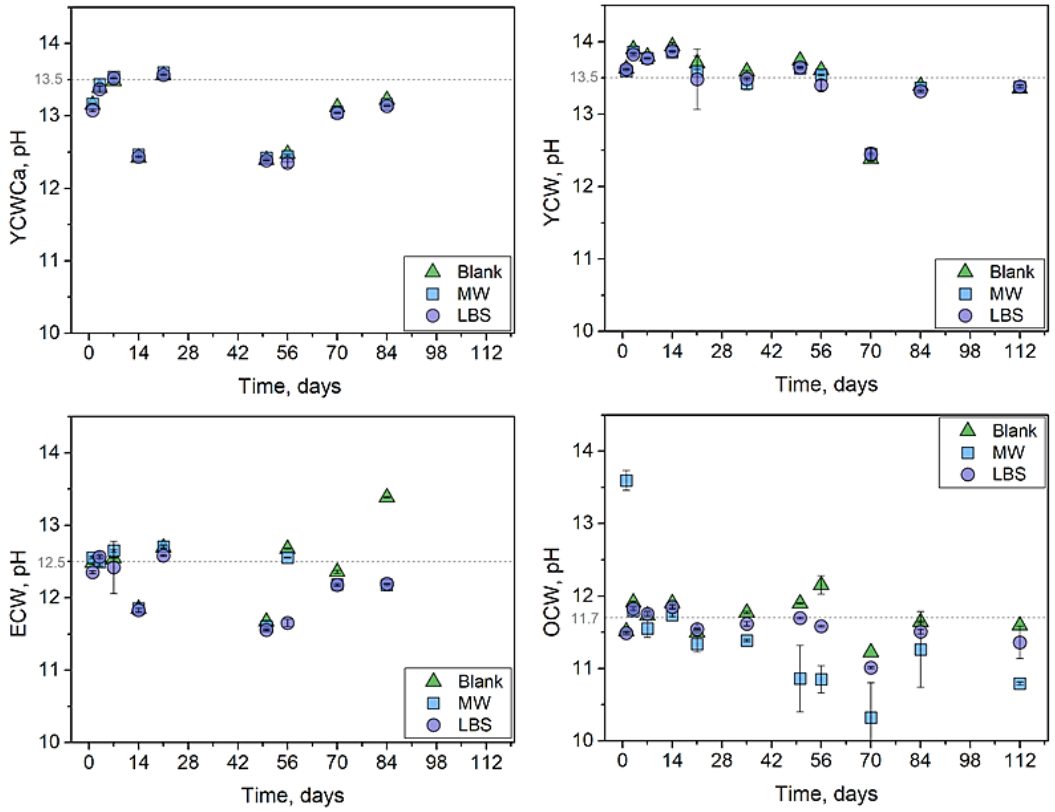

Figure 4.1 pH(RT) measurements for blank solutions of synthetic cement waters, and MW25 & LBS glass powder exposed for 112 days, the dashed line highlights the target pH and is a feature to guide the eye

The pH(RT) of all solutions remained above pH 10 throughout the experiment (Figure 4.1) indicating that they were free from carbonation by atmospheric CO_2. In young cement water solutions (YCW and YCWCa), the blank and sample pH values were similar indicating that the cement waters acted as a buffer throughout the experiment. The average pH for the duration of the experiment for YCWCa was pH(RT) 13.01 ± 0.48 and for YCW was pH(RT) 13.50 ± 0.43. As expected, the pH of the evolved and old cement water solutions (ECW and OCW) was lower than that of the young cement water solutions; the target pH for ECW and OCW was 12.5 and <12, respectively, and the average pH over the duration of the experiments was measured as pH(RT) 12.30 ± 0.50 and pH(RT) 11.56 ± 0.26 for ECW and OCW, respectively. On day 70, a drop in pH was observed in the YCW and OCW systems; this is likely an outlier since both the blank and samples are anomalously low, and the data collected after this sampling point are in accordance with the expected trend. The two different glasses exhibited similar pH values in each of the solutions.

4.2.2. Dissolution Rate Determination for MW25 and LBS glass

The dissolution rates were determined using the normalised mass loss of B and Li. Boron is often used for this purpose since it not retained in any of the glass alteration products[125]. However, studies by Depierre et al.[91] and Utton et al.[59] indicate that B may be retained by the formation of a secondary Ca-borate phase, such as colemanite ($Ca_2B_6O_{11}\cdot 5H_2O$) identified by Backhouse[70], at the glass solution interface.[56] This suggests that in Ca-containing, high pH solutions, it is preferable to use an alternative tracer element; however, since Li is not present in all glasses investigated in this thesis, the normalised mass loss of boron is also reported for consistency throughout. The normalised initial dissolution rates (NR_0, g m^{-2} d^{-1}) for both B and Li, were determined using a linear fit, for all solutions and glasses studied here, are outlined in Table 4.2 and Figures 4.2 to 4.5. It should be noted that the transition time for each condition into the "affinity-controlled" normalised dissolution regime (NR_a, g m^{-2} d^{-1}; i.e., where the dissolution rate slows due to the build-up of soluble species in solution, from the glass) is different, thus the time points between which the initial rate was calculated, is also stated. The figures in Section 4.2.3 show that the normalised mass loss of B, Li, Si, Mg, Al and Na are not equal under any of the experimental conditions, indicating incongruent dissolution. The curves and trends observed for the normalised mass loss of B and Li are similar, however Li was released more rapidly into solution than B, supporting the previous hypothesis that this element may be involved in alteration layer formation.

Table 4.2 Rates (g m^{-2} d^{-1}) of MW25 and LBS based on NR_0 of B (top) and Li (middle), errors were calculated based on the standard error of the gradient.

Initial Rates (**Boron**), NR_0, g m^{-2} d^{-1}				
Glass	YCWCa	YCW	ECW	OCW
MW25	(6.97 ± 1.1) x10^{-2}	(5.11 ± 0.1) x10^{-2}	(0.62 ± 0.01) x10^{-2}	-
LBS	(7.98 ± 0.7) x10^{-2}	(4.52 ± 0.3) x10^{-2}	(1.84 ± 0.1) x10^{-2}	-
Initial Rates (**Lithium**), NR_0, g m^{-2} d^{-1}				
Glass	YCWCa	YCW	ECW	OCW
MW25	(17.68 ± 5.1) x10^{-2}	(7.39 ± 0.1) x10^{-2}	(0.94 ± 0.1) x10^{-2}	-
LBS	(27.8 ± 6.8) x10^{-2}	(12.75 ± 0.1) x10^{-2}	(3.55 ± 0.3) x10^{-2}	-

YCWCa, 0-28 days YCW, 0-32 days ECW, MW 0-42 days & LBS 3-28 days

Affinity-controlled dissolution rate (**Boron**), NR_a, g$m^{-2}$$d^{-1}$				
	YCWCa	YCW	ECW	OCW
MW25	(1.77 ± 0.03) x10^{-2}	(1.43 ± 0.03)x10^{-2}	(0.45 ± 0.01) x10^{-2}	(0.38 ± 0.04) x10^{-2}
LBS	(3.73 ± 0.01) x10^{-2}	(1.88 ± 0.02) x10^{-2}	(0.51 ± 0.02) x10^{-2}	(0.35 ± 0.01) x10^{-2}

Glasses leached in the YCWCa solution (Figure 4.2) exhibited the greatest initial dissolution rates (NR_0) based on NL_B with values of (6.97 ± 1.12) x 10^{-2} g m^{-2} d^{-1} for the MW25 glass, and (7.98 ± 0.69) x 10^{-2} g m^{-2} d^{-1} for LBS determined between 1 and 28 d (Table 4.2). This is somewhat higher than the initial rates obtained by Utton et al[75] in a saturated $Ca(OH)_2$ solution for MW25 and LBS; after the same time period, the reported dissolution rates were found to be (3.8 ± 0.3) x 10^{-2} g m^{-2} d^{-1} and (3.5 ± 4.8) x 10^{-2} g m^{-2} d^{-1} for MW25 and LBS, respectively. The initial rate values of Utton are more comparable with those obtained here for YCW; normalised initial dissolution rates were (5.11 ± 0.10) x 10^{-2} g m^{-2} d^{-1} for MW25 and (4.52 ± 0.3) x 10^{-2} g m^{-2} d^{-1} for LBS, as shown in Figure 4.3. Once MW25 glass dissolution proceeded into the affinity controlled rate regime, a three times reduction in the dissolution rate compared to the initial rates for YCWCa and YCW was observed. LBS experienced a two times reduction in the dissolution rate upon entering the affinity controlled rate regime. For both MW25 and LBS glass, the affinity controlled rate occurred sooner in YCWCa than YCW, 28 d compared to 32 d.

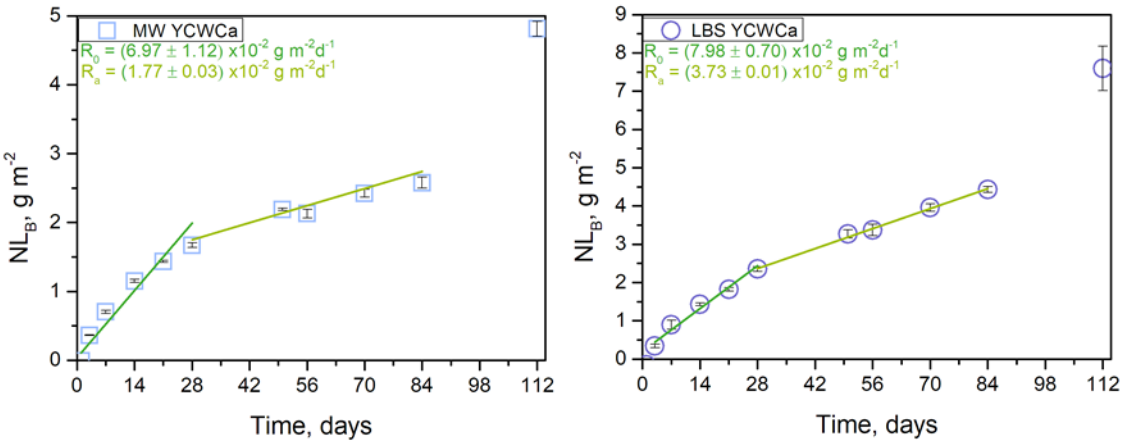

Figure 4.2 Normalised mass loss of B from MW25 (LHS) and LBS (RHS) in YCWCa, displaying rate equations. Errors calculated from the standard error of the slopes.

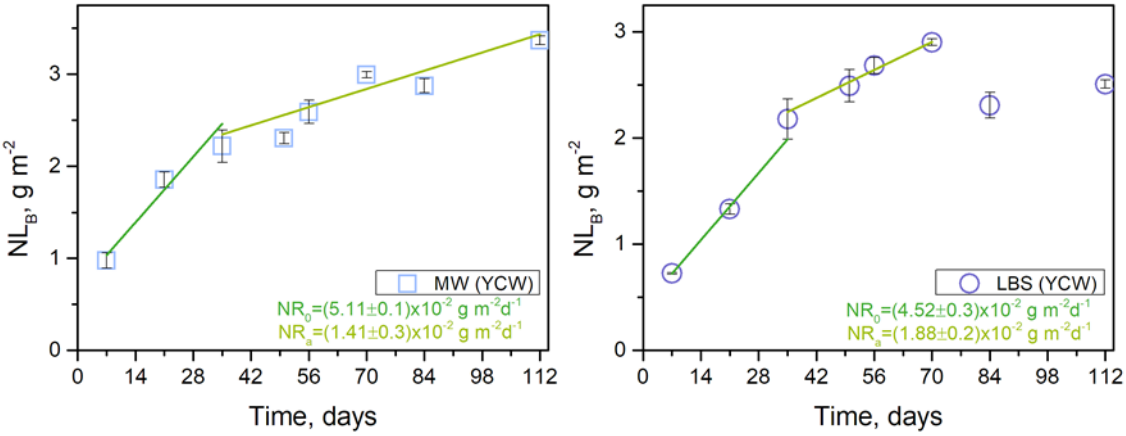

Figure 4.3 Normalised mass loss of B from MW25 (LHS) and LBS (RHS) in YCW, displaying rate equations. Errors calculated from the standard error of the slopes.

The average pH of the ECW solution was pH(RT) 12.30 ± 0.50. With a reduction in pH relative to the young cement solutions, the normalised initial dissolution rate would be expected to decrease because silica is less soluble at pH values close to neutral[126]. Figure 4.5 shows the initial normalised dissolution rate of MW25, calculated from a linear fit between 1 and 84 d, to be lower in ECW than that in the young cement leachates, giving a value of (0.55 ± 0.01) x 10^{-2} g m^{-2} d^{-1}. The linear fit for LBS in this solution was applied between days 3 and 28, giving an NR_0 of (1.84 ± 0.1) x 10^{-2} g m^{-2} d^{-1}. Glass exposed to young cement waters and ECW proceeded to the affinity controlled rate regime, reducing the rate of dissolution by at least half. The normalised affinity controlled rate of dissolution in the OCW (Figure 4.4) was the lowest observed, this is likely due to a reduction in pH and changes in the solution chemistry. The classic rate drop regime (signifying the onset of affinity-controlled dissolution) was not observed in this data set, however, evidence from SEM EDX shows the formation of precipitate phases on the surface of a gel alteration layer indicating that solution saturation was achieved, despite the linearly increasing dissolution trend. Possible explanations for this behaviour will be discussed further in later sections. The affinity controlled rates were (0.38 ± 0.04) x 10^{-2} g m^{-2} d^{-1} for MW25 and (0.35 ± 0.01) x 10^{-2} g m^{-2} d^{-1} for LBS, as calculated over the duration of the experiment.

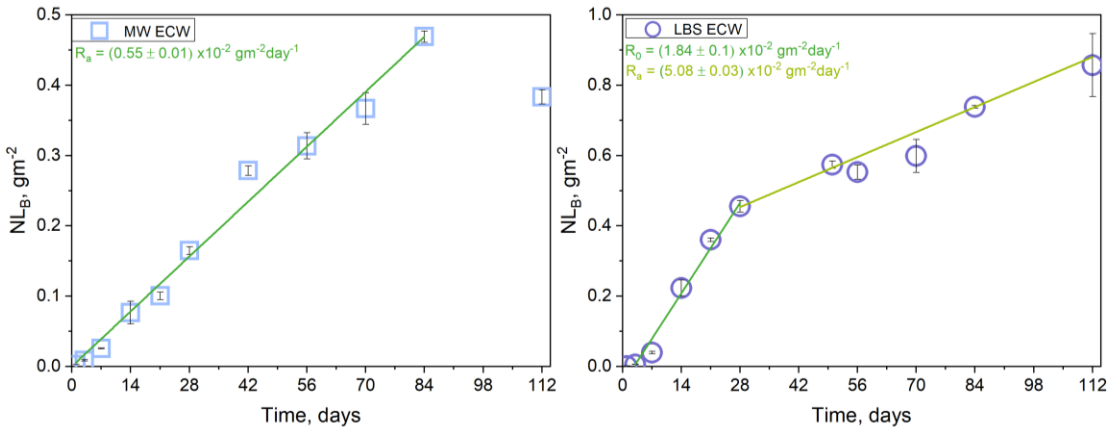

Figure 4.5 Normalised mass loss of B from MW25 (LHS) and LBS (RHS) in ECW, displaying rate equations. Errors calculated from the standard error of the slopes.

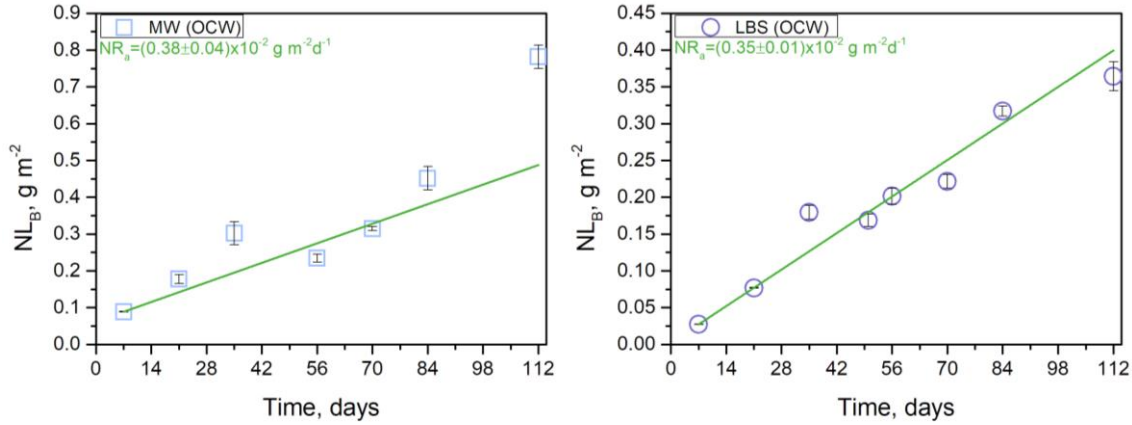

Figure 4.6 Normalised mass loss of B from MW25 (LHS) and LBS (RHS) in OCW, displaying rate equations. Errors calculated from the standard error of the slopes.

4.2.3. Normalised Mass Loss for MW25 and LBS glass

Figure 4.6 describes the normalised mass loss of elements from MW25 and LBS glasses leached in YCWCa. The normalised mass loss of B showed a continual increase, making it difficult to identify the individual stages of glass corrosion. A plateau was not observed, but instead a steady increase in dissolution rate occurred between 84 and 112 d, from 2.58 ± 0.08 g m^{-2} to 4.81 ± 0.11 g m^{-2} for MW25, and from 4.43 ± 0.08 g m^{-2} to 7.59 ± 0.58 g m^{-2}, for LBS these trends indicate the possibility of a rate resumption. Utton *et al*[75] reported the NL_B of MW25 glass in saturated $Ca(OH)_2$ to be ~0.5 gm^{-2}, which is a factor of 10 lower than observed here in YCWCa. Lithium followed a similar trend to B, however for MW25, a plateau was observed for NL_{Li} between 70 and 112 d, this was not seen for LBS.

Silicon was released readily from MW25 over the first 21 d, at which point the rate decreased somewhat but, overall, the NL_{Si} continued to increase until the end of the experiment. There was a continual steady release of Si from the LBS glass throughout the course of the experiment, and no rate drop period was observed. After 84 d, grains of LBS exhibited a thicker alteration layer than MW25 (see Section 4.2.5).

The NL_{Al} was greater for MW25 than for LBS; aluminium was observed to increase in solution until 14 d for LBS and 21 d for MW25, after which time the concentration decreased in both solutions. EDX maps (Section 4.2.4. i.) indicated that the altered layer was rich in Al compared to the pristine glass, suggesting this to be a sink for soluble Al. The NL_{Mg} was very low for both glass compositions, as supported by EDX mapping (Figure 4.14), which revealed an enrichment of Mg in the altered region compared to the pristine glass.

Since the YCWCa solution is mainly composed of NaOH, the NL_{Na} from the glass was difficult to calculate due to high background levels of Na in solution. Nonetheless, both glasses were observed to release Na into solution continuously.

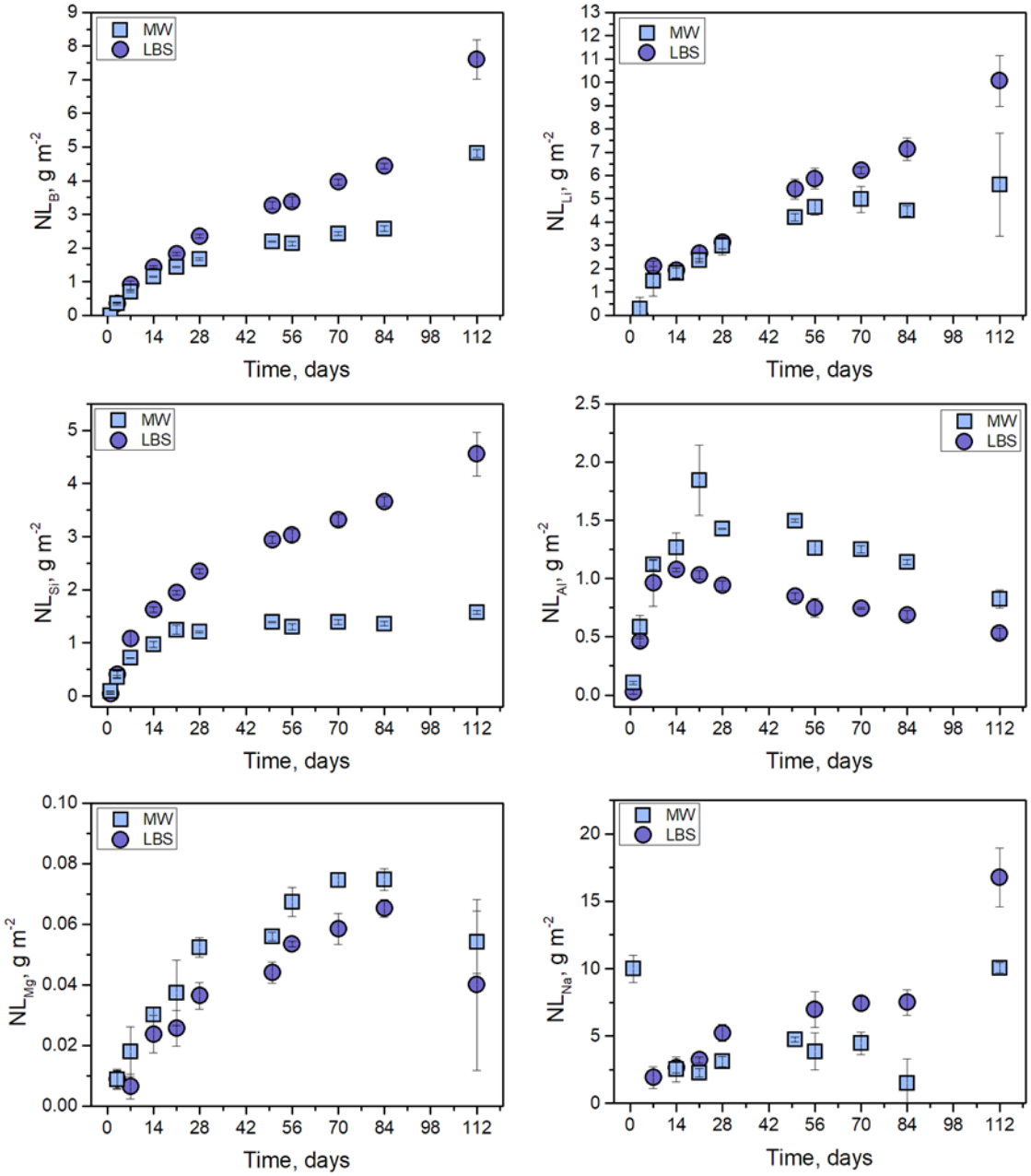

Figure 4.6 Normalised mass loss of elements from MW25 and LBS exposed to YCWCa for 112 days, g m^{-2}. Errors were calculated using the standard deviation of triplicate ICP-OES measurements.

Figure 4.7 shows the normalised mass loss of elements from MW25 and LBS glasses exposed to young cement water (YCW) without the addition of Ca; the initial dissolution rate was somewhat lower in this solution than in YCWCa discussed above (Table 4.2). The NL_B increased until 56 d for both glass compositions, after which point it became fairly constant, giving an NL_B at 112 d of 3.37 ± 0.05 g m^{-2} and 2.51 ± 0.04 g m^{-2} for MW25 and LBS, respectively. The NL_{Li} were quite different to those for B and there was a greater amount of Li released from LBS than from MW25. The maximum NL_{Li} values were 6.27 ± 0.14 g m^{-2} and 9.09 ± 0.31 g m^{-2} for MW25 and LBS.

Silicon was released from both glasses continuously throughout the experiment, and LBS released a greater amount of Si than MW25, reaching a maximum NL_{Si} at 56 d of 5.11 ± 0.07 g m^{-2}. In comparison, the maximum NL_{Si} for MW25 was 1.65 ± 0.07 g m^{-2} at 70 d.

As can be seen in Figure 4.7, the NL_{Al} followed different trends for MW25 and LBS; MW25 increased initially from 1.2 ± 0.1 to 1.8 ± 0.02 g m^{-2}, followed by a decrease to 1.14 ± 0.02 g m^{-2} until the end of the experiment, while for LBS, there was continued removal of Al from solution (excluding the data point at day 56 which is an anomaly); the EDX data associated with these samples show Al present in the alteration products (Figure 4.17 & Figure 4.34). The NL_{Mg} was very low for both glass compositions, but showed a steady increase from day 1 to 84 for both MW25 and LBS.

The NL_{Na} values were found to be within the same range as the results obtained in YCWCa solution. The MW25 and LBS values were similar until 56 d, after which time the values decreased, indicating that either Na dissolution had ceased, or that Na was being removed from solution. EDX mapping revealed a depletion in Na relative to the pristine glass, supporting the former hypothesis (see Figure 4.17 & Figure 4.34).

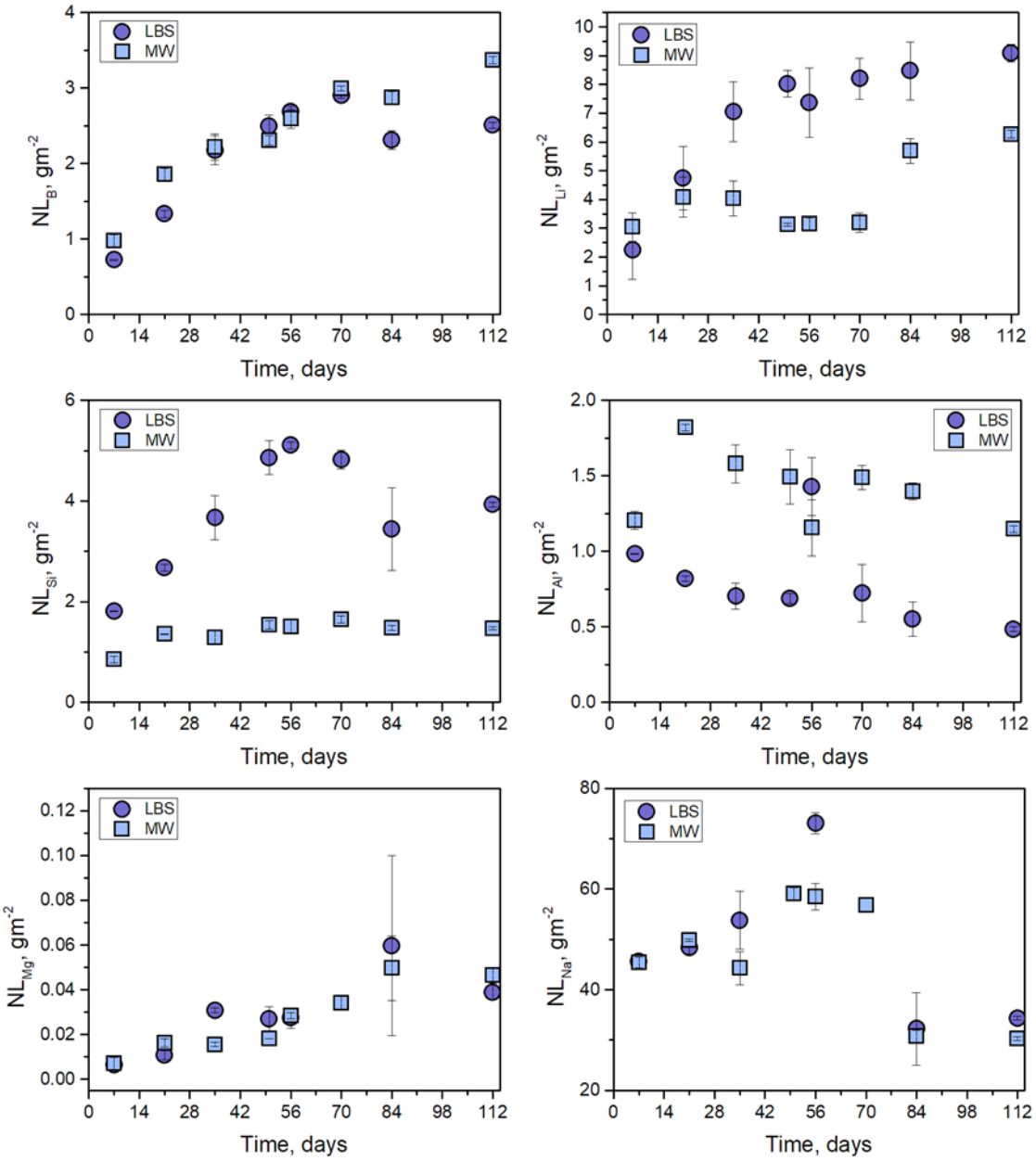

Figure 4.7 Normalised mass loss of elements from MW25 & LBS exposed to YCW for 112 days, g m^{-2}. An anomalous data point NL_{Mg} on day 70 has been removed. Errors were calculated using the standard deviation of triplicate ICP-OES measurements.

In the ECW solution (Figure 4.8) the solution chemistry showed a steady release of B from the glasses, although the final value of NL_B was lower for MW25 than for LBS, giving values of $(3.83 \pm 0.01) \times 10^{-1}$ g m^{-2} and $(8.57 \pm 0.9) \times 10^{-1}$ g m^{-2}, respectively. The NL_{Li} showed a similar trend to that of B for both glass compositions, with greater overall releases of $(7.58 \pm 0.8) \times 10^{-1}$ g m^{-2} and $(9.38 \pm 2.1) \times 10^{-1}$ g m^{-2} for MW25 and LBS.

The NL_{Si} was three orders of magnitude lower than that obtained in YCWCa and YCW (Figure 4.6 and Figure 4.7). There was a significant difference between the two glasses, with MW25 demonstrating an extremely low NL_{Si} of $(0.013 \pm 0.06) \times 10^{-1}$ g m^{-2}, compared with $(2.21 \pm 0.36) \times 10^{-1}$ g m^{-2} for LBS, on day 112. EDX mapping suggests an enrichment in Mg in the alteration layer of MW25, which may be the cause of the low NL_{Si} values; this will be discussed further in Section 4.2.4. iii. The concentration of Mg in solution was very low, however, the NL_{Mg} increased for both glasses until it reached a plateau at around 70 d. NL_{Al} from the MW25 glass increased over the first 28 d, before decreasing and then increasing once again. EDX mapping (Section 4.2.4 and 4.2.5) showed no enrichment of Al in the altered zone, thus the apparent decrease in solution may be a result of the concentration being close to the detection limit of the instrument. The maximum NL_{Al} obtained for MW25 was $(1.86 \pm 0.1) \times 10^{-1}$ g m^{-2} at 84 d and $(1.81 \pm 0.02) \times 10^{-1}$ g m^{-2} at 50 d for LBS.

The NL_{Na} increased for both glass compositions, reaching a plateau at around 28 d for LBS, while a plateau was not observed for MW25.

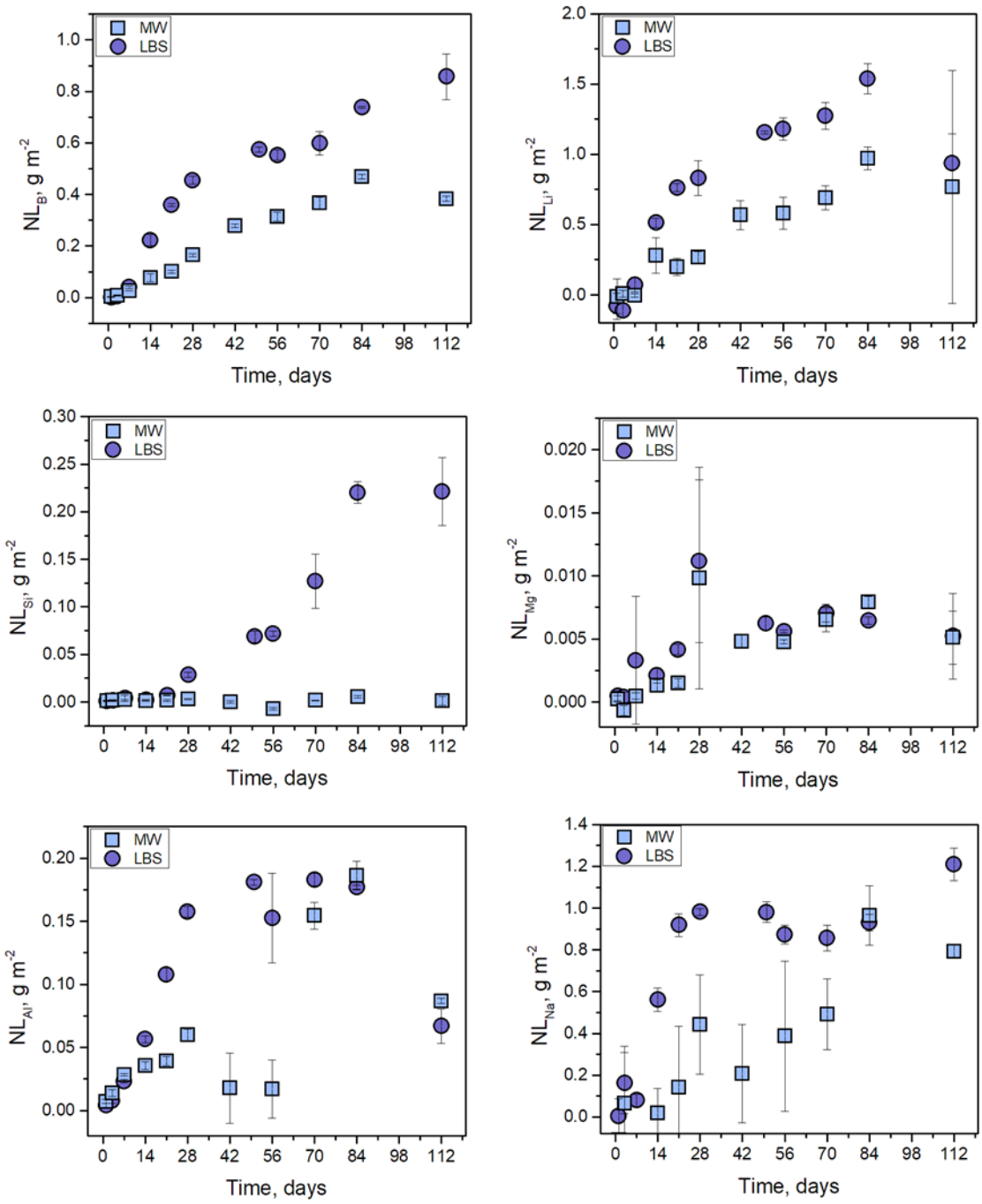

Figure 4.8 Normalised mass loss of elements in MW25 & LBS exposed to ECW for 112 days, g m^{-2}. Errors were calculated using the standard deviation of triplicate ICP-OES measurements.

Corkhill *et al*[61] observed an incubation period for Si dissolution in Ca-rich solutions. They proposed that high Ca concentration in solution prevented the release of Si, however once enough Ca had been removed from solution, Si dissolution was favoured. The LBS glass sample dissolved in ECW exhibited a similar delay in the release of Si to solution (Figure 4.8), which was correlated with the decrease in Ca concentration, shown in Figure 4.9. After 28 d, the Ca concentration dropped to 14.65 ± 2.0 mg L-1 suggesting that Ca was incorporated into a hydrated amorphous silicate layer in this glass, in agreement with EDX maps (Figure 4.20c). Conversely, for MW25 glass, the concentration of Ca in solution decreased much more slowly; by 28 d it was 240 ± 19 mg L^{-1} and by the end of the experiment it reached 40.5 ± 6.8 mg L^{-1}. It is postulated that the high Ca concentration over the first half of the experiment led to Ca-rich precipitates on the surface of the glass restricting the dissolution of the glass hence the very low Si release despite the pH of the solution remaining at ~ pH(RT) 12.3 ± 0.5. This is in agreement with SEM micrographs and elemental analysis discussed later (Section 4.2.4, Figure 4.20).

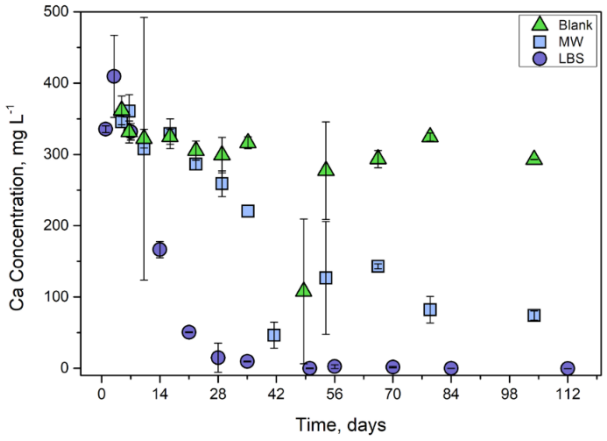

Figure 4.9 Ca concentration in the Blank, MW25 and LBS solutions of ECW. Errors were calculated using the standard deviation of triplicate ICP-OES measurements.

The normalised mass loss data for MW25 and LBS exposed to OCW is outlined in Figure 4.10. A continuous increase in the amount of B was observed during the experiment, with the maximum occurring at 112 d at NL_B values of 0.78 ± 0.03 g m^{-2} and 0.36 ± 0.02 g m^{-2} for MW25 and LBS, respectively. The NL_B values for MW25 and LBS have greater deviation from one another from 84 d onwards. The NL_{Li} was in good agreement with the NL_B.

Silicon exhibited a similar trend in OCW as ECW (with NL_{Si} values significantly lower than in the young cement water compositions). However, in OCW, the NL_{Si} of both glasses were similar, albeit LBS was a little higher than MW25, with NL_{Si} values of 0.11 ± 0.001 g m^{-2} and 0.37 ± 0.04 g m^{-2} at 112 d for MW25 and LBS, respectively. Very little Mg or Al was released

from either glass; the NL_{Mg} remained near zero for the duration of the experiment (the data point at 84 d is, within error) and the solution chemistry indicated that < 0.1 g m^{-2} Al was released. A greater amount of Na was released from LBS than MW25, with NL_{Na} values of (2.57 ± 0.21) g m^{-2} for MW25 and (3.61 ± 0.31) g m^{-2} for LBS.

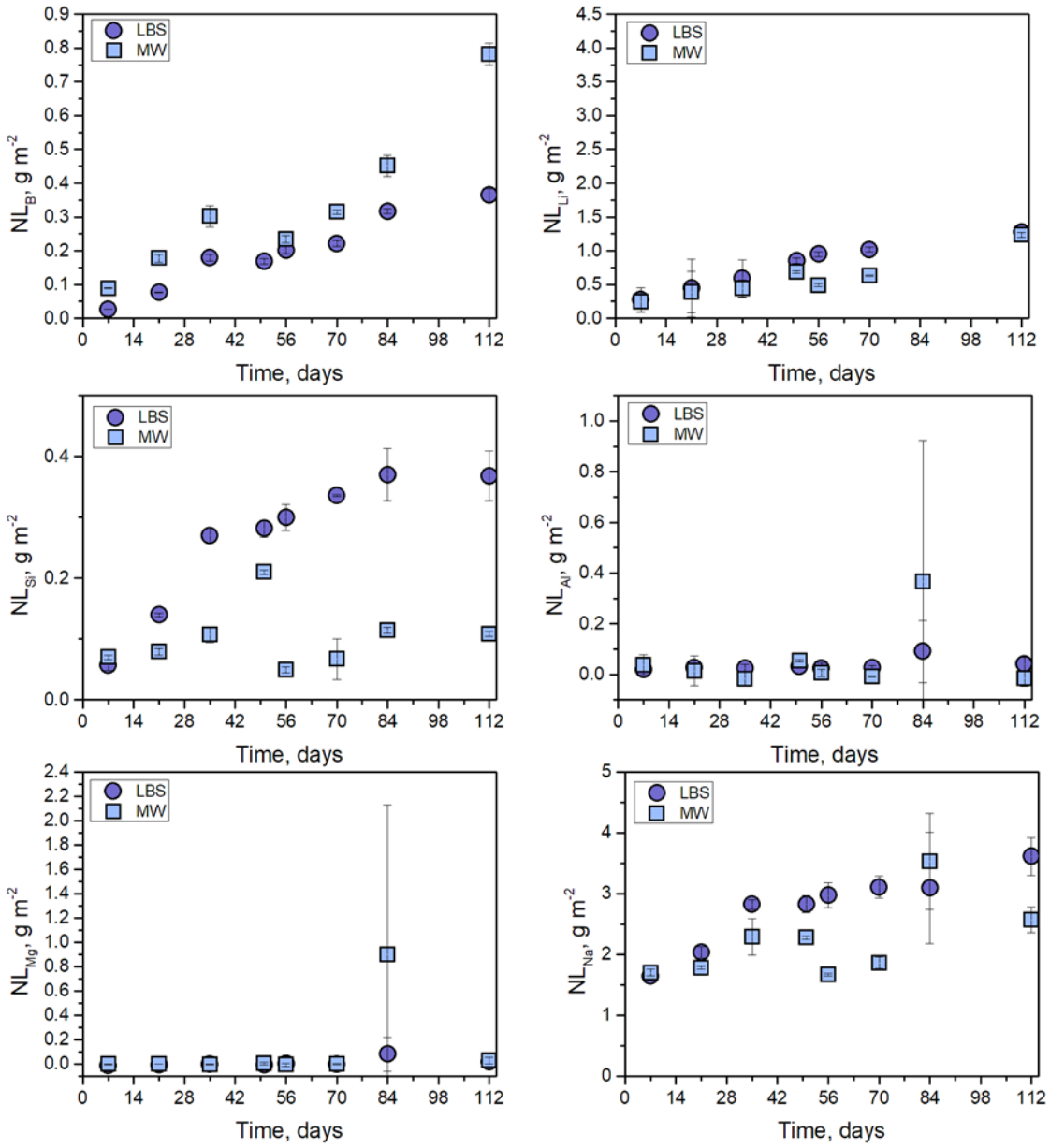

Figure 4.10 Normalised mass loss of elements from MW25 and LBS glass exposed to OCW. Errors were calculated using the standard deviation of triplicate ICP-OES measurements.

4.2.4. Alteration Layer and Secondary Phase Formation on MW25 glass

Figure 4.11 shows the XRD patterns for unreacted MW25 glass, and MW25 subjected to each of the four synthetic cement water solutions investigated, for 84 d. Analysis of pristine MW25 gives rise to an amorphous diffraction pattern in addition to crystalline RuO_2 (PDF 00-040-1290), which is known to readily crystallise from the glass after melting[127]. After leaching in YCWCa, it was possible to discern diffraction peaks for calcite ($CaCO_3$, PDF 00-001-0837) and C-S-H ($CaOSiO_2H_2O$), PDF 00-033-0306) and after leaching in YCW, C-S-H and portlandite ($Ca(OH)_2$, PDF 00-004-0733) were observed. Leaching in ECW resulted in the formation of portlandite, C-S-H and SiO_2 (PDF 01-082-1573), while leaching in OCW resulted in the formation of calcite only. Since the detection limit of XRD for phase identification is low, and it is difficult to observe phases present in concentrations of < 3 wt %, further analysis by micro- and nano-scale techniques was performed to better understand the chemical composition and physical nature of the alteration layers.

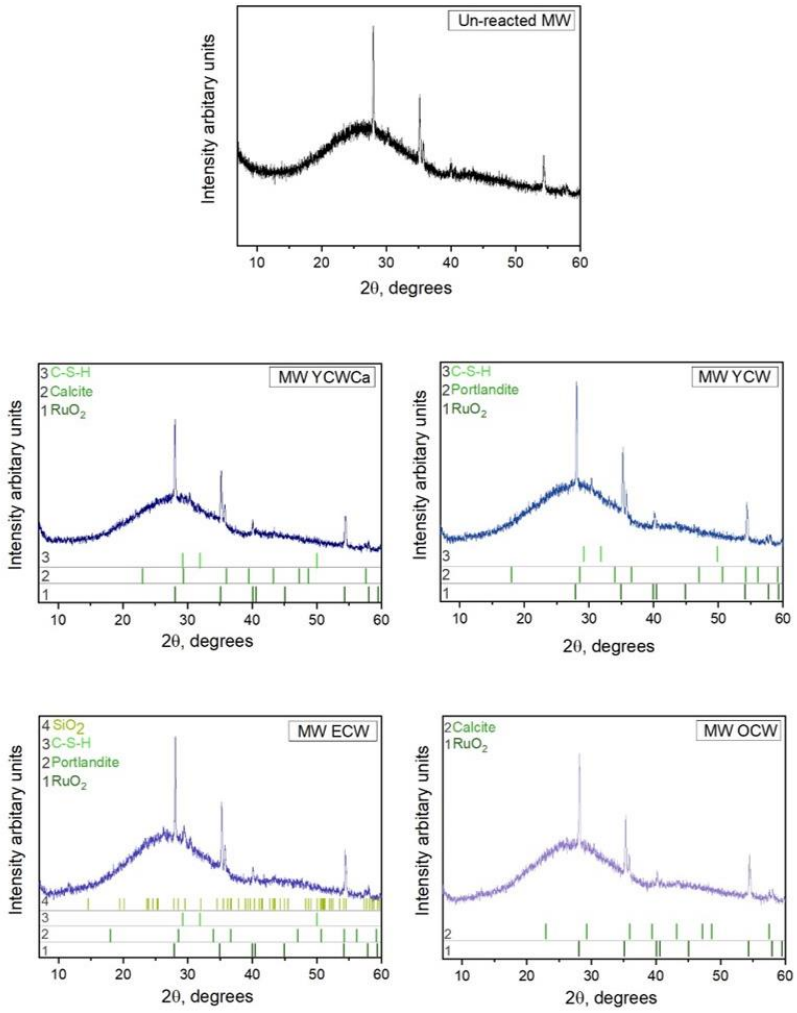

Figure 4.11 Diffraction patterns of MW25 glass powder before dissolution and after leaching in YCWCa, YCW, ECW and OCW for 84 days.

The altered layer thickness of the MW25 glass increased in all solutions except for the YCW solution, which rapidly (after 7 d) formed a 5 μm thick layer. This remained constant in thickness until 84 d (Table 4.3). This suggests that solution saturation may have occurred very rapidly in this solution and that either no further alteration occurred, or the layer was continually dissolving and re-organising for the duration of the experiment. Slow but continued boron and lithium release would suggest the latter. MW25 glass dissolved in young cement waters (YCWCa and YCW) exhibited thick alteration layers, while MW25 glass exposed to evolved and old cement waters had much thinner alteration layers, as shown in Table 4.3.

Table 4.3 Average total altered layer thickness determined by ~ 50 line measurements on 8 grains.

Average Total Layer Thickness, μm				
Time, days	MW25_YCWCa	MW25_YCW	MW25_ECW	MW25_OCW
7	1.59 ± 0.25	4.79 ± 0.59	0.49 ± 0.04	0.62 ± 0.10
21	3.06 ± 0.31	3.12 ± 0.33	0.49 ± 0.04	0.61 ± 0.08
56	4.09 ± 0.71	2.90 ± 0.37	0.86 ± 0.32	1.11 ± 0.43
84	4.62 ± 0.43	3.93 ± 0.57	2.40 ± 0.58	1.32 ± 0.37

Using the initial dissolution rate for B, discerned from Figures in Section 4.2.2, it was possible to calculate the expected altered layer thickness according to Equation 4.1, making the assumption that the glass alteration layer has the same density as the glass.

Eqn. 4.1

$$Calculated\ thickness\ (\mu m) = \frac{Initial\ dissolution\ rate\ (g\ m^{-2} day^{-1})}{Density\ of\ the\ glass\ (g\ m^{-3})} \times Time\ (days)$$

The calculated thickness was shown to be less than the measured values in all solutions except OCW where the calculated value was overestimated by 40 %. It is expected that the measured values should be more than the calculated values since the calculation only accounts for elemental losses from the glass and does not consider that elements are removed from the hyper alkaline leachate and incorporated into the alteration layer increasing the thickness. The opposite trend was observed in OCW and could indicate that the glass was not dissolving at the initial rate for the entire duration of the test. It is not considered that these data are indicative of rate resumption (where the gel layer is dissolved) since the gel showed no signs of elemental depletion and because the average thickness values increased from 0.62 ± 0.1 μm to 1.32 ± 0.3 μm between days 7 and 84. Furthermore, secondary phases were identified by TEM (Figure 4.25) indicating the glass was in the affinity controlled rate regime.

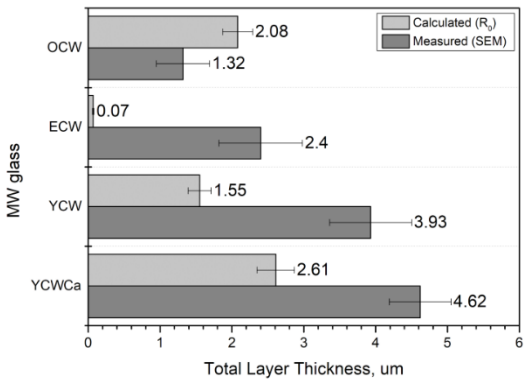

Figure 4.12 Calculated and measured total altered layer thickness for MW25 glass powder after 84 days in YCWCa, YCW, ECW, OCW.

SEM images of the MW25 glass grains dissolved in all of the synthetic cement solutions show altered layers with little or no de-lamination of the altered layer, indicating good sample preparation (Figure 4.13). Despite the samples having ~20 nm of carbon coat, carbon paint and copper tape to reduce charging, some charging was observed even at low (5 kV) energy. The glass grains dissolved in YCWCa and YCW (Figure 4.13 a and c) showed a thick altered layer. The contact between the altered layer and the epoxy resin was sharp however, in the ECW, this was not the case, and an irregular layer was observed partially surrounding grains (Figure 4.13e, highlighted with a yellow line). This is suggestive of the mass precipitation of secondary phases in ECW that was not observed in the other solutions. By comparison with the PhD thesis of *Backhouse (2017)*[70] this region is likely composed of C-S-H precipitates; EDX spot maps confirm this and give a Ca:Si ratio of 1.93. OCW had the least altered glass grains, the average total altered layer thickness after 84 d was 1.32 ± 0.37 µm (Table 4.3). A dense layer was not identified, merely a small change in the grey scale indicating a change in the topological profile.

At higher magnification (Figure 4.13 b, d, f & h) the morphological differences in the alteration products formed as a result of each solution can be seen more clearly. Young cement waters (YCWCa and YCW Figure 4.13 b and d) had an alteration layer comprised of two regions: the first was a thick gel layer ~6 µm wide for YCWCa and ~ 4.6 µm on the YCW sample, the second was different in the two solutions; composed of aggregates of precipitates in the YCWCa solution and fibrous or very porous phases in the YCW solution. In both cases the second region was ~ 1.5 µm in thickness. Glass exposed to ECW (Figure 4.13f) showed three distinct regions: i) the region closest to the pristine glass appeared to be less dense when compared to the other parts of the layer; ii) the thick outer region appeared to be more dense; and iii) the outer rim which was a thin dense band on the outside of the whole alteration layer. MW25 dissolved in OCW solution (Figure 4.13h) exhibited the thinnest alteration layer of all the solutions, with a complex morphology (described further below).

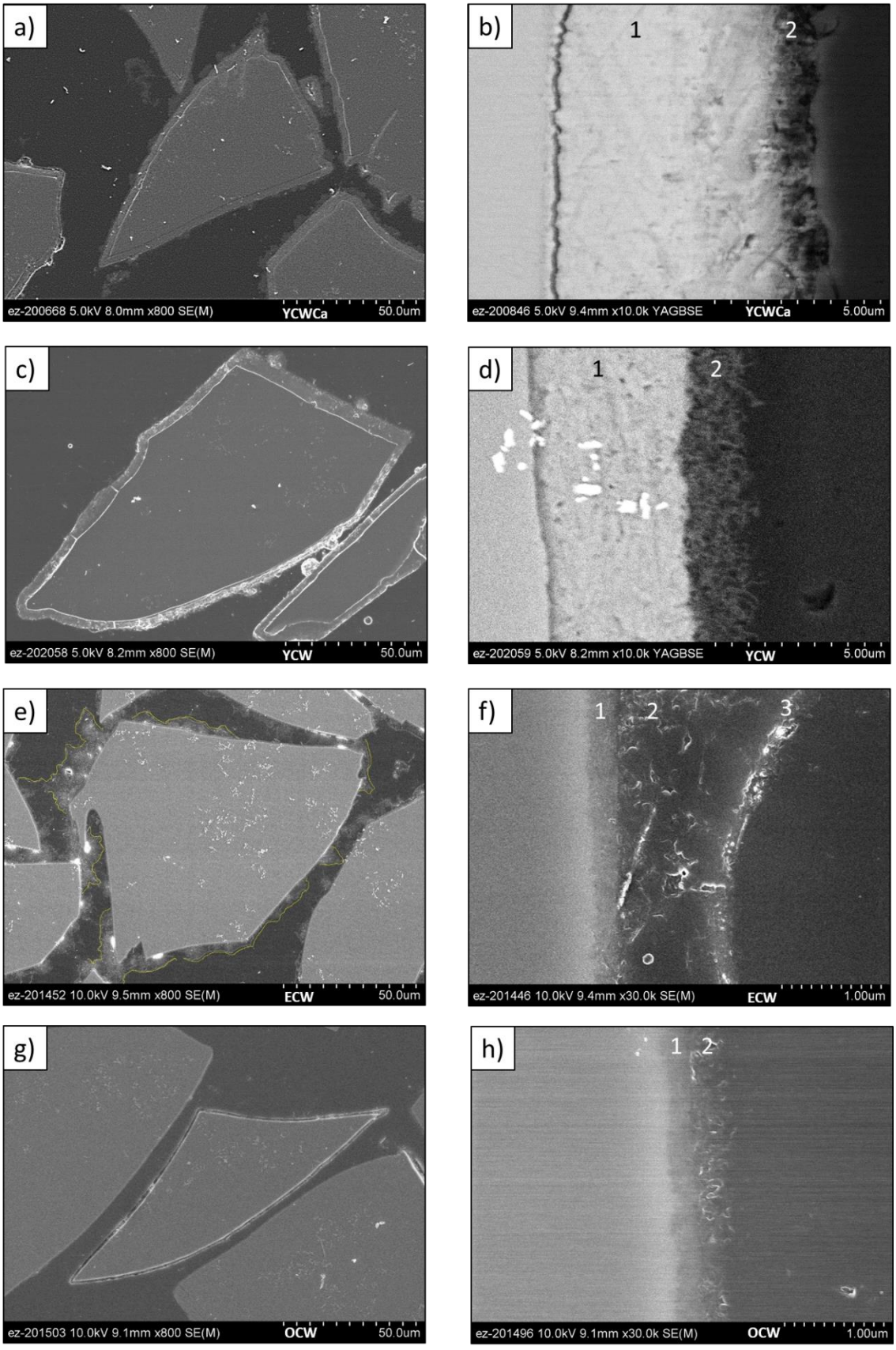

Figure 4.13 Secondary electron micrographs of MW25 glass grain after 84 d leaching; a & b YCWCa, c & d = YCW, e & f = ECW, g & h = OCW, images a, d, f, and h are at x10,000 magnification and the pristine glass is located on the left of each image.

i. MW25 exposed to YCWCa solution

A dense gel layer was observed with two regions; a dense inner region, labelled "1" in Figure *4.14*, and a less dense outer region labelled "2". The entire altered region (Layers 1 and 2 combined) was depleted in Na and Si relative to the pristine glass and significantly enriched in K (Table 4.4). Despite the semi-quantitative nature of these measurements, the very high alkali content (17 at % K) implies that this layer is a K-rich alkali silica gel, with the source of K being from the solution. Elemental spot maps (Table 4.4) of the surface layers indicated that Layer 2 was composed of C-S-H precipitates with a Ca:Si ratio of 0.58. This is within the accepted Ca:Si range of C-S-H, which has end members with a Ca:Si from 0.5 to 2.5[128,58]. In contrast, Layer 1 had a much lower Ca:Si ratio, of 0.13, and also contained significant quantities of K, Al, Mg and Na. The Mg content in the Layer 1 was higher than in the C-S-H layer; this is in agreement with NL_{Mg} data for this solution (Figure 4.7), which showed an initial release and subsequent plateau.

Table 4.4 SEM F50 EDS spot maps associated with Figure 4.14, giving the average elemental composition, (at %) of each alteration layer on the surface of MW25 after 84 d leached in YCWCa.

Element	Na	Mg	Al	Si	S	K	Ca	Fe	Other
at % Spot 9	13.22 ± 0.66	6.68 ± 0.33	13.97 ± 0.00	51.18 ± 2.56	-	0.33 ± 0.02	7.36±0.37	2.26 ± 0.11	1.25 ± 1.83
Avg at% Layer 1 (2)	3.06 ± 2.01	7.13 ± 0.62	13.79 ± 0.23	43.06 ± 0.10	-	17.41 ± 0.94	5.62±0.67	2.79 ± 0.05	1.59 ± 2.38
Avg at% Layer 2 (6)	5.91 ± 1.79	2.57 ± 3.73	10.23 ± 0.79	40.59 ± 3.35	1.32 ± 0.10	15.15 ± 4.28	19.91 ±6.58	1.22 ± 1.90	0.61 ± 1.37

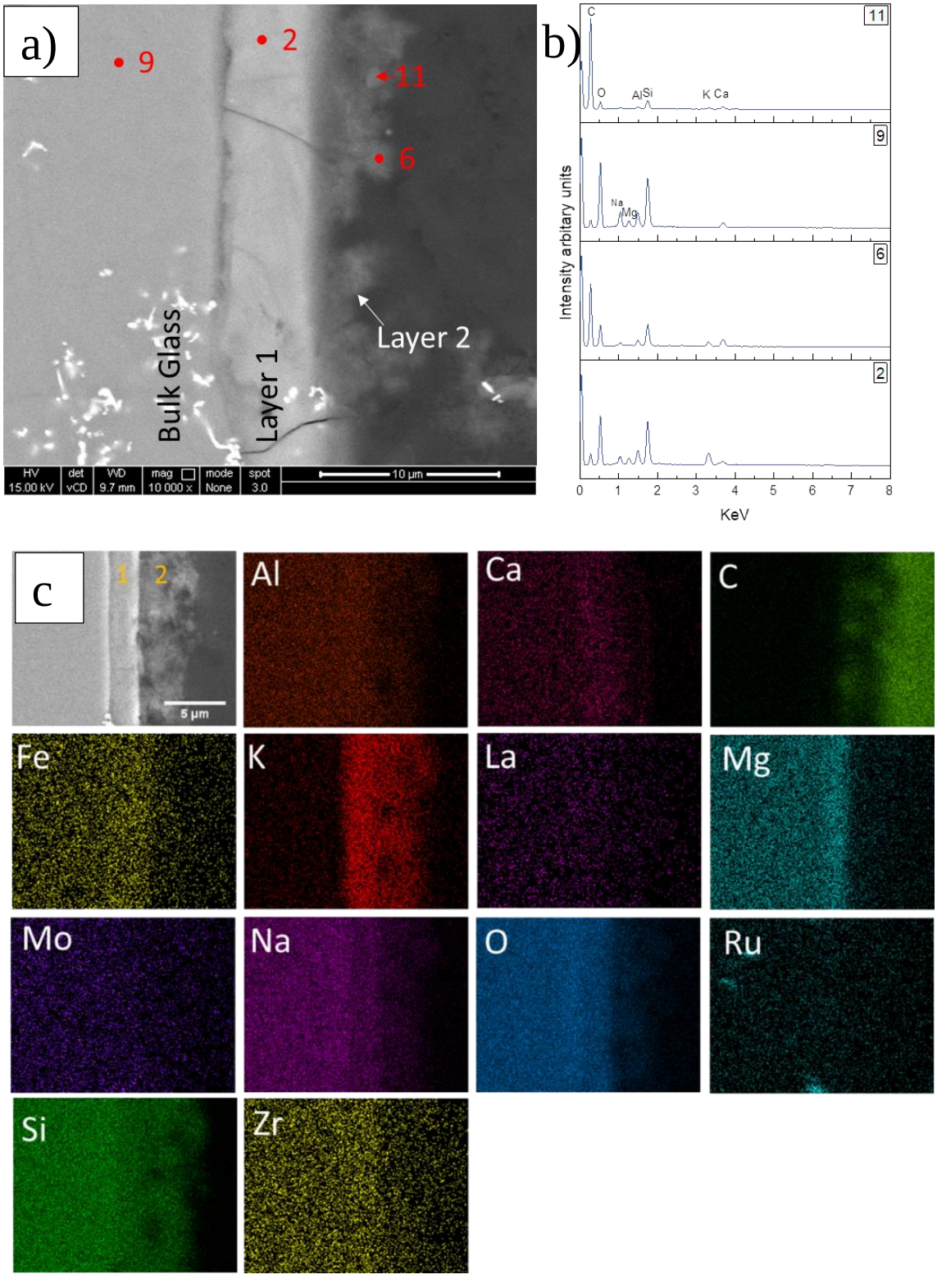

Figure 4.14 SEM EDX analysis of MW25 grain exposed to YCWCa for 84 d; a) BSE image with labels indicating alteration layers and spots at % listed in Table 4.4, b) spectra associated with spots on Fig a, c) elemental maps

A focused ion beam (FIB) section was prepared from an MW25 glass grain, across the boundary between the glass and the alteration layer. The bright field and dark field TEM images shown in Figure 4.15 indicate delamination of the altered layer from the pristine glass. The gel was approximately 1.96 µm thick with an average pore diameter of 2.57 nm (see Chapter 3 for image processing methods to determine porosity and associated error analysis) and a thin band of precipitate on the surface ~ 550 nm thick. Selected area diffraction (SAED) analysis (Figure 4.16) revealed that the gel and precipitate were amorphous, however, it cannot be ruled out that the electron beam amorphized fine precipitates at the surface of the glass. The EDS data shown in Figure 4.16 provides insight into the composition of the regions; the gel and precipitates were composed of elements indicative of an alkali silica gel, with an alkali(s) to silica ratio ([Na,K,Ca]:Si) of 0.45 and 0.40, respectively. Both the gel layer and precipitate were enriched with Mg relative to the bulk glass, with ~3 at % and ~12 at % more Mg than in the glass, respectively. Additionally, the precipitate contained a significant quantity of Fe (4.6 at %).

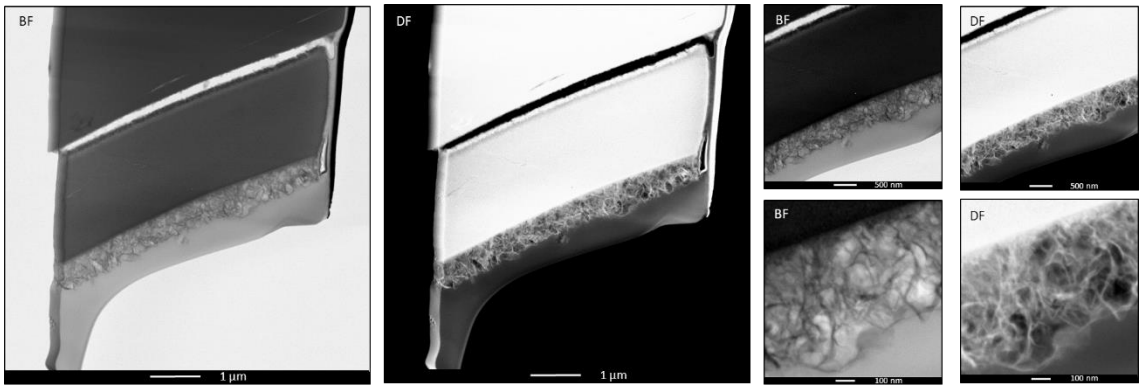

Figure 4.15 MW25 FIB sample post-dissolution in YCWCa, bright and dark field TEM images.

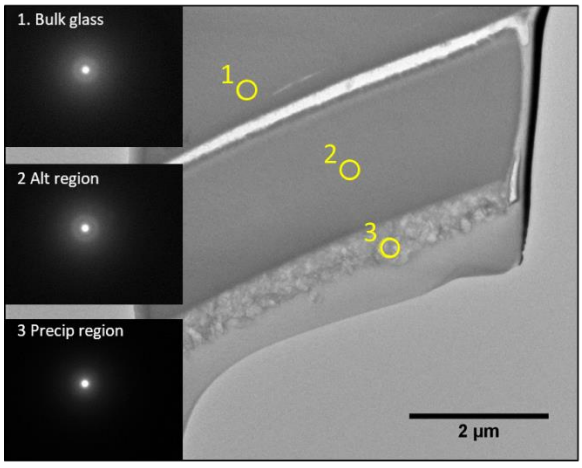

Atomic %	Bulk glass	Alt region	Precip region
Na_2O	8.7	3.5	3.5
Gd_2O_3	0	0.1	0.3
MgO	9.8	12.6	22
Al_2O_3	7.6	8.4	7.7
SiO_2	57.7	49.2	45.1
Cl_2O	0	0.1	1
K_2O	0.3	10.9	11.7
CaO	9.1	7.5	2.9
Cs_2O	0.5	0	0.4
BaO	0.1	0	0
La_2O_3	0.2	0.4	0.1
Ce_2O_3	0.5	0.8	0
Pr_2O_3	0.2	0.4	0
Nd_2O_3	0.9	1.4	0
Cr_2O_3	0.1	0.2	0
Sm_2O_3	0.2	0.2	0
Fe_2O_3	1.8	2.1	4.6
NiO	0.4	0.6	0
SrO	0.4	0.2	0.1
ZrO_2	0.9	1.2	0.3
Mo_2O_3	0.4	0.1	0.1

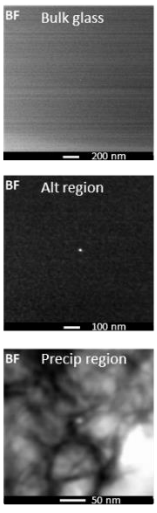

Figure 4.16 MW25 FIB section post-dissolution in YCWCa, SAED and EDS given in atomic % for elements detected in specific regions of the FIB section.

ii. MW25 exposed to YCW solution

Magnox waste glass exposed to YCW without the addition of Ca exhibited corrosion products of a similar morphology and elemental distribution as MW25 glass exposed to YCWCa. The micrographs in Figure 4.17 show the thick uniformed alteration layer surrounding the pristine glass.

Using elemental mapping at higher magnification, three distinct layers were observed (Figure 4.17). Layer 1 appeared dense, enriched with K from solution (8.87 at %), relatively Si-rich (although somewhat depleted with respect to the pristine glass) and depleted in Na relative to the pristine glass. This composition is suggestive of a K-rich alkali silica gel. Layer 2 was ~0.52 µm in thickness and could be distinguished by an enrichment in Mg content (Table 4.5). Layer 3 contained Al, Ca, K, Na and Si and had a "fluffy" morphology, suggestive of precipitation.

Table 4.5 SEM F50 EDS spot maps associated with Figure 4.17 average elemental composition, at % of each alteration layer on the surface of MW25 after 84 d leached in YCW.

Element	Na	Mg	Al	Si	S	K	Ca	Fe	Zn	Other
Avg at% Layer 1 (13)	11.12±4.60	8.93±2.97	11.57±1.68	43.13±12.05	3.10±0.16	8.87±12.56	5.86 ± 1.56	2.67 ± 0.49	4.41±0.46	0.17±0.41
Avg at% Layer 2 (16)	7.00±3.63	9.32±1.55	11.62±2.42	37.58±3.98	1.28±0.06	17.55±1.89	5.07 ± 0.83	2.78 ± 0.91	6.24±1.91	0.35±0.55
Avg at% Layer 3 (17)	5.89±1.49	4.54±4.35	13.09±0.20	42.21±1.22	1.05±0.05	18.14±2.26	8.38 ± 4.32	1.35 ± 0.85	3.76±1.44	0.33±0.52
at % Spot 20	6.54±0.33	1.99±0.10	0.32± 0.02	40.62±2.03	-	21.63±1.08	12.12 ± 0.61	0.70 ± 0.04	0.00±0.00	1.33±0.07

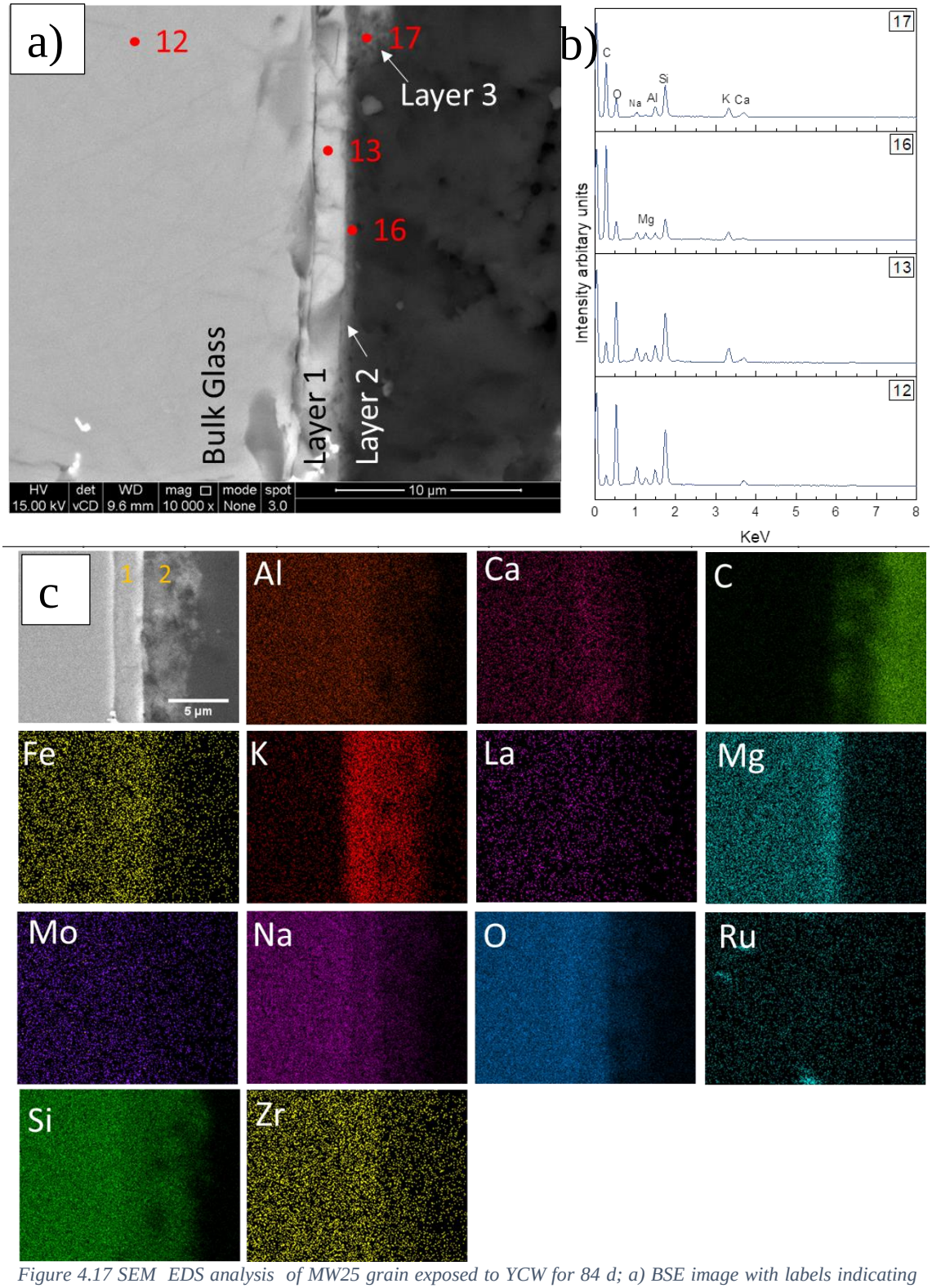

Figure 4.17 SEM EDS analysis of MW25 grain exposed to YCW for 84 d; a) BSE image with labels indicating alteration layers and spots at % listed in Table 4.5, b) spectra associated with spots on Fig a, c) elemental maps

A FIB sample was taken from a MW25 glass grain embedded in epoxy for TEM analysis. Delamination of the alteration products can be observed in the bright and dark field images of the FIB section (Figure 4.18). A gel ~1.68 µm thick was observed on the surface of the unaltered glass, upon which a precipitate layer 0.46 µm thick resided. The precipitate appeared to have similar morphology to that seen in the YCWCa solution (Figure 4.15), however, the diameter of pores in the gel was generally smaller at 1.29 nm. The glass and alteration products were found to be amorphous in nature as determined by SAED, shown in Figure 4.19 (although amorphization of the precipitates by the electron beam cannot be ruled out). The elemental data from EDS measurements indicated that the gel was composed of an alkali silica gel that was rich in Mg. The precipitate phase was significantly enriched in Mg (17 at % above that in the bulk glass) and, similarly to the MW25 exposed to YCW, was also enriched in Fe, at 2.2 at %. Mg-rich alteration products were not observed in the XRD (Figure 4.11), but traces were identified in the SEM EDS.

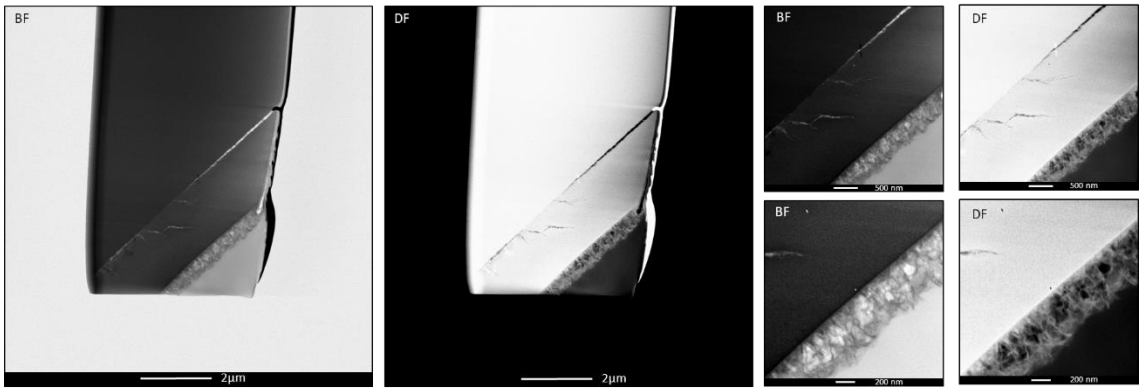

Figure 4.18 MW25 FIB section post-dissolution in YCW, bright and dark field images of the section and high magnification images of the gel and precipitates

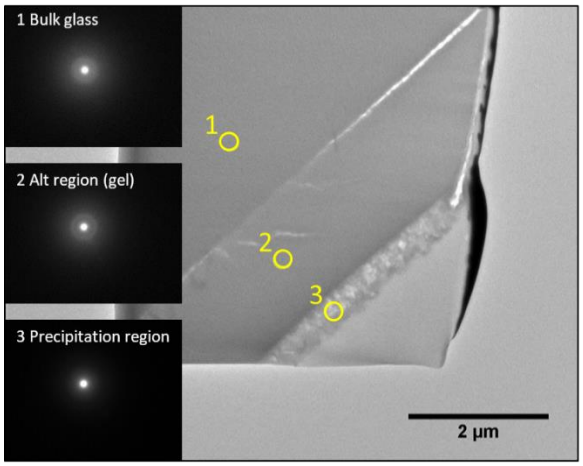

Atomic %	Bulk glass	Alt region	Precip region
Na_2O	10.1	3.7	6
Gd_2O_3	0.3	0.2	0
MgO	9.7	11	26
Al_2O_3	7.6	8.5	6.7
SiO_2	54.7	49.1	37.7
Cl_2O	0.1	0.1	1.1
K_2O	0.4	11.1	14
CaO	9.5	9.1	2.7
Cs_2O	0.6	0	0.3
BaO	0.1	0	0.2
La_2O_3	0.3	0.3	0.1
Ce_2O_3	0.7	0.7	0.2
Pr_2O_3	0.4	0.2	0.1
Nd_2O_3	1.2	1.4	0.1
Cr_2O_3	0.2	0.2	0.1
Sm_2O_3	0.2	0.3	0
Fe_2O_3	1.7	1.9	3.9
NiO	0.4	0.6	0.3
SrO	0.5	0.4	0.1
ZrO_2	1.1	1.2	0.3
Mo_2O_3	0.5	0.1	0.1

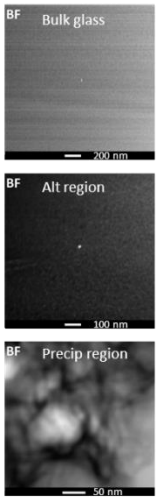

Figure 4.19 MW25 FIB section post-dissolution in YCW, SAED on areas of interest and EDS at % of the glass, alteration region (gel) and precipitation region

iii. MW25 exposed to ECW solution

The evolved cement water solution is significantly different in composition to the young cement waters previously described, being composed mainly of Ca and Na hydroxides with only a small amount of KOH (see Chapter 3, Section 3.1.2). This compositional difference in the solution resulted in significantly different alteration layer phases and morphologies. A thick, dense, uniform gel layer was no longer observed, and leaching in ECW lead to the formation of a thin gel band surrounding the glass grains. An additional outer region of alteration products was formed, which also contained a number of nodule-like features (Figure 4.13e).

Figure 4.20a demonstrates the presence of three alteration layers on the surface of a MW25 glass grain leached in ECW solution. Layer 1, closest to the pristine glass, was thin and enriched in Fe and Mg, which were contained in thin needle-like crystals, which were loosely packed but not detected by XRD (Figure 4.11). Layer 2 contained soluble glass elements (Fe, Al, Si and Zn), with no other alkali ions contributing significantly to this layer other than Ca, which was highly enriched, in accordance with observed removal from solution (Figure 4.9). The Ca:Si ratio of this Layer was 1.94 (Table 4.6), which may indicate the presence of a Ca-silica gel or C-S-H precipitates. Large Ca-rich crystals were observed in this layer, confirmed by XRD to be composed of calcite and portlandite (Figure 4.11). Layer 3 comprised Ca and Si only, and may be responsible for the formation of the Ca-bearing crystals within Layer 2; such a layer may prevent elements released during glass dissolution from being adequately transferred away from the interface towards the bulk solution, resulting in the formation of crystal nucleation sites, forming crystals. Such behaviour was previously observed by Dohmen *et al*[129] for a Si-rich rim. This is the first evidence for the same behaviour in a Ca-Si-rich rim.

Table 4.6 SEM F50 EDS spot maps associated with Figure 4.20 average elemental composition, at % of each alteration layer on the surface of MW25 after 84 d leached in ECW.

Element	Na	Mg	Al	Si	S	K	Ca	Fe	Zn	Other
Avg at% Layer 1 (34)	6.39 ± 2.21	9.16 ± 1.43	12.11 ± 1.34	51.05 ± 1.80	-	-	10.78 ± 2.41	2.02 ± 0.25	6.30 ± 1.10	0.57 ± 0.57
Avg at% Layer 2 (29)	1.80 ± 0.45	0.30 ± 0.31	4.48 ± 0.03	29.76 ± 0.25	-	-	57.66 ± 0.85	1.83 ± 0.08	2.82 ± 0.28	0.26 ± 0.14
Avg at% Layer 3 (31)	1.88 ± 0.89	0.53 ± 0.15	4.02 ± 0.15	-	1.75 - 0.09	-	-	1.10 ± 0.45	-	0.16 ± 0.28
at % Spot 37	13.67 ± 0.68	7.13 ± 0.36	13.09 ± 0.65	51.32 ± 2.33	-	0.09 ± 0.00	7.17 ± 0.36	2.18 ± 0.07	4.47 ± 0.22	0.29 ± 0.37

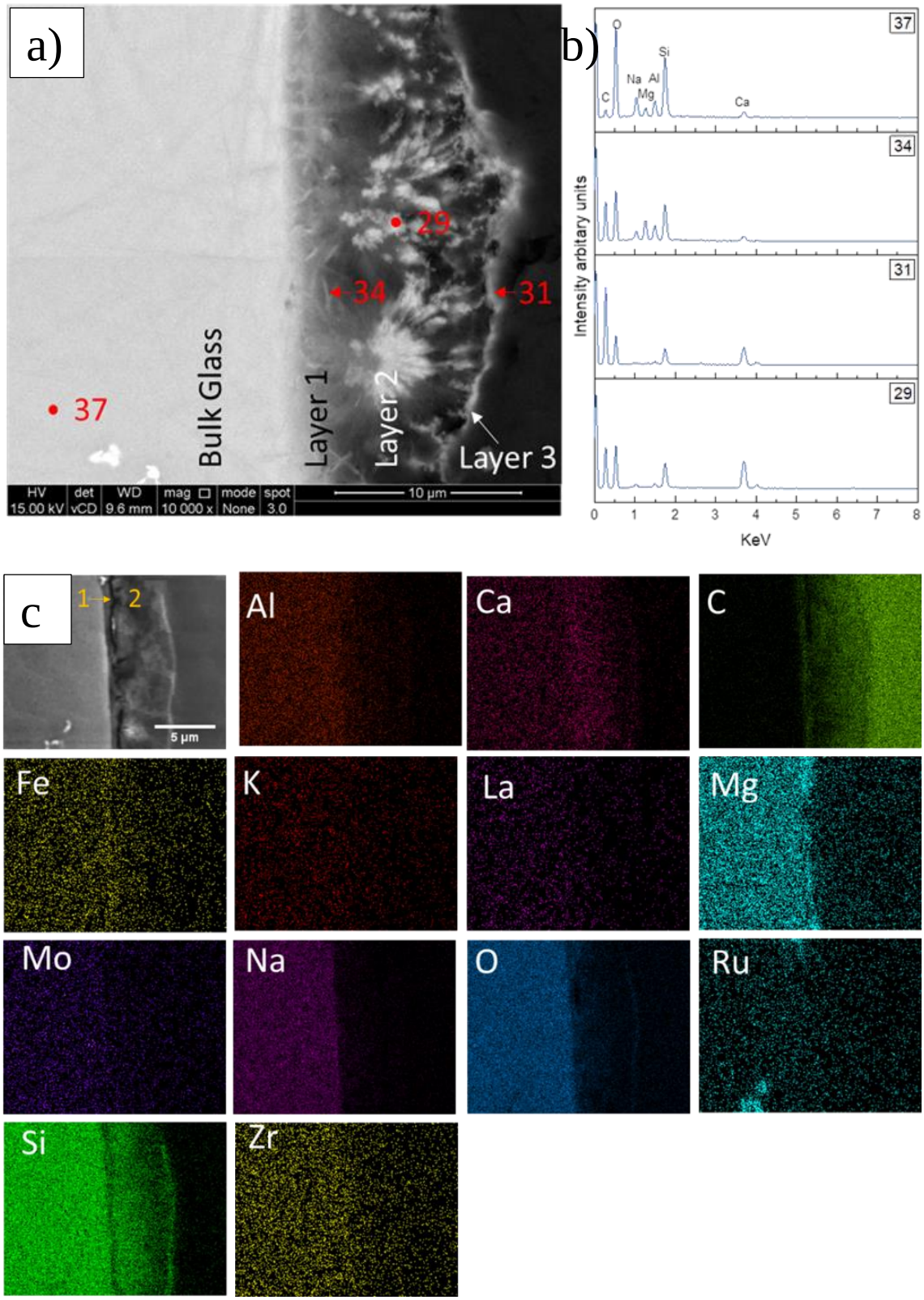

Figure 4.20 EDS analysis of MW25 grain exposed to ECW for 84 d; a) BSE image with labels indicating alteration layers and spots at % listed in Table 4.6, b) spectra associated with spots on Fig a, c) elemental maps

Crystal-like features observed in the SEM were also seen in the TEM FIB section of the same glass, shown in Figure 4.21. The top of the image shows the pristine glass with alteration products residing on the surface of the glass with the bottom region of the section glass from another grain. Key features include a porous gel, ~ 0.48 µm thick, in direct contact with the glass, a large region (~ 1.78 µm thick) of needle-like precipitates, and a region comprising of two gel-like bands. The total thickness of both bands was 0.54 µm with some separation in middle, and the average (mode) diameter of pores in the gel was determined to be 0.45 nm. Diffraction patterns of each region indicated that the gel products were amorphous, however, the boundary between the gel and needle-like precipitate exhibited crystallinity and the needle-like precipitate has also been identified as crystalline. The gel layer closest to the pristine glass (location 1 in Figure 4.22) was rich in Ca and Si, with a Ca:Si ratio of 0.70. The dense precipitate (location 2) had some Si present but was dominated by Ca and, as such, the Ca:Si ratio was 5.23. The needle-like precipitate (location 3) was identified as a C-S-H phase with a Ca:Si ratio of 2.16. This is close to the value obtained from SEM EDS of a similar feature (Figure 4.20 spot 29 Ca:Si ratio of 1.94).

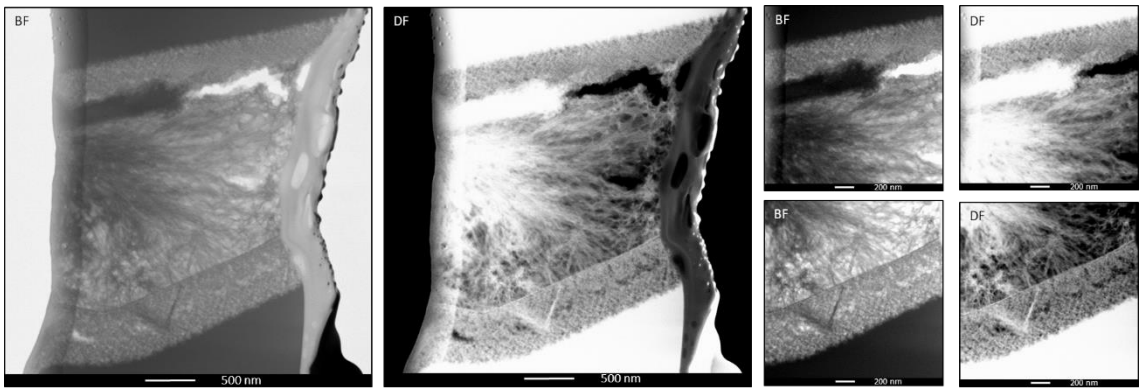

Figure 4.21 MW25 FIB section post-dissolution in ECW, bright field and dark field images of alteration products on the surface of the glass

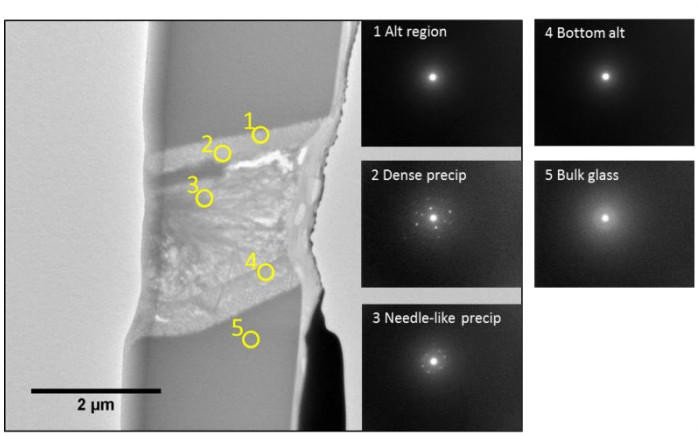

Atomic %	5 Bulk glass	4 Bottom alt	2 Dense precip	3 Needle like precip
Na_2O	9.1	1.2	0	0.6
Gd_2O_3	0	0	0	0
MgO	10.1	1.5	4.9	0.2
Al_2O_3	7.7	3.9	1.8	2
SiO_2	56.9	47.2	14.2	29.9
Cl_2O	0	0.6	0	0.2
K_2O	0	0	0.1	0.1
CaO	9	33.2	74.4	64.6
Cs_2O	0.6	0	0	0
BaO	0.4	0	0.1	0
La_2O_3	0.3	1	0.4	0
Ce_2O_3	0.5	1.6	0.7	0
Pr_2O_3	0.3	1.2	0.3	0
Nd_2O_3	0.9	3.7	1.1	0
Cr_2O_3	0.2	0.2	0.1	0
Sm_2O_3	0.2	0.7	0.2	0
Fe_2O_3	1.8	2.2	0.7	1
NiO	0.4	0.2	0.3	0
SrO	0.4	0.1	0.2	0.1
ZrO_2	0.9	1.5	0.5	1.3
Mo_2O_3	0.3	0	0.1	0.1

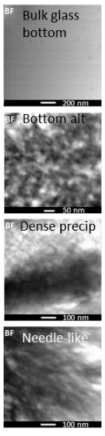

Figure 4.22 MW25 FIB section post-dissolution in ECW, SAED of regions of the alteration products, EDS indicated at % of elements present in alteration products

iv. MW25 exposed to OCW solution

MW25 glass grains exposed to OCW, which is composed of Na and Ca hydroxide in addition to sodium sulphate and calcium carbonate, are shown in Figure 4.13 g and h. The average pH of this solution was pH(RT) 11.56 (Figure 4.1) and the grains exhibited the lowest amount of corrosion as determined by the average alteration layer thickness (Table 4.3). The micrographs in Figure *4.23* provide a representative example of the grains exposed to OCW for 84 days. A very thin alteration layer was observed to surround the glass grains, and at the magnification employed, there was no evidence for an alkali-silica gel or precipitates. Elemental maps (Figure 4.23) from the FE-SEM also do not provide enough detail at x10,000 magnification to identify the composition of any layer. A slight enrichment in Ca is suggested from spot EDX of the layer (Table 4.7), however it should be noted that the spot is considerably larger in size than the layer, thus this may not be strictly representative of the layer chemistry.

Table 4.7. SEM F50 EDS spot maps associated with Figure 4.23 average elemental composition, at % of each alteration layer on the surface of MW25 after 84 d leached in ECW.

Element	Na	Mg	Al	Si	S	K	Ca	Fe	Zn	Other
Bulk Glass (1)	15.87 ± 0.87	7.30 ± 0.33	13.56 ± 0.11	51.69 ± 2.40	-	-	0.13 ± 0.13	1.46 ± 0.28	3.37 ± 0.12	0.49 ± 0.38
Broken surface (6 & 8)	15.41 ± 0.52	7.22 ± 0.24	13.92 ± 0.25	50.89 ± 1.19	-	-	5.78 ± 0.15	1.79 ± 0.30	3.25 ± 0.37	0.59 ± 0.48
Layer1 (3)	9.14 ± 2.50	6.73 ± 0.09	13.04 ± 1.59	46.39 ± 6.03	2.20 ± 0.82	0.05 ± 0.11	13.68 ± 9.21	2.29 ± 0.28	3.84 ± 0.93	0.54 ± 0.58

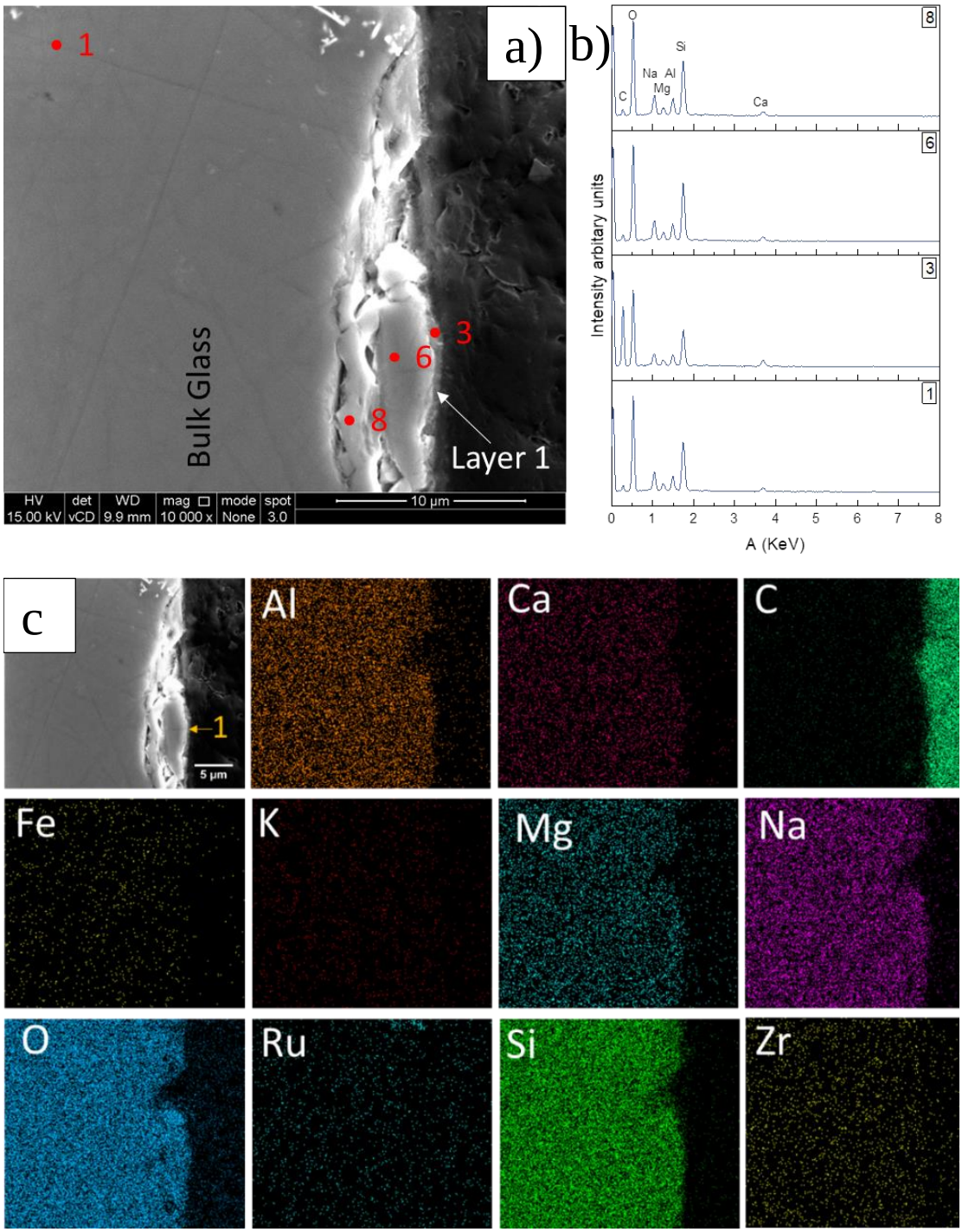

Figure 4.23 SEM EDS analysis of MW25 grain exposed to OCW for 84 d;; a) BSE image with labels indicating alteration layers and spots at % listed in Table 4.7, b) spectra associated with spots on Fig a, c) elemental maps

In contrast to the SEM images, high resolution TEM bright and dark field images (Figure 4.24 & 4.25) showed two bands of alteration products residing on the surface of the pristine glass; the first was a gel-like layer ~ 0.2 µm thick, close to the pristine glass, with a Ca:Si ratio of 0.2. The precipitate on the outer surface was 0.3 µm thick and had an alkali:Si ratio of 0.19. The major component of this region was Mg, which showed an enrichment of +12.2 at % when compared with the bulk glass (Figure 4.25). Visually the pores in the gel layer appeared to be smaller when compared to those in the precipitate layer, however, there was very little difference when calculated; the average pore diameter in the gel was 0.45 nm.

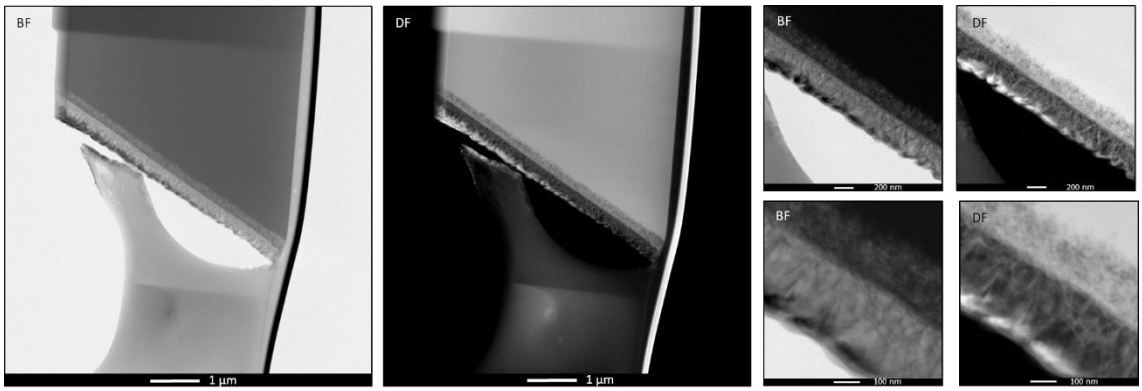

Figure 4.24 MW25 FIB Section post-dissolution in OCW, bright and dark field images of the alteration products present on the surface of the glass

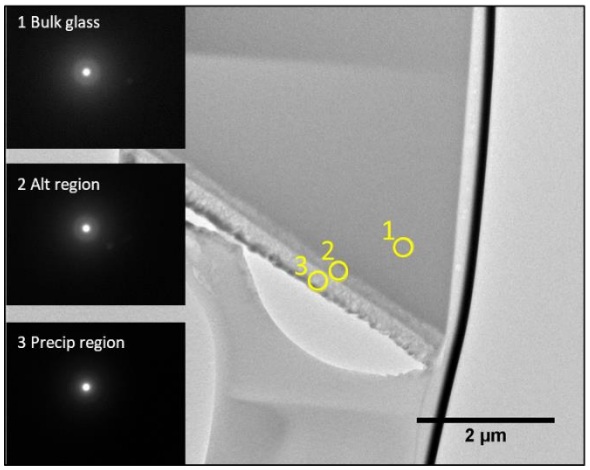

Atomic %	Bulk glass	Alt region	Precip region
Na_2O	8.9	2.5	6.4
Gd_2O_3	0.1	0	1.3
MgO	9.7	4.7	21.2
Al_2O_3	7.7	9.2	7.2
SiO_2	58.5	60.8	55.5
Cl_2O	0	0.1	0.3
K_2O	0	1.5	1
CaO	9	13.5	3.4
Cs_2O	0.4	0.2	0
BaO	0	0.1	0
La_2O_3	0.2	0.4	0
Ce_2O_3	0.3	0.8	0
Pr_2O_3	0.3	0.4	0
Nd_2O_3	0.9	1.4	0.1
Cr_2O_3	0.1	0.1	0
Sm_2O_3	0.2	0.3	0
Fe_2O_3	1.7	1.6	2
NiO	0.5	0.3	0.8
SrO	0.3	0.3	0.2
ZrO_2	0.9	1.5	0.4
Mo_2O_3	0.4	0.2	0.1

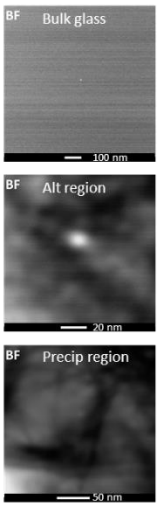

Figure 4.25 MW25 FIB section post-dissolution in OCW, SAED of regions of the glass and alteration products, EDS analysis tabulates are the at % of elements present in the alteration products

4.2.5. Alteration Layer and Secondary Phase Formation on LBS glass

Alteration layers were present on the majority of LBS glass grains in each of the dissolution media. The alteration layers observed on glass exposed to OCW showed a small uniformed layer, close to the pristine glass, while in ECW the layer was much less uniform and was significantly thicker. The alteration layers on glass exposed to the YCWCa and YCW were uniform and thick. X-ray diffraction (Figure 4.26) of the glass grains indicated that, despite the presence of thick alteration layers, they appeared to be largely amorphous. Mineral phase identification should be considered as plausible but not guaranteed, as a number of the major peaks from these minerals may have been suppressed due to the amorphous nature of the samples. Dissolution in YCWCa left portlandite ($Ca(OH)_2$; PDF 00-004-0733) on the surface of LBS glass grains, and in the diffraction pattern for LBS dissolved in YCW, C-S-H ($CaO\text{-}SiO_2\text{-}H_2O$; PDF 00-033-0306) was identified. For glass dissolved in the ECW solution, peaks were identified that have been attributed to calcium aluminium oxide carbonate hydrate ($3CaO{\cdot}Al_2O_3{\cdot}Ca_X.nH_2O$; PDF 00-036-0377), hydrotalcite ($Mg_6Al_2CO_3(OH)_{16}{\cdot}4(H_2O)$; PDF 00-014-0191) in addition to portlandite and C-S-H. This correlates with SEM EDS spot maps and TEM EDS maps of nodules found to be embedded in the alteration layer (see Section 4.2.5 iii). The thin alteration layer on LBS exposed to OCW did not reveal any crystalline diffraction peaks and the x-ray diffraction pattern post-leaching was very similar to the glass before corrosion.

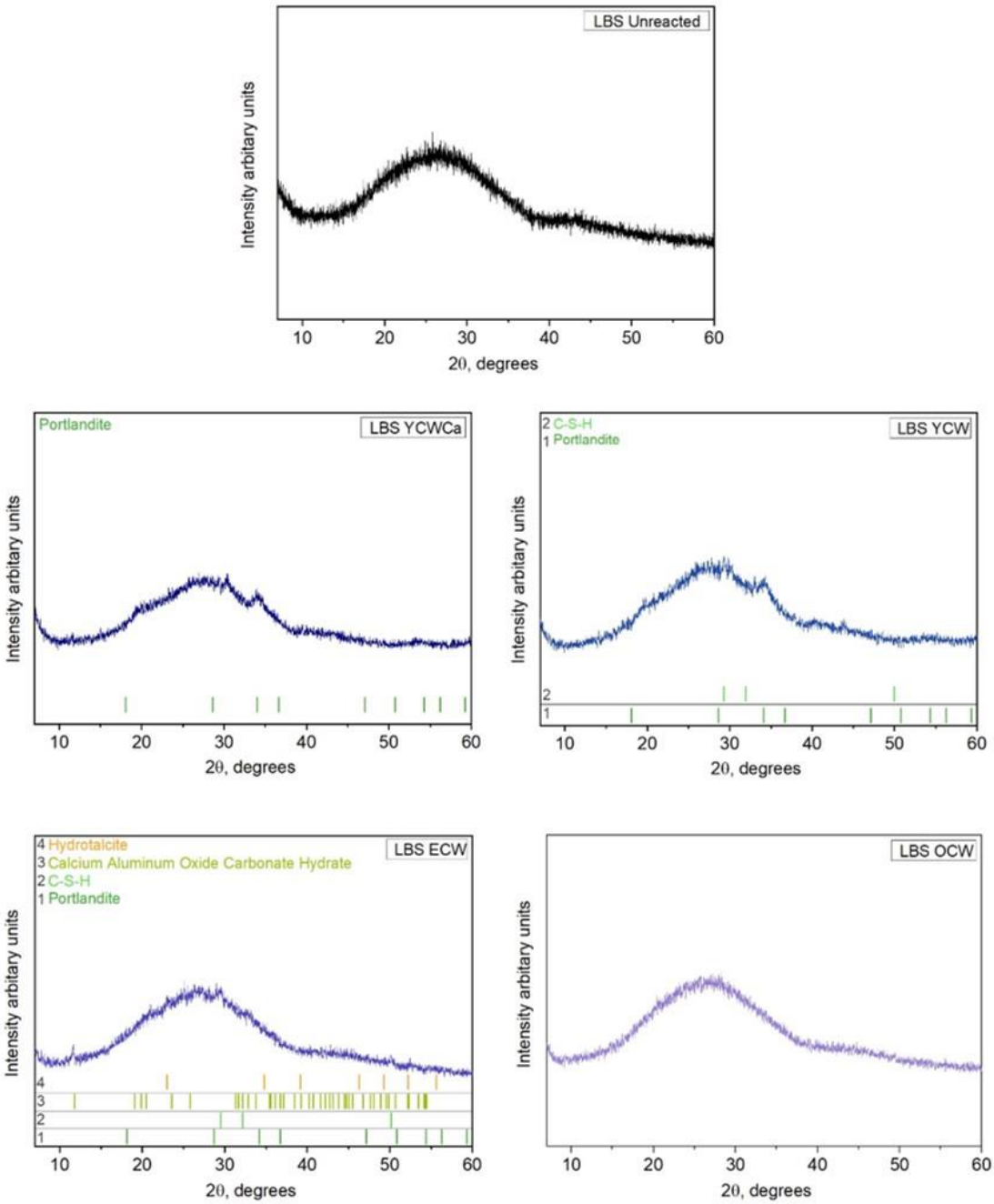

Figure 4.26 Diffraction pattern for LBS exposed to YCWCa, YCW, ECW, OCW for 84 days.

The average total altered layer thickness was calculated based on thickness measurements of at least 5 grains of glass per time point, as outline in Table 4.8. These were imaged using a FE-SEM and the alteration layer was measured using image software (image J). Approximately 50 line measurements were made around the perimeter of each grain and the average was tabulated (Chapter 3).

Table 4.8 Average total altered layer thickness determined by ~50 line measurements on 8 grains.

Average Total Layer Thickness, µm				
Time, days	LBS YCWCa	LBS YCW	LBS ECW	LBS OCW
7	2.00 ± 0.18	2.01 ± 0.18	0.21 ± 0.02	1.98 ± 1.51
21	3.52 ± 0.28	4.69 ± 0.85	2.68 ± 1.09	0.79 ± 0.22
56	3.28 ± 0.74	5.42 ± 0.42	5.38 ± 0.38	1.59 ± 0.75
84	7.58 ± 1.26	7.40 ± 1.20	3.24 ± 0.63	1.04 ± 0.16

There was a discrepancy between the calculated altered layer thicknesses compared to the measured values (Figure 4.27). Measurements were made on grains that were easy to visualise and measure, this will have led to bias in the measurement. Additionally, the initial rate used to make the calculation considers the amount of B released into solution, and does not account for the formation of gel layers or secondary phase precipitates from the solutions.

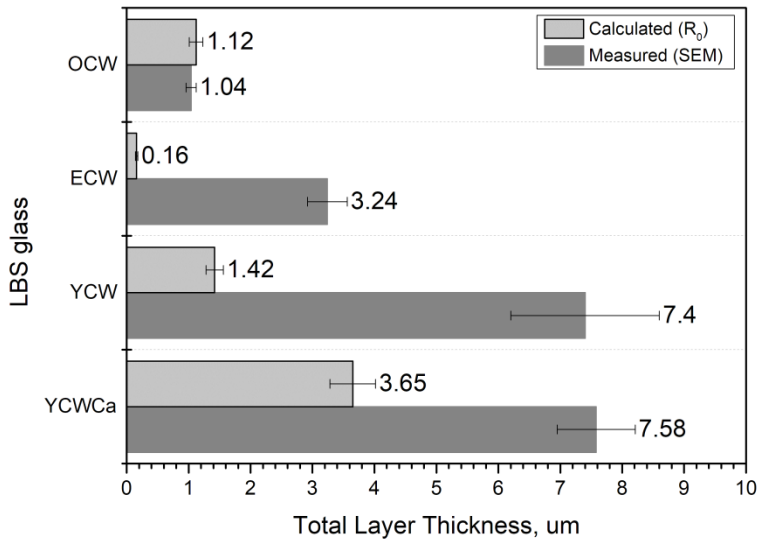

Figure 4.27 Calculated and measured total altered layer thickness for LBS glass powder after 84 days in YCWCa, YCW, ECW, OCW

Figure 4.28 clearly depicts thick alteration layers present on the surface of LBS glass particles. Dissolution in YCWCa (Figure 4.28a) resulted in the formation of a uniformed gel layer with an average thickness of 7.58 ± 1.26 µm (Table 4.8) with no evidence of delamination, indicating that the layer was well-adhered to the pristine glass. At greater magnification (Figure 4.28b) two distinct regions are visible; Layer 1 was a thick gel-like layer next to the pristine glass while Layer 2 resided on top of the gel and interfaced with the solution. The latter was a thin layer with a rough morphology.

The example shown for YCW (Figure 4.28c) clearly depicts a thick altered layer of similar thickness to YCWCa, giving an average value of 7.40 ± 1.20 µm. Cracks were observed for this glass in YCW, which ran perpendicular to the pristine glass; these likely formed during drying, due to differential stresses[34]. At 10,000 times magnification the alteration layer on YCW (Figure *4.28*d) was observed to comprise a thick gel layer, and the outer most surface that interfaced with the solution was thin but appeared to be composed of a high surface area precipitate, similar to that observed on the outer layer of the glass dissolved in ECW, albeit lower in quantity.

The alteration layer on grains of LBS exposed to ECW solution (Figure 4.28e) was of a different morphology to the young cement water solutions; the average thickness was 3.23 ± 0.63 µm and, like the MW25 glass exposed to the same solution, it was not smooth or uniform, and the thickness was not consistent around the entirety of the particle. Furthermore, the outermost region of the layer that directly interfaced with the solution had nodules that were significantly enriched with Ca as determined by EDS analysis on FIB-TEM samples (see below). A thin (0.14 ± 0.16 µm), uniformed layer surrounding glass grains exposed to OCW is shown in Figure 4.28 g and h.

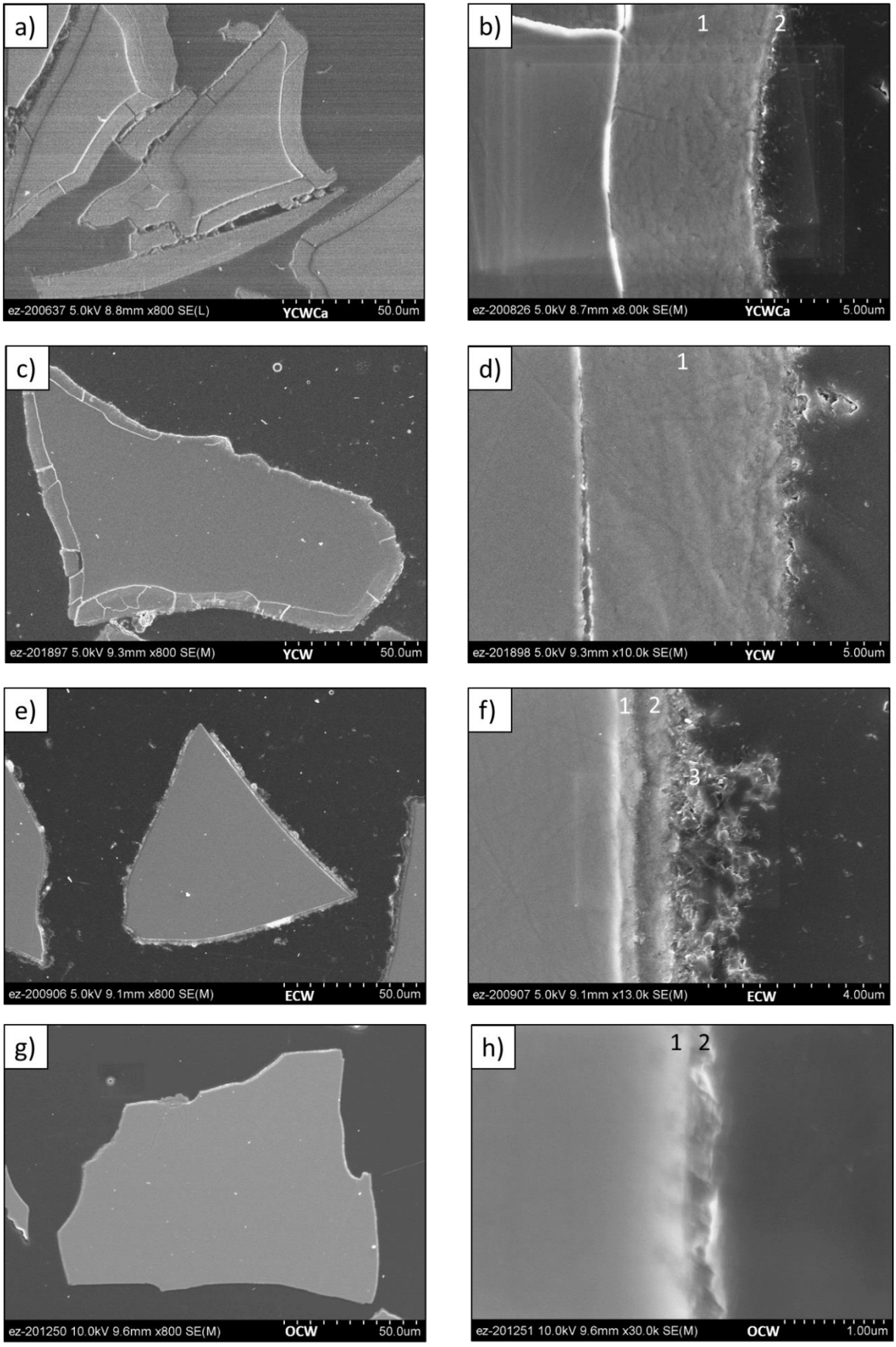

Figure 4.28 Secondary electron micrographs of LBS glass grain after 84 d leaching; a & b YCWCa, c & d = YCW, e & f = ECW, g & h = OCW, images a, d, f, and h are at x10,000 magnification and the pristine glass is located on the left of each image.

i. LBS exposed to YCWCa solution

Elemental maps (Figure 4.29 & 4.33) of the altered zone show two layers present on LBS exposed to YCWCa solution. Layer 1 was dominated by K (Table 4.9), indicating that K removed from the solution became a major contributor to the alteration layer. There was also enrichment of Al, Ca, Fe, Mg, Si and a depletion of Na in this layer, suggesting that this layer can be considered a K-rich alkali-silica gel, with contributions from other alkali elements. Layer 2 was enriched in Ca with isolated regions of portlandite, as identified in spot 7 on Figure 4.29 and confirmed by XRD (Figure 4.26). The bright spots in the back scattered image are indicative of high z contrast elements, which are consistent with the presence of Fe (Table 4.9).

Table 4.9 SEM F50 EDS spot maps associated with Figure 4.29 average elemental composition, at % of each alteration layer on the surface of LBS after 84 d leached in YCWCa.

Element	Na	Mg	Al	Si	S	K	Ca	Fe	Other
Avg at% Layer 1 (2)	7.22 ± 0.27	8.30 ± 0.15	8.65 ± 0.19	46.18 ± 0.10	-	15.16 ± 0.28	-	12.19 ± 0.11	0.62 ± 0.15
Avg at% Layer 2 (4)	9.73 ± 0.78	10.45 ± 0.63	8.92 ± 0.15	38.29 ± 0.86	-	14.06 ± 2.05	3.26 ± 2.15	14.11 ± 0.50	0.60 ± 0.16
at% Spot 6	11.52 ± 0.58	9.79 ± 0.49	8.45 ± 0.42	36.30 ± 1.82	2.69 ± 0.13	16.04 ± 0.80	-	-	0.58 ± 0.57
at % Spot 7	10.21 ± 0.51	8.18 ± 0.41	6.94 ± 0.35	36.30 ± 1.82	0.00 ± 0.00	10.62 ± 0.53	11.14 ± 0.56	-	0.51 ± 0.31

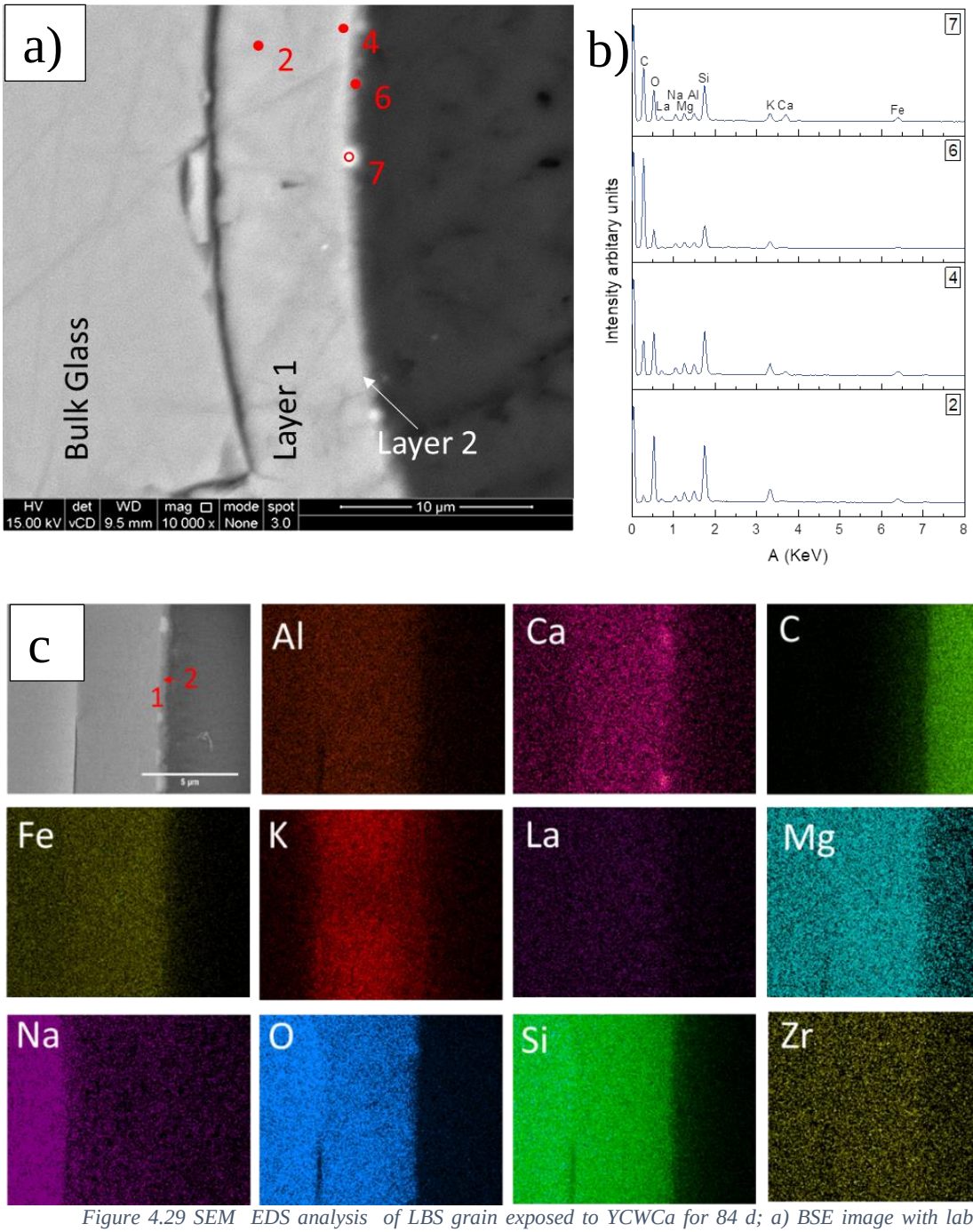

Figure 4.29 SEM EDS analysis of LBS grain exposed to YCWCa for 84 d; a) BSE image with labels indicating alteration layers and spots at % listed in Table 4.9, b) spectra associated with spots on Fig a, c) elemental maps

A FIB sample was taken from the altered region of a grain of LBS glass exposed to YCWCa solution for analysis by TEM. The grain selected exhibited a much smaller altered layer than that observed for many of the other grains exposed to this solution; the average thickness of the altered layer in the FIB section was 1.23 ± 0.8 µm. Figure 4.30 and 4.31 highlight the morphology of the outermost alteration products that interfaced with the solution. There are several distinct features to note; at the boundaries of the gel layer, which is 1.05 ± 0.8 µm thick, a dense rim separates this layer from a series of needle-like ribbons, as can be seen in Figure 4.30c and d. The average (mode) pore diameter within gel layer was 7.55 nm. Within the layer of fine needle-like ribbons, a nodule resided. Selected area diffraction (SAED) spots taken in different regions of the FIB section, including the needle-like ribbons (see region labelled "5", Figure 4.32), indicated that most of the altered layer was amorphous, which may be due to damage from the electron beam. The nodule (region labelled "4", Figure 4.32) produced a crystalline diffraction pattern that was identified as calcite. The source of carbonate is thought to originate from the solution that contained $CaCO_3$ (Chapter 3). It is possible that the needle-like ribbons are amorphous precursors to the formation of clay – like minerals; Abrajano et al.[74] identified similar ribbons as smectite phases (saponite, $Ca_{0.25}(Mg,Fe)_3((Si,Al)_4O_{10})(OH)_2 \cdot n(H_2O)$) on nuclear waste glass after dissolution in deionised water at 90 ^oC.

Elemental maps (Figure 4.33) of the FIB section showed that the gel layer was similar in composition to that of the bulk glass, and confirm the SEM spot analysis that the gel is composed of alkali elements K and Na. The ribbon-like needles appeared to be enriched in Mg, supporting the hypothesis that they may be a clay-like precursor or mineral. The nodule was rich in Ca, confirming the SAED identification of calcite.

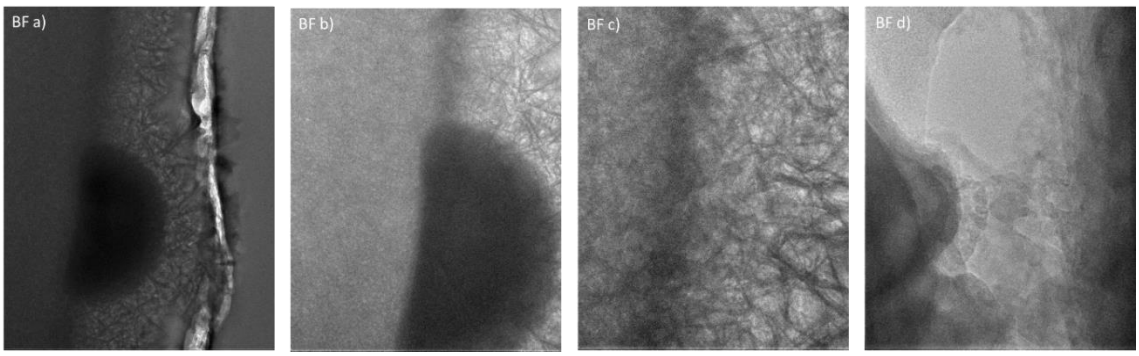

Figure 4.30 TEM (Techni) bright field images of the alteration regions on LBS exposed to YCWCa for 84 d.

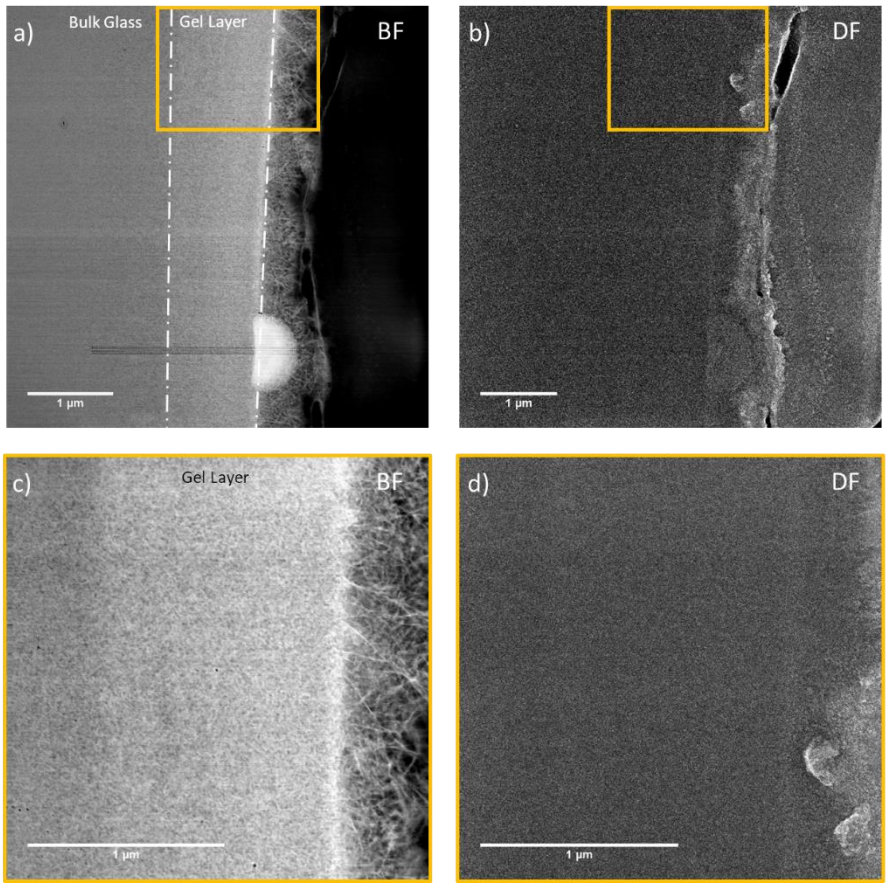

Figure 4.31 TEM (Techni) bright & dark field images of the alteration region on LBS exposed to YCWCa for 84 d.

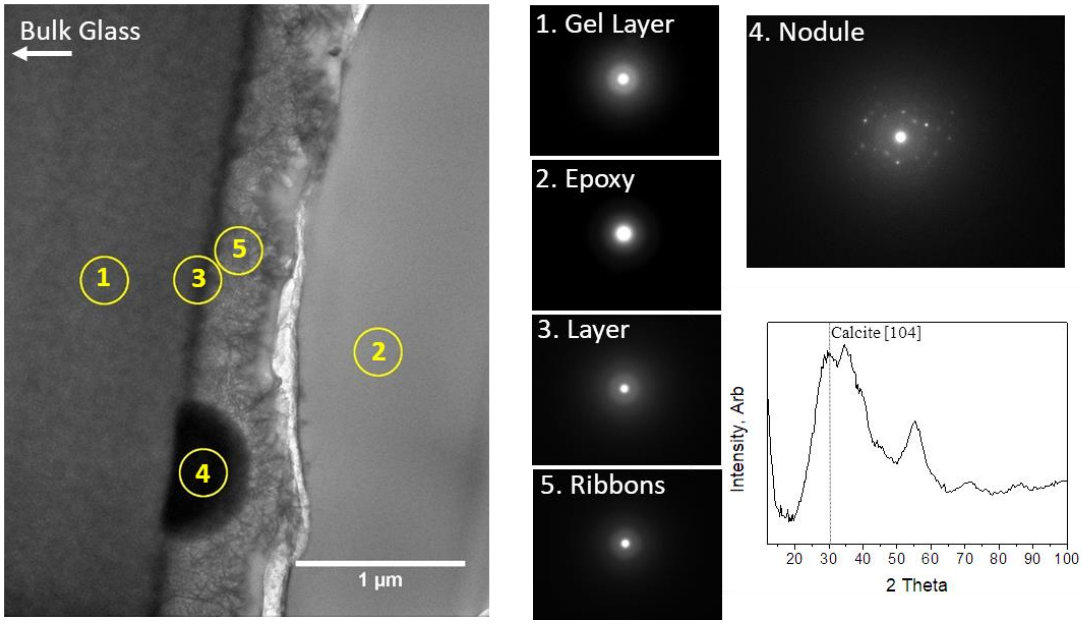

Figure 4.32 TEM (Techni images) and SAED of LBS after leaching in YCWCa for 84 d.

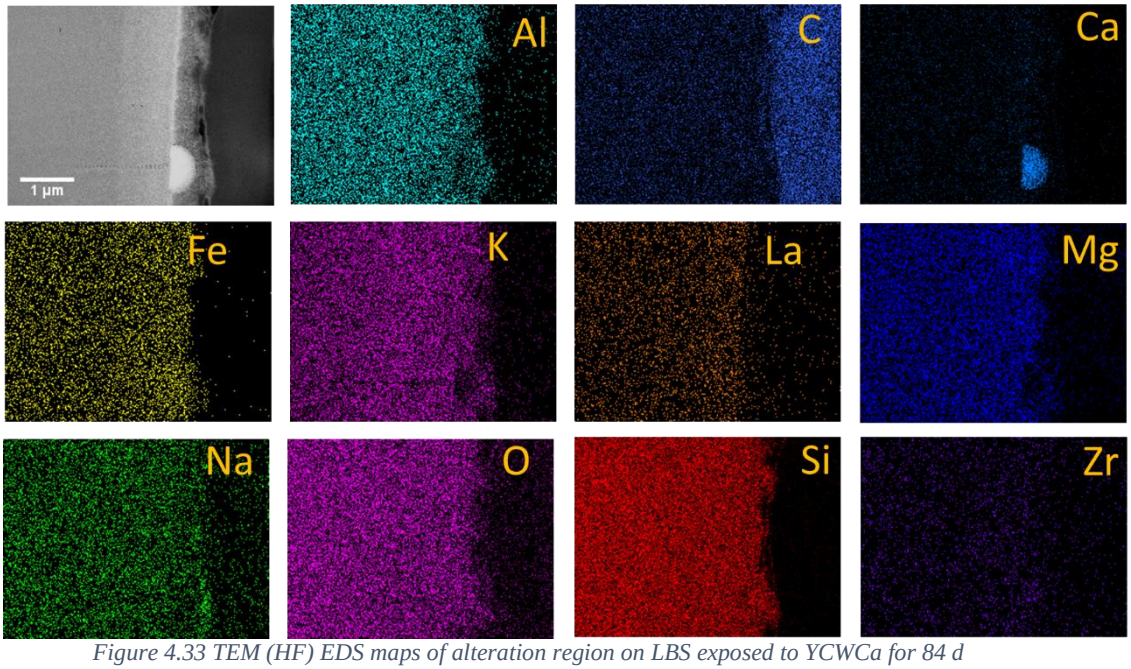

Figure 4.33 TEM (HF) EDS maps of alteration region on LBS exposed to YCWCa for 84 d

.

ii. LBS exposed to YCW solution

Alteration layers on the surface of LBS glass grains after leaching in YCW appeared similar to those exposed to YCWCa solution. Thick uniformed altered layers were observed to surround the grains of glass. At ~x10,000 magnification, (Figure 4.34) multiple layers were apparent. Layers 1 and 2 were composed of K, Si, Mg and Fe, with a small amount of Na, thus are identified as an alkali-silica gel (Figure 4.34c). Both layers had a similar composition, indicating that they are single delaminated layer. Layer 3 was thin and gel-like and was composed of the same elements as in Layers 1 and 2 (albeit at lower apparent concentrations).

Table 4.10 SEM F50 EDS spot maps associated with Figure 4.34 average elemental composition, at % of each alteration layer on the surface of LBS after 84 d leached in YCW.

Element	Na	Mg	Al	Si	K	Ca	Fe	Other
Avg at% Layer 1 (8)	6.44 ± 0.36	7.67 ± 0.20	9.39 ± 0.20	47.53 ± 0.48	16.68 ± 0.05	0.58 ± 0.01	10.35 ± 0.34	0.68 ± 0.14
Avg at% Layer 2 (9)	5.76 ± 0.45	7.54 ± 0.35	11.08 ± 0.43	45.38 ± 0.50	17.78 ± 0.47	0.48 ± 0.08	10.80 ± 0.01	0.60 ± 0.14
Avg at% Layer 3 (10)	7.48 ± 0.31	11.18 ± 1.21	9.45 ± 0.10	40.04 ± 0.53	16.06 ± 1.35	0.29 ± 0.02	14.16 ± 0.69	0.68 ± 0.18
at % Spot 14	21.25 ± 1.06	6.32 ± 0.32	7.14 ± 0.36	54.18 ± 2.71	0.32 ± 0.02	0.68 ± 0.03	9.15 ± 0.46	0.49 ± 0.05

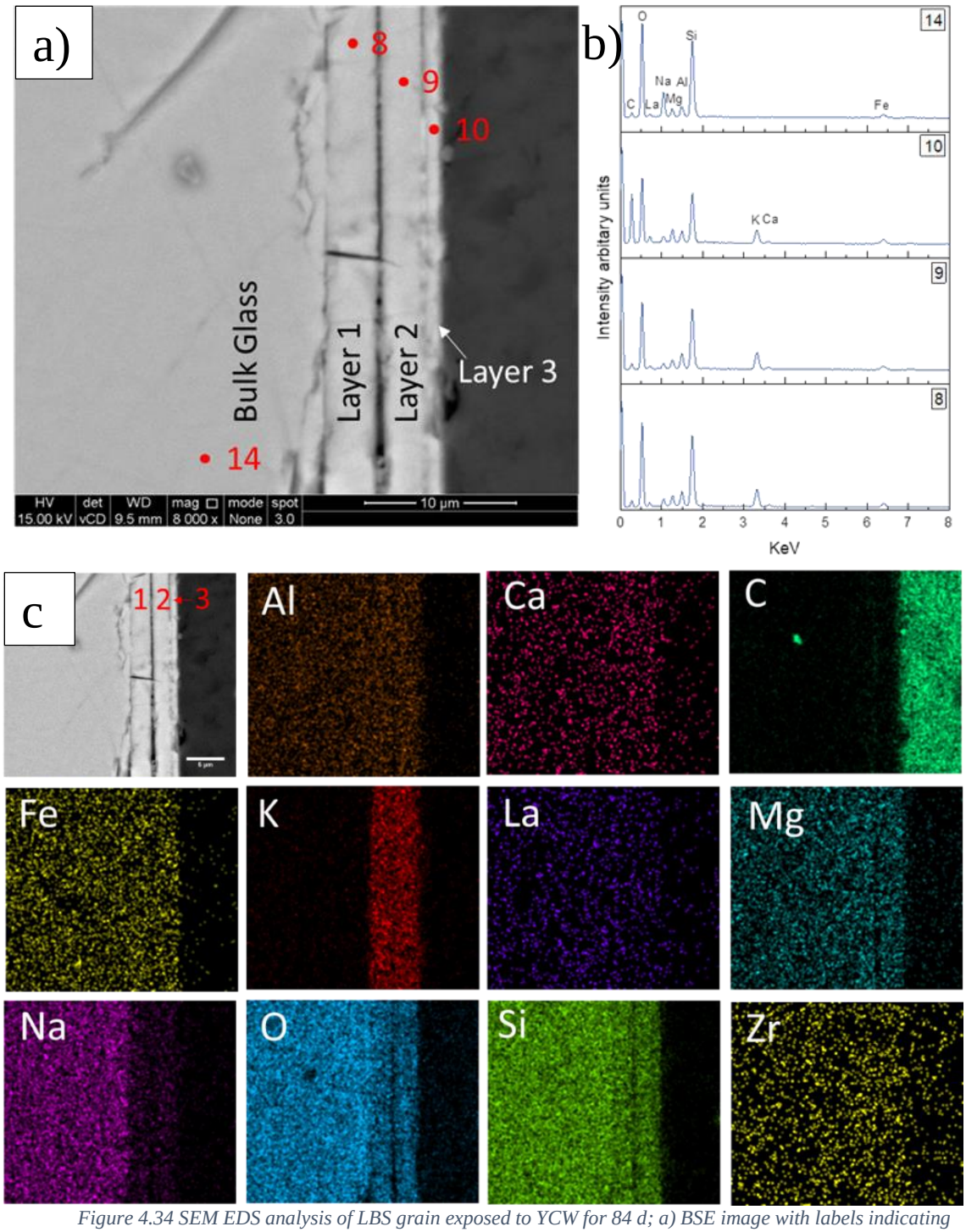

Figure 4.34 SEM EDS analysis of LBS grain exposed to YCW for 84 d; a) BSE image with labels indicating alteration layers and spots at % listed in Table 4.10, b) spectra associated with spots on Fig a, c) elemental maps.

TEM analysis of a small part of the alteration layer, provided high resolution, high magnification images that indicated regions of varying density throughout the layer. Figure 4.35 a to d show the varying morphology of the alteration products. The pore diameter in the gel layer was 1.25 nm based on Figure 4.35b. Three distinct morphologies were observed: i) a sponge-like gel, similar to alkali-silica gels observed in the literature[130] (see SAED spot "3", Figure 4.36); ii) a dense band close to the glass with a wispy morphology (see SAED spot "6",Figure 4.36) and iii) a gel-layer immediately between the pristine glass and the layer with wispy morphology (see SAED spot "2", Figure 4.36). Selected area diffraction across the FIB sample, confirmed that all spots (1-9) exhibited diffuse scattering. The bright region at the top of the micrograph is a hole due to damage incurred by the electron beam. Figure 4.37 shows the TEM elemental maps and, as for the SEM/EDX mapping (Table 4.10 and Figure 4.34), the composition of the alteration products were not dissimilar to that of the bulk glass. The gel layer observed between the glass and the wispy layer (Spot 2, Figure 4.36) had an enrichment of K and Na. The wispy features were composed of Al, Ca, Fe, K, Mg, Na, O and Si. Additionally, an outer layer rich in Al, O and Si was observed in the EDX maps.

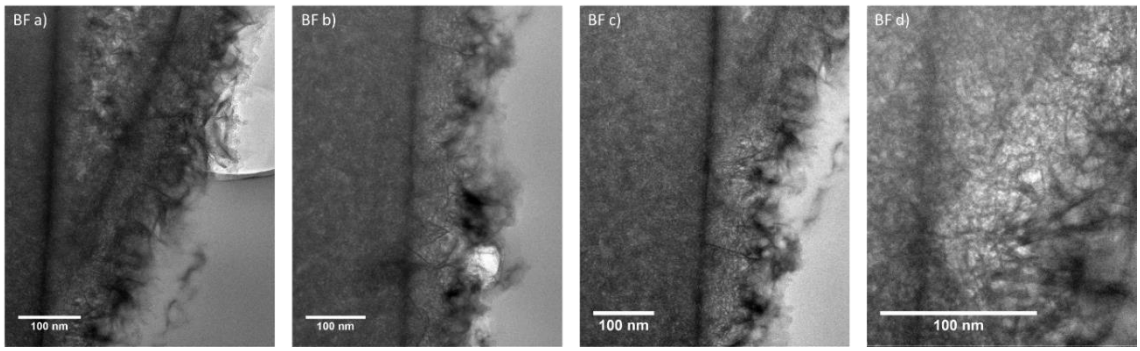

Figure 4.35 High resolution bright field TEM image taken on Hitachi microscope of LBS post 84 d leached in YCW

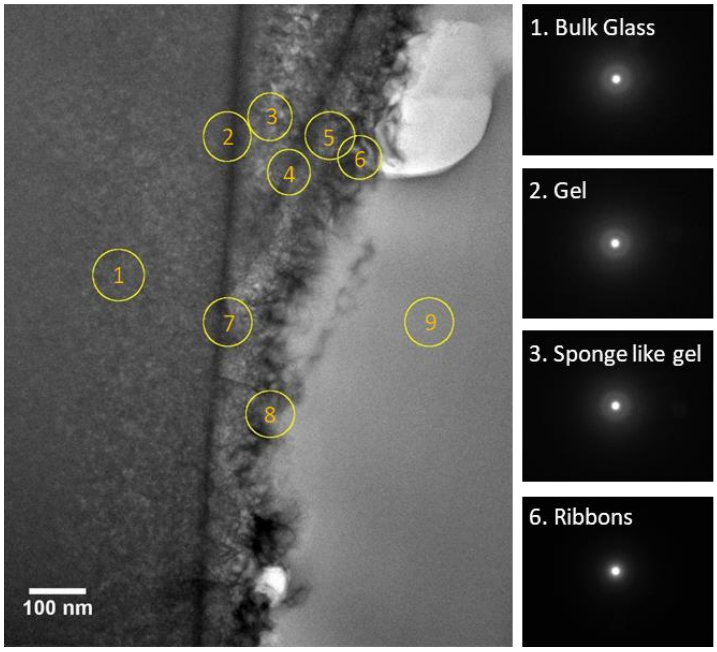

Figure 4.36 SAED of 9 regions of interest on LBS post leached in YCW for 84 d, diffraction patterns for all 9 spots were amorphous, the pattern for regions of distinct morphological differences are shown above.

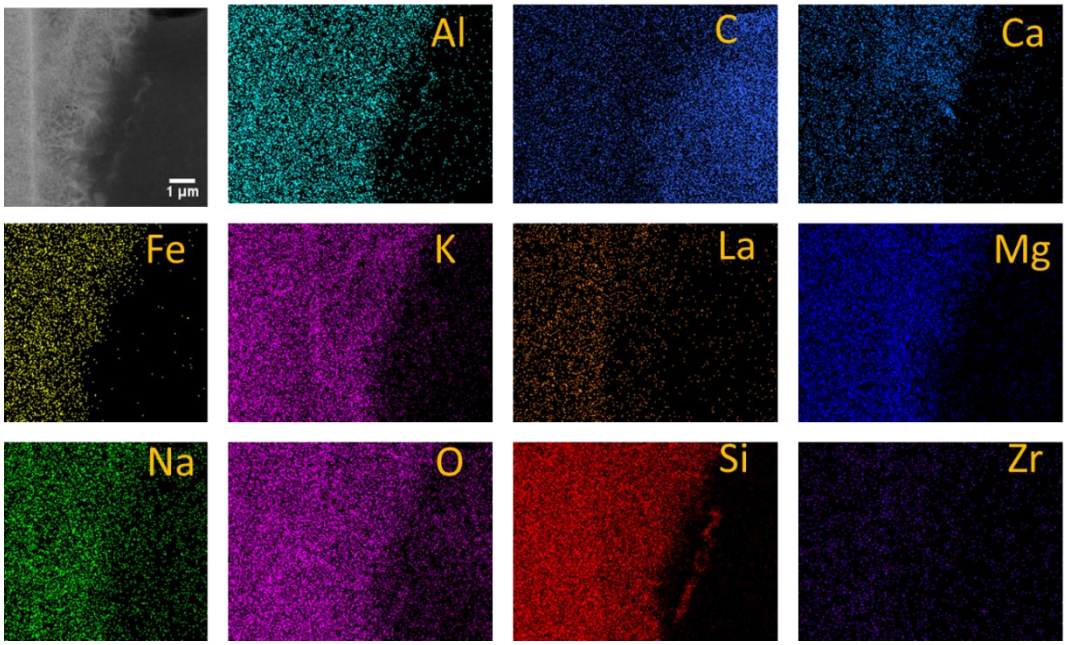

Figure 4.37 Elemental maps of a region of the FIB sample taken on the Hitachi TEM for YCW after 84 d in YCW.

iii. LBS exposed to ECW solution

Exposure of the LBS glass to ECW solution resulted in the formation of an altered layer that was at least half the thickness of those observed in the YCW systems. The average thickness was 3.24 ± 0.63 µm (Table 4.8). The morphology was quite different from that observed for the other solutions; the majority of grains measured exhibited nodules in, or on, the alteration layer. Each of the LBS glass grains shown in Table 4.11 had a non-uniform layer; in the micrograph on the left, the broken surface of the grain can clearly be seen with a layer that has areas of precipitates. The micrograph on the right also shows the presence of nodules.

The SEM images shown in Figure 4.38 show the nodules at higher magnification and also show that the interface of the alteration layer with the solution was rough. A gel-like layer close to the pristine glass was also observed (Layer 1), which had a composition similar to that of the pristine glass with a slight enrichment in Ca compared to the bulk glass, with a Ca:Si ratio of 0.11. Nodules, composed of Ca and Si (Table 4.11) were located on top of the gel-like layer, and the rough morphology on the outermost surface was composed of material that was enriched in Al, Mg, O and Si. The presence of a significant enrichment in Ca is in agreement with the removal of Ca from solution observed for this solution (Figure 4.9) and is indicative of the formation of a alkaline earth-silica gel.

Table 4.11 SEM F50 EDS spot maps associated with Figure 4.38 average elemental composition, at % of each alteration layer on the surface of LBS after 84 d leached in ECW.

Element	Na	Mg	Al	Si	S	K	Ca	Fe	Other
Bulk Glass (15)	23.53 ± 1.18	6.67 ± 0.33	7.52 ± 0.38	53.44 ± 2.67	-	0.10 ± 0.01	0.42 ± 0.02	7.34 ± 0.37	0.49 ± 0.01
Avg at% Layer 1 (16)	12.34 ± 2.47	4.82 ± 1.39	8.93 ± 1.02	54.77 ± 0.33	-	0.07 ± 0.26	6.34 ± 0.79	11.10 ± 1.44	0.82 ± 0.26
Avg at% Layer 2 (25)	5.49 ± 1.13	10.32 ± 1.77	7.60 ± 0.55	41.88 ± 3.61	4.44 ± 1.54	-	18.20 ± 1.52	6.30 ± 0.59	0.07 ± 0.27
at % Spot 19	7.75 ± 0.39	5.57 ± 0.28	8.73 ± 0.44	45.21 ± 2.26	3.39 ± 0.17	0.10 ± 0.01	15.26 ± 0.76	8.66 ± 0.43	1.27 ± 0.28

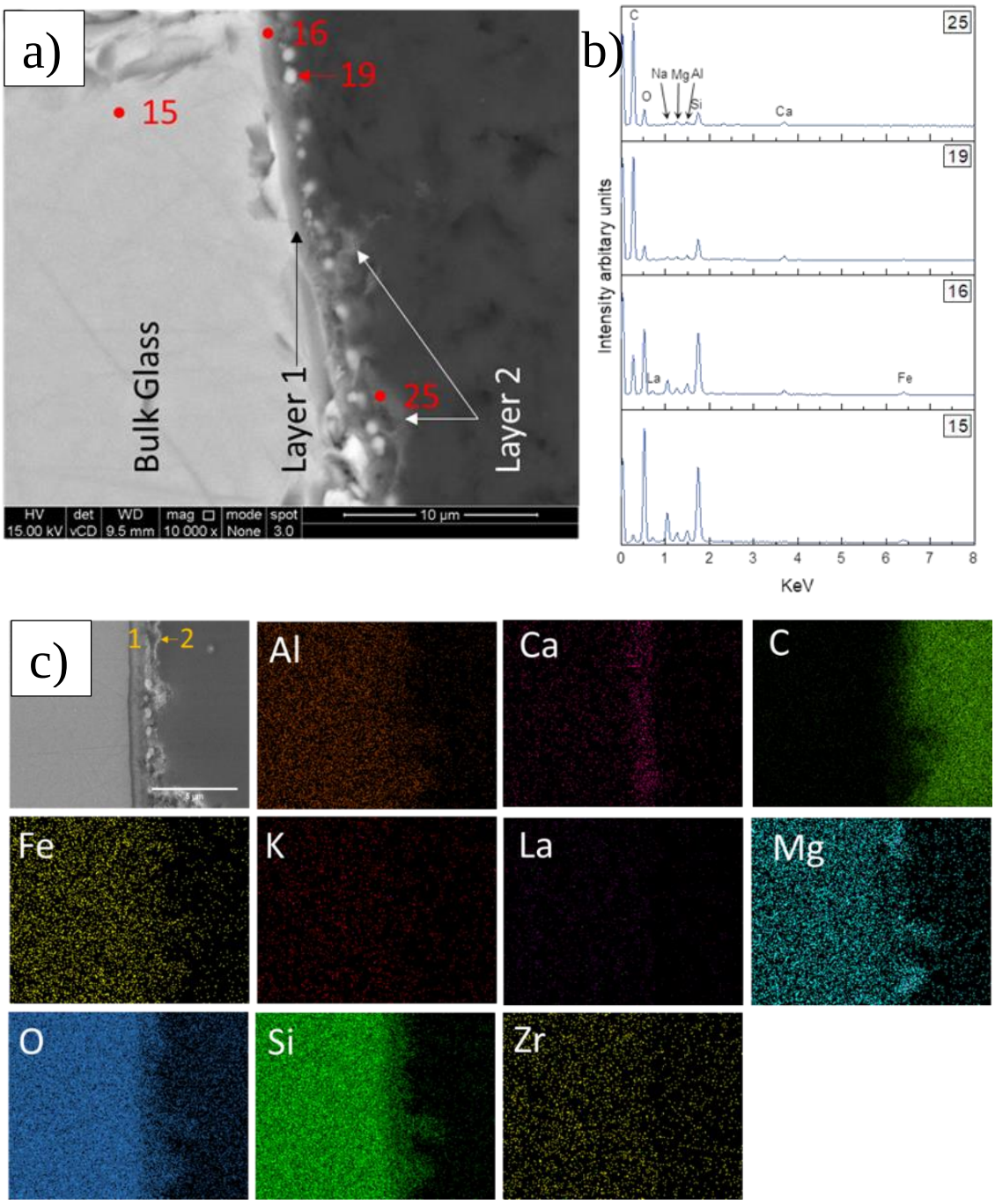

Figure 4.38 SEM EDS analysis of LBS grain exposed to ECW for 84 d; a) BSE image with labels indicating alteration layers and spots at % listed in Table 4.11, b) spectra associated with spots on Fig a, c) elemental maps.

The FIB section selected for the LBS sample exposed to ECW solution (Figure 4.39) showed glass on the left hand side of each image and alteration products on top of the glass. Several distinct regions were observed: firstly a gel-like layer, with an average (mode) pore diameter of 3.67 nm, was observed close to the pristine glass; and secondly nodules, with an average diameter of 334 ± 53 nm were found embedded within a layer that had fibrous ribbons, which appeared to propagate from the gel region, distributed throughout. All of the SAED spots exhibited diffuse scattering including the gel (see SAED spot "2",Figure 4.40), nodules (see SAED spot "4") and "clay-like" material (see SAED spot "6"); the sample preparation (i.e., over-thinned) or electron beam damage could be a contributing factor to the amorphous nature of the nodules.

EDX mapping (Figure 4.41) showed that, as for the other solutions, Ca was enriched in the alteration layer and the nodules, which also contained Al and Si with a small amount of Fe. The fibrous ribbons were composed of Ca and Si.

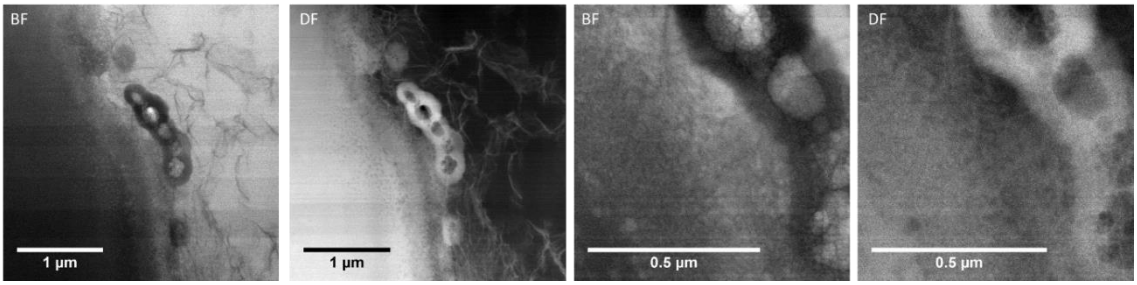

Figure 4.39 High resolution bright and dark field TEM (Hitachi) images of LBS exposed to ECW for 84 days left hand side of each image is the glass

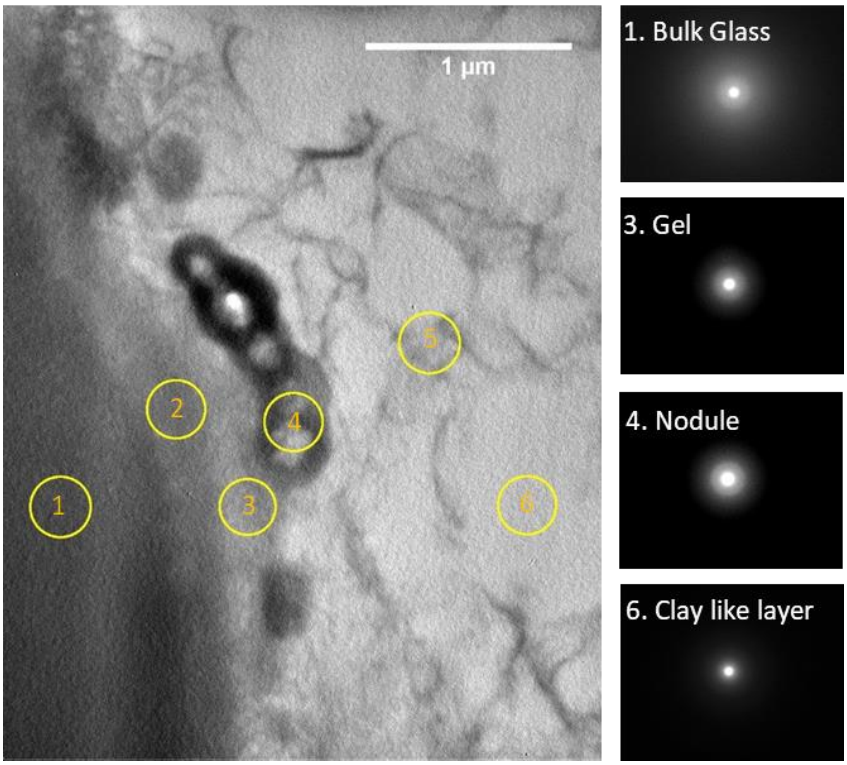

Figure 4.40 Bright field TEM (Hitachi) image and SAED of LBS exposed to ECW for 84 days, spots 1-6 exhibited diffuse scattering, spots taken in areas of morphological interest are shown above .

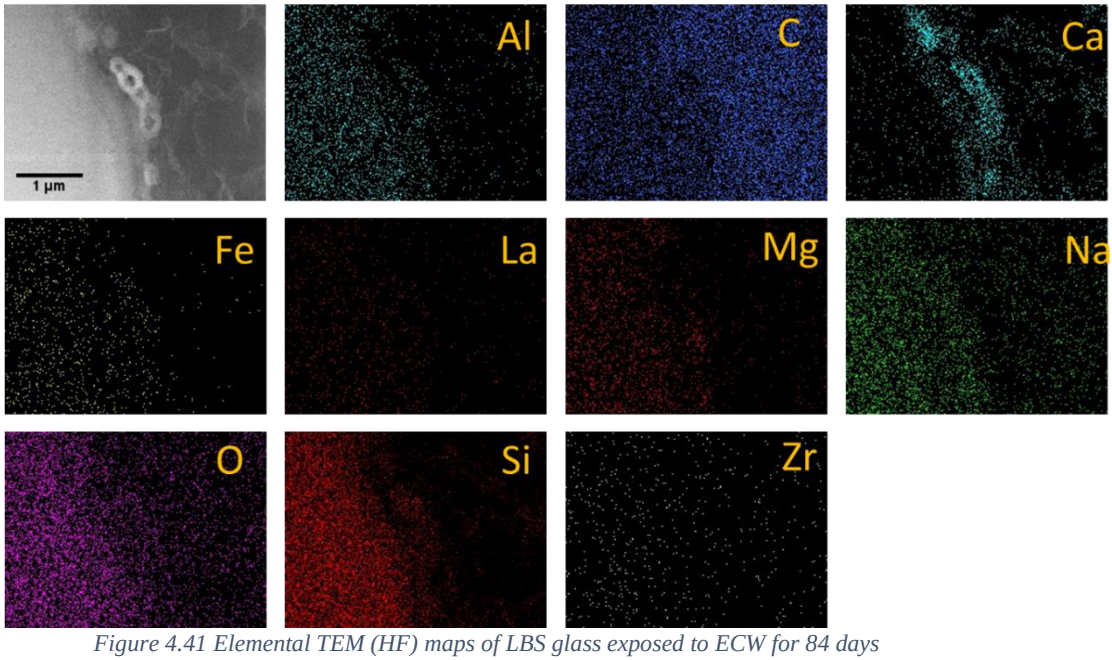

Figure 4.41 Elemental TEM (HF) maps of LBS glass exposed to ECW for 84 days

iv. LBS exposed to OCW solution

Exposure of LBS glass to OCW resulted in the least amount of alteration after 84 days. The average thickness was measured to be 1.04 ± 0.11 µm (Table 4.8). Figure 4.28 g and h illustrate the significant difference in the morphology of the alteration products surrounding the grains of LBS exposed to OCW, as compared to the other solutions. A very thin layer surrounded the grains and there was no evidence of surface precipitates. Upon first inspection, the x10000 magnification SEM images (Table 4.12 & Figure 4.42) appear to show two altered regions, however, elemental analysis would suggest that there is only one altered gel layer, 0.90 ± 0.17 µm thick, residing on top of a region of fractured glass. Elemental maps and SAED (Table 4.12 & Figure 4.42) confirm that this is one layer, with a composition very similar to the pristine glass with slight enrichment of Zr, Fe, Ca and K (Table 4.12).

Table 4.12 SEM F50 EDS spot maps associated with Figure 4.42 average elemental composition, at % of each alteration layer on the surface of LBS after 84 d leached in ECW.

Element	Na	Mg	Al	Si	K	Ca	Fe	Zr
Bulk Glass (1)	21.08 ± 0.04	6.10 ± 0.23	9.43 ± 0.20	55.75 ± 0.20	0.16 ± 0.01	0.50 ± 0.04	6.72 ± 0.06	0.39 ± 0.14
Broken Surface (3)	19.88 ± 1.28	5.88 ± 0.39	9.09 ± 0.06	56.08 ± 1.12	0.13 ± 0.07	0.59 ± 0.01	7.93 ± 0.76	0.49 ± 0.13
Avg at% Layer 1 (6)	19.73 ± 1.07	5.96 ± 0.30	9.13 ± 0.19	56.57 ± 0.91	0.32 ± 0.10	0.54 ± 0.18	7.03 ± 0.17	0.54 ± 0.28

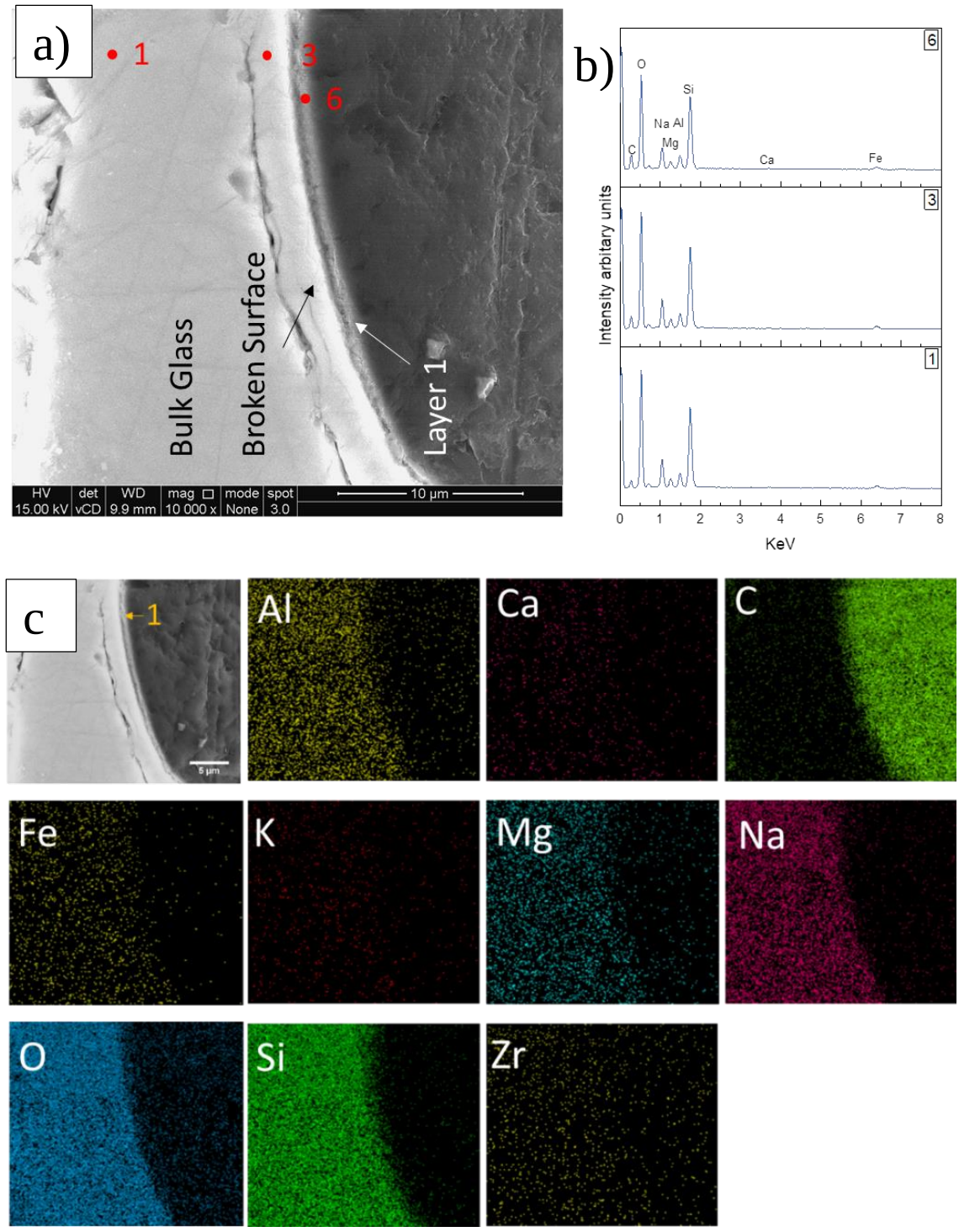

Figure 4.42 SEM EDS analysis of LBS grain exposed to OCW for 84 d; a) BSE image with labels indicating alteration layers and spots at % listed in Table 4.12, b) spectra associated with spots on Fig a, c) elemental maps.

The FIB section of the LBS glass (Figure 4.43) showed that the very thin alteration layer (< 1µm). It was composed of two distinct bands; the first was a gel layer where the average pore diameter within the gel was 1.21 nm and the second was a layer of ribbons. At the interface between the gel and the glass, pits were observed (Figure 4.43b). High magnification images of these pits (Figure 4.43 d and e) show them be filled with closely packed ribbons. Diffraction analysis of the distinct band confirmed that the layers were amorphous with diffuse rings visible in the SAED patterns (Figure 4.44), although amorphization caused by electron beam damage cannot be ruled out. TEM elemental maps (Figure 4.45) were in agreement with those from SEM/EDX, and showed that the gel layer was composed of Al, Si, Na, Ca, O and Si, and the ribbons were composed of Al, Mg, O and Si, with a trace amount of Ca. The outer layer was rich in Si and Na, however it is not possible to determine if the Na used to form this outer rim on the alteration layer is from the glass or the solution. The Cu and Ga identified in this outer rim are likely contamination from the FIB process, indicating it to be a relic of sample preparation.

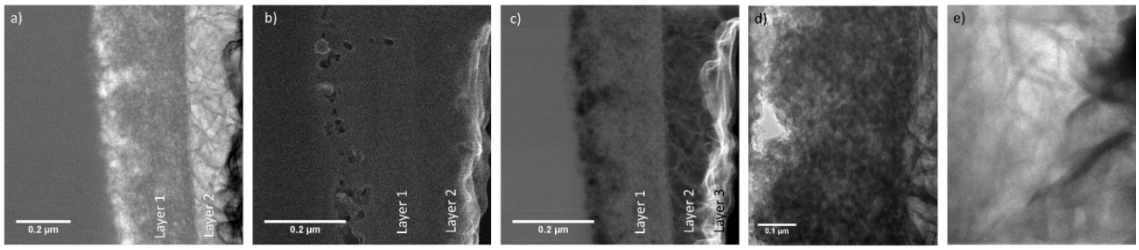

Figure 4.43 High resolution TEM (HF) images of LBS post-dissolution in OCW for 84 d, images a= bright field, b= SEM, c= dark field, pristine glass on LHS alt products RHS, 2 distinct layers labelled, d & e images of ribbons

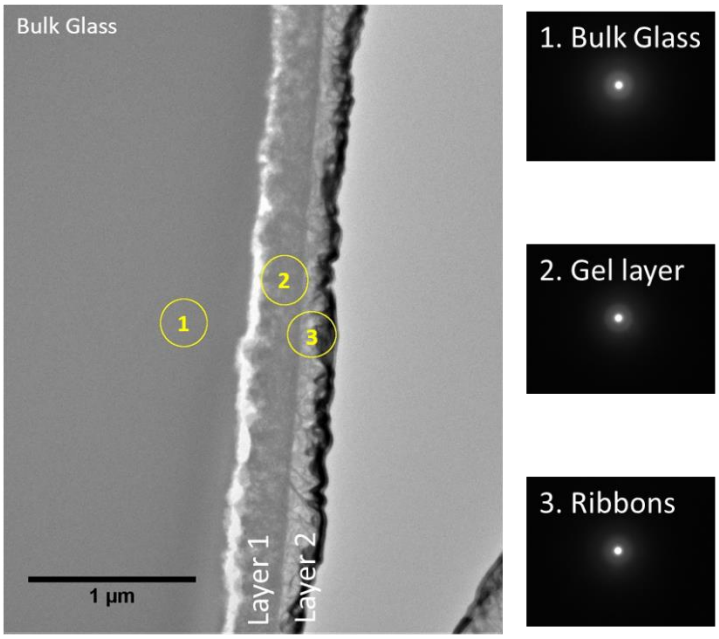

Figure 4.44 SAED from FIB section of LBS glass grain, images taken on Hitachi TEM.

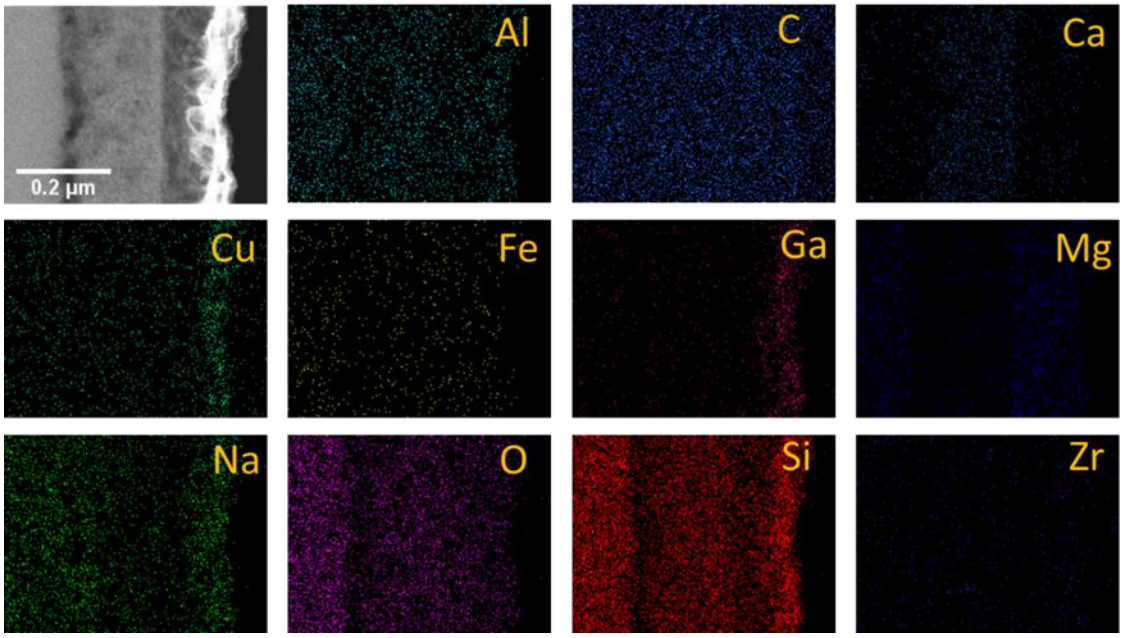

Figure 4.45 Elemental maps from HF TEM of LBS post dissolution in OCW for 84 d.

4.3. Discussion

The aim of this study was to elucidate the dissolution mechanisms of simulant nuclear waste glass in synthetic cement solutions representative of a cementitious GDF in equilibrium with groundwater. This was achieved by utilising two UK relevant nuclear simulant glasses for HLW (MW25) and ILW (LBS).

It was found that the young cement waters (YCW and YCWCa) were approximately ten times more corrosive towards the glasses than the evolved and old cement water solutions for MW25, and approximately 6 times more corrosive towards LBS glass, based on the initial dissolution rates (Table 4.2 and Table 4.13). The formation of an alteration layer, almost twice as thick as the evolved and old solutions, was observed in the young solutions (Table 4.3 and Table 4.8).

Compared with other studies conducted previously on MW25 glass (Table 4.13), the initial dissolution rate obtained for MW25 exposed to YCWCa solution was similar to that obtained for saturated $Ca(OH)_2$ solution (Backhouse[70]). Backhouse observed alteration layers that were 11 to 14 µm thick after 1 year of leaching in $Ca(OH)_2$. Four distinct layers were identified by Backhouse: a Ca- and Si-rich phase; a Mg-and Al-rich phase; a rim containing Fe-rich particles, and; precipitates on the surface, containing Ca, Si and Mg.

Table 4.13 Comparison of initial dissolution rates for MW25 glass in the present study and available literature (all studies carried out at SA/V 1200 m^{-1})

Reference	Rate gm^{-2} d^{-1}	R_0 Time	Glass	Experiment details
Present Study	0.067 ± 0.011	0-28	MW25	50°C, pH(RT) 13.01, YCWCa soln.
	0.051 ± 0.001	0-32	MW25	50°C, pH(RT) 13.5, YCW soln.
	0.006 ± 0.0001	0-42	MW25	50°C, pH(RT) 12.3 , ECW soln.
	0.007 ± 0.0006	0-112	MW25	50°C, pH(RT) 11.56, OCW soln.
Backhouse[70]	0.062 ± 0.0009	0-14	MW	50°C, pH 12.5, $Ca(OH)_2$ sat.soln.
Utton[75]	0.029 ± 0.003	0-21	MW	40°C, pH 12-11.7, $Ca(OH)_2$
Utton[75]	0.156 ± 0.010	0-21	MW	40°C, pH 12-10.7, 0.03M NaOH
Abraitis[131]	0.358 ± 0.39	0-28	MW	60°C, pH 9.6, $NaHCO_3$/KOH soln.
AMEC[132] *	0.033 ± 0.003	0-56	MW	40°C, pH ?, deionised H_2O
Utton[75]	0.024 ± 0.004	0-21	MW	40°C, pH 9.8, demineralised H_2O
Zwicky[133]	0.15	0-28	MW	90°C, pH ? , deionised H_2O
Present Study	0.078 ± 0.007	0-28	LBS	50°C, pH(RT) 13.01, YCWCa soln.
	0.045 ± 0.003	0-32	LBS	50°C, pH(RT) 13.5, YCW soln.
	0.018 ± 0.001	3-28	LBS	50°C, pH(RT) 12.3, ECW soln.
	0.004 ± 0.0001	0-112	LBS	50°C, pH(RT) 11.56, OCW soln.
Utton[59]	0.043 ± 0.0024	0-7	LBS	50°C, pH 12.37, $Ca(OH)_2$

(1) * Calculated (by C. Mann) from the published data

The data presented in this Chapter highlight the significant influence of alteration layer composition and morphology on the dissolution rate. A significant drop in the affinity controlled rate was observed when compared to the initial rate of dissolution for the young cement waters, as shown in Figure 4.2 and *Figure 4.3*. This can be correlated with the formation of a thick gel layer on the surface of the glass sample as shown in Figure 4.46. In ECW solution there was no significant drop in the affinity controlled rate (Figure 4.5) indicating that the gel does not passivate dissolution, however, the rate of dissolution was low despite the solution being at pH(RT) 12.5. As discussed above, in OCW it was not possible to observe the initial rate and transition to an affinity controlled rate (Figure 4.6). Several factors are responsible for this behaviour, as discussed below and in the subsequent sections.

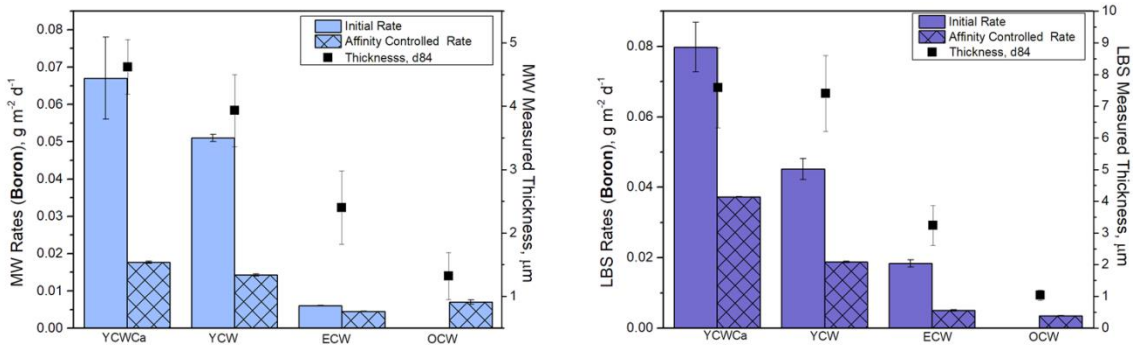

Figure 4.46 MW25 and LBS initial rate (NR_0) Vs residual rate (NR_a), based on NL_B and the measured thickness of the alteration layer at day 84. YCWCa; NR_0= 0-28, NR_a= 28 -84 d, YCW; NR_0= 0.32, NR_a= MW25 32-112 d, LBS 32-70 d, ECW; MW25 NR_0 = 0-42, NR_a= 42-84 d, LBS NR_0= 3-28, NR_a= 28-112 d, OCW; NR_0= 0-112 d (remained in initial rate regime)

4.3.1. Alkali- and alkaline earth-silica gel composition and morphology

Amorphous alkali- and alkaline earth-silica gels were observed to form on the surface of both MW25 and LBS depending on the synthetic cement water solution composition. Such gels are commonly observed in Portland cement concrete hydration, caused by the reaction between silica cement clinker phases and alkali hydroxide ions in the pore solution[134,135]. In these gels, Na^+ or K^+ charge balance the silicate, aluminate or sulphate ions instead of Ca^{2+} in the gel structure[136,137]. In the current study, the silicate and aluminate species are provided by the glass, the alkali elements are predominantly present in the synthetic cement waters and the alkaline earth elements are present in the glass (e.g. Mg) and / or the solution (e.g. Ca). The composition of the alkali / alkaline-earth silica gel was found to vary as a function of the initial solution composition, and to a lesser extent, the glass composition (particularly with respect to Mg and Ca). The alkali to silica ratio of the gel layer (Table 4.14) occurred in the expected range for Portland cements, of 0.05 to

0.6 for $(Na_2O+K_2O):SiO_2$ and from 0 to 0.2 for $(CaO+MgO):SiO_2$ (molar ratios)[135,138]. The MW25 glass composition exceeded the typical (CaO+MgO):Si ratio range for alkali/alkaline-earth silica gels in Portland cement, while the LBS did not. This can be attributed to the significantly greater (x 10) content of Ca in MW25 than LBS; a greater amount of Ca was available to charge balance $[AlO_4]^-$ in the gel.

Table 4.14 shows that Al is present in the gel under all experimental conditions. It is reasonable to expect that, at the high pH values encountered in cement solutions, the cations in solution enter the gel network to charge balance the negative Si ($Si(OH)_3^-$ and $Si(OH)_2^{2-}$) and Al ($[AlO_4]^-$) species. In the young cement waters it is evident that K is the dominant counter-ion in the silica gel. In the evolved cement solution, where Ca dominates the solution chemistry, Ca is the principle charge balancing cation, while in the old cement water solution, the gel layer is ostensibly a Ca-silica gel containing small quantities of all of the other alkali and alkaline earth cations. On the basis of the current work, there is insufficient evidence to conclude which cation charge balances which negative species in the gel, but it is clear that a multi-cation silica gel layer is formed in all solutions, with varying proportions of alkali and alkaline earth elements.

Table 4.14 Alkali: Si ratios for the gel and precipitate formed under each experimental condition, the threshold for alkali silica gels are as follows; Na + K :Si ratio 0.05-0.6, Ca + Mg: Si = 0-0.26 and C-S-H Ca:Si ratio 0.4-2.5(atomic ratios)

		at % of individual elements						Alkali :Si ratio							
Conditions		Na	Mg	Al	Si	K	Ca	Ca:Si	K:Si	Na:Si	Mg:Si	Al:Si	Na + K :Si	Ca + Mg :Si	Na+Mg+ K+Ca :Si
MW25 YCWCa	Gel	3.06	7.13	13.79	43.06	17.41	5.62	0.13	0.40	0.07	0.17	0.32	0.48	0.30	0.77
	Precip	5.91	2.57	10.23	40.59	15.15	19.91	0.49	0.37	0.15	0.06	0.25	0.52	0.55	1.07
MW25 YCW	Gel	11.12	8.93	11.57	43.13	17.55	5.07	0.12	0.41	0.26	0.21	0.27	0.66	0.32	0.99
	Precip	5.89	4.54	13.09	42.21	18.14	8.38	0.20	0.43	0.14	0.11	0.31	0.57	0.31	0.88
MW25 ECW	Gel	6.39	9.16	12.11	51.05	0.00	10.78	0.21	0.00	0.13	0.18	0.24	0.13	0.39	0.52
	Precip	1.80	0.30	4.48	29.76	0.00	57.66	1.94	0.00	0.06	0.01	0.15	0.06	1.95	2.01
MW25 OCW	Gel	9.14	6.73	13.04	46.39	0.05	13.68	0.29	0.00	0.20	0.15	0.28	0.20	0.44	0.64
LBS YCWCa	Gel	7.22	8.30	8.65	46.18	15.16	0.00	0.00	0.33	0.16	0.18	0.19	0.48	0.18	0.66
	Precip	9.73	10.45	8.92	38.29	14.06	3.26	0.09	0.37	0.25	0.27	0.23	0.62	0.36	0.98
LBS YCW	Gel	5.76	7.54	11.08	45.38	17.78	0.48	0.01	0.39	0.13	0.17	0.24	0.52	0.18	0.70
	Precip	7.48	11.18	9.45	40.04	16.06	0.29	0.01	0.40	0.19	0.28	0.24	0.59	0.29	0.87
LBS ECW	Gel	12.34	4.82	8.93	54.77	0.07	6.34	0.12	0.00	0.23	0.09	0.16	0.23	0.20	0.43
	Precip	5.49	10.32	7.60	41.88	0.00	18.20	0.43	0.00	0.13	0.25	0.18	0.13	0.68	0.81
LBS OCW	Gel	19.73	5.96	9.13	56.57	0.32	0.54	0.01	0.01	0.35	0.11	0.16	0.35	0.11	0.47

Preferential cation selectivity in the gel at near neutral pH has been reported by several authors (Collin et al.[45], Dove[139,140] and Icenhower[141]). Each cation has a characteristic solvation sphere, which is the time-averaged number of solvent molecules adjacent to an ion in an aqueous medium,

and also a characteristic ion hydration, which describes the number of water molecules in the solvation shells. Since the dissolution rate of glass is controlled by the protonation of Si-O bonds, where water acts as a nucleophile in exchange with Si-O (dissociating to form OH^-), the rate of silica hydrolysis is correlated with the solvent properties of the hydrated cation[45]. The frequency of hydrated ion exchange, k_{ex}, of the alkali and alkali-earth cations present in the synthetic cement solutions occurs in the order: $K^+ > Na^+ > Ca^{2+} > Mg^{2+}$ (Table 4.15). Thus, K is more likely to be attracted to the silica surface than Mg, as observed in the present study. Dove[140] postulated that *competitive ion interactions* occur at the Si-surface when both alkali and alkaline earth cations are combined in solution in the presence of quartz at neutral pH. Consider the reaction between a metal cation (Me) and a silica surface:

$$>SiO^- + Me^{n+} \rightarrow >SiO—ME^{(n+-1)} \qquad \textbf{4.2}$$

Where the charge of the Me is dependent on the average number of deprotonated surface sites, $>Si\text{-}O^-$, through the interaction (or adsorption) constant, $K_{ad,i}$. For the cations relevant to the present study, we find:

$$>SiO^- + Mg^{2+} \rightarrow >SiO—Mg^+ \qquad K_{ad\,Mg} \qquad \textbf{4.2a}$$

$$>SiO^- + Ca^{2+} \rightarrow >SiO—Ca^+ \qquad K_{ad\,Ca} \qquad \textbf{4.2b}$$

$$>SiO^- + Na^+ \rightarrow >SiO—Na \qquad K_{ad\,Na} \qquad \textbf{4.2c}$$

$$>SiO^- + K^+ \rightarrow >SiO—K \qquad K_{ad\,K} \qquad \textbf{4.2d}$$

Table 4.15 Cation and solvation properties taken from Dove and Nix[142]

Cation	R_{ionic}, Å	r_{hy}, Å	ΔG_{hy}, KJmol^{-1}	K_{ex}, s^{-1}	K_{ad}
Mg^{2+}	0.72	4.28	273.9	$10^{5.2}$	$10^{-6.2}$
Ca^{2+}	1.00	4.12	586.8	$10^{8.5}$	$10^{-5.9}$
Na^{+}	1.02	3.58	678.9	$10^{9.0}$	$12^{-6.2}$
K^{+}	1.38	3.31	752.8	$10^{5.2}$	$13^{-6.2}$
$H_3SiO_4^-$				$10^{0.52}$	

R_{ionic} = ionic radii from Atkins[143]

r_{hy}= Hydrated radii at 25 ºC, 1 bar and ΔG_{hy} from Conway[144]

K_{ex} =Ligand exchange rate for oxygens in primary hydration sheath around cation from Burgess[145] except silicic acid from Kinrade[146] by ^{17}O NMR

It is clear from Table 4.15 that Na and K retain significant water shielding upon interaction. This enhances the attraction of these elements to the silica surface and thus increases the dissolution rate. In contrast, Mg and Ca have low water shielding, reducing their attraction at the surface (and giving rise to a relatively lower dissolution rate). However these alkaline earth elements have the greatest adsorption constants (as measured empirically, see Dove[139] and references therein), explaining why only a small fraction of Ca^{2+} and Mg^{2+} need be present in an aqueous solution to become incorporated into the gel layer. This may partially explain why the dissolution rates observed in the young cement waters are greater than those observed in ECW and OCW. Since the basis for the nucleophilic attack of Si-O by water is the electrostatic attraction of water molecules to the silica surface, it is not surprising that this reaction occurs more rapidly at high pH.

4.3.2. Alteration layer morphology

The pore diameter measurements of the gel, calculated from TEM images, shown in Figure 3.15 and 3.16, are listed in Table 4.16, using a particle size analyser, average (mode values) fret diameter is listed below in nm (see Chapter 3, Section 3.3.4 for image processing). Readers are directed to the histograms in Figure 4.47 and 4.48 to observe the data range. The breadth of this data demonstrates the large uncertainty of porosity analysis using this technique. Notwithstanding these uncertainties, the average pore diameter of the gel in the young cement water was at least twice the size of that in the evolved and old cement waters, for both glass compositions.

Table 4.16 Average (mode) diameter of pores in the gel, readers are directed to the histograms to determine the range in the data.

Average (mode) pore diameter of the **gel**, nm				
	YCWCa	YCW	ECW	OCW
MW25	2.57	1.29	0.45	0.45
LBS	7.55	1.25	3.67	1.21

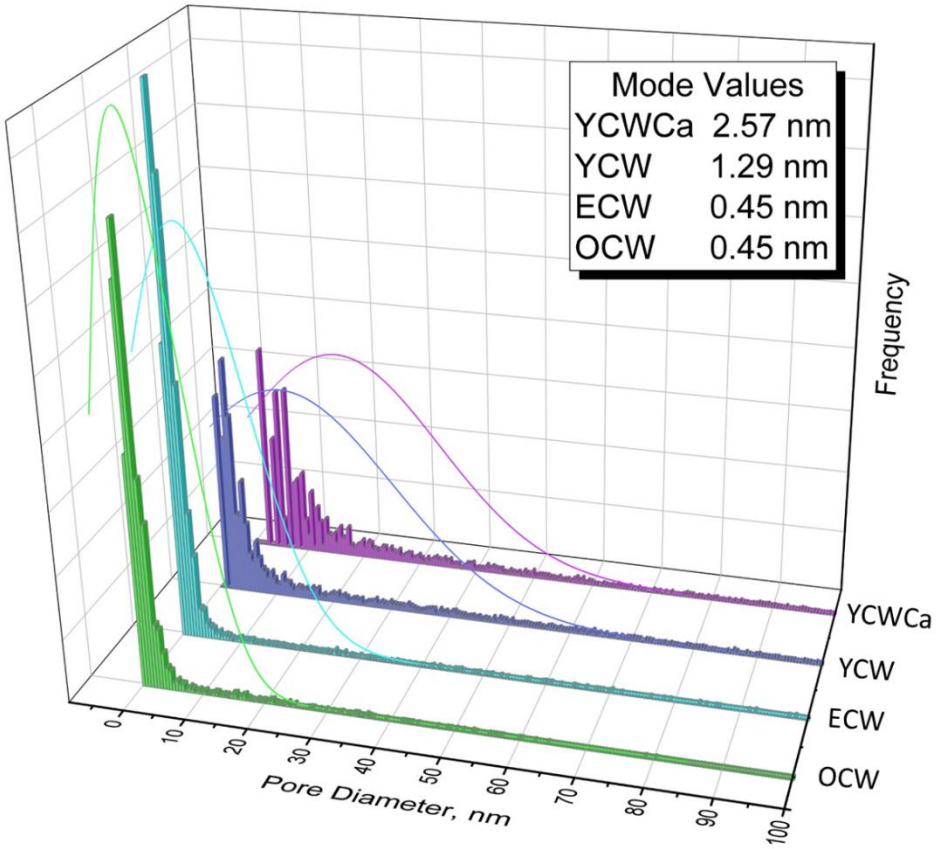

Figure 4.47 Histograms of the data obtained for the pore diameter measurements of MW25 glasses from TEM image; the mode value is listed as these values have been quoted throughout Section 4.2.4.

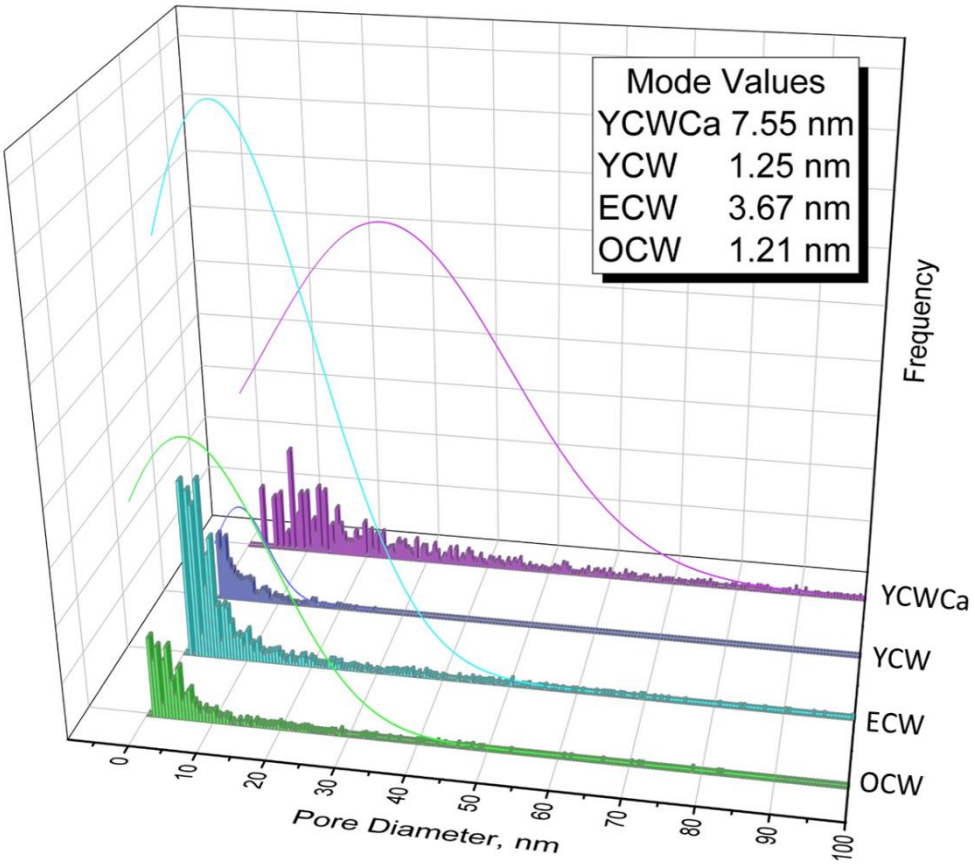

Figure 4.48 Histograms of the data obtained for the pore diameter measurements of MW25 glasses from TEM image; the mode value is listed as these values have been quoted throughout Section 4.2.5.

The porosity of the gel layer was found to be correlated with the pH of the cement leachate solution; the higher the pH, the greater the average pore diameter. These results are in agreement with Kaspar et al[51] who confirmed that as the pH of the leaching solution increased, the void fraction in the gel of the International Simple Glass increased due to the electrostatic repulsion between negatively charged silica spheres in the gel layer. The pH of the evolved and old cement solutions was lower than that of the young cement solutions; the corresponding pore size was also smaller. Such observations are in accordance with the Iler[32] model of silica condensation at high pH and in the presence of salts (Chapter 2, Section 2.3).

The composition of the alkali/alkaline earth-silica gel may also influence the observed porosity. For example, in the young cement solutions, which had a large average pore size, the major cation in solution is KOH. At the surface of the glass, KOH completely dissociates[148] and the large monovalent K cation moves into the silica network (for charge compensation). This causes a physical disruption of the gel network, owing to the large ionic radius of the cation[149,150], resulting

in enhanced dissolution rates. Elemental spot analysis confirmed that the gel formed in both of the young cement water systems was a Na/K-rich alkali-silica gel, which exhibited greater diameter pores compared to Ca-rich silica gels formed in the evolved and old cement solutions (Table 4.16), indicating that ionic radius (Table 4.15) of the alkali / alkaline-earth cation influences the porosity.

4.3.3. Secondary precipitates: (Nano)crystalline Alkali-Silicate Hydrates & Smectite clays)

Precipitation of secondary phases can alter the solution chemistry (notably pH) and influence the glass dissolution rates and mechanisms[151], as discussed in Chapter 2. All of the glass samples investigated in this Chapter exhibited the formation of secondary phases on top of the gel layer. The composition of the precipitates varied due to changes in solution composition (Table 4.14).
In addition to developing thick alkali / alkaline earth - silica gel layers, the young cement waters promoted the formation of a band of precipitates at least half as thick as the gel. For the MW25 glass, the precipitates were loosely packed ribbons (Figure 4.49 a and b), whereas for the LBS glass, precipitates appeared to be more needle-like, but were still loosely packed (Figure 4.49 d and e). Dissolution in ECW generated very different alteration layers in both glasses (Figure 4.49 c and f)). When examined by SEM, the MW25 glass dissolved in ECW solution had a needle-filled alkaline earth-silica gel layer, where the needles were rich in Mg, Na and Al. Also present were large crystal-like precipitates identified as calcite and portlandite (Figure 4.11), and a reaction rim rich in Ca and Si. In analysis of this sample by TEM, the needles were not observed in the gel layer, however a radiating fibrous material (Figure 4.21), like the crystals were seen in the SEM. In ECW solution, the LBS glass composition exhibited a dense alkaline earth-silica gel next to the pristine glass, with Ca-Si rich nodules located on top or in the alkaline earth-silica gel. An outer surface (Figure 4.38) appeared to be clay-like with ribbons scattered throughout. Dissolution of the glass in OCW resulted in the development of a thin gel layer of similar composition to the bulk glass with wispy loosely packed precipitates, for both glass compositions.

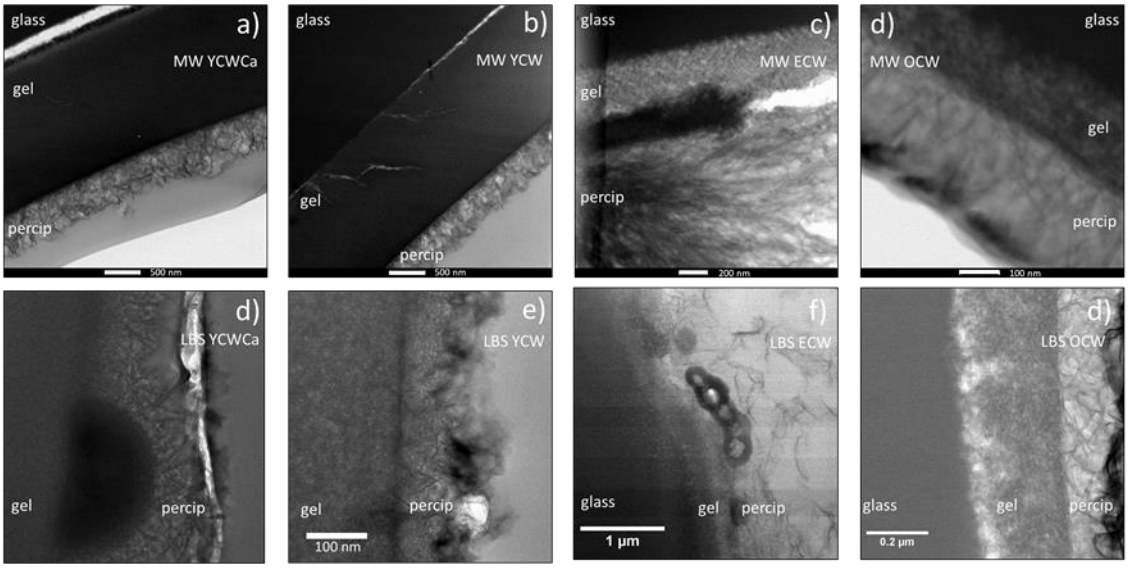

Figure 4.49 Collage of TEM BF images of alteration products on MW25 top row and LBS bottom row, moving from left to right YCWCa, YCW, ECW and OCW

Alkali- / alkaline-earth silicate hydrates, which may be nanocrystalline in nature, form when an alkali or alkali earth ions precipitate with dissolved Si (from the glass). Calcium silicate hydrate (C-S-H) is one such phase that is commonly identified as a precipitate on corroded glass surfaces in the literature (see Chapter 2); this phase was observed in the present study on the surface of glasses leached in the evolved cement water solutions by SEM / EDS and XRD analysis. In the young cement water solutions, K is the major alkali in solution, and SEM and TEM / EDS confirmed the formation of a K- and Si- rich precipitate with similar needle-like morphology to C-S-H. This precipitate was x-ray amorphous in all of the techniques applied here, so has been assigned as an unknown K-rich alkali-silicate hydrate.

C-S-H precipitates can act to protect the glass when there is a limited amount of Ca in solution[61,23,54] which was observed here for the synthetic cement waters. However, if there is an unlimited supply of Ca, then Si can be constantly removed from the gel and glass to form C-S-H, which ensures that the rate of glass dissolution remains high. The same should be true for alkali-silicate hydrates, if the alkali is abundant then continual formation of secondary phases keeps the dissolution rate elevated; this appears to be the case in the young cement water solutions.

The lack of a visible “rate drop” regime for the ECW and OCW solutions (Figure 4.5) is likely due to the presence of significant quantities of Mg in solution (from the glass). Mg readily precipitates as Mg-silicate or Mg-aluminate secondary phases, which consume Al and Si which are leached from the glass into the solution, promoting further dissolution. However, in the YCW(Ca) solutions, Mg is not soluble so the formation of these phases is precluded and the “rate

drop" regime is clearly observed. Analysis of the alteration layers agree with this hypothesis; Mg-Al-Si rich precipitates are observed in ECW and OCW, however, such phases are absent in the young cement waters. Despite preferentially precipitating as secondary silicate or aluminate phases, it is clear that a small proportion of Mg is also observed within the gel layer. The TEM / EDS data in Section 4.2.4 shows the precipitates formed on the surface of MW25 glass in YCWCa, YCW and OCW to be Mg-rich.

Magnesium is often associated with phyllosilicate clay secondary precipitates, including smectite clay. Phyllosilicates are layered structures (known as layered double hydroxides, LDH), composed of polymeric sheets of SiO_4 tetrahedra linked to sheets of $(Al,Mg,Fe)(O,OH)_6$ octahedra in a 2:1 formation (Figure 4.50). Smectites have a net negative charge due to isomorphous substitutions of Si^{4+} by Al^{3+} at tetrahedral sites, and Al^{3+} by Mg^{2+} or Mg^{2+} by Li^{+} at octahedral sites. The layers are charge balanced by alkaline earth or alkali metal ions (Na^{+}, K^{+}, Ca^{2+}, Mg^{2+}) which act as charge compensators at interlayer sites[136]. These cations affect the amount of water that can be absorbed and thus, the interlayer space distance. For two cations of equal valence, the more weakly hydrated will tend to partition into the smectite interlayer phase, which is subaqueous[152]. The hydrated ionic radius[144] of Mg^{2+} is 4.3 Å and of Ca^{2+} is 4.1 Å. Therefore, it is more likely that Ca^{2+} will take up residence in the gel or smectite phases. However, since Ca^{2+} preferentially enters the silica gel, Mg^{2+} is available to form phyllosilicates. The layered double hydroxide, hydrotalcite ($Mg_6Al_2CO_3(OH)_{16}\cdot 4(H_2O)$), was identified on the surface of LBS glass exposed to ECW, confirming the presence of such Mg and Al LDH phases.

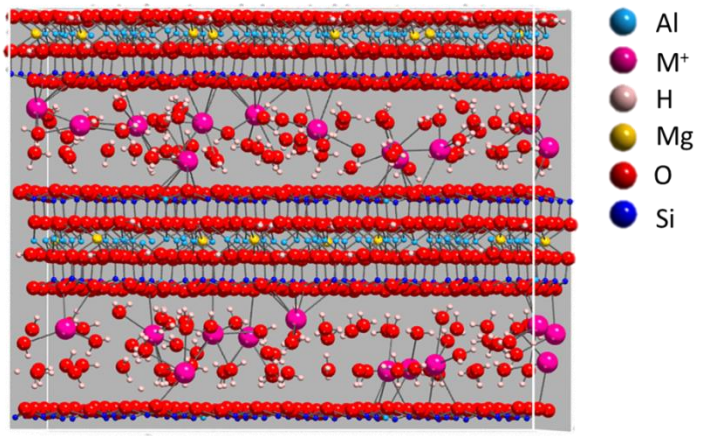

Figure 4.50 Smectite clay illustration taken from Ngouana[153] the structure of hydrated Montmorillonite, the top band in the image is Al and Mg layer, followed by Si layer, the large interlayer space is occupied by hydrated M^{+} cations, the sequence repeats.

TEM images of the LBS glass composition, after dissolution in ECW solution revealed the presence of a ribbon-like precipitate. Unfortunately, without further chemical analysis it was not

possible to determine the composition of this region, however, visually it appeared to be similar to clay layers observed by Zwicky[133], Abrajano[74], Thien[154] and Curti[72, 155]. These authors all reported the occurrence of phyllosilicate minerals including smectite (amorphous hydroxide-silica precipitates[156]), hectorite ($Na_{0.3}(Mg,Li)_3Si_4O_{10}(OH)_2$), saponite ($Ca_{0.25}(Mg,Fe)_3((Si,Al)_4O_{10})(OH)_2 \cdot n(H_2O)$) and montmorillonite ($Na_{0.2}Ca_{0.1}Al_2Si_4O_{10}(OH)_2(H_2O)_{10}$) forming on simulant nuclear waste glass at temperatures of 90 ^oC or above. Thein observed the presence of aluminous hectorites or Li-saponite at 50 ^oC[154].

Smectite clays are known as swelling clays[152] and the presence of Mg^{2+} seems to be essential to their formation[157]. Under basic conditions (pH 10 or greater) only 10 mg L^{-1} of Mg is required in solution for smectite minerals to form and this is only possible when the precipitate contains at least 6 % of MgO[156]. Precipitates formed on the surface of the LBS glass leached in ECW contained 10.3 at % Mg (SEM spot analysis, Table 4.10). Thien et al.[82] concluded that Mg had dual effects on the long term alteration of French AVM glass; first, the consumption of Si to form aluminous hectorites lead to the partial dissolution of the protective gel layer, second, Mg incorporation into the gel layer, improved its passivating properties[80]. In the present study, it was not possible to identify Mg-silicate phases, rather Mg-aluminate phases were observed, suggesting that consumption of Al plays an important role in maintaining dissolution rates. When Al is consumed during the formation of secondary phases[42] there is the possibility of rate resumption; further work is required to ascertain this behaviour for Mg-bearing glass compositions.

4.3.4. Formation of nodules

The formation of Ca-rich nodules observed on the glasses exposed to ECW solution can be explained by aggregation of Ca ions in the gel through cluster-cluster mechanisms. Due to the low (<0.45 mol L^{-1}) Ca concentration in the ECW solution (0.015 mol L^{-1}) only partial aggregation occurred, as outlined in Figure 4.51, adapted from Gaboriaud[158]. In this mechanism, oligomer silicate aggregates densify through cluster-cluster processes. Negatively charged silica clusters agglomerate due to the proximity of a Ca^{2+} counter ion acting as a charge compensator[159]. Further densification of aggregates occurs through the addition of monomers of Si from solution; this process will cease when all the Ca has been removed from solution[158].

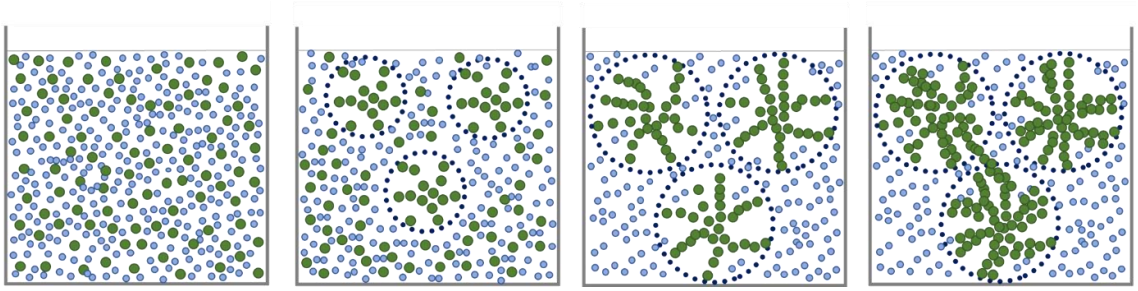

Figure 4.51 Schematic representation of the aggregation processes involved in gel formation taken from Gaboriaud [158] (larger green circles represent Si).

4.3.5. Formation of a reaction rim

The formation of the silica reaction rim, as observed on MW25 and LBS glass in ECW solution (Figure 4.20 and Figure 4.38), has implications for the dissolution of the glass. Dohmen et al.[129] stated that as the reaction rim thickens, transportation of the elements released from glass during dissolution will be hindered[129], thus an accumulation of elements in the interstitial fluid (between the rim and pristine glass) will result in local changes in the pH and potentially saturation, both of which can led to further alteration. The pH of the ECW solution is pH(RT) ~12.3, so it would be expected that trapping of solution in the interstitial region should not induce significant additional alteration.

Silica recondensation time has been shown to increase in the presence of alkalis, in the following order Na > K > Li[42]. Ca has been shown to rapidly promote Si recondensation[158]. As such, Si-rich reaction rims are observed to form more readily in the Ca-rich ECW and OCW solutions than in the young cement solutions.

4.4. Conclusions

Dissolution of HLW and ILW simulant glasses was performed in a range of synthetic cement solutions designed to mimic an aging Portland cement. The rate of dissolution increased in the order OCW≈ECW >YCWCa≈YCW, the differences in dissolution rate are attributed to the composition and morphology (porosity) of the alteration layer formed, which is strongly dependent on the alkali / alkali-earth composition of the leachate, and the pH, although the separate influences of solution composition and pH could not be discerned using the present experimental approach (see Chapter 8 for Further Work to address this).

Evidence is presented for the presence of alkali-/alkaline-earth silica gels and the mechanisms of their formation proposed, including the role of Ca, Na, K and Mg as charge compensators for negatively charged species in the gel layer. The propensity for exchange of hydrated cations with silica indicates that a K-silica gel layer will form preferentially over a Na-and Ca-silica gel layers, although only a small concentration of Ca and Mg need be present to form Ca- or Mg- containing silica gels. The data presented here supports this theory, however in the mixed alkali/alkaline earth solutions, all cations (including Mg from the glass) are found in the gel layers. This highlights the necessity for the use of mixed alkali/ alkaline earth solutions in dissolution experiments rather than simplified solutions composed of one cation, for example $Ca(OH)_2$, NaOH or KOH, to understand glass dissolution in a cementitious disposal facility.

The role of Mg, present in both glass compositions, is likely responsible for maintaining dissolution rates in a linearly increasing regime in OCW and ECW solutions, facilitated by the formation of Mg-Al-(Fe)-Si rich precipitates of layered double hydroxides and possibly smectite clays.

In the presence of synthetic cementitious leachates, MW25 glass exhibits better durability than LBS as evidenced by lower dissolution rates and more dense alteration layers. Despite the presence of a highly alkaline cementitious water contacting simulant HLW glass, its low dissolution rates are favourable, and comparable to existing studies, implying that alkali and alkaline-earth ions (K, Na and Ca) in solution can have a positive impact. Nevertheless, further research is required to elucidate the potential for Mg-bearing secondary precipitates to facilitate "rate resumption" at longer durations of dissolution.

4.5. Appendix

4.5.1. Calcium and Potassium Solution Concentration Data

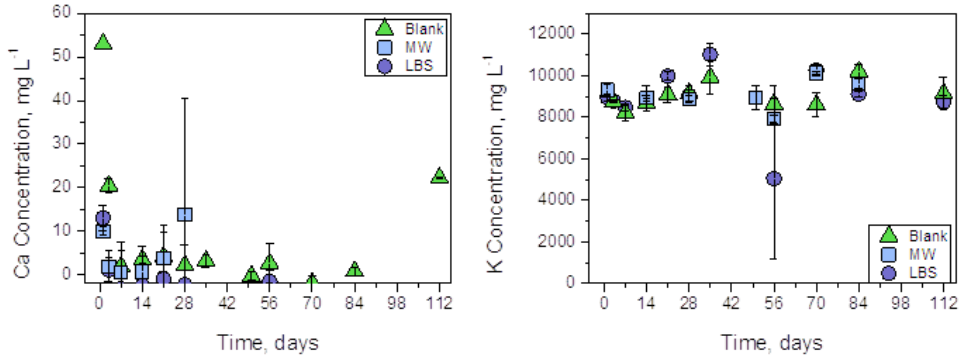

Figure 4.52 Concentration of Ca and K for Blank, MW25 and LBS in YCWCa

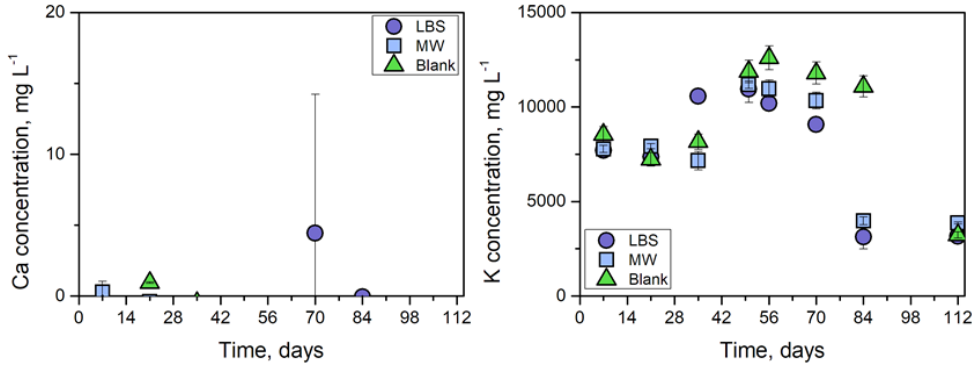

Figure 4.53 Concentration of Ca and K for Blank, MW25 and LBS in YCW

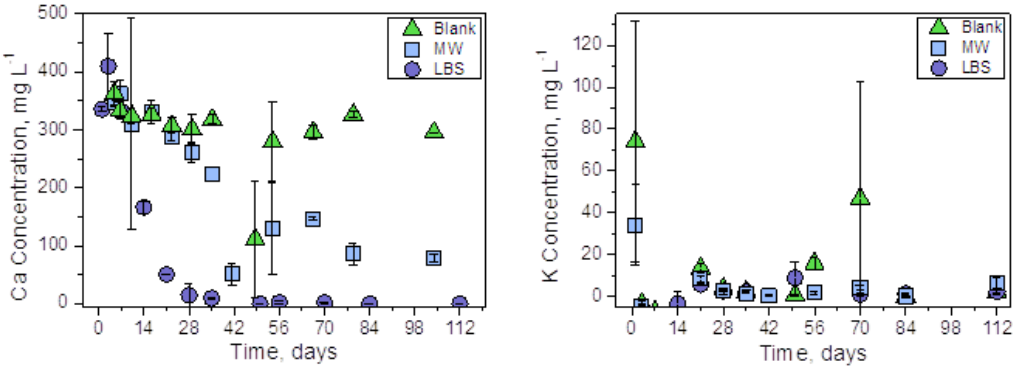

Figure 4.54 Concentration of Ca and K for Blank, MW25 and LBS in ECW

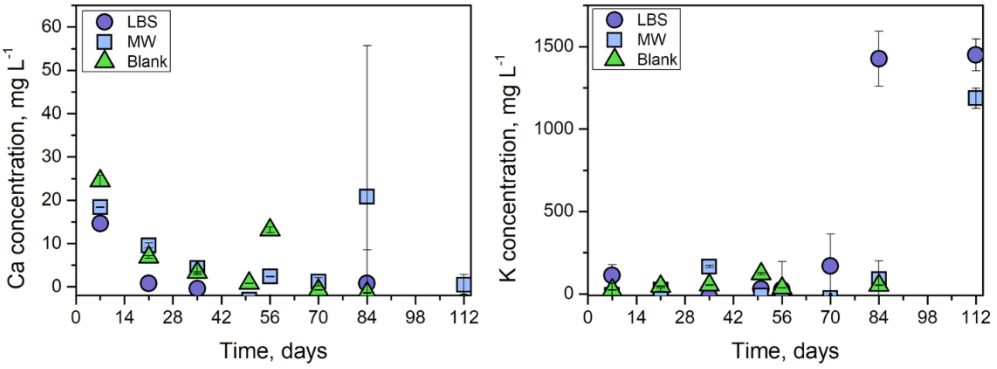

Figure 4.55 Concentration of Ca and K from Blank, MW25 and LBS in OCW

Chapter 5. Influence of Young Cement Water on the dissolution mechanisms of the International Simple Glass

5.1. Introduction

An international collaboration between the UK, Belgium, France, Germany, Japan and the USA began due to the need for development of reliable performance assessment models. The nations listed previously all immobilise HLW in a borosilicate glass and are considering a multi-barrier approach to waste disposal in a GDF[33]. Any nuclear waste management policy is dependent on the safety assessment of geological disposal of HLW, and it is challenging to produce a safety assessment if there is no consensus on the mechanisms controlling long term dissolution rates of HLW glass.

A common glass formulation was created to allow collaborators to compare results. The International Simple Glass (ISG) is a six component simplified version of SON68, (simulant French R7T7) with the following composition (mol %); 60.2 SiO_2, 16.0 B_2O_3, 12.6 Na_2O, 3.8 Al_2O_3, 5.7 CaO and 1.7 ZrO_2. These oxides are commonly found in boroaluminosilicate nuclear glasses and the ratio matches that of SON68[33].

Both the UK and Belgian disposal concepts for nuclear waste will utilise cementitious materials (as previously described in Chapter 4, Section 4.1), and as such it is imperative that the interactions between glass and cement leachates are studied. Several studies have investigated the glass dissolution mechanisms in the presence of simple hyperalkaline media, for example $Ca(OH)_2$, NaOH or KOH leachates. Few studies have investigated the role of cementitious leachates, which contain mixed alkali and alkali earth ions in addition to a range of other elements[53,54,83].

The inclusion of ISG in this thesis is vital for helping validate the mechanistic models of glass dissolution over geological time scales. The objective was to gain a deeper understanding of glass dissolution in cement leachate solution. A two year leaching study was conducted with young cement leachate assumed to be in equilibrium with portlandite (referred to as YCWCa) on the dissolution of ISG powders and monoliths at 30 ^{o}C and 70 ^{o}C. This work was a collaboration; SCK.CEN conducted the initial experimental work and geochemical modelling and C. Mann completed characterisation of monolith samples at the UoS and Oak Ridge National Labs.

5.2. Results

5.2.1. pH

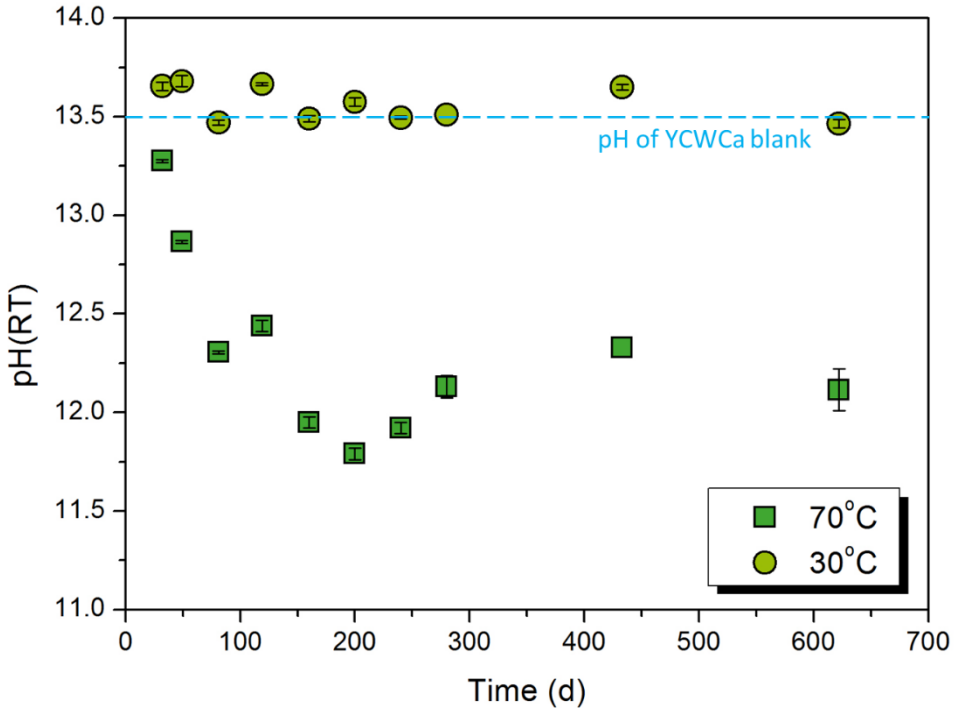

Figure 5.1Measured pH (room temperature, RT) for ISG glass powder exposed to YCWCa for 622 days at 30 °C and 70 °C.

The YCWCa solution maintained a high pH throughout the duration of the experiments, the average pH of the blank solutions was pH(RT) 13.5; at 30 °C it was constant and remained at the value of the blank solution (pH(RT) 13.5), while at 70 °C a decline to pH(RT) 12 was observed in Figure 5.1.

5.2.2. Dissolution rate determination

The normalised mass loss (NL_i) for Si, B, Al and Zr is given in Figure 5.2; the corresponding elemental release of Si, B, Ca and Al with time at 30 °C and 70 °C is shown in Figure 5.3. Dissolution rates were obtained from linear regression of NL_B data (Figure 5.2a & e). At 30 °C the concentration of B continuously increased throughout the experiment, resulting in a dissolution rate of (4.00 ± 0.15) x 10^{-3} g m^{-2} d^{-1} (Figure 5.2a). In contrast, at 70 °C, after a rapid increase in B concentration at 32 days, there was little further dissolution of this element (Figure 5.3). The dissolution rate during the initial rapid increase was (4.42 ± 0.40) x 10^{-2} g m^2 d^{-1} and in the plateau was (8.84 ± 3.99) x 10^{-4} g m^{-2} d^{-1} (Figure 5.2e).

At both temperatures, the release of Al to solution was initially high, but was subsequently observed to decrease, indicative of the incorporation of Al into alteration layers or secondary phases. The release of Si to solution was significantly different at 30 °C and 70 °C (Figure 5.3); at the lower temperature, there was an almost linear increase in the concentration of Si released, reaching a final concentration of ~100 mmol L^{-1} after 622 days (Figure 5.3), while at the higher temperature, the concentration was ~220 mmol L^{-1} after only 32 days, at which point a slight decrease was observed. Regardless of the temperature, the concentration of Ca, which was initially present in the solution and the glass, decreased at the beginning of the experiments to levels below 0.05 mmol L^{-1} (values of 0.044 ± 0.001 mmol L^{-1} and 0.047 ± 0.003 mmol L^{-1} were measured at 30 °C and 70 °C, respectively). The removal of Ca from solution over the initial 32 days is indicative of the formation of a Ca containing alteration layer.

The concentration of Zr remained lower than 400 µmol L^{-1} at 30 °C and 150 µmol L^{-1} at 70 °C, indicating that it may also have been incorporated in the glass alteration layer (Figure 5.2), and the concentration of K, a major constituent of the YCWCa, was observed to decrease at both temperatures; the initial concentration was 367 mmol L^{-1} and after 622 days at 30 °C and 70 °C, the concentration fell to ~300 mmol L^{-1} and ~175 mmol L^{-1} respectively, once again indicating incorporation into the glass alteration layer.

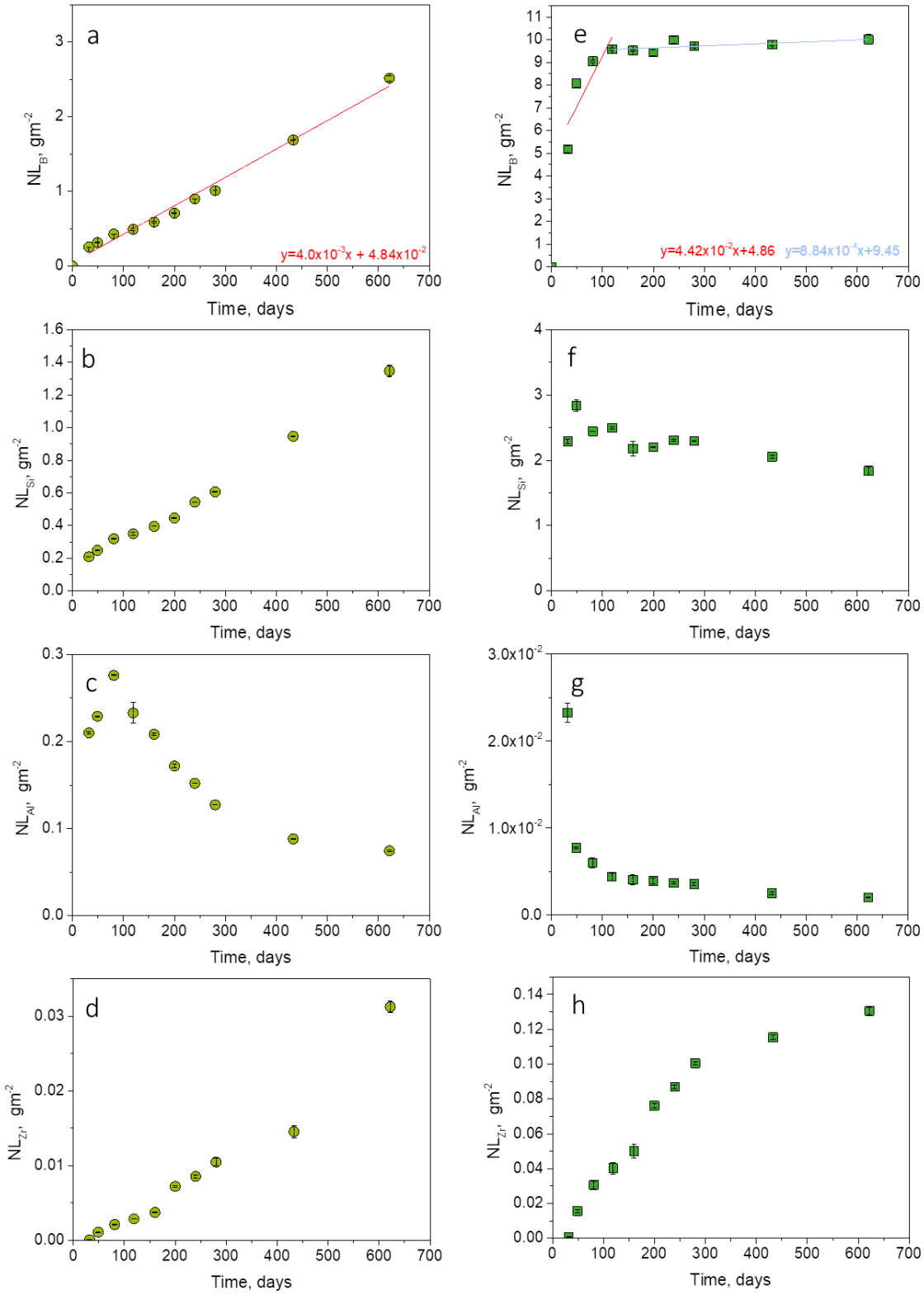

Figure 5.2 Normalised mass loss of glass components in ISG in YCWCa for 622 d at 30 °C: (a) NL_B (reported in g m^{-2} and showing calculated dissolution rates in g m^{-2} d^{-1} derived from linear regression); (b) NL_{Si}; (c) NL_{Al} (d) NL_{Zr}; and comparative analysis at 70 °C: (e) NL_B (showing calculated dissolution rates in g m^{-2} d^{-1}); (f) NL_{Si}; (g) NL_{Al} (h) NL_{Zr}.

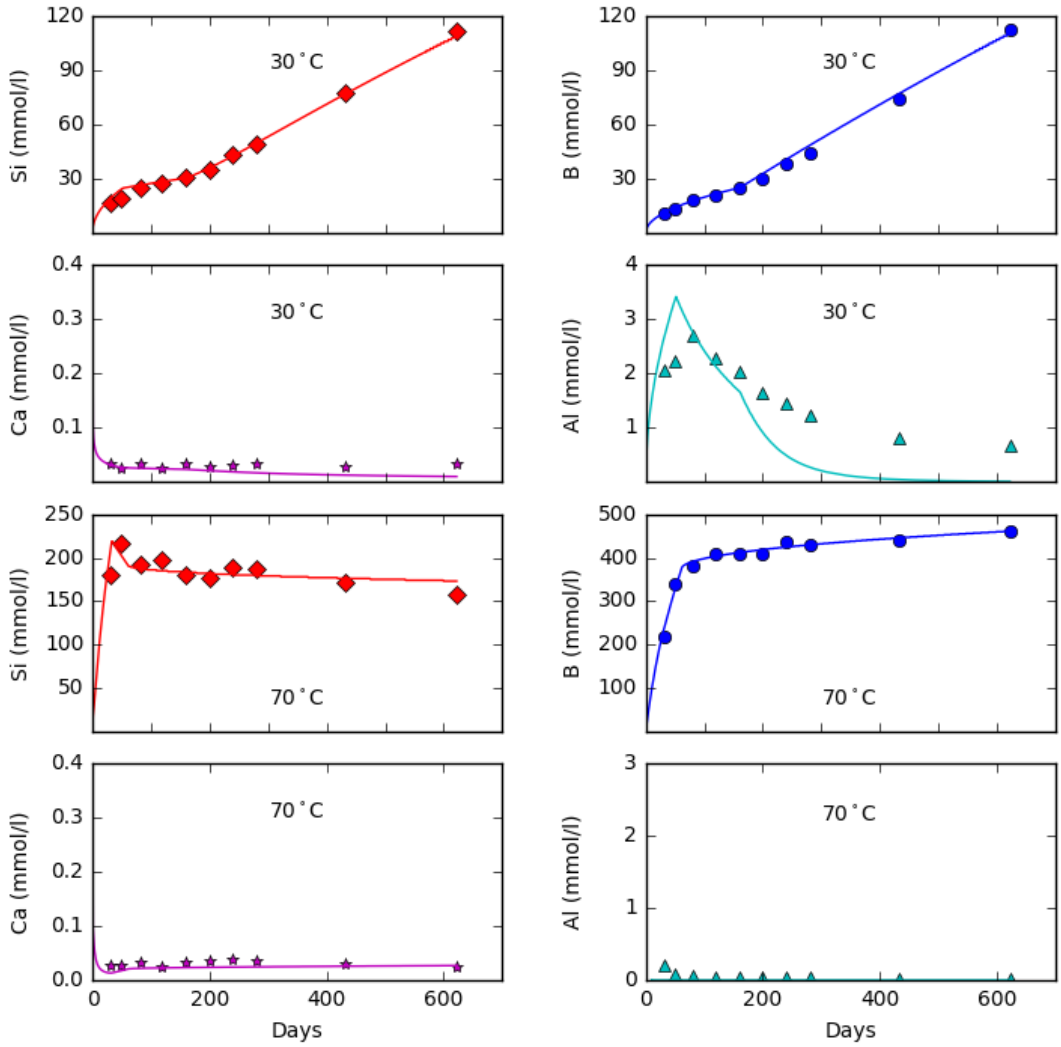

Figure 5.3 Measured (points) vs modelled (lines) concentrations of Si, B, Ca and Al in YCWCa at 30°C and 70°C.

5.2.3. Geochemical modelling

Two different models were applied to simulate the experimental dissolution results: (1) an affinity-based model (Eqn. 3.6) where congruent dissolution is driven by the undersaturation of the solution with respect to silica; and (2) a diffusion model (Eqn. 3.7 and accompanied by Eqn. 3.8) that describes 'diffusion-through-alteration-layer-dissolution', i.e. when the alteration products (gel and precipitates) cover the glass surface and limit solute transport, decreasing the dissolution rate. The results of geochemical modelling are shown in Figure 5.3 and Eqns. 3.6 - 3.8 were applied to the model. Further details are listed in Chapter 3, Section 3.3.1.

$$\frac{dm}{dt} = -A_0 \left(\frac{m}{m_0}\right)^{\frac{2}{3}} r_0(T, pH) \left(1 - \frac{[Si]}{[Si_{sat}]}\right) \qquad \textbf{Eqn. 3.6}$$

$$\frac{dm}{dt} = -A_0 \left(\frac{m}{m_0}\right)^{\frac{2}{3}} \rho \sqrt{\frac{D}{\pi t}} \qquad \textbf{Eqn. 3.7}$$

$$C_i = \frac{2A_0\rho}{VM_i} \left(\frac{m}{m_0}\right)^{\frac{2}{3}} x_i \sqrt{\frac{D_i t}{\pi}} \qquad \textbf{Eqn. 3.8}$$

At 30 °C, particularly prior to 160 days of dissolution, the diffusion-through-alteration-layer-dissolution equation (Eqn. 3.7) described the glass dissolution well. This is evidenced by a parabolic increase of B and Si concentration with time before 160 days, as was previously observed for SON68 subject to leaching under the same conditions[83]. After more than 160 d of dissolution, the B and Si concentrations were observed to increase linearly with time. It was only possible to model this behaviour by the application of Eqn. 3.6, although since there was still a rapid increase in Si concentration at the end of the experiment, i.e. no Si-saturation, the Si saturation term was omitted; this suggests that the glass dissolved uninhibitedly after 160 days. At this time, the diffusion step was no longer rate limiting; the change in the dominant mechanism of dissolution suggests a change in the properties of the alteration layer after this time.

The calculated diffusion coefficients (using Eqns. 3.7 and 3.8) of B and Si at 30 °C were (2.78 ± 0.78) x 10^{-21} m^2 s^{-1} and (8.49 ± 2.37) x 10^{-22} m^2 s^{-1}, respectively. This is somewhat higher than that measured by Gin et al.[160], who calculated a diffusion coefficient of hydrous species through the passivating layer of ISG, at pH 9 and 90 °C, to be 1.3 x 10^{-23} m^2 s^{-1}. This difference will be discussed further in the following sections.

For the experiment at 70 °C, Si concentrations were initially high and then decreased throughout the experiment, indicating that Si precipitation exceeded Si dissolution. The affinity term in Eqn. 3.6 (with silica saturation included) gave a reasonable fit for Al and Ca concentrations. For B at 70 °C, after the initial rapid increase associated with the degradation of the glass network, the release rate decreased after about 60 days, but did not reach a steady state value. The decrease was possibly due to the presence of precipitated phases on the glass surface that limit the transport of solution to and from the glass interface, inhibiting further dissolution. From 60 days of dissolution onwards, Eqns. 3.7 and 3.8 were applied to calculate the diffusion coefficient through precipitation products. The calculated value based on B was 1.95 x 10^{-20} m^2 s^{-1}. This is 2 to 4 orders of magnitude higher than the reported residual B diffusion coefficients for ISG in Si saturated solutions, which suggests that alteration layers formed in YCWCa solution had a higher porosity[161].

5.2.4. Alteration layer and secondary phase analysis

The X-ray diffraction patterns of ISG monoliths are shown in (Figure 5.4), exposure to YCWCa for 622 days at 30 °C did not result in significant crystalline secondary phases, as determined by the diffuse scattering. At 70 °C diffraction peaks could be indexed to: the phyllosilicate, rhodesite [$(Ca,Na_2, K_2)_8Si_{16}O_{40}.11H_2O$] (PDF 00-022-1253)[162] (corresponding to needle-like crystallites in Figure 5.8Figure 5.9Figure 5.8); the zeolite, phillipsite-K [$Na_4KA_{l5}Si_{11}O_{32}.10H_2O$] (PDF 01-073-1419)[163] (corresponding the rhombohedral crystallites in Figure 5.8Figure 5.9); and silicon oxide [SiO_2] (PDF 01-082-1573)[164]. None of the crystallites formed were found to contain Zr, indicating that this element was exclusively partitioned into the gel layer, in agreement with previous studies[85,70].

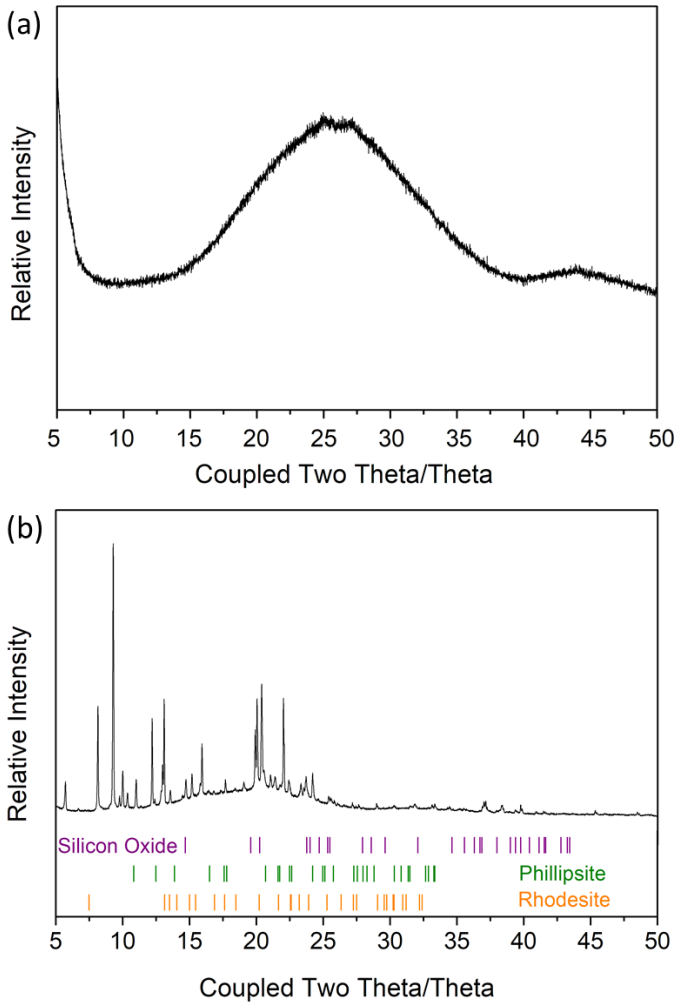

Figure 5.4 Diffraction patterns for monolith samples exposed to YCWCa for 622 days at: (a) 30 °C and; (b) 70 °C. Phases indexed at 70 °C were: rhodesite [$(Ca, Na_2 K_2)_8Si_{16}O_{40}.11H_2O$, PDF 00-022-1253]; phillipsite-K [$Na_4KAl_5Si_{11}O_{32}.10H_2O$, PDF 01-073-1419]; and silicon oxide [SiO_2, PDF 01-082-1573].

Figure 5.5 shows the alteration layers formed on the surface of ISG powders and monoliths at both 30 °C (Figure 5.5a & b) and 70 °C (Figure 5.5c & d). At 30 °C an amorphous alteration layer, 2 to 10 μm in thickness, was observed on the glass powders, as shown in Figure 5.5a, and on the monolithic specimen from the same experiment, shown in Figure 5.5 b. This layer was divided into three regions; a dense band on the outer edge of the layer (i.e., in contact with solution), a more porous region close to the surface of the glass and, in between, a finely banded region, where the bands were "scalloped" in morphology, with a convex boundary towards the surface of the glass, as previously observed by Dohmen et al.[129]. Dissolution at 70 °C also resulted in the formation of a gel layer with multiple bands, as shown in Figure 5.5c and 5.5d. The average thickness of the altered layer was 15.6 ± 0.9 μm and the altered glass fraction (AGF) was 41.2 ± 0.1 %, similar to that observed for SON68 dissolved in KOH at 90 °C for 365 days[52].

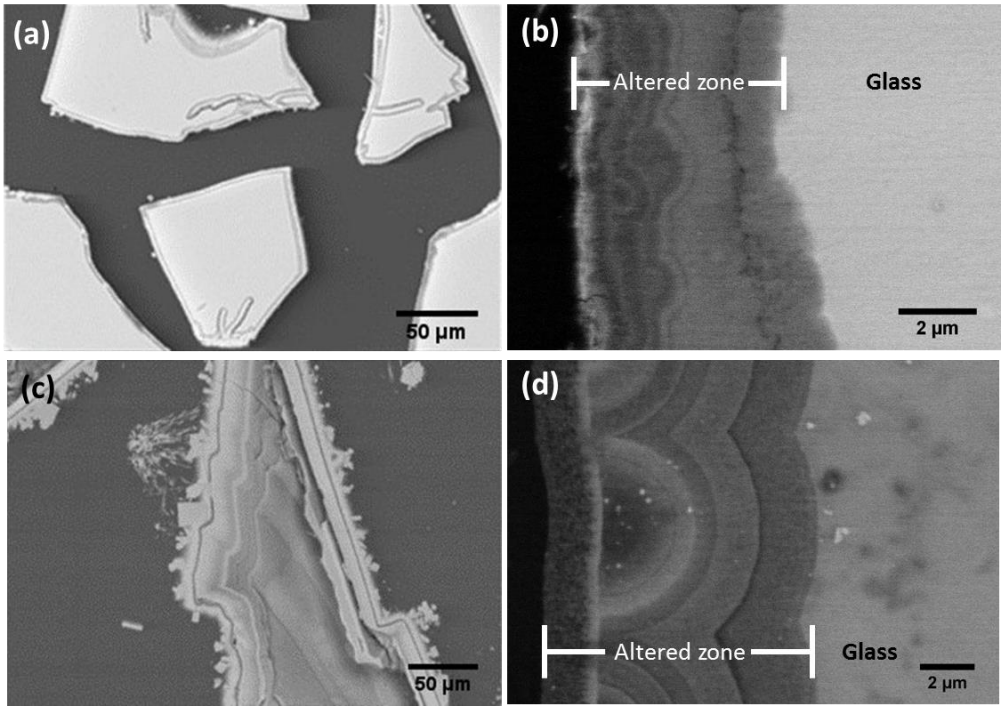

Figure 5.5 Alteration layers formed on surface of ISG after 622 days for powder and 721 days for the monoliths; 30°C: (a) powder; and (b) monolith; 70°C: (c) powder; and (d) monolith.

At 70 °C the alteration layer surrounding the monolith was not uniform Figure 5.6 demonstrations the variations observed along the length of the cross-sectioned monolith. Images a-d all exhibit multiple layers with a porous band which was in contact with the solution, secondary precipitates are visible on top of the alteration gel layers in Figure 5.6c & d. Perpendicular cracking of the alteration layers can be seen in addition to regions that have pulled away from the surface of the sample leading to the ingress of epoxy during sample preparation.

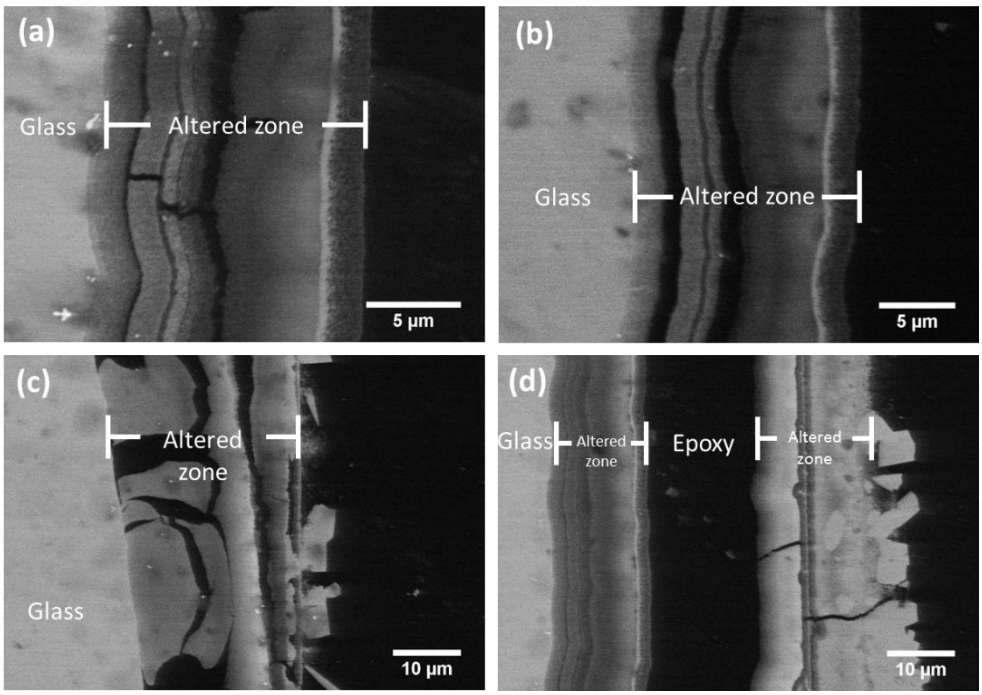

Figure 5.6 BSE images of the alteration layer on ISG monoliths exposed to YCWCa at 70 °C for 721 d.

The composition of the bands observed at 30 ºC (Figure 5.7) within this portion of the layer appeared to be the same, comprising Si, Al, Na, K, Ca and Zr, with an Al/Si ratio of 0.22 ± 0.04 (compared to an Al/Si ratio of 0.12 in the bulk glass and of 1.20 in the blank YCWCa solution). The Ca/Si ratio in the gel layer was ~0.25, which is significantly lower than expected for C-S-H (typical end members have a Ca/Si ratio of 0.6 and 1.2). The average altered layer thickness, as measured on monolith samples, was 5.7 ± 0.2 µm (Figure 5.5 b), and the AGF was 11.3 ± 0.7 %.

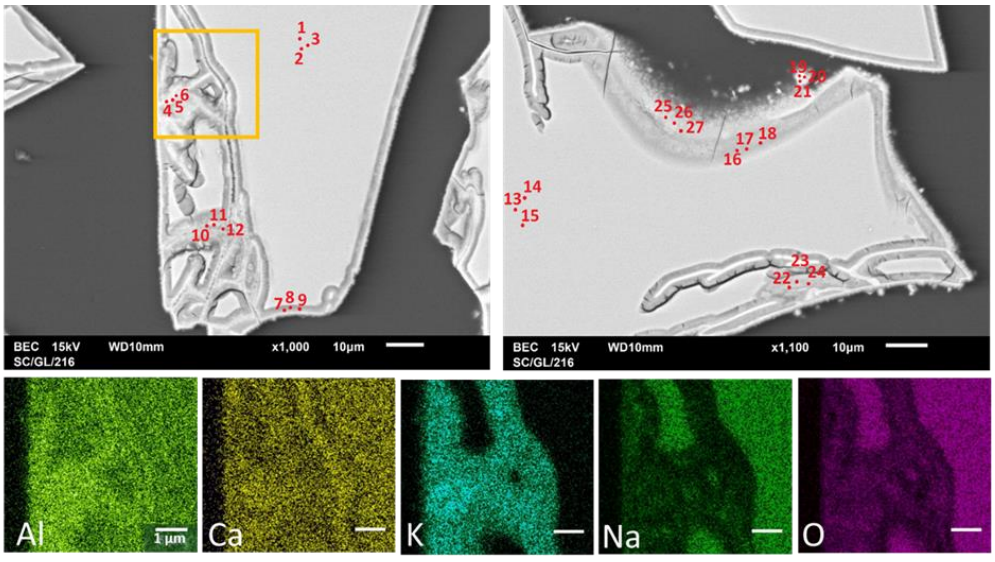

Weight %	O	Na	Al	Si	K	Ca	Zr
Spots 1-3	53.6 ± 0.3	5.8 ± 0.9	3.6 ± 0.2	29.8 ± 0.7	-	4.6 ± 0.1	2.7 ± 0.0
Spots 4-6	43.2 ± 0.8	3.5 ± 0.5	6.4 ± 0.3	22.1 ± 0.8	15.2 ± 1.6	4.7 ± 0.4	5.0 ± 0.1
Spots 7-9	48.4 ± 0.8	1.4 ± 0.1	5.0 ± 0.2	22.1 ± 0.8	11.7 ± 2.1	7.4 ± 0.8	4.0 ± 0.1
Spots 10-12	37.7 ± 4.0	4.5 ± 1.1	6.1 ± 0.6	24.2 ± 2.2	15.8 ± 2.1	7.3 ± 0.9	4.5 ± 0.5
Spots 13-15	53.1 ± 0.1	6.7 ± 0.2	3.5 ± 0.1	29.3 ± 0.2	-	4.8 ± 0.0	2.7 ± 0.1
Spots 16-18	41.1 ± 1.0	4.8 ± 0.4	5.2 ± 0.3	33.4 ± 1.2	5.6 ± 1.3	5.9 ± 0.1	4.1 ± 0.3
Spots 19-21	46.2 ± 2.8	1.8 ± 0.0	4.5 ± 0.5	22.9 ± 1.3	12.8 ± 1.4	8.4 ± 0.5	3.4 ± 0.4
Spots 22-23	41.2 ± 2.8	3.5 ± 0.5	5.6 ± 0.5	27.7 ± 3.8	11.8 ± 2.5	6.4 ± 0.4	4.0 ± 0.5
Spots 25-27	42.3 ± 1.8	2.2 ± 0.1	5.7 ± 0.2	25.4 ± 1.2	13.1 ± 0.9	7.2 ± 0.6	4.2 ± 0.0

Figure 5.7 SEM pictures corresponding EDX data (average of labelled spots) for ISG powder altered for 622 days in YCWCa at 30 ºC

Figure 5.8 shows high magnification SEM images of the glass powder after dissolution at 70 ºC. Indicating multiple alteration layers on the surface of the glass, EDX indicated that there was no variation in the composition among the layers. Framboidal and radiating acicular crystallites, ranging in size from 5 to 60 µm in length, were observed to form around the outer edge of glass grains reacted at 70 °C (Figure 5.5 c), but were absent in experiments at 30 °C. The bands on the monolith were composed of Si, Al, Na, K, Ca and Zr with an Al/Si ratio of 0.04 ± 0.003 (considerably lower than the bulk glass). EDX analysis of the crystalline phases at 70 °C (Figure 5.8 and Figure 5.9) indicated two distinct compositions; needle-like crystallites were enriched in K, Si and Ca (Figure 5.9, e.g. EDX spots 45 – 48), while crystallites with a rhombohedral morphology were composed of K, Si and Al (Figure 5.8, e.g. EDX spots 12 - 15). EDX results were in good agreement with XRD analysis (Figure 5.4), where diffraction peaks could be indexed to: the phyllosilicate, rhodesite (corresponding to needle-like crystallites in Figure 5.8 and Figure 5.9); the zeolite, phillipsite-K (corresponding the rhombohedral crystallites in Figure 5.8 and Figure 5.9); and silicon oxide.

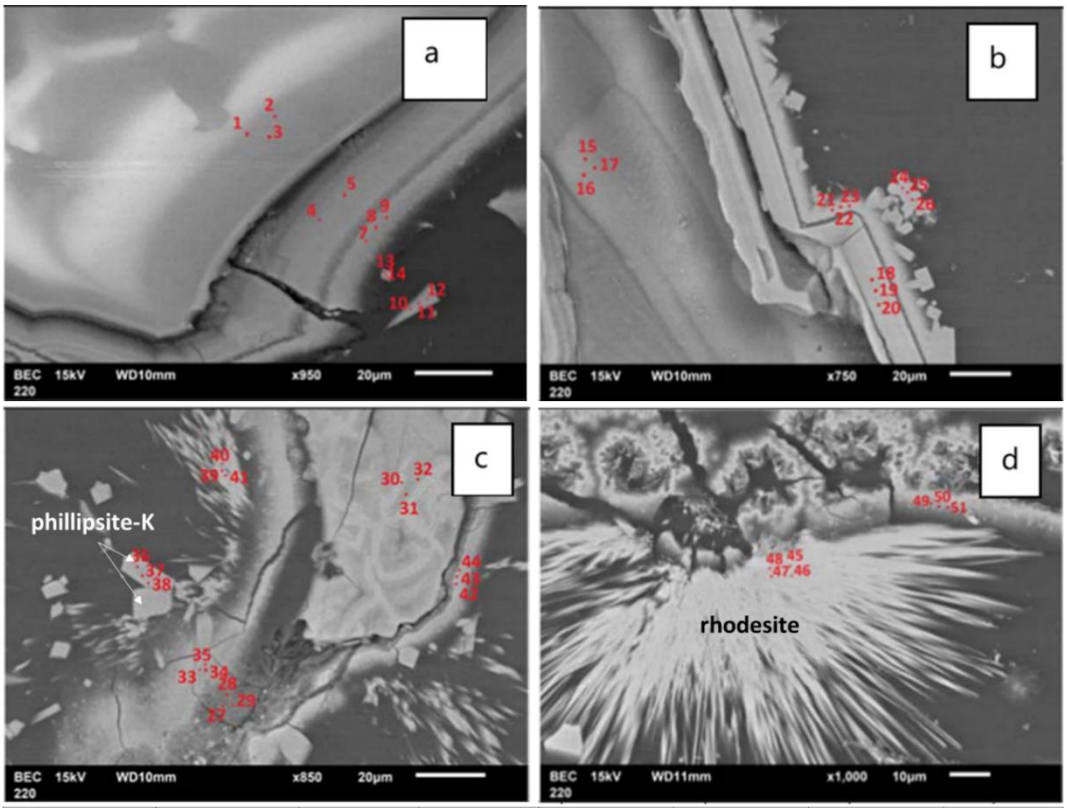

Weight %	O	Na	Al	Si	K	Ca	Zr
Spots 1-3	57.1 ± 0.5	8.5 ± 0.6	3.1 ± 0.0	25.0 ± 0.1	-	3.9 ± 0.2	2.4 ± 0.1
Spots 4-5	46.5 ± 0.6	3.3 ± 0.4	4.9 ± 0.0	28.0 ± 1.1	13.3 ± 1.2	1.8 ± 0.1	4.7 ± -
Spots 7-9	51.5 ± 1.3	4.8 ± 0.8	0.9 ± 0.1	22.8 ± 0.2	9.2 ± 0.3	10.6 ± 0.4	0.4 ± -
Spots 10-12	51.5 ± 2.5	2.7 ± 0.9	6.9 ± 0.7	24.6 ± 1.6	14.3 ± 3.8	-	-
Spots 13-14	65.0 ± 1.6	1.4 ± 0.0	3.2 ± 0.4	17.3 ± 0.4	7.9 ± 0.8	3.2 ± 0.4	-
Spots 15-17	50.9 ± 2.1	2.3 ± 0.1	4.9 ± 0.2	27.7 ± 1.4	9.7 ± 0.7	-	4.5 ± 0.2
Spots 18-20	44.7 ± 1.4	2.2 ± 0.1	5.9 ± 0.6	30.7 ± 1.6	10.2 ± 1.1	0.8 ± 0.4	5.6 ± 0.2
Spots 21-23	51.0 ± 0.5	2.4 ± 0.1	0.9 ± 0.1	25.8 ± 0.5	7.5 ± 0.2	11.6 ± 0.2	1.0 ± 0.2
Spots 24-26	49.8 ± 0.5	0.6 ± 0.2	8.0 ± 0.3	27.3 ± 1.7	14.2 ± 1.4	-	-
Spots 27-29	42.5 ± 2.0	4.4 ± 0.5	1.2 ± 0.1	28.0 ± 1.1	10.0 ± 0.1	12.7 ± 0.4	1.1 ± 0.1
Spots 30-32	46.6 ± 1.2	3.0 ± 0.4	5.9 ± 0.7	28.4 ± 1.0	9.0 ± 0.2	1.7 ± 0.3	5.4 ± 0.1
Spots 45-48	47.3 ± 1.6	2.3 ± 0.1	- ± -	31.8 ± 1.4	5.5 ± 0.1	13.2 ± 0.3	- ± -
Spots 49-51	42.1 ± 2.9	4.1 ± 0.5	1.0 ± 0.1	29.5 ± 2.1	9.8 ± 0.8	11.7 ± 0.6	1.8 ± 0.1

Figure 5.8 SEM pictures and corresponding EDX data (average of labelled spots) for ISG powder altered for 622 days in YCWCa at 70 °C.

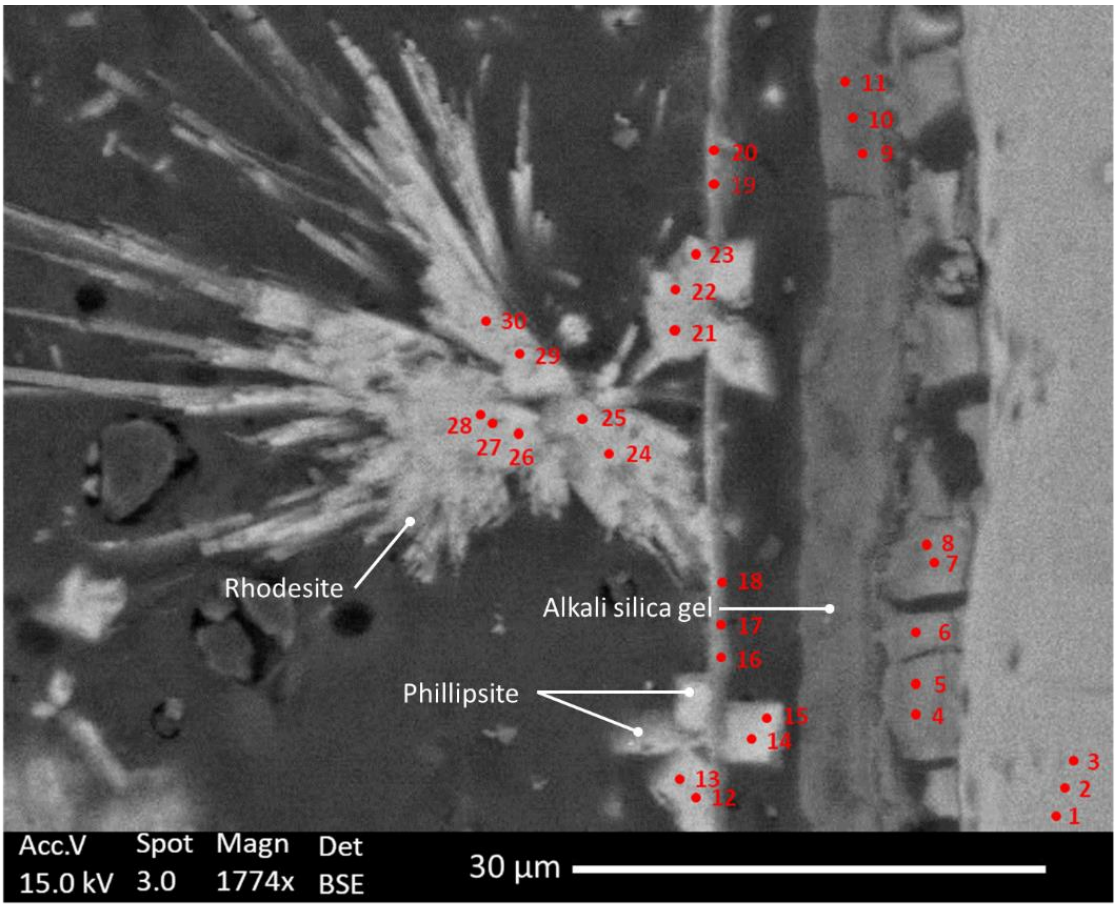

Weight %	O	Na	Al	Si	K	Ca	Zr
Spots 1-3	57.2 ± 0.4	8.1 ± 0.1	3.1 ± 0.2	27.4 ± 1.2	-	3.3 ± 0.1	2.6 ± -
Spots 4-8	48.3 ± 1.3	2.3 ± 0.2	1.8 ± 0.2	29.8 ± 1.0	6.9 ± 0.4	-	12.6 ± 0.8
Spots 9-11	51.0 ± 2.6	3.6 ± 0.8	2.6 ± 0.3	25.4 ± 0.7	7.7 ± 0.7	-	8.2 ± 0.8
Spots12-15	60.0 ± 2.5	-	7.1 ± 0.5	26.1 ± 1.7	6.8 ± 0.7	-	-
Spots 16-20	55.4 ± 2.7	3.3 ± 0.7	2.1 ± 0.3	19.1 ± 1.0	6.3 ± 1.3	1.9 ± 0.3	11.8 ± 0.7
Spots 21-23	58.0 ± 1.4	1.7 ± 0.0	7.0 ± 0.7	26.7 ± 0.7	7.7 ± 0.4	-	-
Spots 24-30	57.6 ± 2.1	1.9 ± 0.1	-	27.8 ± 1.2	4.5 ± 0.4	8.7 ± 0.5	-

Figure 5.9 SEM picture and corresponding EDX data (average of labelled spots) for an ISG monolith altered for 721 days in YCWCa at 70 °C. Phases are labelled according to chemical composition, and as informed by XRD analysis.

FIB-sections prepared from monoliths withdrawn from YCWCa solution after 721 days of dissolution at 70 °C were analysed by TEM, as shown in Figure 5.10 Figure 5.11 . The scalloped altered layers identified in SEM were also observed at this scale; the band closest to the glass surface was Band 1 (Figure 5.10). Each of the layers was composed of Ca, Zr, Al, K, O and Si, and there was no change in relative concentration of each element within each band (see Figure 5.12). Therefore the observed differences in intensity in the dark field (DF) and secondary electron (SE) images (Figure 5.10) can be attributed to variations in the void volume (i.e. porosity) in each band.

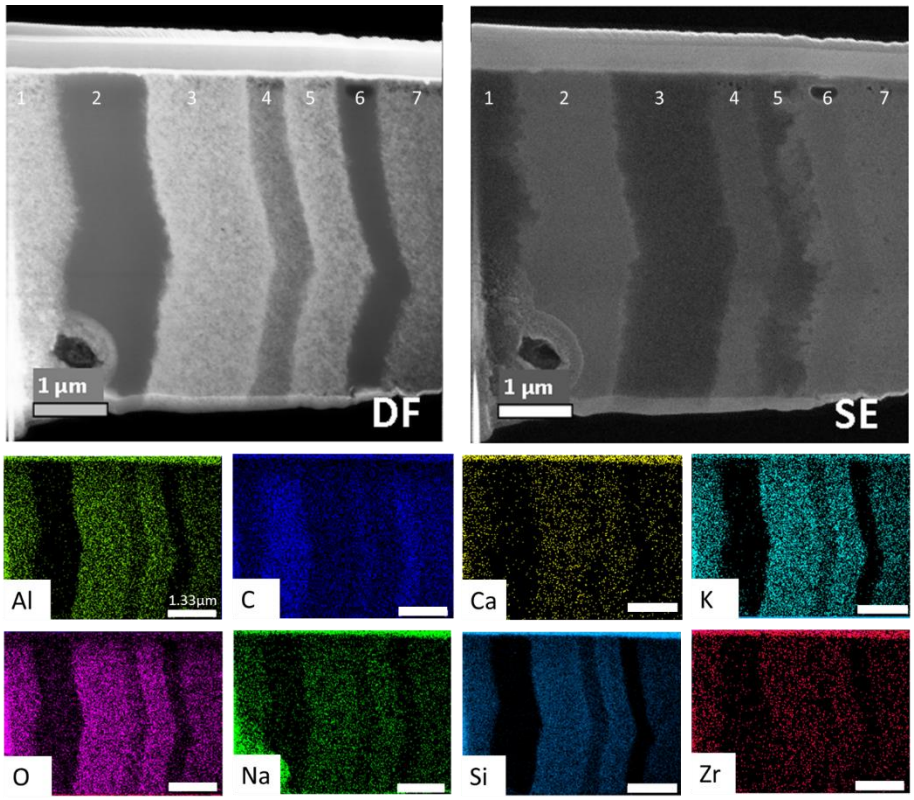

Figure 5.10 Scanning Transmission Electron Microscopy (STEM) dark-field scanning TEM (DF STEM) and Secondary Electron STEM images and energy-dispersive spectroscopy images of a focused ion beam (FIB) section removed from a monolith of ISG leached for 721 d at 70 °C. Individual STEM-EDX images are provided for Al, C, Ca, K, O, Na, Si, and Zr. The middle section of the alteration layer is shown; Band 1 is located closest to (but not in contact with) the bulk glass, and Band 7 is towards (but not in contact with) the solution. Bands 2 and 6 are filled with epoxy resin.

Higher magnification TEM images (Figure 5.11) confirmed the existence of microstructural variation between the bands; each of the layers exhibited a "speckled" pattern of apparently different porosity. This type of porosity may be attributed to the presence of individual silica spheres[32], and the corresponding interstitial space between these spheres; this has been previously observed in the post-nucleation ripening of silica gels[161,129]. It is well understood that the combined influence of high pH and the presence of cationic species can influence polymerisation of Si-OH gels; at high pH values, the negatively charged silica species, $Si(OH)^{3-}$ and $Si(OH)_2^{2-}$, experience repulsion due to their negative charge, which prevents aggregation and gives rise to large interstitial pores between poorly aggregated silica. However, the presence of other cationic species can compensate for this charge, allowing aggregation and gel formation. The data shown in Figure 5.10 indicate that the cations Ca, K, Na and the anions Si, Al and Zr contributed to the formation of an alumino-alkali-silica gel at the surface of ISG reacted in YCWCa solution. Since

the layers were not found to change significantly in composition, the small variations in pH, which would influence the silica aggregation process and the resulting size of the silica spheres, may be the cause of the varied porosity.

Image analysis, using grey scale thresholding and assuming a constant composition, gave an average pore radius across the whole layer, ranging from 7 – 15 nm, somewhat higher than observed in similar glasses at lower pH. For example, the R7T7 glass was reported to have an altered layer porosity of ~2 nm in static leaching conditions at pH 7 – 9.36 pores of 5 nm were measured for SON68 at pH 9.37 and pores of ~1 µm were observed in LAWB45 glass[165]. However, our results are in excellent agreement with Ferrand et al.[54], who measured a pore radius size of 10 nm for SON68 reacted in cement water[54]. Diffraction patterns obtained using Selective Area Electron Diffraction (SAED; Figure 5.11) revealed each of the bands to be amorphous.

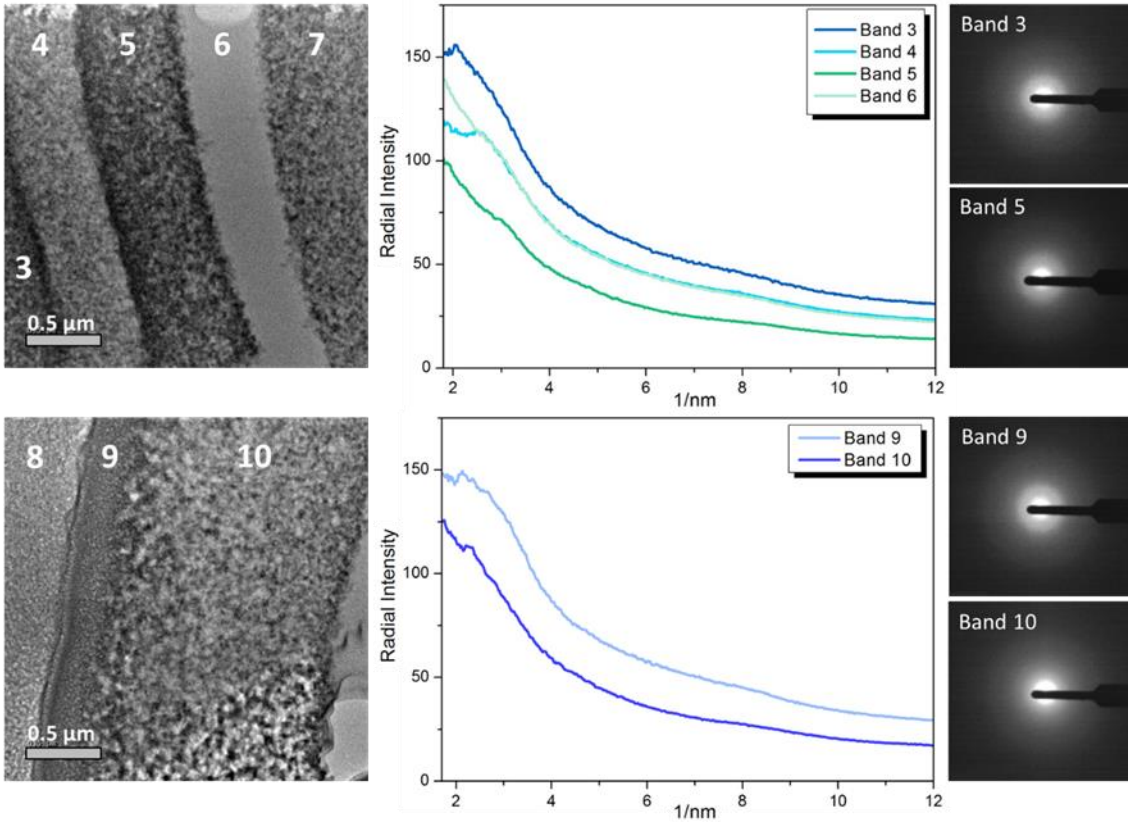

Figure 5.11 Transmission Electron Microscope images of ISG reacted in YCWCa for 721 d at 70 °C, showing the variation in porosity of the different bands (numbered 3 to 10) in the alteration layer, with the corresponding SAED patterns.

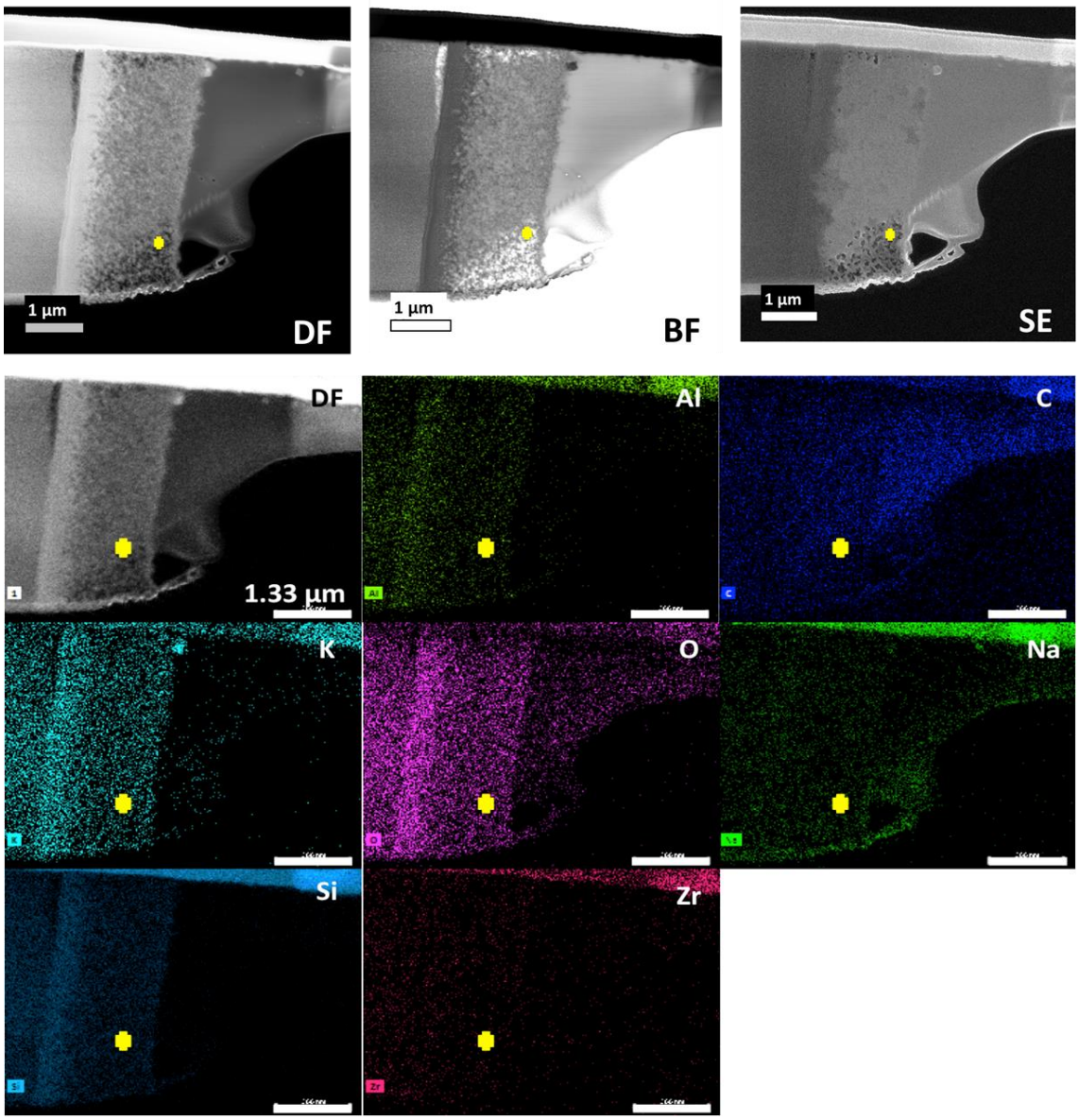

Figure 5.12 Transmission electron microscopy dark field (DF), bright field (BF) and secondary electron (SE) images, and EDX maps of ISG reacted in YCWCa for 721 days at 70 °C showing a lack of significant difference in chemical composition over the band. The observed contrast difference in the bright-field and dark-field images is attributed to the presence of void space (i.e. porosity); the secondary electron image near the yellow region illustrates the presence of irregular shaped craters on the surface of the sample that result in the observed image contrast. These irregular shaped craters are distributed throughout the thickness of the band and represent features that cause the image contrast, which corresponds to void space (porosity) in the band.

5.3. Discussion

5.3.1. Mechanism and kinetics of ISG dissolution in YCWCa solution

The dissolution of ISG in YCWCa can be described by two key stages: 1) the formation of a porous, Zr-containing alkali alumino-silica gel, during which time rapid dissolution occurs; and 2) the precipitation of a crust of zeolite and phyllosilicate crystalline phases. The latter were only observed at 70 °C once the dissolution rate had slowed. In both stages, the high pH and the composition of the cement leachate solution was found to exert a significant influence on the dissolution behaviour, as described below.

5.3.2. Alkali alumino-silica gel formation.

As discussed previously, polymerisation of silicic acid by condensation reactions results in nucleation of a porous gel that becomes more dense as reorganisation and Ostwald ripening takes place[129,25,166]. The TEM data presented in this study, which showed a speckled, porous morphology, provides compelling evidence that an alkali alumino-silica gel is formed at the surface of ISG leached in cementitious solution, where the high pH of the leachate solution causes repulsion among the negatively charged silica particles, negatively influencing the polymerisation of silica anions, and forming large interstitial pores between silica gel particles. Our results, in agreement with those for SON68 at high pH[54], and also for ISG, where the void fraction of the gel was found to increase as a function of increasing pH[51], indicate that the pore radius of the gel at the pH of the cement leachate investigated (pH(RT)13.5) is approximately twice the size of that in gels formed in circum-neutral pH solutions. Consequently, the calculated B diffusion coefficients in the present study were 2 to 4 orders of magnitude higher than those of ISG in Si saturated solutions, demonstrating the dramatic influence of YCWCa solution on ISG dissolution[160].

The chemical composition of the solution clearly had a significant influence on the formation of the alteration layers. The uptake of K, Ca, Na, Zr and Al into the silica gel indicates that the alteration layer was in equilibrium with the solution, and is evidence that solution cations were readily transported into the open pore network of the gel layer. Alkali / alkali-earth cation incorporation into the gel layer is likely driven by charge compensation for anionic species in the silica gel. For example, recent studies by Collin et al.[45] showed that Ca is the preferred charge balancing cation for $[AlO4]^-$ units in the gel of ISG at pH 7.

The presence of these cations has an apparently detrimental effect on the glass alteration (e.g. higher diffusivity than observed for the same glass at circumneutral pH)[160]. Previous studies have shown that in the presence of the alkali species, Na and K, the rate of quartz dissolution was significantly enhanced[140]. This was attributed to the fact that these elements have a high frequency of solvent exchange (the rate at which primary solvation waters of a cation exchange with the surrounding aqueous environment) than the other alkali / alkali earths, which increases the frequency of silica hydrolysis and thus the rate of dissolution[140]. It follows that in the presence of Na and K, under the high pH conditions experienced by the ISG in this investigation, the rate limiting step of dissolution was the breakage of Si-O-Si bonds. This is in agreement with previous studies of the UK nuclear waste simulant, MW25, at high pH, where investigation of dissolution rate parameters at pH(RT) 8, 10 and 12 showed incongruent leaching of Si when compared to Na and B[28]. Since Ca has a much lower frequency of solvent exchange, it is less likely to enhance the dissolution rate of glass than K or Na, but nevertheless, due to its divalent charge, it is a more efficient charge balancing cation than the alkali elements, and is thus incorporated readily into the gel, as seen in numerous previous studies.e.g.[23,52–55,59,61,70,167]

At 30 °C, the glass dissolution mechanism appeared to change upon the consumption of Al from the solution (at 160 days, Figure 5.3); at this time the dissolution rate could no longer be modelled with a diffusion term, but rather by an affinity-type model with the affinity term (i.e. saturation of Si) removed. One possible explanation for this behaviour could be as follows: the incorporation of Na, K and Ca in the gel (to charge compensate negatively charged Si, Al and Zr species) gave rise to a diffusion-controlled dissolution rate until the gel layer became positively charged (i.e., it contained an excess of K, Na and Ca required to charge balance $[AlO4]^-$, $[ZrO6]^{2-}$, $Si(OH)^{3-}$ and $Si(OH)_2^{2-}$units). At this time (160 days), dissolved $[AlO4]^-$ species in solution were attracted to the gel layer, but since there was no further Ca^{2+} in solution to provide charge balance these anions (Figure 5.3), the less efficient charge balancing cations, K^+ and Na^+, provided charge balance. In the presence of K and Na at high pH, the aluminosilicate species, $(OH)_a AlOSiO_n(OH)_{(3-n)}^{(n+1)}$, where n = 1 to 3, has been shown to precipitate not as a nano-sized gel, but rather as much larger granules[168]. It is possible that the change in dissolution rate observed at 30 °C and 160 days, when Al was incorporated to the gel, was the result of the precipitation of poorly charge-balanced aluminosilicate species, which, due to their granular nature, gave rise to the presence of large voids (or a more open pore network) in the gel layer, allowing for rapid dissolution. This hypothesis requires experimental validation, but does not seem implausible since it has been previously shown that $[ZrO_6]^{2-}$ may become incorporated in silica gel formed on ISG when

leached at high pH[70,167] inhibiting restructuring of the gel layer, enhancing porosity and thus increasing dissolution[96,169].

From the results presented here, it is not possible to discern the individual effects of high pH and cation incorporation in the silica gel layer on the development of porosity and the enhancement of dissolution rate, but it is evident that both play a significant role in maintaining an open pore network through which solution and glass species can be transported. Although the inclusion of a K-bearing alkali-silica gel improved the geochemical model fit, it is clear that the other cations present also participated in gel layer formation; further studies should be directed at elucidating the relative roles of the alkali and alkali-earth cations on gel layer formation and glass dissolution.

5.3.3. Secondary Phase Precipitation

At 70 °C, the extent of dissolution of ISG was greater than at 30 °C (e.g. the AGF was 11 ± 1 % and 41 ± 1% for 30 °C and 70 °C, respectively) and the release of elements could be modelled with an affinity-based model, accounting for the precipitation of the zeolite phase, phillipsite-K, and also for C-S-H (Figure 5.3). In contrast with previous studies of ISG dissolution at high pH[70,167], and our own geochemical modelling, there was no evidence for C-S-H precipitates. Their absence is due to the low Ca concentration in solution and the propensity for Ca incorporation into silica gel[140]. Zeolite and phyllosilicate phases were precipitated on the outside of the alkali alumino-silica gel, indicating that gel formation preceded precipitation of secondary phases. Previous studies of ISG leached in water show no secondary precipitates[167], thus highlighting the significant role of solution species, particularly the alkali and alkali earth elements in cement water, and pH in the alteration of glasses.

Comparing the Al dissolution data for 30 °C and 70 °C, it is clear that at 30 °C, where no zeolites were observed to form, significant quantities of Al remained in solution (albeit decreasing towards the end of the experiment), while at 70 °C, almost all of the Al had been consumed from solution. Despite this, the Al/Si ratio of the gel layer at 70 °C was significantly lower than at 30 °C (0.04 compared with 0.22, respectively; the Al/Si ratio in the bulk glass was 0.12). As such, it may be concluded that the zeolite and phyllosilicate phases formed at 70 °C were nucleated from the gel layer, as proposed by previous studies[170, 171]. This is in agreement with the hypothesis presented above; if Al was weakly bound to the gel layer as large granules of aluminosilicate, it may have provided a ready source for the formation of secondary phases. The other alkali / alkali-earths within the gel layer were found as major zeolite- and phyllosilicate-forming elements, however

since they were present in high concentration in solution (particularly Na and K), the source of these elements could be the solution or the gel.

The consumption of Al from the gel to form zeolites has previously been related to the onset of glass alteration resumption (or Stage III dissolution behaviour)[170,171], as has a reduction in the pH of the solution, also seen in the present study at 70 °C (Figure 5.1). Although we do not observe a resumption in alteration, it is possible that given more time, the consumption of Al from the gel layer, and alkali / alkali earths from the solution or gel, forming zeolites and phyllosilicates may destabilise the gel to the extent that rate resumption is observed. It is important to note that the influence of cation species in the gel layer on rate resumption is not well understood; from the data presented in the current study it can be postulated that the presence of these elements does not appear to stabilise it entirely.

Chapter 6. Dissolution of Simulant Nuclear Waste as a Function of Evolving Cement Leachate Chemistry

6.1. Introduction

Being able to predict the long term durability of nuclear waste glass in a disposal environment is a requirement for the safety case for disposal in the UK. Research to date has focused on better understanding of the mechanisms for glass corrosion at early stages of water ingress, or by simulating porewaters of different ages and examining their effects individually. For example, work at SCK.CEN and in the previous chapters of this thesis have investigated the impact on glass dissolution of synthetic cement waters with compositions of Portland cement porewaters representative of different ages.

Although an understanding of the effects of individual cement pore solutions is informative to models of glass corrosion, there have been no studies to date aimed at elucidating the effects of an evolving cement porewater chemistry on glass dissolution, i.e., going from young to old cement leachates, followed by dilute groundwater, more representative of the geochemical conditions in a cementitious geological disposal facility in the long term. Therefore, this Chapter aims to investigate the dissolution behaviour of three glasses MW25, LBS and ISG as they are sequentially moved through a series of synthetic cement water solutions, simulating the effect of cement porewater ageing. Samples were moved, after 28 days, from an evolved cement water (ECW) solution to an old cement water (OCW) solution and then finally to a synthetic granitic groundwater (GW) solution.

A schematic of the sequential test is outlined in Figure 6.1. The glass monoliths remained in the original test vessel, and solutions mimicking aging cement leachates were added. The vessel was sealed and placed in an inert atmosphere at 50 ^{o}C for 28 days. After this time, the solution was removed, prior to addition of the next solution in the ageing scheme. All sampling and solution handling was conducted in an inert atmosphere glove box to prevent carbonation.

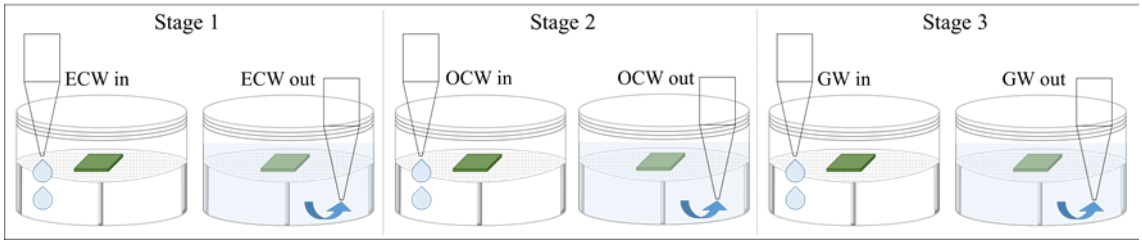

Figure 6.1 Schematic of sequential dissolution test, the monoliths remained in the original test vessel, and solutions mimicking aging cement leachates where added, the vessel was sealed and placed in an inert atmosphere at 50 ^{o}C for 28 days after which the solution was removed and aliquots taken, and the next solution added to the test vessel and placed back in the oven, and repeated once more for the GW solution.

6.2. Results (Sequential dissolution of MW25, LBS & ISG in an evolving system)

6.2.1. pH

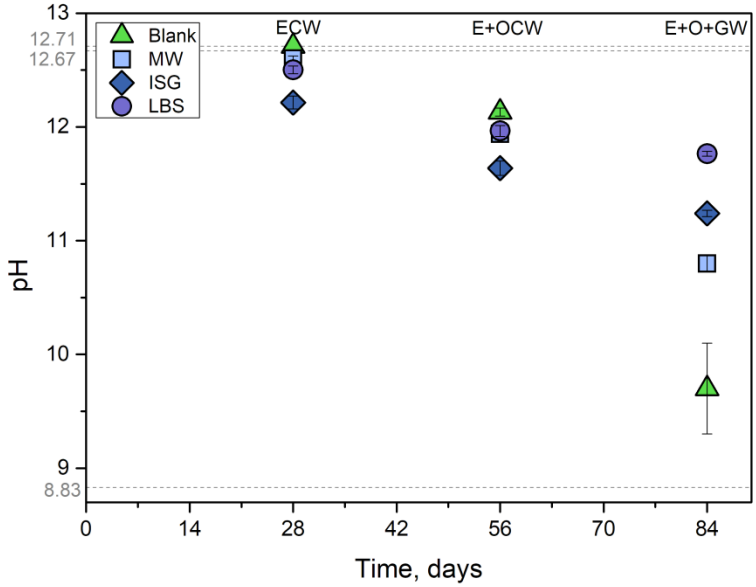

Figure 6.2 Average pH(RT) of sequential dissolution test, of glass powders MW25, LBS and ISG exposed to ECW for 28 days followed by exposure to OCW for a further 28days and finally a step involving granitic groundwater for 28 days. Dashed lines indicate the pH(RT) of the initial solutions ECW = 12.71, OCW= 12.67 and GW= 8.83

As Portland cement ages, the pH of the pore solution diminishes. The same is true of the synthetic cement water solutions utilised in this test; the initial pH of the blank solutions are outlined in Figure 6.2. The pH(RT) of ECW was 12.7 ± 0.3 and upon addition of glass monoliths (data not shown), the pH(RT) remained close to 12.7. When powdered glass samples were added (Figure 6.2), the pH(RT) reduced to 12.6 ± 0.02 for MW25, 12.5 ± 0.03 for LBS and 12.22 ± 0.06 for ISG.

On day 28, the ECW solution was removed from the test vessels, and OCW solution was added, altering the pH and solution chemistry of the leachate in contact with the glass as follows: solutions containing MW25 powders had a pH(RT) of 11.94 ± 0.05, solutions containing LBS powders had a pH(RT) of 11.97 ± 0.05, and solutions containing ISG has a pH(RT) of 11.64 ± 0.06. The pH of the monolith samples averaged at pH(RT) 12.3 ± 0.27. On day 56, the OCW solution was removed from the test vessel and a granitic GW solution was added. The initial pH(RT) of the GW solution was 9.7 ± 0.4 in the blank, and when it came into contact with MW25 glass powder, the pH increased to pH(RT) 10.8 ± 0.07, to pH(RT) 11.77 ± 0.02 with LBS powders,

and with ISG powder, the pH increased to pH(RT) 11.24 ± 0.03. The monoliths averaged a pH(RT) of 10.13 ± 0.02 outlined in Table 6.1.

Table 6.1 pH(RT) data from sequential tests for both monoliths and powder static leaching

Solution	ECW	E + OCW	E + O + GW
Time, days	28	56	84
Blank pH(RT)	12.70 ± 0.03	12.13 ± 0.04	9.70 ± 0.40
Monolith			
MW25	12.70 ± 0.01	12.70 ± 0.05	10.12 ± 0.10
LBS	12.68 ± 0.05	12.23 ± 0.11	10.16 ± 0.10
ISG	12.70 ± 0.01	12.22 ± 0.01	10.12 ± 0.10
Powder			
MW25	12.60 ± 0.02	11.94 ± 0.05	10.80 ± 0.07
LBS	12.50 ± 0.03	11.97 ± 0.05	11.77 ± 0.02
ISG	12.22 ± 0.06	11.64 ± 0.06	11.24 ± 0.03

6.2.2. Normalised mass loss during sequential dissolution for MW25, LBS & ISG

Aliquots were removed on days 28, 56 and 84 when the solutions were changed. Figure 6.3 describes the normalised mass loss of elements from MW25, LBS and ISG glasses leached in the three sequential, synthetic solutions. With a reduction in pH it would be expected that the normalised mass loss of elements from the glass would reduce.

Boron was used as the tracer element in this test as it is present in all glasses. In the ECW solution, ISG was the least durable glass, as evidenced by a NL_B value of 1.24 ± 0.14 g m^{-2}. The MW25 and LBS glasses gave similar NL_B values of 0.53 ± 0.09 and 0.48 ± 0.05 g m^{-2}, respectively. When the ECW solution was removed and replaced with OCW solution, the mass loss of B was similar for all three glasses at ~ 0.3 g m^{-2}, however upon replacement of OCW solution with GW solution, the NL_B values diverged; the NL_B of MW25 increased significantly, while in LBS it increased a little. For ISG, the NL_B decreased further in comparison to the previous solution in the sequence. The NL_{Li} data for MW25 and LBS followed the same trend as that observed for NL_B.

With the evolving leachates ISG displayed a decrease in the amount of Na released from the glass into solution, LBS exhibited a decrease when the ECW solution was exchanged for OCW, but the amount of Na released into solution increased by 21% with GW in the test vessels. MW25 increased the amount of Na released into solution with each change of the leachate.

The NL_{Si} showed that as the leachate evolved, the amount of Si leached from ISG reduced with time, however the opposite was observed for MW25 and LBS glasses. It is possible that the Si-gel layer that formed on ISG in the ECW was sufficiently dense to restrict the transport of soluble elements Si, Na and B (Figure 6.16 exhibits the alteration layers formed on ISG). The behaviour of a simplified glass is significantly different from a complex simulant waste glass.

In general, it appears that when the leachate was changed from ECW solution to OCW solution, the glass corrosion reduced (as determined by NL_i). However, introduction of the granitic groundwater resulted in rapid corrosion and the elements B, Li, Na and Si all increased in concentration in solution, except for ISG. It is worth noting that the Al levels remained low in all solutions and decreased with time and evolving leachates.

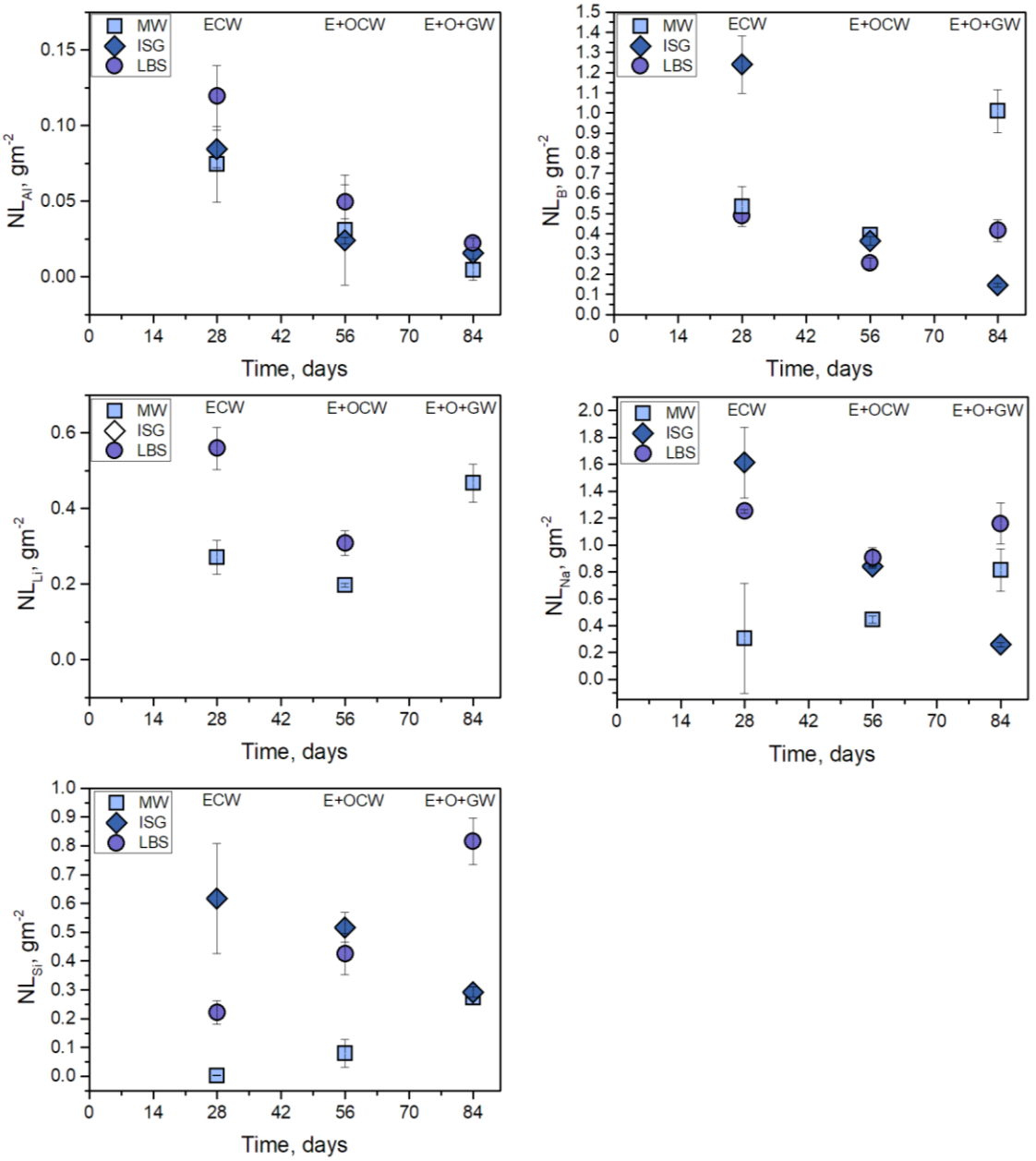

Figure 6.3 Normalised mass loss from sequential dissolution of glass powders MW25, LBS and ISG exposed to ECW for 28days followed by exposure to OCW for a further 28days and finally a step involving granitic groundwater for 28 days.

Figure 6.4 depicts the concentration variations of Ca, K, Mg and S in solution. The source of K and S are the leachates, Ca is present in both the glasses and leachates and Mg is present in the MW25 and LBS glass and GW leachate. The concentration of Ca and K decreased as the leachate evolved. The blank GW solution contained 6.00 ± 0.19 mg L^{-1} of Mg and when contacted with glass powder the Mg concentration significantly decreased. This may be due to precipitation of brucite ($Mg(OH)_2$) due to the high pH, or due to the precipitation of alternative Mg-bearing phases; XRD (Figure 6.5) confirms the latter through the identification of hydrotalcite. When

comparing concentrations of Ca in the blank, it is apparent that in the presence of the MW25 and LBS glass compositions Ca concentrations rapidly decreased (perhaps due to precipitation of Ca-Si bearing phases), while the decrease was far less pronounced for ISG. Similarly, in the final solution of the sequence (GW), the presence of ISG resulted in a greater decrease in the concentration of K than for the MW25 glass (which had a similar K concentration as the blank), indicating that K plays a more important role in the alteration layer formation of ISG than MW25 and, to a lesser extent, LBS.

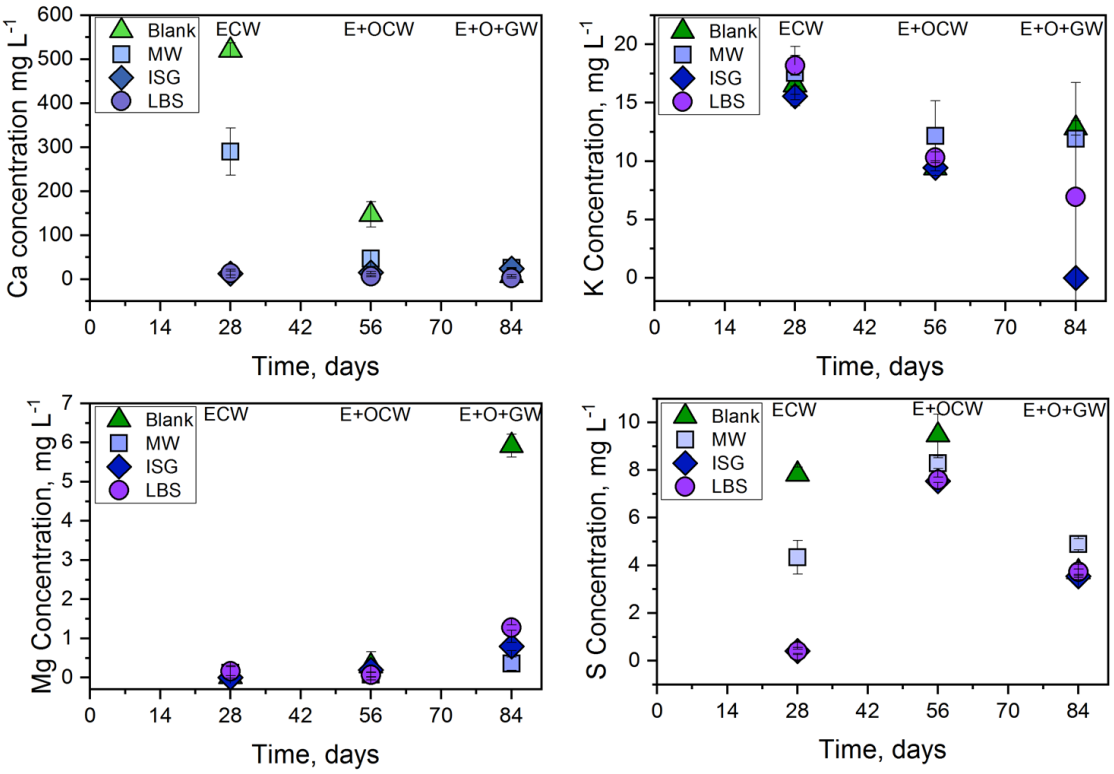

Figure 6.4 Concentration of elements in the blank solutions and solutions contacted with MW25, ISG and LBS glass powder. The only source of K and S are the leachate solutions, Ca is found both in the glass and solution, the Mg content in the ECW and E+OCW solutions was close to 0 mg L^{-1} the concentration of Mg in the blank GW solution was 5.9 mg L^{-1}.

6.2.3. Alteration layer formation on MW25 glass

The x-ray diffraction patterns of MW25 glass monoliths are shown in Figure 6.5. Exposure to ECW solution lead to the formation of calcite ($CaCO_3$; PDF 00-001-0837), C-S-H ($CaOSiO_2H_2O$; PDF 00-033-0306) and hydrotalcite ($Mg_6Al_2CO_3(OH)_6 \bullet 4(H_2O)$; PDF 00-014-0191); these phases remained present when the monolith was exposed to OCW and GW solutions, however the intensity and crystallinity changed with time and solution composition. In the ECW solution, hydrotalcite was the major phase and a broad peak observed at 32° 2θ was indicative of the presence of C-S-H. In the OCW solution, the hydrotalcite peaks reduced in intensity and C-S-H was the major phase; the bottom of the C-S-H peak at 32° 2θ was broad and after dissolution in the GW, this narrowed, indicating a development of crystallinity.

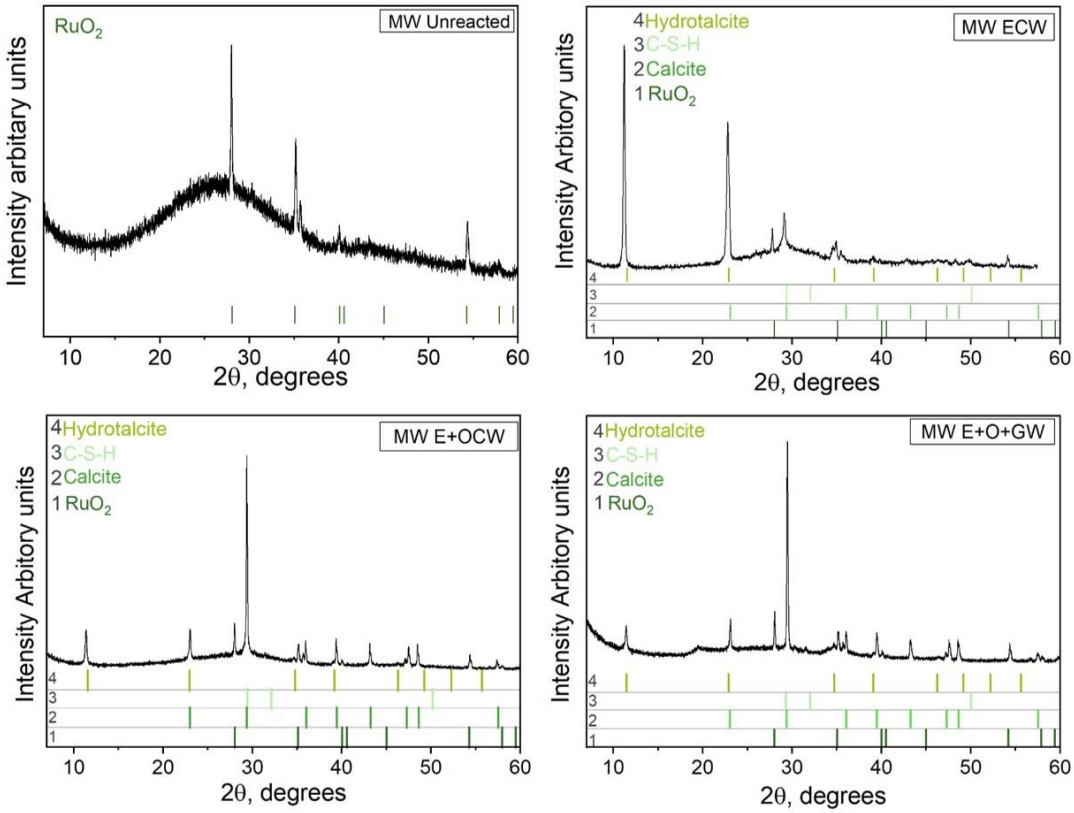

Figure 6.5 Diffraction patterns of MW25 monoliths exposed to ECW for 28 days, subsequently to OCW for 28 days and subsequently to GW for 28 days.

The alteration layers that developed on the surface of MW25 glass monoliths appeared different after exposure to each synthetic solution. Due to unforeseen sampling issues, it was not possible to image the monolith that moved from the ECW to OCW solutions at 28 days; instead, Figure 6.6a shows a monolith exposed to ECW for six months (hence the thick alteration products

present). The surfaces of MW25 leached in OCW for 28 days and then GW for an additional 28 days are shown in Figure 6.6b and c, respectively.

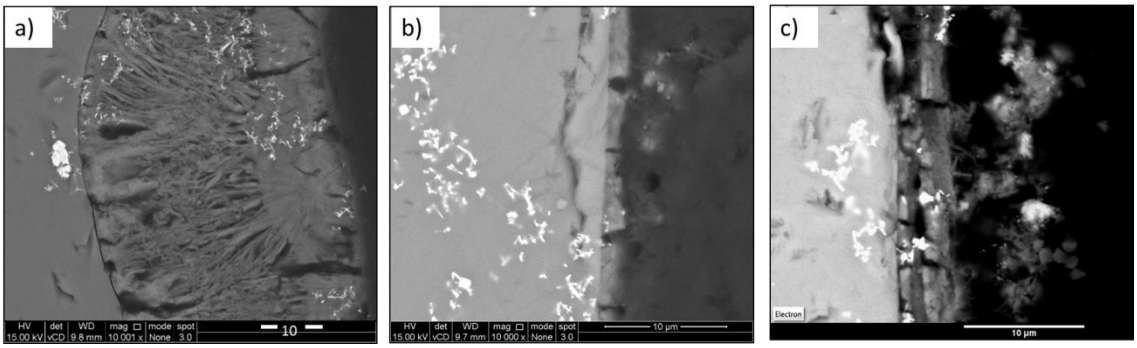

Figure 6.6 SEM images of a) MW25 exposed to ECW for 6 months, b) MW25 monolith exposed to ECW for 28 days followed by 28 days in OCW, c) MW25 monolith exposed to ECW for 28 days, followed by OCW then GW for 28 days each.

i. MW25 glass dissolution in ECW solution

The total thickness of the layers formed on the surface of the MW25 monolith (Figure 6.7) was 40.50 ± 2.85 µm after 6 months of dissolution in ECW solution. The whole alteration layer was rich in K and Zr and also contained Na and Al. It was possible to distinguish two regions from the elemental mapping: the first (Layer 1), adjacent to the glass, was rich in Mg compared to the bulk glass and the outer layer (Layer 2). The Mg-rich areas included needle-like phases that also contained Si, K, Fe and Ca. The Mg:Si ratio was 1.14, and the Ca:Si ratio was 0.53 (Layer 1 Spot 10). Layer 2, on the outer region of the alteration layer, was enriched in Ca, K and Si and also contained elevated concentrations of Mg (with respect to the bulk glass). The Ca:Si ratio in this region was 0.42. It is possible that Layer 2 acted as an outer rim, as the features in Layer 1 appear to originate from Layer 2 and grow towards the bulk glass. This complex alteration layer appears to comprise a mixed alkali- / alkaline-earth silica gel, in addition to precipitate phases comprised of multiple elements.

Table 6.2 SEM EDS spot maps associated with (Figure 6..7)average elemental compositions at % of each alteration layer on the surface of MW25 monolith after 6 months leached in ECW.

Element Avg At %	Si	Fe	K	Al	Mg	Na	Ca	Zr	Other
Bulk glass (1)	50.67 ± 1.05	2.44 ± 0.25	0.13 ± 0.19	12.64 ± 0.02	7.19 ± 0.15	12.77 ± 2.34	6.82 ± 0.50	0.61 ± 0.33	7.05 ± 3.39
Layer 1 (10)	21.78 ± 2.23	7.23 ± 0.96	12.10 ± 0.38	5.98 ± 0.47	24.83 ± 0.76	3.39 ± 1.72	11.73 ± 1.20	2.12 ± 0.31	9.09 ± 7.88
Layer 1 (14)	29.19 ± 0.20	7.06 ± 0.04	12.48 ± 0.09	5.96 ± 0.16	23.23 ± 0.41	3.15 ± 0.29	9.24 ± 0.92	2.65 ± 0.11	5.02 ± 1.07
Layer 1 (7)	24.68 ± 0.73	8.64 ± 0.70	11.12 ± 0.41	7.89 ± 0.58	27.16 ± 0.99	3.50 ± 0.43	11.41 ± 0.74	2.24 ± 0.22	2.68 ± 0.64
Layer 2 (4)	36.57 ± 5.04	5.82 ± 1.16	15.25 ± 1.87	3.19 ± 0.59	13.10 ± 5.29	3.63 ± 0.45	15.42 ± 1.53	1.92 ± 0.54	2.44 ± 0.71

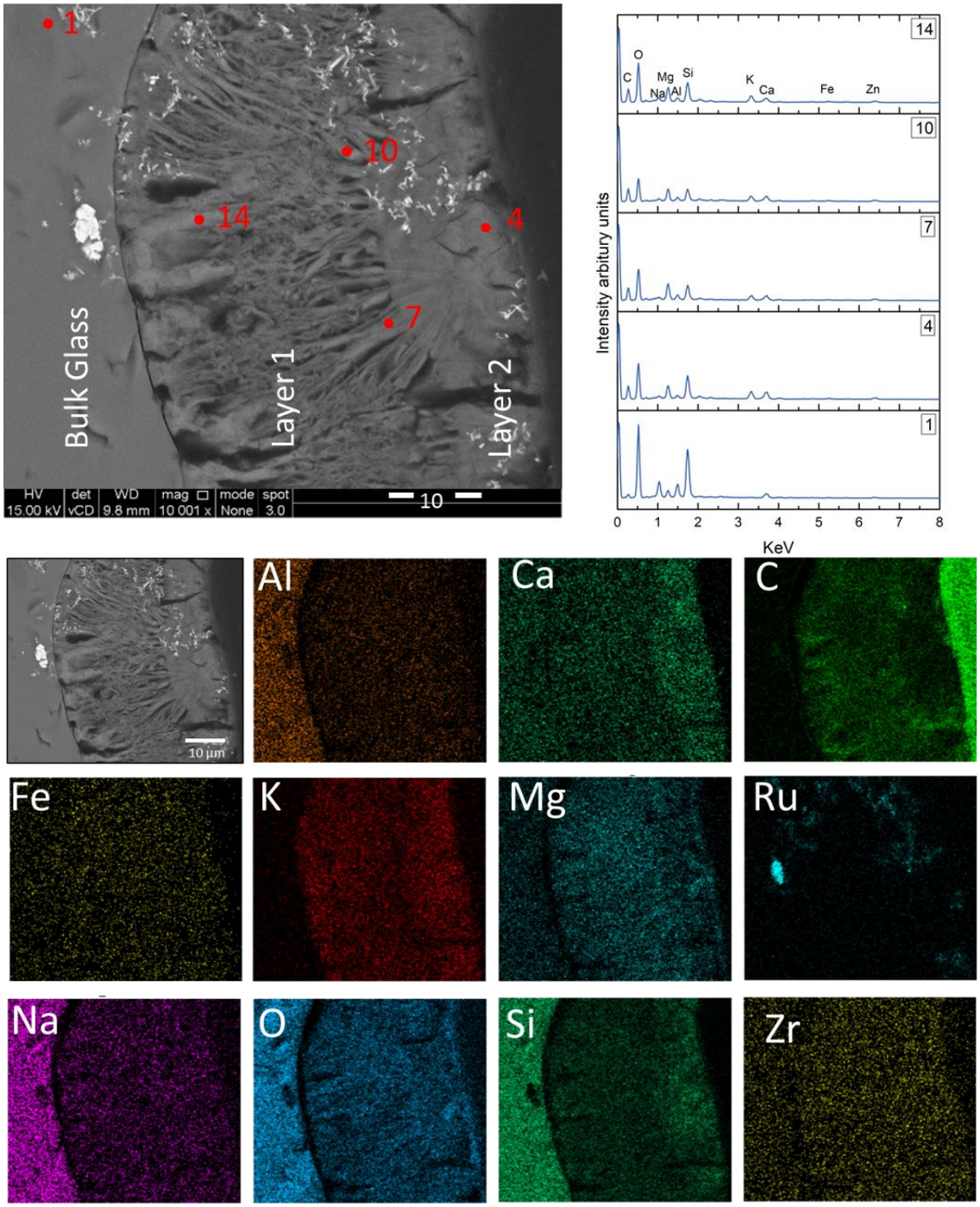

Figure 6.7 SEM elemental spot map of MW25 monolith exposed to ECW for 6 months EDS spot maps

ii. MW25 dissolution in ECW+ OCW solution

The SEM image shown in Figure 6.8 depicts the alteration products on a monolith of MW25 glass after exposure to ECW for 28 days followed by 28 days in OCW. There are two distinct alteration products: Layer 1 had the same composition as the bulk glass (Table 6.3) suggesting that this region is an area of broken glass at the surface of the monolith. The elemental analysis of Layer 2 identifies depletion of Al, Mg and Na with enrichment of Ca relative to the bulk glass. The total thickness of this layer, identified as Ca-silica gel (Layer 2) was 1.43 ± 0.24 µm and had a Ca:Si ratio of 0.28. Residing on the surface of the Ca-silica gel were clusters of precipitates identified by grey scale variations on the BSE micrograph. Elemental maps confirm that these contain Ca and Mg and are likely precipitated phases. Significantly, there appears to be little or no K in the altered layers, indicating that the K incorporated in alteration layers in ECW solution had been leached, or otherwise redistributed. An alternative explanation may be that the K incorporation into alteration layers in the sample exposed to ECW in Figure 6.6 (for 6 months) requires longer time scales than 28 days to be achieved.

Table 6.3 SEM EDS spot maps associated with Figure 6.8, average elemental compositions at % of each alteration layer on the surface of MW25 monolith after28 days leached in ECW followed by 28 days in OCW.

Element Avg At %	Si	Fe	K	Al	Mg	Na	Ca	Zr	Other
Bulk glass (32)	50.81 ± 2.46	2.21 ± 0.35	-	12.51 ± 0.48	6.87 ± 0.22	13.32 ± 0.47	7.51 ± 0.74	0.80 ± 0.07	1.34 ± 1.50
Layer 1 (35)	50.52 ± 0.85	1.84 ± 0.25	-	12.75 ± 0.45	7.42 ± 0.20	14.89 ± 1.04	6.37 ± 0.31	0.98 ± 0.26	1.22 ± 1.64
Layer 2 (38)	49.79 ± 0.78	3.42 ± 0.61	-	6.15 ± 0.69	3.77 ± 0.45	6.88 ± 1.16	14.10 ± 1.33	3.17 ± 0.65	2.18 ± 2.56

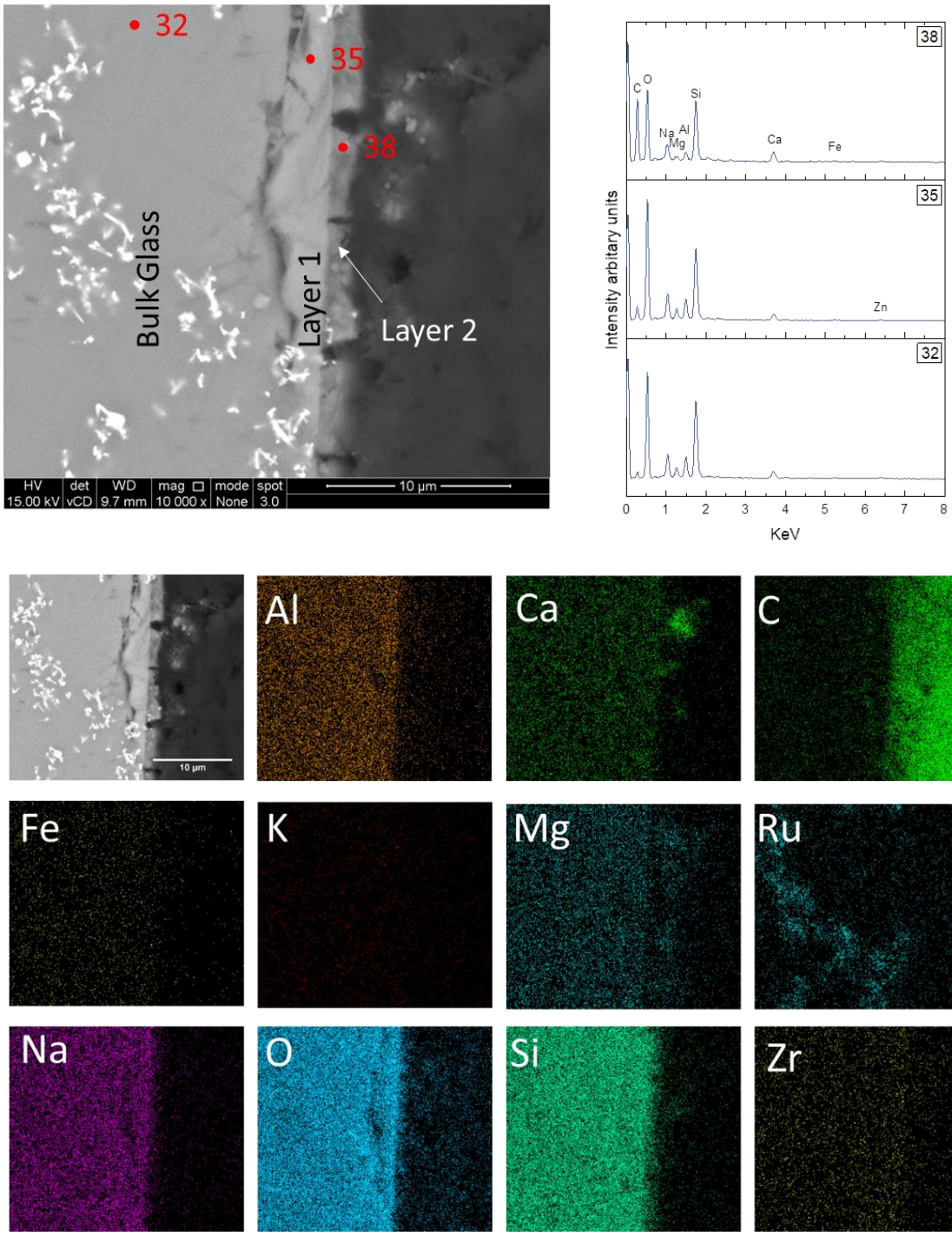

Figure 6.8 Elemental maps of MW25 monolith exposed to ECW for 28 days and subsequently moved into OCW for a further 28 days

iii. Dissolution of MW25 in ECW + OCW + GW solutions

Figure 6.9 depicts a BSE micrograph of an MW25 monolith after being leached in ECW solution followed by OCW solution, and finally a 28 day period in GW solution. Four layers were identified on the micrograph based on grey scale variations; EDS analysis identified slight variations in Mg content in the layers. Layer 1, in direct contact with the pristine glass, exhibited cracks perpendicular to the alteration layers. Such cracks are often associated with sample preparation. Layers 1 - 4 have compositions indicative of silica gels (Table 6.4), with Layers 1 and 3 containing twice as much Zr ~4 at % compared to Layers 2 and 3 with ~2 at %. Layer 2 was significantly depleted in Na compared to the pristine glass and Ca content was also reduced; Fe and Mg were enriched in this layer, which also contained Al. Layer 3 had reduced concentration of Al and Mg compared with the pristine glass, and elevated concentrations of Fe, Na and Ca compared to Layer 2. Finally, Layer 4 had the lowest Si content of the four gel bands, with an enrichment of Fe and Mg, with slight reductions in Al and Ca and significant reduction in Na compared to the pristine glass. Clearly, Mg, Fe, Zr, and to a lesser extent, Ca and Al were incorporated into this silica gel layer. Notable once again is the absence of K from the initial dissolution of MW25 in ECW.

The precipitates that formed on the surface of the gel layers can be categorised as follows: Precipitate 1 comprised deposits of C from the sample preparation; Precipitate 2 is the bright region identified by 'spot 34', which is identified as a Ca-rich particle (XRD analysis (Figure 6.5) recorded the presence of calcite ($CaCO_3$) and we attribute these particles accordingly); Precipitate 3 exhibited a large surface area and was abundant all over the sample – this is attributed to a Ca-Mg-Si containing precipitate with a Ca:Si ratio of 1.04 and a Mg:Si ratio of 0.7. Given the significant quantity of Al also present in this phase it is postulated to be the double layered hydroxide, hydrotalcite ($Mg_4Al_2(OH)_{14}.3H_2O$), which was identified by XRD analysis (Figure 6.5). The incorporation of Ca indicates that this is Mg/Ca variant of the hydrotalcite phase[172,173], or that a Ca-silica gel surrounds Mg-rich hydrotalcite.

Table 6.4 SEM EDS spot maps associated with Figure 6.9, average elemental compositions at % of each alteration layer on the surface of MW25 monolith after 28 days exposed to ECW and subsequently moved into OCW for a further 28 days and finally a GW solution for 28 days.

Element Avg At %	Si	Fe	K	Al	Mg	Na	Ca	Zr	Other
Bulk glass (17)	51.81 ± 0.60	2.29 ± 0.32	0.09 ± 0.06	12.66 ± 0.51	6.92 ± 0.20	12.39 ± 2.21	6.67 ± 0.43	0.85 ± 0.11	1.58 ± 2.13
Layer 1 (20)	45.17 ± 8.47	4.03 ± 0.75	0.04 ± 0.05	9.45 ± 1.00	6.03 ± 0.35	6.77 ± 0.94	4.97 ± 1.18	4.11 ± 1.33	3.89 ± 5.56
Layer 2 (23)	42.33 ± 9.27	5.60 ± 1.22	0.07 ± 0.21	9.76 ± 1.80	10.70 ± 1.38	2.95 ± 1.16	4.40 ± 0.93	2.84 ± 0.44	4.93 ± 3.97
Layer 3 (24)	42.73 ± 1.86	6.14 ± 0.29	-	8.74 ± 0.79	6.90 ± 0.63	4.10 ± 0.53	6.37 ± 0.46	3.52 ± 0.39	4.33 ± 2.77
Layer 4 (28)	40.15 ± 1.29	4.99 ± 0.11	-	10.58 ± 0.91	11.90 ± 2.32	2.69 ± 0.36	6.19 ± 0.67	1.97 ± 0.14	3.93 ± 2.42
Precipitate1 (40)	29.90 ± 9.29	-	0.76 ± 1.22	0.37 ± 4.23	12.73 ± 9.18	9.58 ± 4.49	3.02 ± 1.97	-	14.79 ± 11.90
Precipitate2 (34)	5.59 ± 5.59	-	0.09 ± 0.09	2.51 ± 2.51	6.10 ± 6.10	0.50 ± 0.50	82.09 ± 82.09	0.02 ± 0.02	0.72 ± 0.01
Percipitate 3 (37)	26.80 ± 11.21	3.02 ± 1.71	-	11.23 ± 5.13	18.81 ± 8.00	2.17 ± 0.56	28.10 ± 26.37	0.20 ± 0.30	2.83 ± 1.59

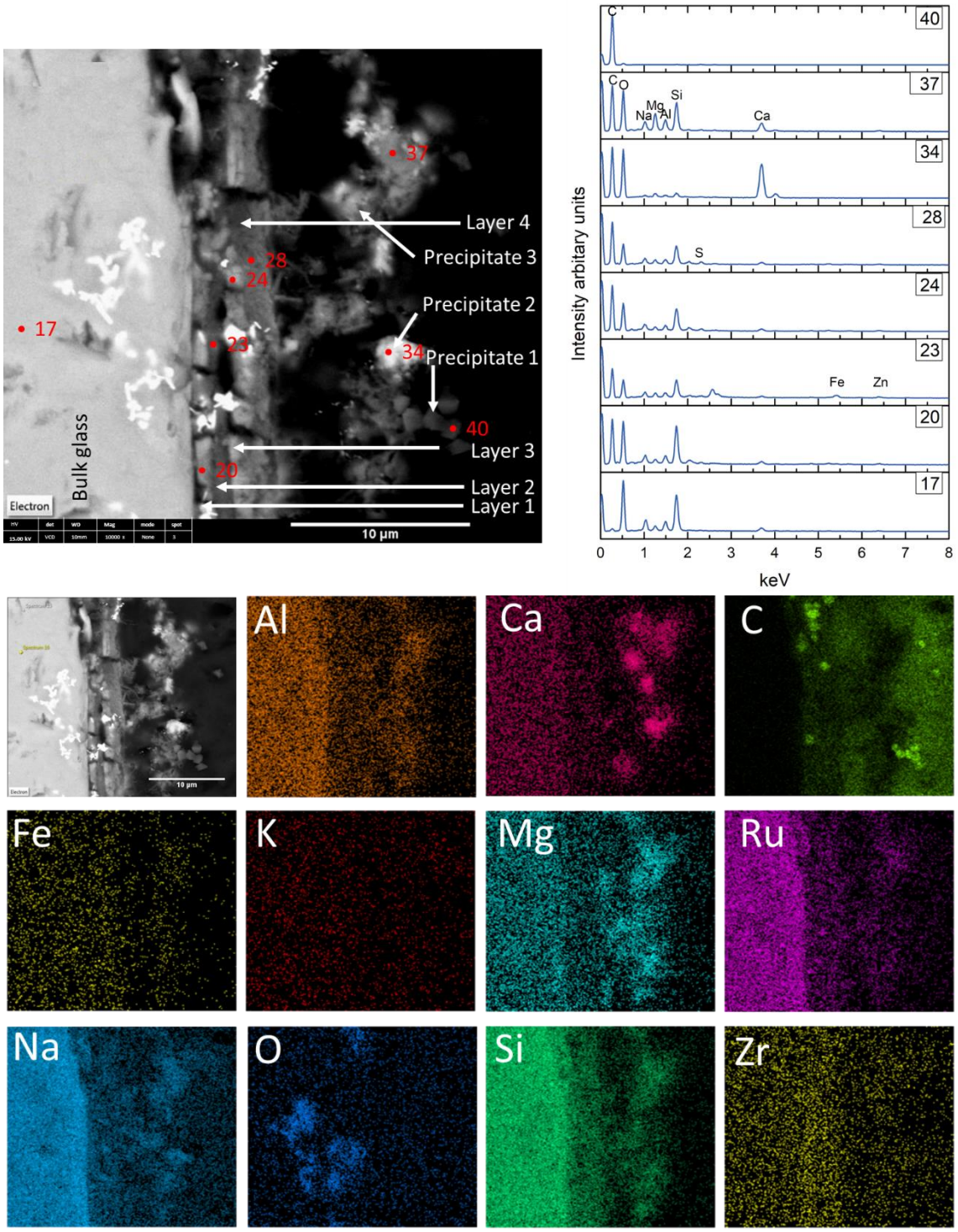

Figure 6.9 Elemental maps of MW25 monolith exposed to ECW for 28 days and subsequently moved to OCW for a further 28 days and finally leached in GW for 28 days.

6.2.4. Alteration layer formation on LBS glass

The x-ray diffraction patterns of LBS glass monoliths are shown in Figure 6.10. Exposure to ECW solution for 28 days lead to the formation of calcite ($CaCO_3$; PDF 00-001-0837), C-S-H ($CaOSiO_2H_2O$; PDF 00-033-0306) and hydrotalcite ($Mg_6Al_2CO_3(OH)_6{\bullet}4(H_2O)$; PDF 00-014-0191). After 28 days in ECW solution followed by 28 days in OCW solution, the same phases were identified, except for calcite, which was not present. There was also a reduction in the diffuse scattering in this sample. The diffraction pattern of LBS glass after exposure for a further 28 days to GW solution showed greater crystallinity of the hydrotalcite (sharper diffraction peaks) and the presence of C-S-H.

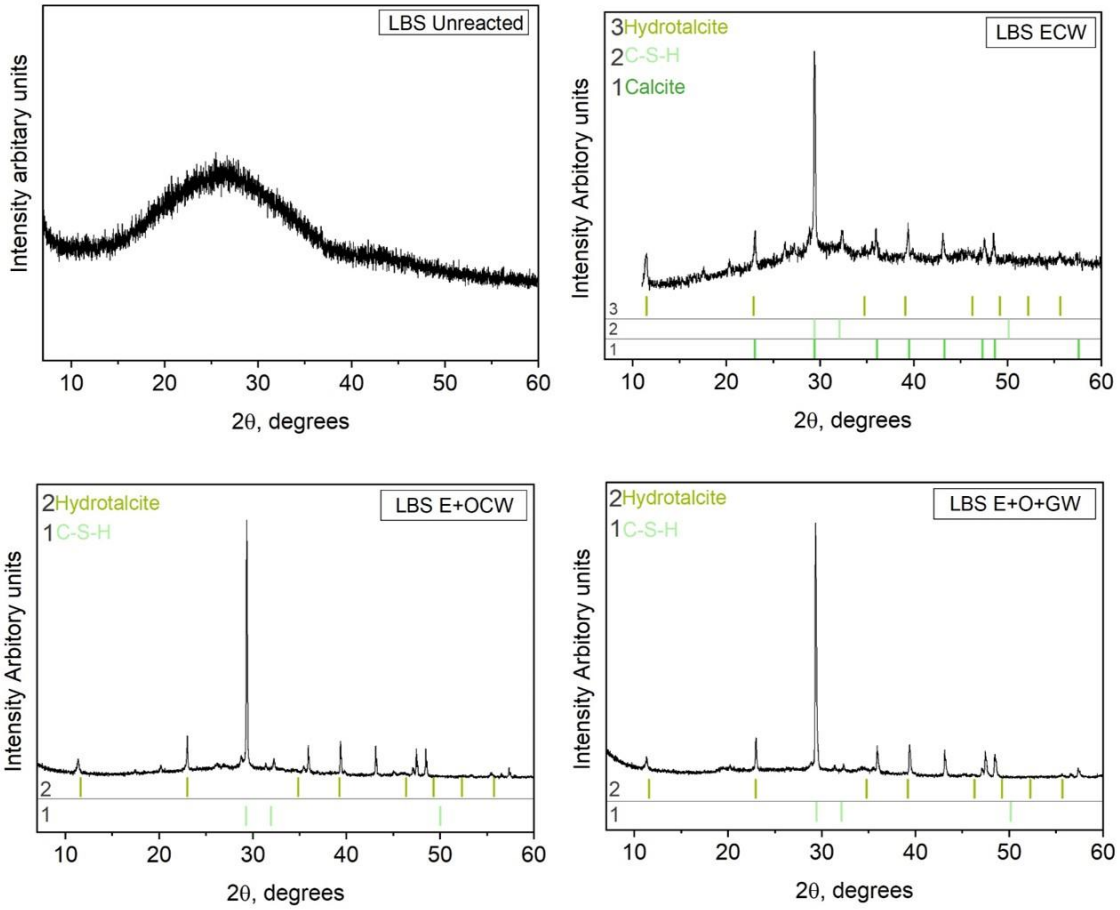

Figure 6.10 Diffraction patterns of LBS monoliths exposed to ECW for 6 months, ECW and OCW 28 days in each solution and ECW+OCW and GW 28 days in each solution.

Figure 6.11a-c show the alteration products formed on the surface of LBS glass after the sequential dissolution experiment (as discussed previously, experimental constraints prevented analysis of the 28 day ECW sample, so a six month sample is shown for completeness). Alteration layers formed after 28 days in ECW solution followed by 28 days in OCW solution comprised a gel layer with nodular precipitates. After an additional 28 days in GW solution, a thicker gel layer was formed with chain-like nodule precipitates on the outer surface of the gel.

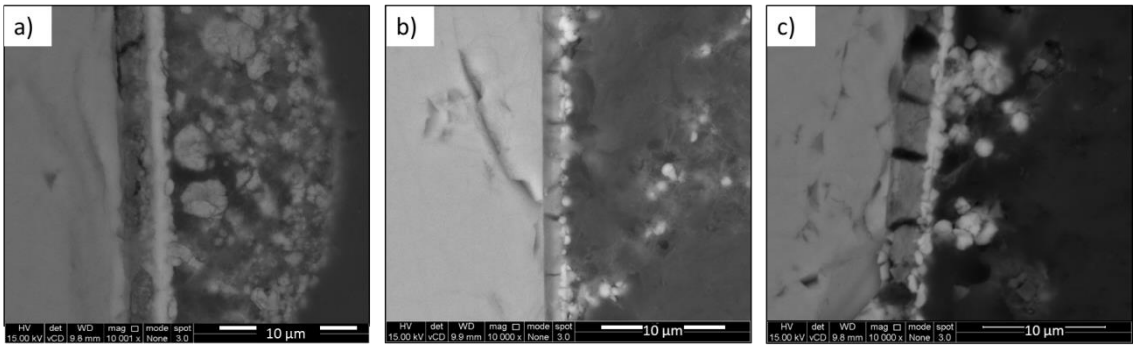

Figure 6.11 LBS monolith glass exposed to a) ECW for 6 months, b) ECW then OCW for 28 days each, and c) ECW +OCW +GW for 28 days in each condition.

i. Dissolution of LBS in ECW solution

There were three distinct alteration layers that formed on the surface of the LBS monolith after 6 months (Figure 6.12); the total thickness was 16.68 ± 1.35 µm. EDS spot 19 (Table 6.5) confirms that Layer 1 is a Ca-silica gel with an average thickness of 2.41 ± 0.28 µm that also contains an appreciable quantity of Fe and small amounts of Al, Mg and Na. The Ca:Si ratio of this layer was 0.37. Layer 2 was also identified as a Ca-Si layer, 1.58 ± 0.30 µm in thickness. The Ca:Si ratio of this layer was higher than Layer 1, at 1.08. The precipitates that formed on the outer surface of the monolith (Layer 3) extended the thickness of the alteration products significantly. EDS analysis indicated that these clumps were Ca-rich; spot 25 shows the nodules as mainly being composed of Ca with a small amount of Si. Other nodules in Layer 3 contained much greater quantities of Si and trace amounts of Fe, Al, Mg and Na. Unlike MW25 glass, Zr and K did not seem to play a significant role in alteration layer formation in ECW solution, while Fe was a key contributor to the silica gel layer composition.

Table 6.5 SEM EDS spot maps associated with Figure 6.12, average elemental compositions at % of each alteration layer on the surface of LBS monolith after 6 months exposed to ECW.

Element	Si	Fe	K	Al	Mg	Na	Ca	Zr	Other
Avt At% Bulk glass (16)	55.84± 0.64	9.35± 0.46	0.30± 0.06	7.19± 0.49	6.17± 0.18	19.24± 0.74	0.73± 0.05	0.39± 0.13	0.45± 0.29
Avg At% Layer 1 (19)	51.47± 3.04	11.53± 1.18	0.22± 0.22	3.26± 0.97	2.62± 1.00	6.67± 2.06	19.18± 5.74	0.61± 0.71	0.83± 1.07
Avg At% Layer 2 (22)	31.20± 0.37	15.13± 1.11	0.12± 0.20	5.49± 0.23	5.01± 1.04	6.81± 0.47	33.75± 2.19	0.92± 0.15	0.61± 0.62
Avg At% Layer 3 large spherules (25)	9.39± 3.28	1.10± 0.13	0.01± 0.37	0.84± 0.25	0.33± 0.42	2.69± 1.28	84.48± 5.27	0.12± 0.20	0.37± 0.32
Avg At % Layer 3 other (28)	33.53± 5.06	1.17± 0.33	0.08± 0.19	2.38± 0.29	1.90± 0.30	6.35± 0.29	52.88± 6.35	0.09± 0.35	-

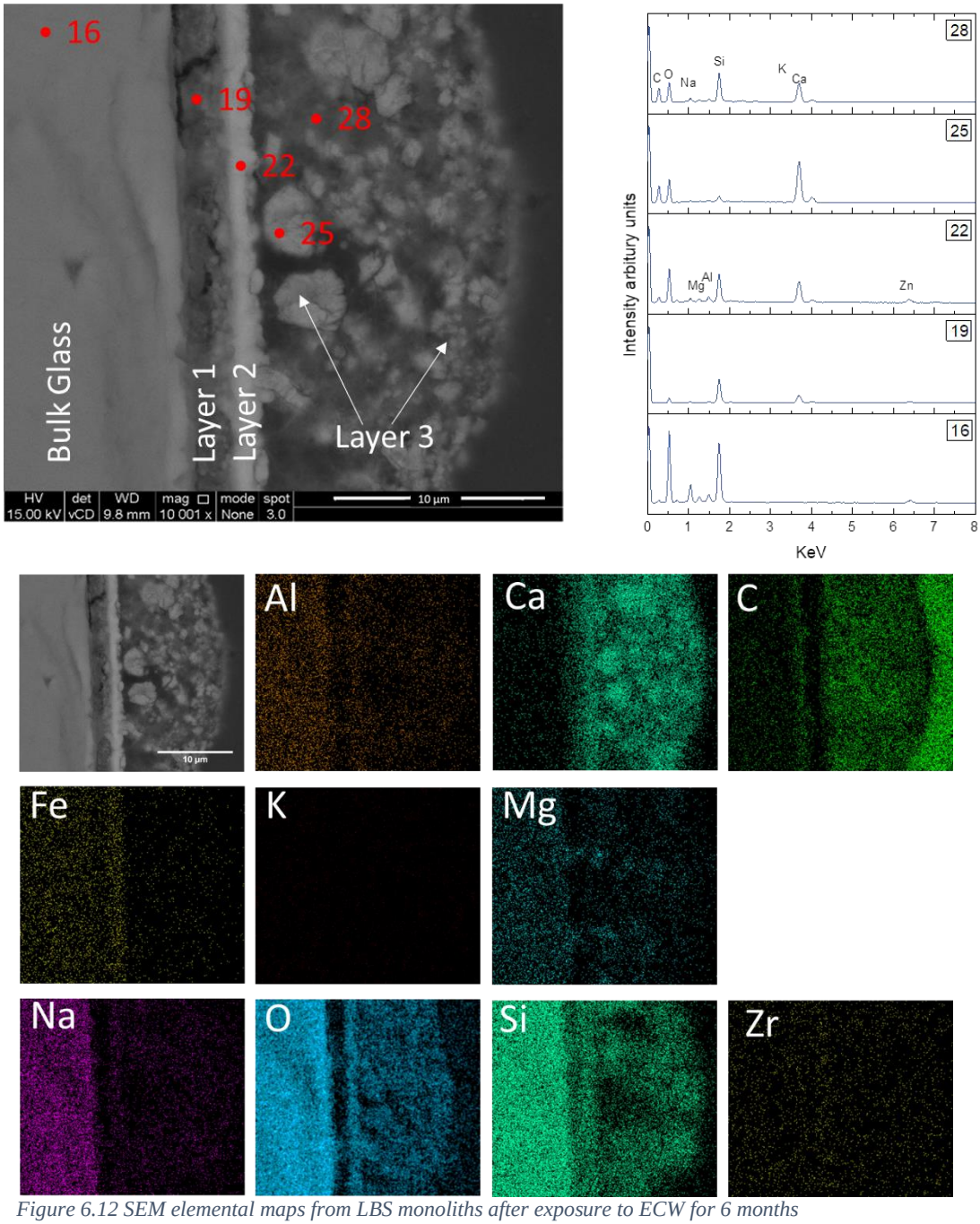

Figure 6.12 SEM elemental maps from LBS monoliths after exposure to ECW for 6 months

ii. Dissolution of LBS in ECW+ OCW solutions

The SEM micrograph of an LBS glass monolith after sequential exposure to ECW and OCW solutions (28 days in each) is shown in Figure 6.13. A Ca and Fe-rich silica gel layer (Table 6.6), 1.87 ± 0.15 µm in thickness, was observed. A second layer (Layer 2) resided on the outside of Layer 1 and comprised small nodules with a very bright BSE contrast; EDS confirmed these nodules to be rich in Ca and Fe. The Ca:Si ratio of the nodules was 1.2, compared with 0.2 for the Ca-silica gel layer in Layer 1. EDS 'Spot 11' was taken on a region of small needle-like phase, and was found to be rich in Mg, Ca and Si (Table 6.6). XRD analysis (Figure 6.10) identified the phase hydrotalcite, a Mg-bearing double layered hydroxide which has a platy morphology which, if viewed in cross-section, would appear to be needle-like. As discussed in Section 6.2.3.iii, while hydrotalcite is nominally a Mg-bearing phase, it is possible to incorporate Ca[172,173]. XRD analysis also confirmed the presence of C-S-H; all of the alteration layers identified in this sample by SEM contained significant amounts of Ca, Fe and Si, and Layer 2 had a Ca:Si ratio that falls into the accepted range for C-S-H (0.5 to 2.5[128,58]).

Table 6.6 SEM EDS spot maps associated with Figure 6.13, average elemental compositions at % of each alteration layer on the surface of LBS monolith after 28 days exposed to ECW and a further 28 days in OCW.

Element	Si	Fe	K	Al	Mg	Na	Ca	Zr	Other
Avt At% Bulk glass (1)	55.76± 0.29	8.42± 0.41	0.23± 0.11	7.26± 0.08	6.16± 0.08	19.72± 0.07	0.60± 0.06	0.28± 0.07	0.59± 51.52
Avg At% Layer 1 (4)	52.37± 0.49	10.23± 0.63	0.27± 0.18	4.71± 0.44	3.84± 0.51	12.52± 1.79	10.72± 1.82	1.39± 0.16	1.31± 49.29
Avg At% Layer 2, nodules (7)	30.87± 10.09	13.49± 2.02	0.02± 0.03	3.96± 1.68	5.55± 6.72	3.33± 2.33	37.40± 16.28	0.98± 0.50	1.49± 50.52
Avg At % Layer 3 other (11)	37.05± 23.33	7.89± 0.35	0.08± 0.16	6.86± 5.95	19.59± 21.36	2.75± 1.59	18.79± 10.91	0.38± 0.30	2.11± 54.45
Avg At % epoxy (12-13)	23.39± 0.90	7.59± 1.18	0.00± 0.00	5.89± 0.11	16.86± 2.07	4.02± 0.23	22.19± 1.83	1.02± 0.39	6.88± 46.46

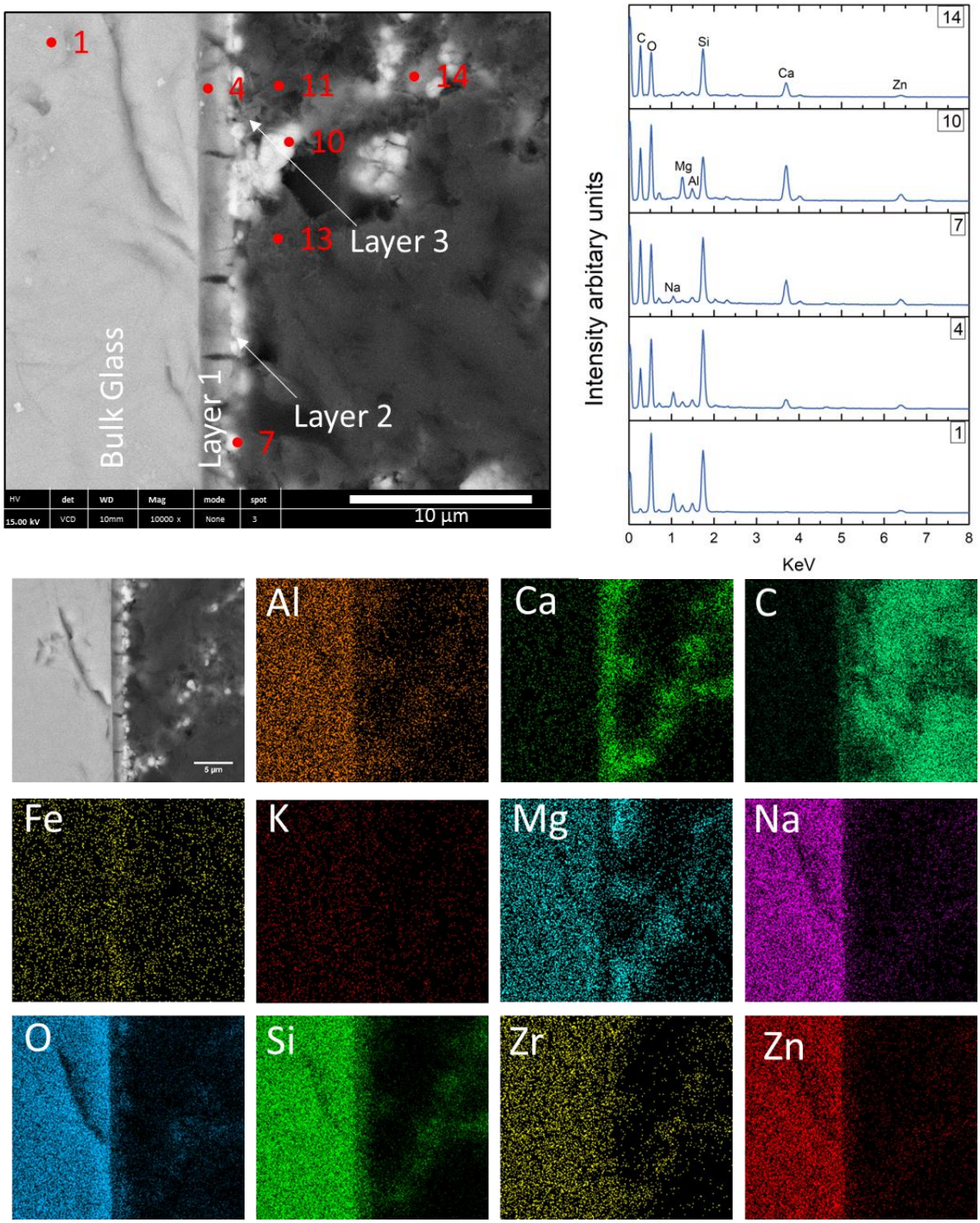

Figure 6.13 SEM elemental maps of LBS monolith after exposure to ECW for 28 days and OCW for a further 28 days

iii. Dissolution of LBS in ECW + OCW + GW solutions

Three distinct phases formed on the surface of the LBS sample shown in Figure 6.14. Layer 1 is composed of an Fe- and Ca-rich silica gel (containing > 40 at % Si and nearly 20 at % Fe) which also contained Al, Mg and Na. The total thickness of Layer 1 was 2.90 ± 0.27 µm. Elemental maps indicate depletion of Al in this layer relative to the bulk glass. A thin band of nodules in a chain-like arrangement formed Layer 2, which had a composition similar to Layer 1, but with more Al and a significantly higher concentration of Ca. The nodules attached to Layer 2 were rich in Si, Fe and Ca, with a Ca:Si ratio of 0.68. XRD analysis (Figure 6.10) identified the presence of semi-crystalline C-S-H on the surface of the glass sample. While the Ca:Si ratio of the nodules observed here is within the acceptable range for C-S-H, the morphology is unusual for C-S-H, which typically form wispy precipitates (e.g. see Chapter 4). Thirdly were precipitates composed of Mg-silicate with a Mg:Si ratio ~ 1.0, identified by EDS spots 13 and 14. XRD analysis did not identify any Mg-silicate phases, suggesting that either these phases are amorphous, or more likely, that they were present in concentrations below the detection limit of the XRD. It may be possible to discern the nature of these phases by performing longer timescale experiments, or using TEM / SAED analysis techniques.

Table 6.7 SEM EDS spot maps associated with Figure 6.14, average elemental compositions at % of each alteration layer on the surface of LBS monolith after 28 days exposed to ECW followed by 2 days in OCW and finally 28 days in GW.

Element Avg At %	Si	Fe	K	Al	Mg	Na	Ca	S	Zr	Other
Bulk glass (1)	55.30± 0.36	8.67± 0.13	0.25± 0.09	7.38± 0.16	6.20± 0.06	20.17± 0.05	0.56±0.01	- ± -	0.54± 0.13	0.71± 0.06
Layer 1 (3)	43.22± 1.55	19.51± 1.22	0.11± 0.13	3.64± 0.36	3.13± 0.48	6.62± 1.42	9.54±1.34	4.06± 0.32	2.83± 1.38	2.93± 1.77
Layer 2 (6)	34.99± 1.31	16.63± 1.11	0.17± 0.09	7.11± 0.54	7.79± 3.78	6.65± 3.21	23.83±1.00	1.73± 1.22	0.73± 0.17	0.46± 0.02
Nodules (9)	32.38± 3.92	17.50± 2.05	0.20± 0.10	6.49± 1.17	8.08± 1.22	3.12± 0.72	29.32±10.09	2.86± -	0.53± 0.18	-
Whispy precipitates (14)	29.30± 3.74	9.81± 1.64	0.25± 0.32	10.35± 0.79	29.35± 4.78	2.07± 2.19	5.61±5.89	7.64± 1.96	0.52± 0.23	-
X-silicate (13)	32.49± 4.79	8.21± 0.61	0.06± 0.01	11.66± 1.82	28.48± 6.92	0.95± 0.03	7.67±7.06	6.15± 3.07	0.33± 0.98	-

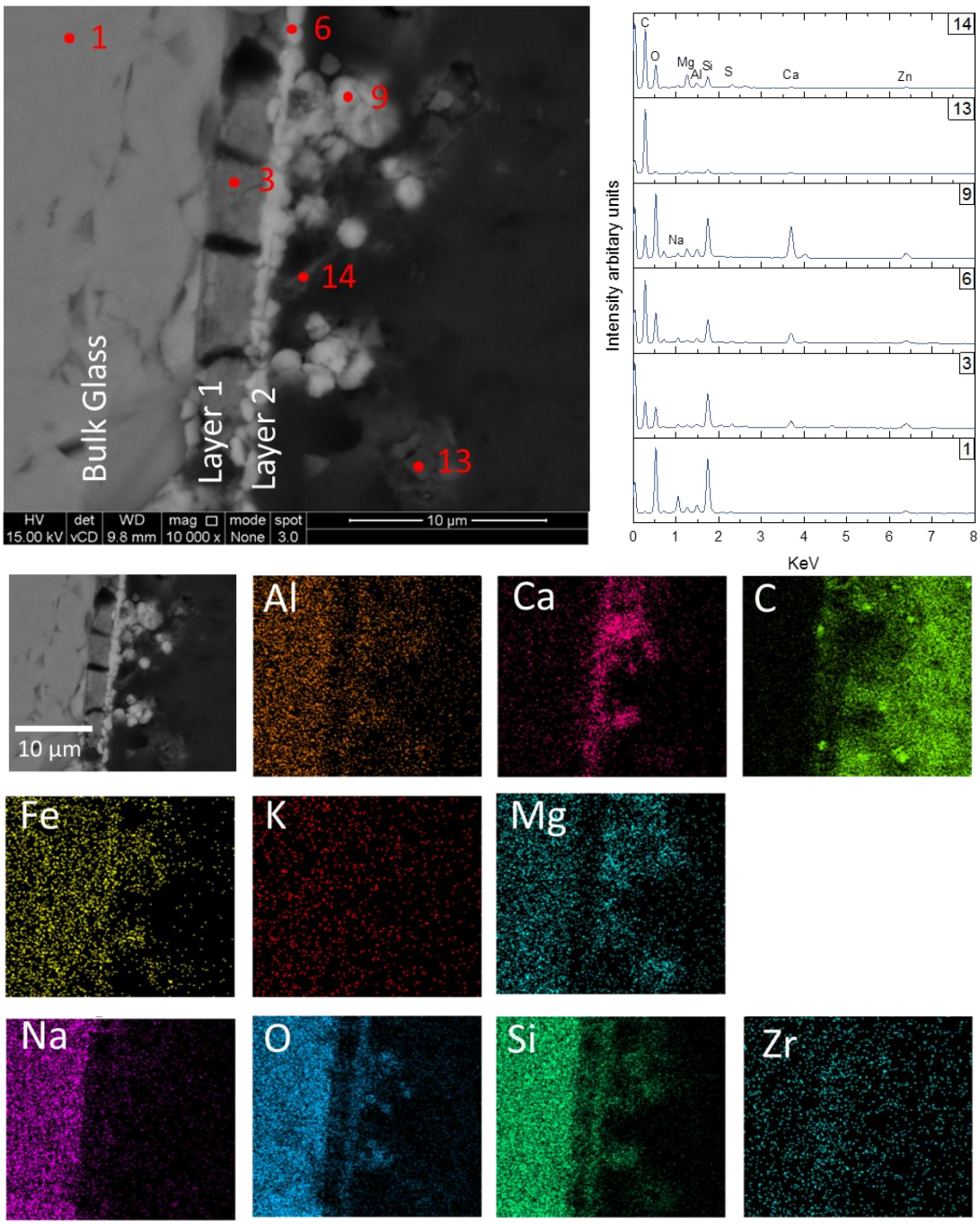

Figure 6.14 SEM elemental maps of LBS monolith after exposure to ECW for 28 days and OCW for a further 28 days and finally 28 days in GW.

6.2.5. Alteration layer formation on ISG glass

X-ray diffraction patterns for ISG monolith samples after dissolution in the sequential dissolution test revealed the presence of calcite ($CaCO_3$; PDF 00-001-0837) and C-S-H ($CaOSiO_2H_2O$; PDF 00-033-0306) after exposure to ECW solution for 28 days; the peak at 32.05^o 2θ, attributed to C-S-H, is broad indicating the poorly crystalline nature of this phase. In contrast, after an additional 28 days of exposure to OCW solution, this peak sharpened considerably, behaviour that may attributed to development of crystallinity. Calcite was also present under these conditions.

The diffraction pattern collected for ISG exposed sequentially to ECW + OCW + GW showed the same diffuse scattering observed for the pristine glass in addition to a peak at 30.3 ^{o} 2θ. This is attributed to the phyllosilicate phase, rhodesite ($K_{0.6}Na_{0.4}HCa_2Si_8O_{19}$•5($H_2O$); PDF 00-022-1253). This is in agreement with the solution chemistry data for K in GW solution (Figure 6.4), which showed a significant decrease in K concentration in the presence of ISG when compared to the blank solution. Ferrand et al.[174] identified rhodesite on the surface of ISG exposed to synthetic young cement water at 70 ^{o}C and it was identified on the surface of ISG in the presence of YCW and YCWCa in Chapter 4. It was also possible to identify some small, broad peaks associated with calcite and C-S-H.

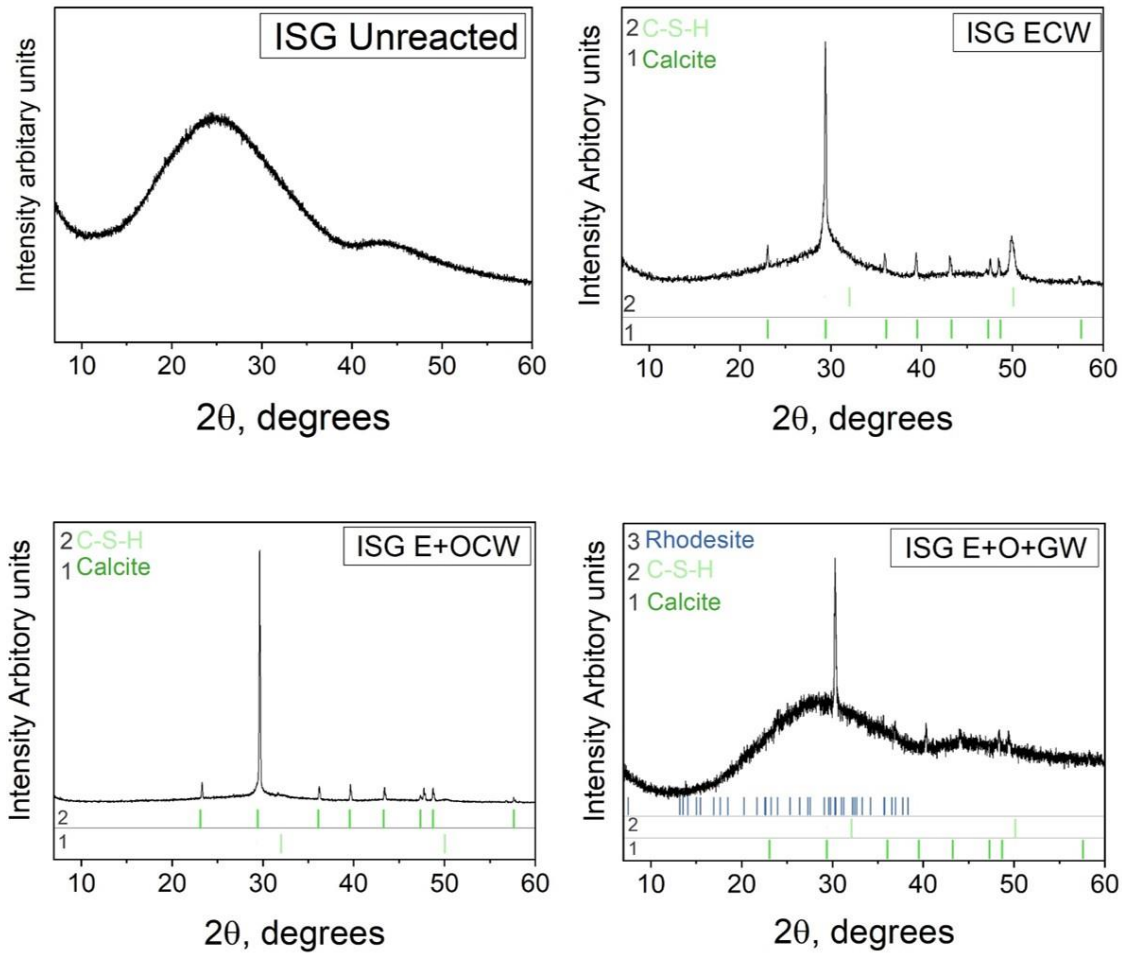

Figure 6 15 Diffraction patterns of ISG monoliths exposed to ECW for 6 months, ECW and OCW 28 days in each solution and ECW+OCW and GW 28 days in each solution.

The alteration layers that developed on the surface of the ISG samples during the sequential tests manifest as finely banded layers. Figure 6.16a depicts a BSE micrograph of an ISG monolith after 6 months in ECW. Multiple thin bands were observed in the alteration layer and large blocky particles were embedded in the epoxy. When ISG was exposed to ECW + OCW solutions, the thickness of the alteration products was the same as the ISG exposed to 6 months in ECW (4.05 ± 0.19 μm in ECW and 4.22 ± 0.25 μm ECW + OCW), despite the large difference in time scales. A single gel layer with three banded layers residing on top of the gel was observed.

Sequential dissolution of ISG in ECW + OCW + GW (28 days each) resulted in the formation of a gel next to the pristine glass, followed by a band of nodular precipitates with bright z-contrast in the BSE micrograph. There was a large gap between this layer and the next, which was likely due to delamination during sample preparation. The outer layer appeared similar in morphology to that observed in ECW + OCW solutions, with thin bands. In the bottom right hand side of the image, a precipitate phase with a large surface area can be seen.

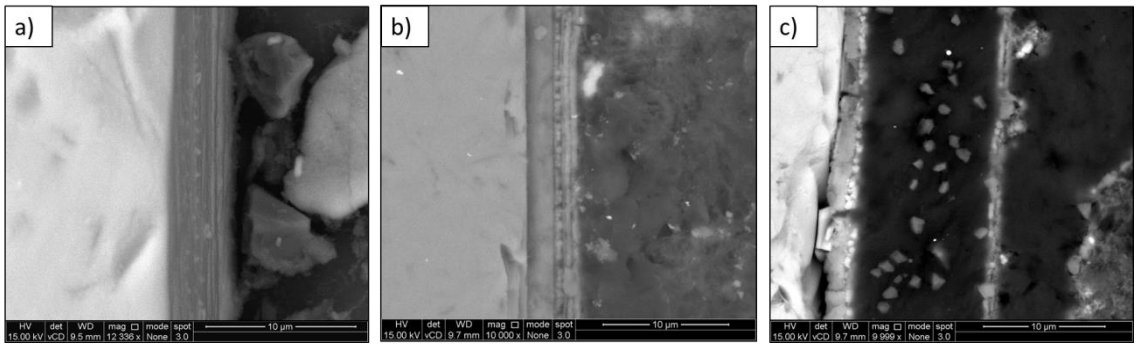

Figure 6.16 ISG monolith glass exposed to ECW for 6 months, centre image ECW +OCW for 28 days each, RHS ECW +OCW +GW for 28 days in each condition

i. Dissolution of ISG in ECW solution

Dissolution of ISG in ECW solution for 6 months resulted in the formation of multiple bands on the surface of the glass (Figure 6.16). Layer 1, in direct contact with the glass was a band of Ca-silica gel (Ca:Si ratio of 1.6, Table 6.10) with striations throughout. Layer 2 comprised small nodules that contained a higher quantity of Fe, Mg and Ca compared to the bulk glass. The Ca:Si ratio of Layer 2 was 0.33. Layer 3 was a thin band with a lighter grey contrast in the BSE image; it had a similar Ca content as in the bulk glass and contained significantly elevated concentrations of Na with a small amount of Al. The precipitate on the surface of the glass was composed of Na, Al, Ca and Si (spot 53, Table 6.9 and Figure 6.17). Diffraction analysis of the monolith did not reveal any Na-bearing phases, only calcite and C-S-H, however, previous studies[26175] of the dissolution of ISG in high pH solution have observed the formation of the zeolite phase, analcime ($NaAlSi_2O_6 \cdot H_2O$) which has a composition consistent with the EDS analysis (except for Ca; perhaps C-S-H coats the analcime precipitate).

Table 6.10 SEM EDS spot maps associated with Figure 6.17, average elemental compositions at % of each alteration layer on the surface of ISG monolith after 6 months exposed to ECW.

Element Avg At %	Si	Fe	K	Al	Mg	Na	Ca	Zr	Other
Bulk glass (41)	67.20 ± 1.03	0.02 ± 0.03	0.07 ± 0.09	7.59 ± 0.21	0.03 ± 0.05	14.90 ± 2.11	7.89 ± 1.09	2.17 ± 0.39	0.06 ± 0.06
Layer 1 (44)	29.50 ± 1.47	0.00 ± 0.00	1.42 ± 1.43	3.29 ± 3.02	4.18 ± 3.24	6.98 ± 5.10	45.12 ± 2.84	0.89 ± 1.11	4.30 ± 5.16
Layer 2 (47)	41.85 ± 12.82	8.60 ± 7.81	1.56 ± 1.36	3.01 ± 3.12	5.34 ± 4.13	8.13 ± 6.35	14.04 ± 6.70	3.66 ± 3.36	6.91 ± 8.25
Layer 3 (50)	57.76 ± 14.37	5.90 ± 5.69	0.00 ± 0.00	3.55 ± 2.15	1.82 ± 0.76	17.62 ± 12.36	9.14 ± 4.17	2.55 ± 1.57	0.84 ± 1.43
Precipitate1 (53)	37.19 ± 1.86	24.06 ± 1.20	0.01 ± 0.00	9.75 ± 0.49	2.39 ± 0.12	12.75 ± 0.64	12.94 ± 0.65	0.90 ± 0.05	0.00 ± 0.00
Precipitate2 (56)	60.65 ± 3.07	0.00 ± 0.00	1.01 ± 1.01	6.38 ± 2.59	3.12 ± 4.32	21.86 ± 1.69	4.71 ± 3.31	0.26 ± 0.46	1.00 ± 2.46

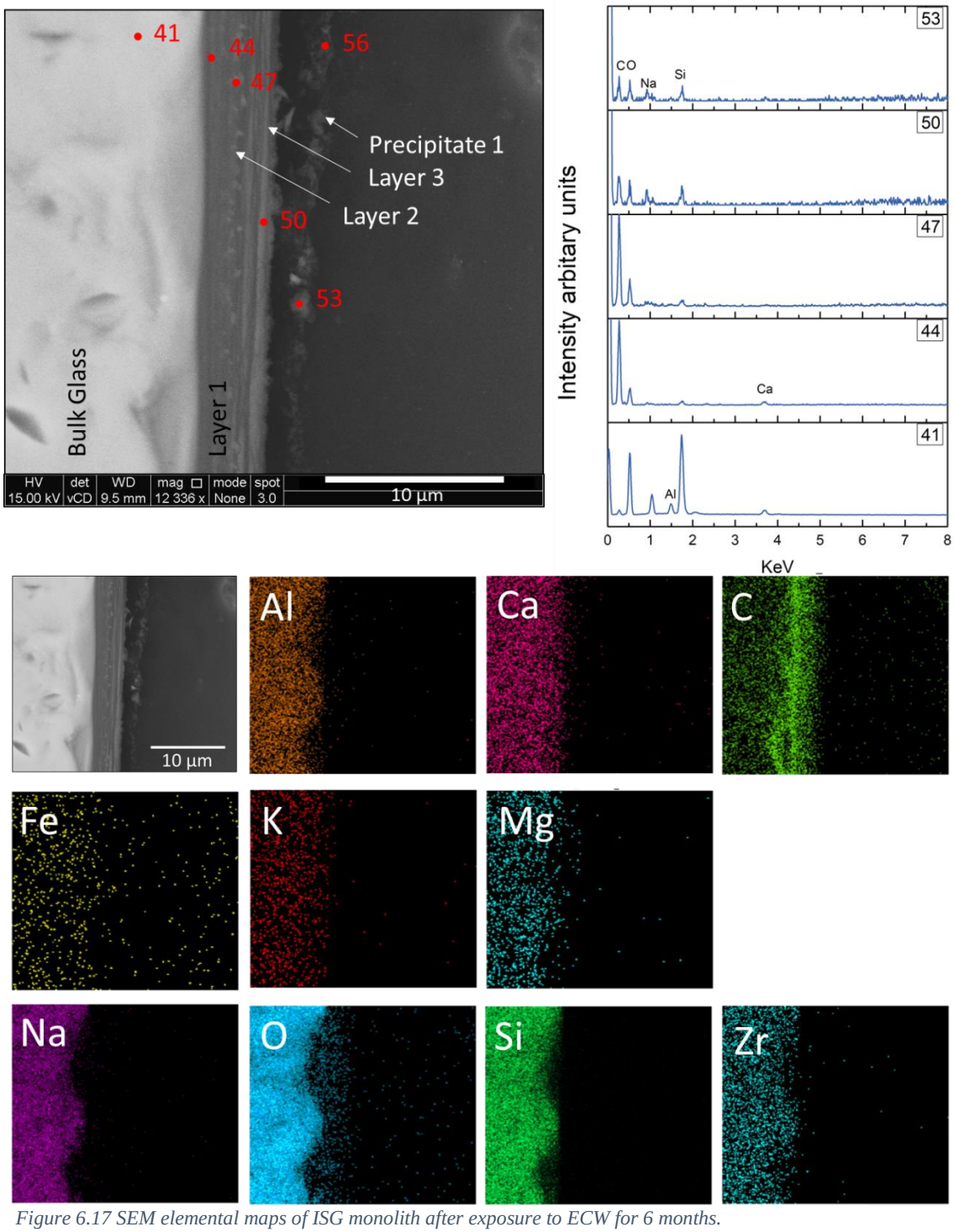

Figure 6.17 SEM elemental maps of ISG monolith after exposure to ECW for 6 months.

ii. Dissolution of ISG in ECW + OCW solutions

The alteration layers formed on the surface of ISG monolith after 28 days in ECW solution followed by 28 days in OCW solution resulted in alteration products with a total thickness of 4.22 ± 0.25 µm. The Ca-Si gel layer (Layer 1), in direct contact with the glass, was 2.27 ± 0.06 µm thick and had a Ca:Si ratio of 0.30. Layer 2 was also composed of Ca and Si (with a Ca:Si ratio of 0.43) and was packed with small nodules. Layers 3 and 4 were thin bands with uniform morphology, comprised of Ca, Si, Al and Na (the Ca:Si ratio was 0.47). The presence of Zr in the gel (Layer 1) is evident from the spot maps outlined in Table 6.11 but significant enrichment was observed in Layers 2, 3 and 4 in similar quantities ~10.5 at %, similar banding was observed by Backhouse[70] and Gin et al.[167] for ISG in high pH solutions.

The elemental maps in Figure 6.18 are taken from a different section on the monolith. The resolution was not sufficient to distinguish compositional variation in the thin alteration bands, however, it was possible to confirm the alteration layers are enriched with Ca.

Table 6.11 SEM EDS spot maps associated with Figure 6.18, average elemental compositions at % of each alteration layer on the surface of LBS monolith after 28 days exposed to ECW followed by 2 days in OCW.

Element Avg At %	Si	Fe	K	Al	Mg	Na	Ca	Zr	Other
Bulk glass (62)	67.18 ± 0.26	0.05 ± 0.05	0.12 ± 0.14	7.62 ± 0.28	0.18 ± 0.07	15.98 ± 0.24	6.61 ± 0.13	2.18 ± 0.23	0.47 ± 0.19
Layer 1 (65)	48.29 ± 0.75	-	0.04 ± 0.18	4.78 ± 0.05	0.07 ± 0.04	7.08 ± 0.61	34.38 ± 0.93	3.85 ± 0.35	1.62 ± 0.40
Layer 2 (68)	40.54 ± 0.55	-	0.06 ± 0.15	3.28 ± 0.12	-	5.66 ± 0.45	39.07 ± 0.70	10.40 ± 0.07	1.29 ± 0.23
Layer 3 (71)	36.68 ± 0.23	-	0.01 ± 0.02	2.93 ± 0.32	0.10 ± 0.30	7.64 ± 0.50	39.67 ± 1.05	10.40 ± 0.19	1.39 ± 0.77
Layer 4 (74)	36.64 ± 1.53	0.03 ± 0.20	-	3.31 ± 0.51	0.35 ± 0.17	7.47 ± 1.68	33.94 ± 0.35	11.14 ± 1.11	4.70 ± 0.42

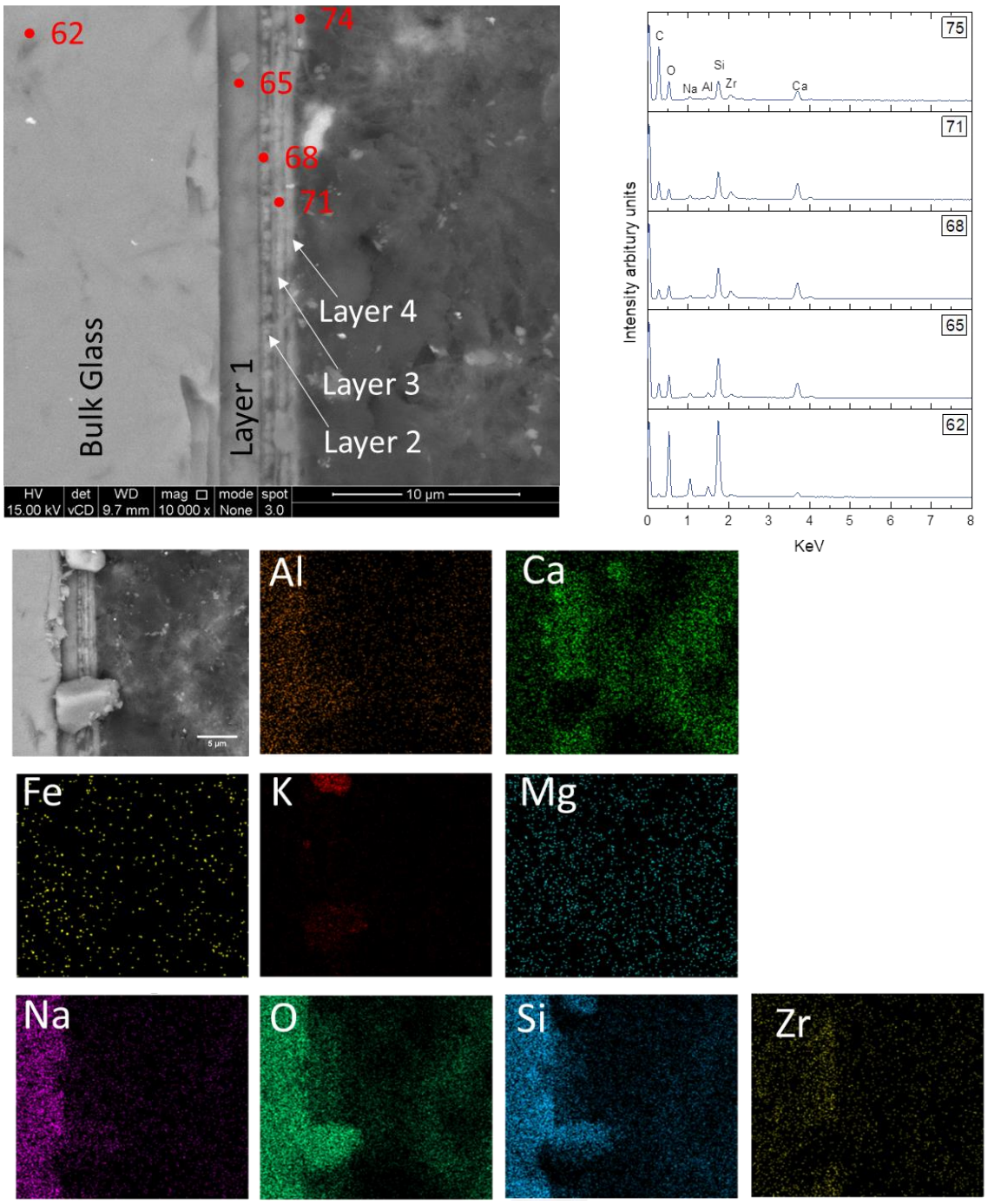

Figure 6.18 SEM elemental maps of ISG after exposure to ECW for 28day followed by 28 days in OCW

iii. Dissolution of ISG in ECW + OCW + GW solutions

In direct contact with the ISG glass (Figure 6.19) was a layer of silica gel containing Ca, Zr and Al (Layer 1); it exhibited a Ca:Si ratio of 0.3. Directly on top of the gel layer were nodules, but identification of the composition was not possible due to the low resolution of the analysis performed. The gel was 1.59 ± 0.22 µm thick and the combined thickness of the gel and the nodules was 2.27 ± 0.39 µm. A large gap, sparsely filled with S, C and Cl-rich particles, between Layers 2 and 3 are attributed to epoxy resin and contamination resulting from carbon sputtering prior to analysis by SEM. Layer 3 was 0.99 ± 0.15 µm thick and was composed of Ca, Si, Zr, Al and Mg. The latter must have originated from the solution since there is no Mg in the ISG composition; this is consistent with solution concentration data for Mg (Figure 6.4) that showed a significantly lower Mg content than in the blank. On the far right side of the micrograph, a Mg, Al and S-bearing silica phase (with an Mg:Si ratio of 0.44) was observed; this composition is indicative of the precipitation of phyllosilicate minerals. XRD identified rhodesite $(Ca,Na_2,K_2)_8Si_{16}O_{40}\cdot 11H_2O$, however in Figure 6.19 the presence of rhodesite was not evident, this image only depicts a small percentage of the sample.

Table 6.12 SEM EDS spot maps associated with Figure 6.19, average elemental compositions at % of each alteration layer on the surface of LBS monolith after 28 days exposed to ECW followed by 2 days in OCW and finally 28 days in GW.

Element Avg At %	Si	Fe	K	Al	Mg	Na	Ca	Zr	Other
Bulk glass (16)	32.01 ± 1.81	-	0.02 ± 0.01	3.80 ± 0.16	0.06 ± 0.04	8.90 ± 0.38	2.83 ± 0.10	1.01 ± 0.00	-
Layer 1 (18)	51.37 ± 1.09	0.14 ± 0.15	0.26 ± 0.14	5.59 ± 0.29	0.37 ± 0.07	8.23 ± 1.52	15.54 ± 0.81	14.12 ± 1.28	2.19 ± 1.04
Layer 2 (21)	45.30 ± 0.64	-	0.29 ± 0.32	5.46 ± 0.23	0.48 ± 0.46	3.28 ± 1.12	19.27 ± 0.19	16.55 ± 0.05	4.76 ± 1.18
Precipitates(24)	9.36 ± 2.38	-	-	4.07 ± 3.18	0.95 ± 6.87	0.40 ± 5.96	5.84 ± 2.30	3.42 ± 4.68	50.75 ± 14.30
Layer 3 (27)	45.05 ± 0.28	-	0.34 ± 0.09	8.64 ± 0.04	1.31 ± 0.13	1.40 ± 0.15	21.07 ± 0.52	13.18 ± 0.42	4.64 ± 1.19
Mg-silicate (34)	50.16 ± 0.79	-	-	9.10 ± 0.42	22.20 ± 1.19	0.48 ± 0.27	4.93 ± 0.35	2.15 ± 0.34	5.67 ± 2.73

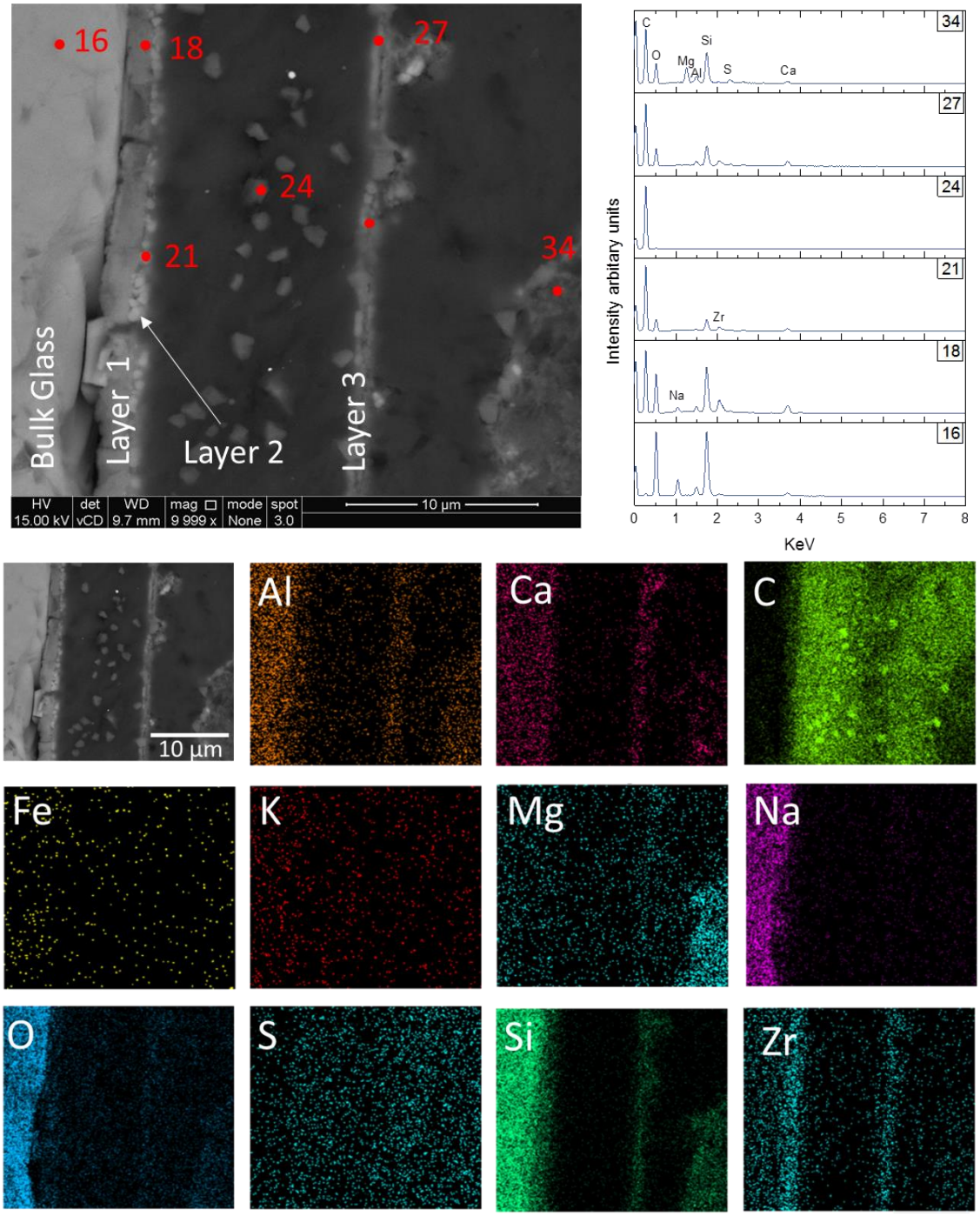

Figure 6.19 SEM elemental maps of ISG after exposure to ECW, OCW and groundwater for 28 days in each condition

6.2.6. Geochemical modelling

The concentration data from ICP-OES analysis for the sequential dissolution experiment were input into PHREEQC using the Hatches thermodynamic database (Figure 6.20). Blank solutions containing no glass, but experiencing removal of solution after 28 days and replacement with the next solution in the sequence were first modelled to understand the solution conditions prior to glass dissolution. The Ca-Si phases (C-S-H and tobermorite) were saturated in ECW and OCW blank solutions; in GW solution, which contains little Ca, they were significantly undersaturated. This was also the case for the other major Ca-bearing phase, Portlandite, and also ettringite. The Mg-bearing phases, talc and saponite-K, were saturated in all blank solutions, and their saturation index increased in the GW blank solution compared to the ECW and OCW blank solutions. The Mg-clay, sepiolite, was undersaturated in ECW and OCW blank solutions, but became saturated in GW blank solution. In contrast, having been saturated in ECW and OCW blank solutions, hydrotalcite was predicted to be undersaturated in the GW blank, and the saturation index of brucite was decreased in GW blank solution (as expected for a lower pH solution). Goethite was undersaturated in ECW and OCW solutions, but saturated in the GW solution.

The geochemical models of the glass-solution interactions did not deviate significantly from the trends observed for the blank solutions (Figure 6.20). The only deviation to note is hydrotalcite; in the blank solutions, it was predicted to be undersaturated in ECW and GW but saturated in the OCW. Upon contact with glass powder, hydrotalcite was predicted to be saturated, or in equilibrium, with all solutions. Undersaturation in the ECW blank can be explained by the low Al and Mg concentrations measured $(10.0 \pm 0.5) \times 10^{-3}$ mg L^{-1} and $(2.00 \pm 0.01) \times 10^{-2}$ mg L^{-1} respectively. When the ECW was replaced by OCW solution, the Al concentration remained the same and a slight increase in the Mg concentration was measured (0.33 ± 0.02 mg L^{-1}), hence the precipitation of hydrotalcite. Replacement of the leachate with groundwater resulted in very low Al concentrations $(2.2 \pm 0.1) \times 10^{-2}$ mg L^{-1} and elevated Mg concentration 5.84 ± 0.29 mg L^{-1}, it is likely there was simply not enough Al in the GW blank solution to form hydrotalcite.

There was no deviation for other phases identified, for example, portlandite and C-S-H were saturated in blank and glass-containing solutions of ECW and OCW. Changing the leachate to GW solution resulted in these phases becoming undersaturated or, in the case of LBS, close to equilibrium. Significantly, taken as a whole, these geochemical modelling results indicate that the solution chemistry exerts a greater influence than glass composition on the formation of secondary phases.

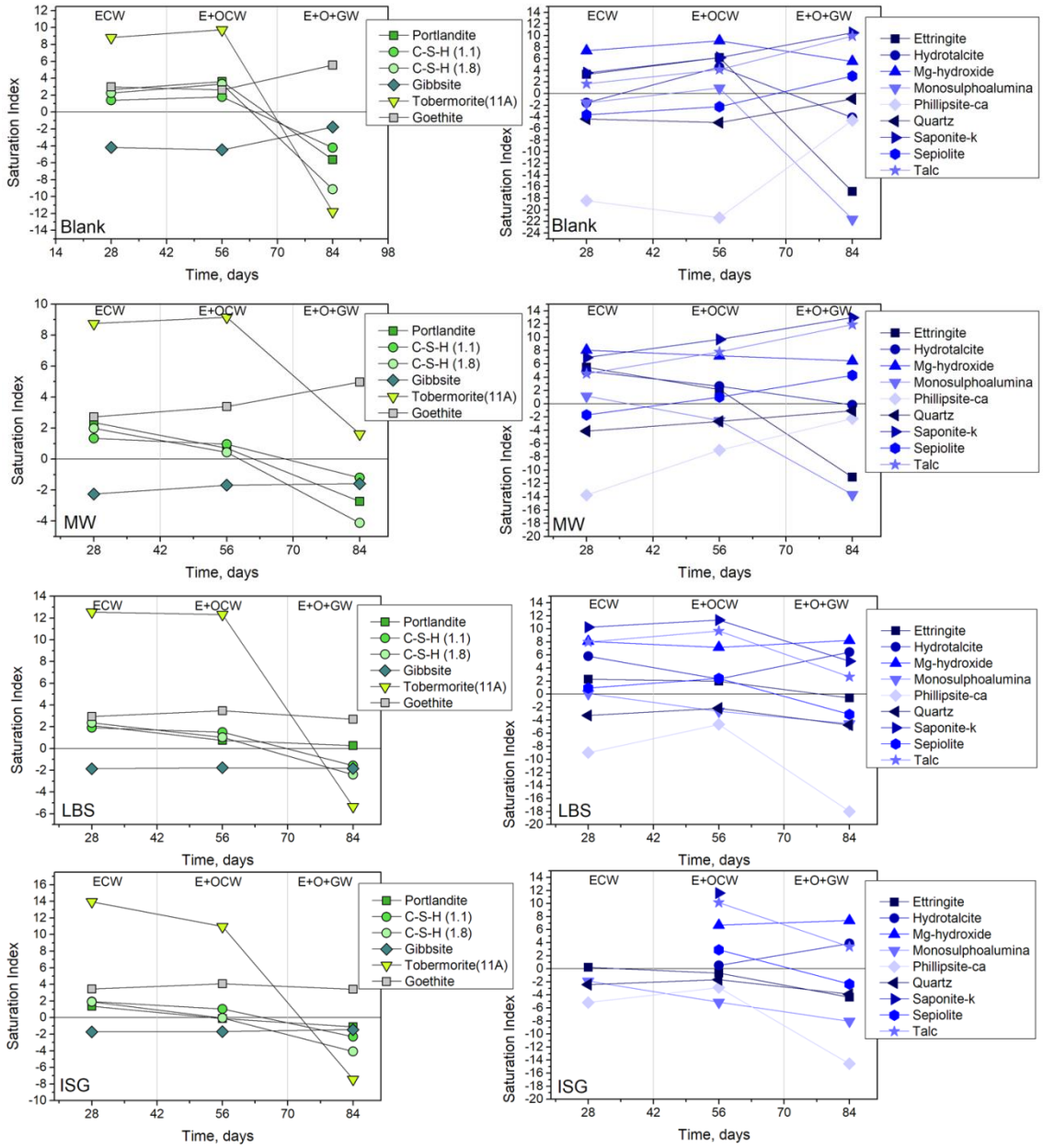

Figure 6.20 Geochemical modelling of the blank synthetic cement waters and granitic groundwater, and the solution chemistry after dissolution with MW25, LBS and ISG glass powder present in the test vessels. PHREEQC and Hatches database.

6.3. Discussion

The aim of this study was to investigate the influence of an evolving cement porewater chemistry on the dissolution mechanisms of simulant glass wasteforms, mimicking a geological disposal facility at long timescales. This initial study was conducted at 50 ^{o}C under static leaching conditions; the glass was first exposed to ECW for 28 days, then OCW and finally a granitic groundwater for 28 days each.

6.3.1. The influence of glass composition on glass dissolution rates

It would be reasonable to expect that as the solution aged and the pH decreased, the amount of corrosion (as measured by NL_B) would decrease. The dissolution rate of the complex glasses (MW25 and LBS) decreased a little as the solution changed toward more evolved compositions. ISG exhibited the greatest decrease in dissolution from ECW to OCW, indicating that, to a certain extent, dissolution is controlled by glass composition. For all the glass compositions the introduction of GW was the biggest influence. The NL data in Figure 6.3 show a reduction in the amount of B leached from the glass into the solutions; from 1.24 ± 0.14 g m^{-2} in ECW, to 0.36 ± 0.02 g m^{-2} and finally 0.14 ± 0.01 g m^{-2} after E + O + GW leachates. It is evident from the data presented in Figure 6. that the simulant waste glasses (MW25 and LBS) behave differently when compared to ISG, (other authors have observed differences in dissolution rates and alteration products between simple glasses and complex nuclear glasses[26,76,176,177]). The effect of pH can be disregarded because the pH was very similar for all three glasses in each of the solutions (see Figure 6.2).

Dissolution of ISG lead to the formation of alteration layers that were morphologically and chemically different to those formed on MW25 and LBS glass. ISG exhibited banding; SEM EDX showed the bands / layers to be rich in Zr. Similar banding has been observed on ISG in highly alkaline solutions by other authors; Backhouse[70] in saturated $Ca(OH)_2$, Gin et al.[167] in KOH, and in Chapter 5 of this thesis (the leachate was synthetic young cement water with added Ca).

It has been shown that Zr is insoluble at $pH_{90\ oC}$ <10.5 (Lobanova et al[178] and Cailleteau et al.[96,169]), however, in highly alkaline solutions, Zr is mobile and can be heterogeneously distributed in silica alteration layers. Gin et al. [167] and Backhouse[70] observed enrichment of Zr in some layers while it was absent in others, suggesting dissolution / re-precipitation of Zr-silicate gels. Incorporation of Zr into Si-gel has been shown to inhibit restructuring of the gel layer (enhancing porosity and thus dissolution) [96,169]. In Chapter 5 ISG exposed to YCWCa resulted in disruption of the Si-gel

and lead to the formation of a Ca-silica gel with dense Si-Zr layers that restricted fluid transportation, decreasing the glass dissolution rate. In this Chapter, Zr rich bands were identified in the BSE micrographs (Figure 6.), however the EDS associated with these images were not of high enough resolution to distinguish if the bands observed were Zr-rich or depleted. Zirconium was not identified in the precipitate indicating that the element is exclusively partitioned into the alkali-silica gel. The accumulation of alkali and alkaline earth ions in the alkali silica gel are able to charge balance the negative $[ZrO_6]^{2-}$ species[45].

It is evident from the SEM EDS data (Table 6.5) that LBS samples exhibited significant incorporation of Fe in the gel and secondary precipitates that formed on the glass in each of the aging leachates (an increase of 10 at % in the gel compared to the bulk LBS glass, MW25 only experienced an increase of 2 at %). Iron has been shown to have a dual effect on dissolution kinetics by Gin et al.[179]; it can cause the gel to restructure leading to improved passivating properties[180], or it can promote dissolution by precipitating Fe-silicate secondary phases. It is thought that the dissolution kinetics of low Fe-containing glasses (MW25) is controlled by passivation while Fe-rich glasses (LBS) are controlled by precipitation of Fe-silicate phases. The rate of dissolution for MW25 and LBS in ECW (Chapter 4, Table 4.2) was $(0.62 \pm 0.01) \times 10^{-2}$ and $(1.84 \pm 0.1) \times 10^{-2}$ g m^{-2} d^{-1}, indicating that the Fe-rich (10.2 wt%/ 4.2 mol%) LBS dissolved faster than MW25 which had a low Fe content (2.38 wt % / 0.99 mol %), favouring the second of the two effects postulated by Gin et al. The behaviour of Fe in glass dissolution, and particularly for Fe-rich waste streams under consideration for vitrification, requires further study.

6.3.2. The effects of an evolving geochemistry on glass dissolution and alteration layer formation

The MW25 and LBS compositions experienced a reduction in the concentration of B in solution when the leachate was changed from ECW to OCW, but an increase when the leachate was replaced with GW solution, indicating that the dilute nature of the GW facilitates enhanced dissolution. This effect was reversed for the ISG composition, as discussed further below.

The normalised mass loss of B from the MW25 and LBS glass compositions in OCW solution, from Chapter 4, is shown in Figure 6.21. Also plotted on this graph are the NL_B data resulting from exposure of the glasses to the sequential solutions investigated in this Chapter. This graphs serves the purpose of highlighting the fact that, even though the glasses had a high NL_B in ECW, when the solution was replaced with OCW, the NL_B dropped to the same level as for the OCW

solution in Chapter 4, when there was no replacement. This is especially evident for the LBS glass composition. This suggests that although alteration layers had formed on the surface of the glasses during exposure to ECW for 28 days, their presence did not significantly alter the dissolution behaviour in OCW (if they did, the NL_B values for ECW + OCW would be extremely different to those for OCW alone). These data also highlight the significant effect that granitic groundwater has on the dissolution of MW25, as compared to all of the cementitous solutions. This effect seems to be lower for the LBS glass composition, but nevertheless, shows that the dilute nature of the GW solution facilitates enhanced dissolution.

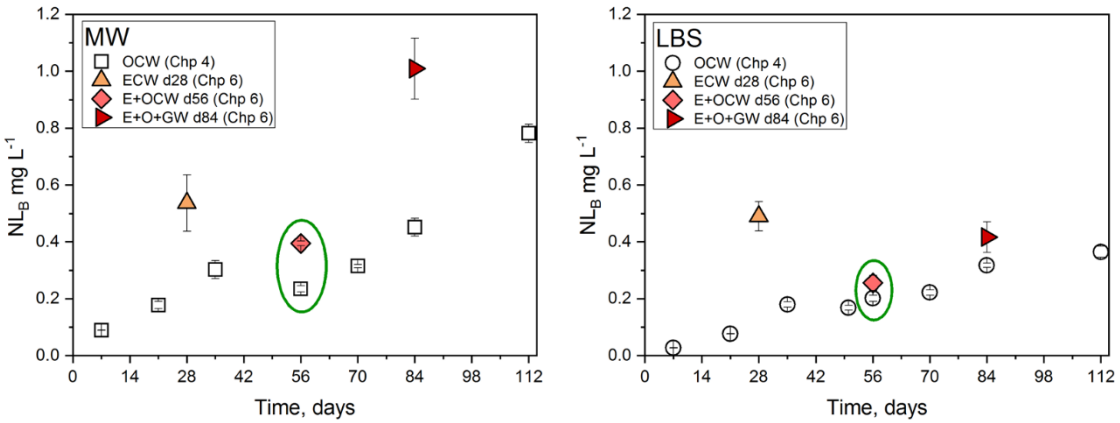

Figure 6.21 Comparison between OCW NL_B data from Chapter 4 and the sequential NL_B obtained in Chapter 6

Diffraction patterns of MW25 and LBS showed that precipitated phases, and particularly C-S-H, increased in crystallinity when the ECW solution was replaced with OCW and also with GW. This correlates with the formation of C-S-H precipitates on the surface of the gel layer (as identified by XRD Figure 6.5 and 6.6). Concurrently, the Ca:Si ratio of the precipitated phases was observed to increase for MW25 glass as the leachate was replaced (Table 6.12). This is in agreement with the development of a more Ca-rich, crystalline C-S-H. XRD and SEM EDS of LBS in ECW solution confirmed that the dominant alteration phase was C-S-H when the leachate was replaced with OCW and GW. As for MW25, the diffraction pattern became more crystalline as more precipitates formed on the surface of the glass. However, for the LBS glass, the EDS data show the precipitates to be Mg-rich in OCW solution (corresponding to hydrotalcite identified by XRD) and Fe-rich in the GW solution. The Fe-rich phase was not identified by XRD, therefore it is likely to be amorphous Fe-silicates.

ISG behaved differently to the MW25 and LBS glasses, most notably, the dissolution rate (as shown by the NL_B) decreased throughout the sequence of solutions, even in the GW solution, which caused the MW25 and, to a lesser extent, the LBS glass, to rapidly dissolve. This may be due to the nature of the alteration layers, including the Zr-rich silica gel (as described in the

previous Section), and also the precipitated phases. For the precipitates formed on the surface of ISG, the Ca:Si ratio increased after the ECW solution was replaced with OCW solution. This correlates with C-S-H becoming more crystalline as identified by XRD. The diffraction pattern after exposure to GW is completely amorphous, with an area of diffuse scattering indicative of poorly-crystalline C-S-H. Thus, it is hypothesised that the C-S-H precipitates acted to protect the ISG from dissolution in GW solution, by themselves dissolving. Evidence for dissolved alteration products was seen in Figure 6.19 which shows the absence of Zr bands on the ISG sample after exposure to GW. The dissolution of precipitated layers would reduce the diffusion gradient bringing the system towards equilibrium, therefore reducing the loss of B from the glass. The same mechanism, but controlled by Fe-silicate precipitates, may explain why the LBS glass did not dissolve as rapidly as MW25 when in the presence of GW solution.

In all of the glasses studied, and all of the solutions, the silica gel that formed was composed of mixed alkali/alkali earth ions from solution.

Table 6.13 Alkali:Si ratios for the gel and precipitates formed under each experimental condition, the threshold for alkali silica gels are as follows; Na + K :Si ratio 0.05-0.6, Ca + Mg :Si 0-0.26 and C-S-H Ca:Si ratio 0.4-2.5 (atomic ratios)

		at % of individual elements							Alkali:Si ratio								
Conditions		Na	Mg	Al	Si	K	Ca	Fe	Ca:Si	K:Si	Na:Si	Mg:Si	Al:Si	Fe:Si	Na+K:Si	Ca+Mg:Si	Na+Mg+K+Ca:Si
MW ECW	gel	3.39	24.83	5.98	21.78	12.1	11.73	-	0.54	0.56	0.16	1.14	0.27	-	0.71	1.68	2.39
	precip	-	-	-	-	-	-	-	-	-	-	-	-	-	-	-	-
MW E+OCW	gel	14.89	7.42	12.75	50.52	-	6.37	-	0.13	-	0.29	0.15	0.25	-	0.29	0.27	0.57
	precip	6.88	3.77	6.15	49.79	-	14.1	-	0.28	-	0.14	0.08	0.12	-	0.14	0.36	0.50
MW E+O+GW	gel	6.77	6.03	9.45	45.17	0.04	4.97	-	0.11	-	0.15	0.13	0.21	-	0.15	0.24	0.39
	precip	2.17	18.81	11.23	26.8	-	28.1	-	1.05	-	0.08	0.70	0.42	-	0.08	1.75	1.83
LBS ECW	gel	6.67	2.62	3.26	51.47	0.22	19.18	11.53	0.37	-	0.13	0.05	0.06	0.22	0.13	0.42	0.56
	precip	6.35	1.9	2.38	33.53	0.08	52.88	1.17	1.58	-	0.19	0.06	0.07	0.03	0.19	1.63	1.83
LBS E+OCW	gel	12.52	3.84	4.71	52.37	0.27	10.72	10.23	0.20	-	0.24	0.07	0.09	0.20	0.24	0.28	0.52
	precip	2.75	19.59	6.86	37.05	0.08	18.79	7.89	0.51	-	0.07	0.53	0.19	0.21	0.08	1.04	1.11
LBS E+O+GW	gel	6.62	3.13	3.64	43.22	0.11	9.54	19.51	0.22	-	0.15	0.07	0.08	0.45	0.16	0.29	0.45
	precip	3.12	8.08	6.49	32.38	0.25	29.32	17.5	0.91	0.01	0.10	0.25	0.20	0.54	0.10	1.16	1.26
ISG ECW	gel	6.89	4.18	3.29	29.5	1.42	45.12	-	1.53	0.05	0.23	0.14	0.11	-	0.28	1.67	1.95
	precip	12.75	2.39	9.75	37.19	0.01	12.94	24.06	0.35	-	0.34	0.06	0.26	0.65	0.34	0.41	0.76
ISG E+OCW	gel	7.08	0.07	4.78	48.29	0.04	34.38	-	0.71	-	0.15	-	0.10	-	0.15	0.71	0.86
	precip	7.47	0.35	3.31	36.64	-	33.94	0.03	0.93	-	0.20	0.01	0.09	-	0.20	0.94	1.14
ISG E+O+GW	gel	8.23	0.37	5.59	51.37	0.26	15.54	0.14	0.30	0.01	0.16	0.01	0.11	-	0.17	0.31	0.47
	precip	0.48	22.2	9.1	50.16	-	4.93	-	0.10	-	0.01	0.44	0.18	-	0.01	0.54	0.55

6.3.3. Implications for waste disposal

To underpin the developing safety case for the geological disposal of vitrified wastes, it is important that dissolution behaviour under changing conditions, i.e., as the cement utilised in the construction and backfill materials evolves and groundwater penetrates these materials, can be predicted. The results presented in this Chapter indicate that dissolution of simulant waste glasses in groundwater occurs more rapidly than in evolved and old synthetic cement leachates but, at least in the case of simplified model glasses like the ISG, the precipitates *may* have a protective nature. Further work should be focused at understanding the dissolution rate of various alteration layer phases in groundwater solutions, so that their protective properties can be understood.

The data presented here have shown that complex multi-layer alteration products form on the surface of glasses in a short space of time, despite the glasses experiencing saturated and dilute conditions in a cyclical fashion, resulting in dissolution and re-precipitation of secondary precipitates and possibly gel phases. Through the introduction of fresh leachate, the concentration and type of soluble species in solution is altered and the pH changes. This has a strong influence on the nature of precipitated phases, as seen here for the increasing crystallinity and changing composition of C-S-H, and the formation of rhodesite [$(K_{0.6}Na_{0.4}HCa_2Si_8O_{19}\cdot 5(H_2O)$] on the surface of ISG exposed to GW solution. Although not observed on the timescales of the investigation presented here, such changes in solution chemistry and precipitated phases has been linked to the onset of stage III (rate resumption) dissolution behaviour.

Resumption of dissolution is defined by the sudden acceleration of the glass alteration rate after the residual rate regime[26]. The currently recognised mechanism for rate resumption involves a rise in pH (to above pH 11) and the precipitation of zeolite phases. These are grown at the expense of the aluminosilicate alteration layer gel[181] by consuming Si and Al from the gel, leading to the breakdown of the alteration layer, a change in Si and Al solubility, and the renewed dissolution of the glass at a rate greater than the residual rate. There is still much uncertainty about how this occurs, but under the high pH conditions of a cementitious disposal facility, the formation of any phase that can consume Si and Al from the glass should be considered a potential risk to rate resumption. Further research is required to investigate the role of C-S-H and other phyllosilicate minerals (such as hydrotalcite and rhodesite) in rate resumption.

The presence of Fe has been linked to enhanced glass alteration. Significant amounts of Fe are likely to be present in a GDF post-closure due to corrosion of the steel canisters housing the vitrified waste. Iron enhances glass alteration through two processes: i) precipitation of Fe-silicates, which could act to continually remove Si from solution or the gel (reducing the protective properties of the gel[73]); and ii) formation of an amorphous Fe-rich gel layer[181,182]. In the current study Fe was identified in the alkali-gel and as Fe-silicates on the LBS glass. The source of Fe in this instance was the glass, however in a disposal facility environment all glass compositions will be exposed to large quantities of dissolved Fe therefore increasing the probability of enhanced glass dissolution.

This research emphasises the requirement for glass dissolution studies that consider the impact of canister corrosion and saturation of the engineered barriers by groundwater.

Chapter 7. Glass Dissolution using BFS:PC- and NRVB-equilibrated Water

7.1. Introduction

Until now, this thesis has focused on the dissolution of glass in synthetic cement waters that were conceptualised from a Portland cement (PC), with no additives. In reality, the cements used within a geological disposal facility will be varied in composition, and will contain various supplementary cementitious materials (SCMs) added to Portland cement to alter their properties for specific tasks. For example, in the KBS-3 geological disposal concept of Sweden, Finland and France (also under consideration for the UK's HLW) it is envisaged that a "low pH" cement (pH of ≤ 11)[183] will be used to line vaults within the disposal facility and to act as plugs and seals for bentonite-clad disposal vaults. In such cements, the pH is lowered by the addition of blast furnace slag (BFS, a largely amorphous material that is a by-product from the iron and steel industry[184]) and / or silica fume. There is very little free portlandite in low pH cements, resulting in a cement composed mostly of C-S-H. This has benefits to the disposal concept including approximately 50% less hydroxyl ions than conventional Portland cement, for a given volume of cement[183]; pH ≤ 11 is considered acceptable for avoiding alteration of bentonite[185].

One of the conceptual scenarios for UK ILW disposal, in a hard rock geology, plans to use a high-pH cement, composed of Portland cement, $Ca(OH)_2$ and $CaCO_3$. The Ca-rich fillers in this cement, known as the Nirex Reference Vault Backfill (NRVB), confer some specific properties, important for the safety functions of the GDF, which include: low strength to allow for retrieval of the waste packages if required; high porosity to facilitate gas transportation; large surface areas for radionuclide sorption; and conditioning of ground water to a high pH to retard the transportation of radionuclides[7,5], by reducing their solubility[186,187].

Due to the use of widely different SCMs, the composition and proportion of cement phases that form upon the hydration of BFS:PC and NRVB are significantly different. NRVB contains a significantly high proportion of Ca and carbonate (6.44 wt % $CaCO_3$), while a BFS:PC cement, typically blended at a ratio of 3:1 BFS:PC for construction applications[188], consists of calcium silicates and aluminosilicates (from the pozzolanic reaction of BFS) and a much lower concentration of $CaCO_3$ (2.49 wt %). There are significant differences in the content of Ca, K, and Si in each of the cement materials. Thus, when groundwater contacts these cements it is expected that the cement pore solution will exhibit different compositions.

To understand the effects that different cements may have on the dissolution of nuclear waste glass, this Chapter will compare the effects of BFS:PC (5.67:1)- and NRVB- equilibrated water (eq. water) on the dissolution mechanisms and kinetics of simulant glass wasteforms. The behaviour of MW25 glass (expected to contact solutions of BFS:PC cement in a GDF) and LBS glass (expected to contact solutions of NRVB cement in a GDF) are investigated, in addition to the International Simple Glass (ISG), allowing a comparison between other literature studies on dissolution in simplified solutions and also those on synthetic cement solutions in Chapters 4 to 6.

The methodology to prepare cement-equilibrated waters is described fully in Chapter 3. In brief: hardened cement pastes of NRVB and BFS:PC were cured for 826 days and equilibrated with deaerated UHQ water[3] for 28 days. The solutions were filtered prior to use in crushed glass powder (PCT-B) experiments. The resulting solution compositions are shown in Table 7.1. Samples of glass were contacted with these solutions at 50 °C for 112 days.

Table 7.1 Composition of NRVB and BFS:PC eq. water, mg L^{-1}, measured by ICP-OES. The values listed below are the average of all the blank samples throughout the 112 day experiment, errors are the standard deviation taken across each time point. Carbonate contributions were calculated from TG-MS data listed in Chapter 2.

Element	Concentration, mg L^{-1}	
	NRVB pH(RT) 12.65 ± 0.2	BFS:PC pH(RT) 12.53 ± 0.2
Ca	766 ± 59	487 ± 28
Na	13 ± 10	43 ± 6
K	36 ± 5	74 ± 7
Al	0.08 ± 0.2	1.96 ± 0.7
Si	1.79 ± 1.4	0.34 ± 1.4
*Mg	16 ± 9. *	0.30 ± 0.2
Fe	1.57 ± 0.7	1.67 ± 1.4
S	10 ± 7	13.5 ± 1.5
*$CaCO_3$	0.88	0.88

*Mg conc = 0 day 1-42, day 56 onwards ~ 20 mg L^{-1}
*$CaCO_3$ conc= calculated based on the dissolution of calcite in the hardened cement pastes using PHREEQC

[3] For simplicity, the hardened cement pastes were equilibrated in UHQ to gain a full understanding of the influence of cement composition on glass dissolution. Although previous Chapters assumed cement was equilibrated with clay groundwater, the necessary geochemical data to model NRVB or low-pH cement in granite, clay or saline water are not yet available; this is the topic of a current sister-PhD project ongoing at The University of Sheffield, and data will be forthcoming in the future.

7.2. Results (MW25, LBS & ISG in Equilibrated Cement Waters)

7.2.1. pH

Crushed glass with a surface area to volume ratio of ~1200 m^{-1} was exposed to cement equilibrated waters in static PCT-B tests. Figure 7.1 shows the pH of the cement equilibrated solutions over the course of the 112 d experiment.

It is well evidenced that pore solution from Portland cement pastes and BFS:PC pastes are in the range of pH(RT) 12.4 to 13.5 (thus, within this Chapter, the BFS:PC cement is not a "low-pH" cement, but rather a lower pH cement than NRVB)[8]. The measured pH of both blank solutions was observed to reside in this region. The average value for the BFS:PC eq. water blank was pH(RT) 12.5 ± 0.2 and for the NRVB-eq. water blank was similar, at a value of pH(RT) 12.7 ± 0.2. The MW25 and LBS glasses had a similar pH (within error). ISG exhibited a significant reduction in the pH(RT), from 12.5 ± 0.1 at 1 d to 11.3 ± 0.1 at 70 d, in the BFS:PC solution, indicating a potential removal of OH^- ions from the cement leachate. The pH remained above pH 10 in all cases, suggesting that carbonation of the solutions by atmospheric CO_2 did not occur.

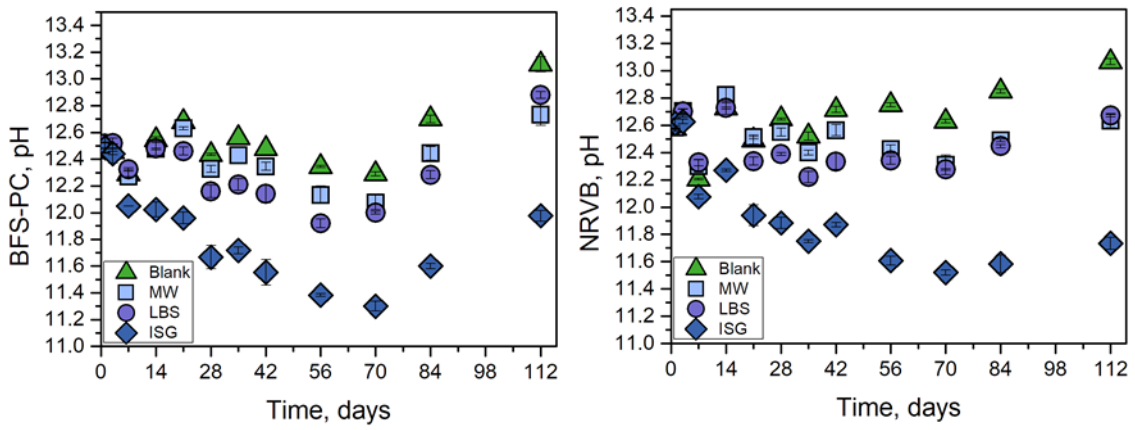

Figure 7.1 pH(RT) measurements for NRVB and BFS:PC eq. solutions without (blank) and upon contact with MW25, LBS and ISG.

7.2.2. Comparison of dissolution rates determined for MW25, LBS & ISG leached in BFS:PC and NRVB-equilibrated water

The dissolution rates of MW25, LBS and ISG were determined using the normalised mass loss of B as a tracer element (since not all glasses contained Li, this allows direct comparison of rates as a function of glass composition). The measured initial rates, calculated from the data points before the rate drop regime (identified by the slow-down of dissolution), are given in Table 7.2, in addition to the residual rate.

Table 7.2 Initial and Residual Rates, g m^{-2} d^{-1} for all glasses leached in NRVB and BFS:PC eq. water.

	Initial Rates (NR_0) NL_B, g m^{-2} d^{-1}		Residual Rates (NR_a) NL_B, g m^{-2} d^{-1}	
	BFS:PC	NRVB	BFS:PC	NRVB
MW25	(0.31 ± 0.01) x10^{-2}	(1.17 ± 0.09) x10^{-2}	(0.06 ± 0.01) x10^{-2}	(0.38 ± 0.02) x10^{-2}
LBS		(1.42 ± 0.30) x10^{-2}	(0.41 ± 0.03) x10^{-2}	(0.32 ± 0.01) x10^{-2}
ISG	(1.61 ± 0.03) x10^{-2}	(2.21 ± 0.38) x10^{-2}	(0.11 ± 0.04) x10^{-2}	(0.33 ± 0.05) x10^{-2}
NR_0(1-42 or 1-21 days)			NR_a (to 112 days)	
NR_0(1-56 or 112 days)				

Based on the initial rates for BFS:PC eq. water, ISG exhibited the fastest dissolution rate, as measured over the first 21 d at (1.61 ± 0.03) x 10^{-2} g $m^{-2}d^{-1}$. The lowest initial dissolution rate was exhibited by MW25, with a rate of (0.31 ±0.01) x 10^{-2} g m^{-2} d^{-1}, as calculated over the initial 21 d. The residual rate for MW25 and ISG was approximately an order of magnitude lower than the initial rates. It was not possible to calculate an initial rate for LBS as it did exhibit a "rate drop", however, the formation of a gel layer, as determined by SEM shown in Figure 7.7, confirms that the glass did enter the residual rate regime. The corresponding dissolution rate was an order of magnitude greater than those observed for MW25 and ISG.

For glasses dissolved in NRVB eq. water, the initial rate was between 1 to 5 times greater (depending on glass composition) than for glasses dissolved in BFS:PC eq. water. ISG exhibited the fastest initial rate when exposed to NRVB eq. water, as measured over the first 42 d, at (2.21 ± 0.3) x10^{-2} g m^{-2} d^{-1}. The residual rates for MW25 and LBS were three times lower than the initial rates obtained; ISG exhibited a 6-fold reduction in the rate of dissolution, from (2.21 ± 0.38) x10^{-2} g $m^{-2}d^{-1}$ in the initial regime to (0.33± 0.05) x10^{-2} g m^{-2} d^{-1} in the residual rate.

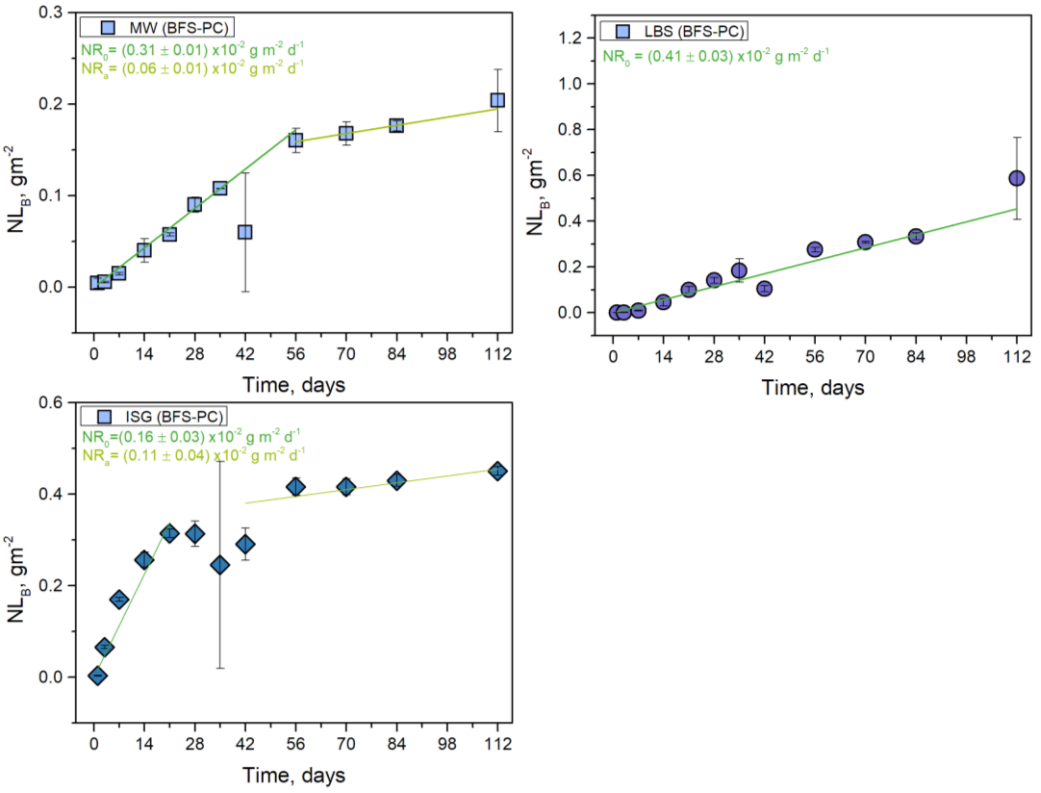

*Figure 7.2 Glass dissolution rates, g m^{-2} d^{-1} for MW25, LBS and ISG exposed to **BFS:PC** eq. cement water.*

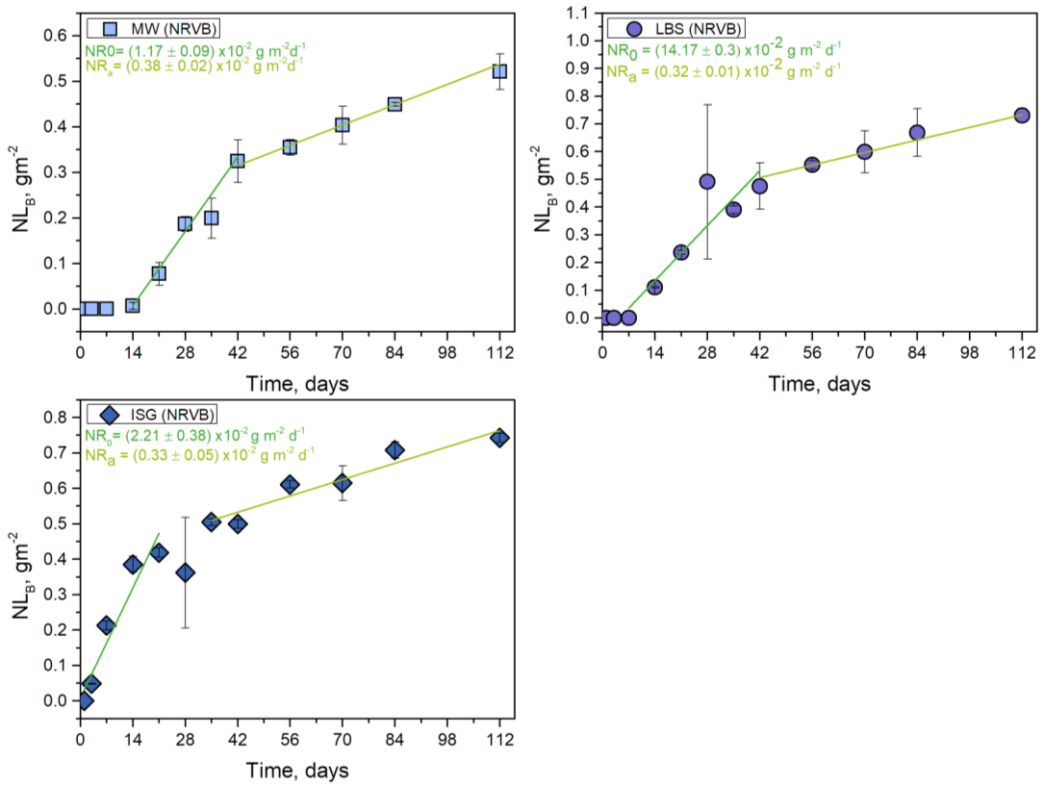

*Figure 7.3 Glass dissolution rates, g m^{-2} d^{-1} for MW25, LBS and ISG glass exposed to **NRVB** eq. waters*

7.2.3. Normalised Mass Loss of elements from MW25, LBS & ISG leached in in BFS:PC equilibrated water

The normalised mass loss of elements from MW25, LBS and ISG in BFS:PC eq. water as determined from ICP-OES analysis of filtered sacrificial triplicate aliquots, is depicted in Figure 7.4. Generally, LBS was observed to release a greater amount of each element from the glass to the solution when compared with MW25 and, as the experiment progressed, the separation between the NL_i values of LBS and MW25 increased. ISG generally had the highest NL_i values compared with the other glasses, as might be expected from its simplified 6-component composition, with the exception of Al (discussed later).

An increase in the release of B from all glass compositions was observed. ISG released the greatest amount of B, with the maximum normalised mass loss of NL_B $(45.1 \pm 0.9) \times 10^{-2}$ g m^{-2} after 112 d. The LBS glass composition released less B than the ISG, with the exception of the final time point when the greatest normalised mass loss of B occurred (NL_B = $(58.62 \pm 2.9) \times 10^{-2}$ g m^{-2}). The NL_B for MW25 was approximately half that of ISG, giving a maximum value of $(20.37 \pm 3.4) \times 10^{-2}$ g m^{-2} after 112 d. The NL_{Li} for MW25 and LBS increased from $(1.38 \pm 0.90) \times 10^{-2}$ g m^{-2} to $(49.0 \pm 8.0) \times 10^{-2}$ g m^{-2} for MW25 and $(123.0 \pm 34.0) \times 10^{-2}$ g m^{-2} for LBS after 112 d. For the first 28 d the values were similar, followed by a more rapid release of Li from LBS (in agreement with the NL_B).

The NL_{Si} values remained close to zero for the first 14 days for ISG before continued release was observed with a maximum NL_{Si} value of $(5.70 \pm 0.02) \times 10^{-2}$ g m^{-2} at day 112. LBS exhibited a "Si-incubation" period for the first 28 days (during which time no Si was released). After 28 d, the NL_{Si} increased until a maximum of $(8.33 \pm 0.4) \times 10^{-2}$ g m^{-2} was reached at 112 d. The NL_{Si} of MW25 also remained close to zero, but in contrast to the other glass compositions, it remained at this value for the duration of the experiment; the maximum NL_{Si} for this glass was $(0.39 \pm 0.05) \times 10^{-2}$ g m^{-2} at day 112.

Aluminium was continuously released into solution for MW25 and LBS, however for ISG, after an initial increase, Al was consumed from solution after 21 days. This may be explained by an Al-enriched layer close to the pristine glass, as observed in the SEM EDS analysis (see Section 7.2.4). The normalised mass loss of Mg was low for MW25 and LBS, with values of < 0.015 g m^{-2}. Mg is not present within ISG, therefore is not reported here. Sodium followed a similar trend to Li, with the data points for MW25 and LBS being very close to zero for the first

28 d, after which time the NL_{Na} values increased to $(60.0 \pm 10.2) \times 10^{-2}$ g m^{-2} and $(195.0 \pm 60.0) \times 10^{-2}$ g m^{-2} at 112 d.

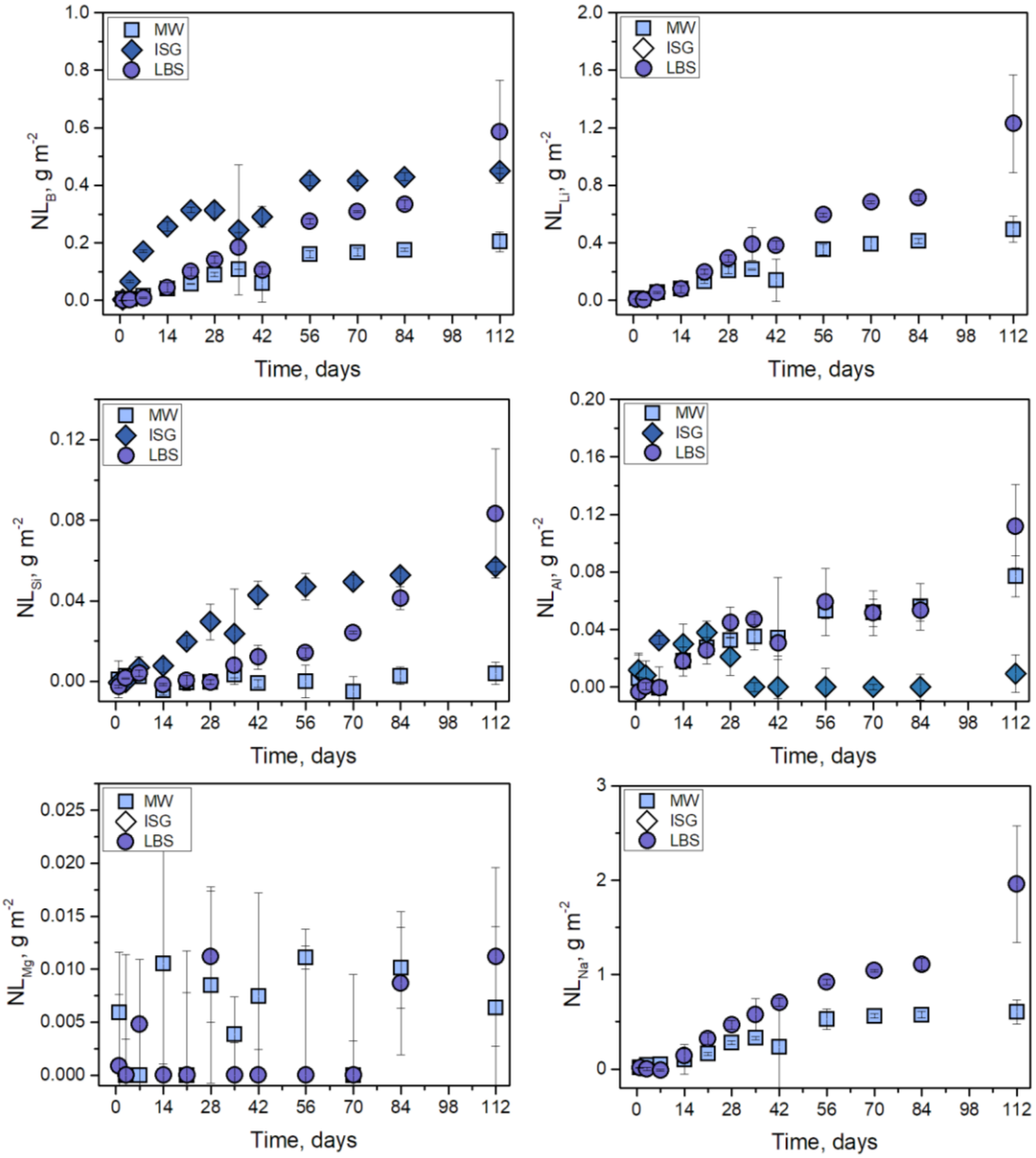

Figure 7.4 Normalised mass loss of elements from MW25, LBS and ISG glass powders exposed to BFS:PC eq. water for 112 days.

The major alkali and alkali earth components of equilibrated BFS:PC water are K and Ca, Figure *7.5* indicates that the concentration of Ca in the blank solutions remained around 800 mgL$^{-1,}$ while in the presence of glass powder, the concentration of Ca in BFS:PC eq. water diminished. This correlates with the formation of a Ca-containing silica gel surrounding the glass grains

(Section 7.2.4). Calcium is removed from solution most rapidly in ISG, and the other glasses follow the trend of ISG > LBS > MW25. The concentration of K in solution did not differ from the blank within error.

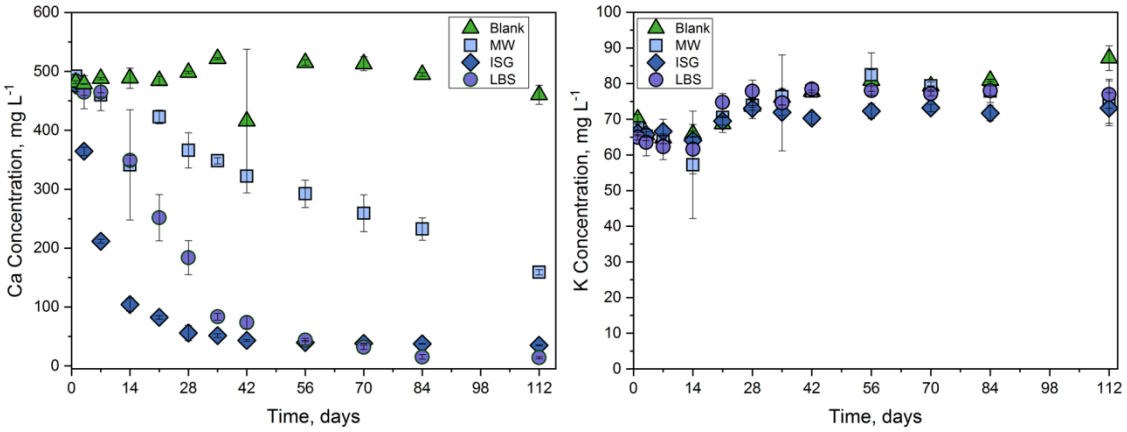

Figure 7.5 Concentration of Ca and K in BFS:PC eq. water over the duration of the experiment, errors are calculated based on the standard deviation of triplicate ICP results.

7.2.4. Alteration Layer Formation in BFS:PC-equilibrated water for MW25, LBS & ISG

The x-ray diffraction patterns of unreacted glasses are displayed on the left hand side of Figure 7.6 and the corresponding patterns obtained after 84 days of exposure to BFS:PC eq. water are on the right hand side. The results obtained show that, after leaching, calcite ($CaCO_3$; PDF 00-001-0837) and hydrotalcite ($Mg_6Al_2CO_3(OH)_6.4(H_2O)$; PDF 00-014- 0191) are present on the surface of MW25 glass grains. The presence of hydrotalcite requires the leaching of Mg and Al from the glass, in addition to the presence of carbonate. It is unlikely that, due to the high pH of the blank solutions, the source of the carbonate was atmospheric CO_2. X-ray diffraction of the initial cement material (Chapter 3, Section 3.1.4)) confirms the presence of carbonate in the form of calcite, which has subsequently leached into the equilibration solution and supported formation of the layered double hydroxide (LDH) phase, hydrotalcite. A similar Mg- and Al-containing LDH phase was reported by Backhouse in his investigation of MW25 glass dissolution in a saturated $Ca(OH)_2$ solution, however due to the imposed preclusion of carbonate through their experimental methods, the hydroxide end-member of the same phase, meixnerite ($Mg_6Al_2(OH)_{18}{\cdot}4.5H_2O$), was observed.

For LBS and ISG, the only identifiable feature observed in the diffraction pattern of samples after dissolution was an area of diffuse scattering at approximately ~29.4 ^{o} 2θ. This is indicative of the presence of poorly crystalline C-S-H ($CaOSiO_2H_2O$; PDF 00-033-0306). The absence of hydrotalcite in the diffraction pattern for LBS is intriguing, since this glass also contains a relatively high proportion of Mg (5.89 mol% in LBS compared with 6.02 mol% in MW25), however the detection limit of the XRD may not be sufficient to reveal the complete alteration layer mineral assemblage.

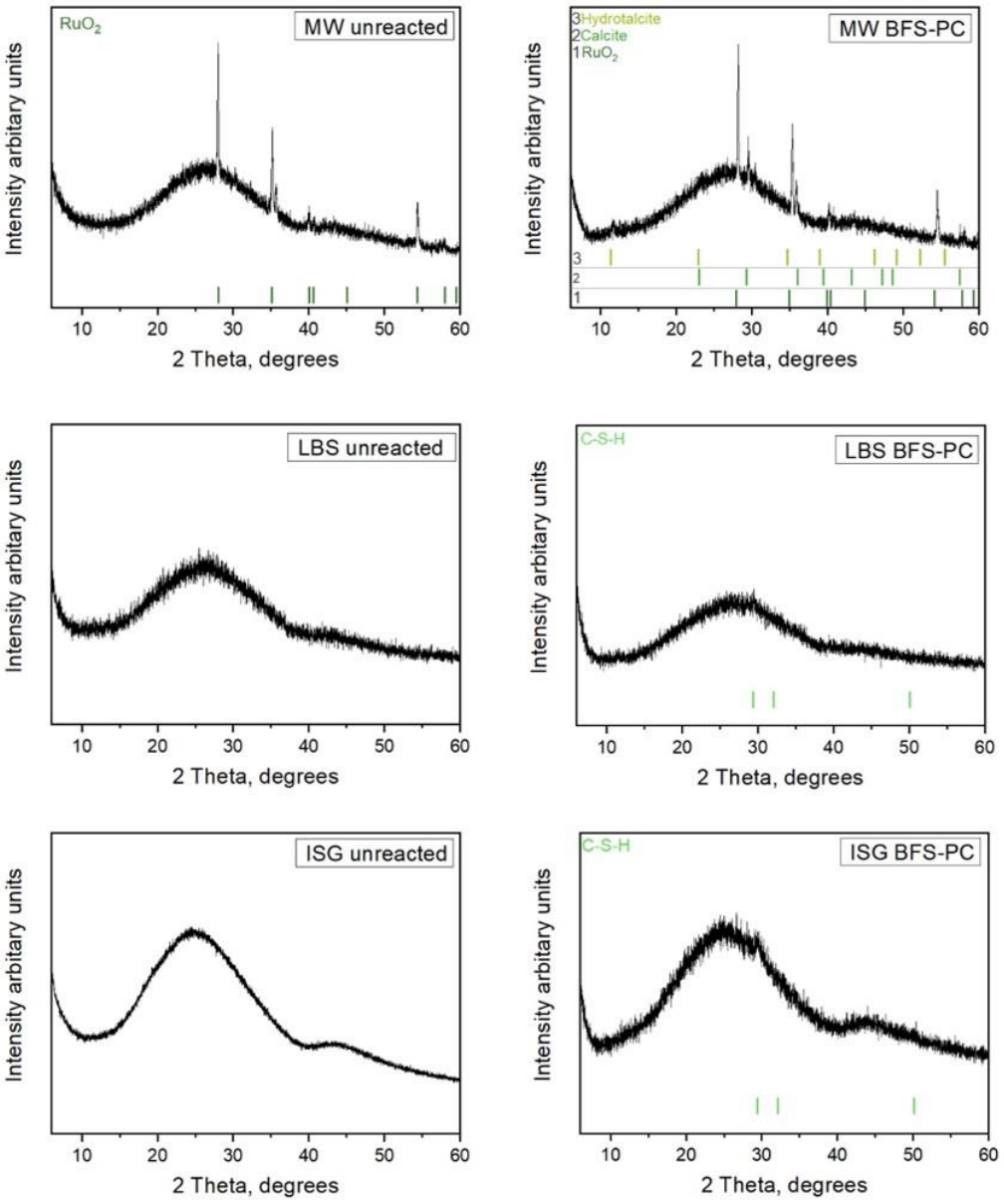

Figure 7.6 Diffraction patterns of MW25, LBS and ISG glass grains before (LHS) and after 84 days of dissolution in BFS:PC eq. water (RHS).

The measured alteration layer thicknesses are shown in Figure 7.7 and Table 7.3. The ISG exhibited the greatest alteration layer thickness, at 5.31 ± 0.16 μm, based on the average thickness taken from > 40 line measurements on a minimum of 5 grains. The average thickness of the alteration layers on MW25 was 4.63 ± 0.46 μm and on LBS was slightly lower, at 3.96 ± 0.06 μm. The measured thicknesses are considerably greater than those predicted using the boron equivalent thickness method (which uses the NL_B in the initial rate to predict the equivalent thickness of the alteration layer assuming congruent dissolution of all elements, Table 7.3); this clearly shows that species from the solution, rather than the glass influenced the alteration layer formation.

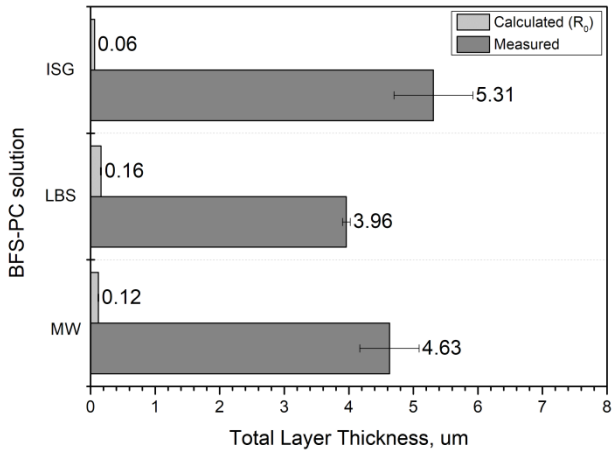

Figure 7.7 Altered layer thickness, measured using SEM line measurements and calculated using the initial dissolution rate (error calculated based on the standard deviation of all measurements ~300 measurements for each glass)

Table 7.3 Total altered layer thickness; measured by image processing electron micrographs, calculated using the initial dissolution rate, and calculated using equivalent boron thickness

Alteration Layer Thickness, μm after 84 d in BFS:PC equilibrated water			
	Measured, μm	Calculated (R_0), μm	Equivalent B thickness, μm
ISG	5.31 ± 0.61	0.06 ± 0.00	0.24 ± 0.005
LBS	3.96 ± 0.06	0.16 ± 0.01	0.36 ± 0.01
MW25	4.63 ± 0.46	0.12 ± 0.01	0.095 ± 0.01

Powders of each glass, subjected to BFS:PC eq. water for 84 days were analysed by SEM/EDX. Alteration products were visible on all glasses, however, the morphology was not consistent between the three glass compositions, as shown in Figure 7.8.

On the MW25 glass samples, bright flecks within the bulk of the glass (Figure 7.8) indicated the existence of Ru, present as RuO_2 crystalline impurity in the glass (see also Figure 7.9). The edge of the grain shown in Figure 7.9 is broken, however a thin alteration layer surrounded the entire grain. The layer surrounding the LBS grain (see Figure 7.10), consisted of a thin gel-like layer surrounded by a brighter layer that did not follow the outline of the glass grain. On the outside of this, several precipitates were observed. Very few of the ISG grains appeared to have smooth surfaces; this is to be expected when glass is crushed and no actions are made to reduce the stress on the glass, however it was unusual to see such a large proportion of grains to be damaged in this way. The small fractures at the surface of the ISG glass (as seen in Figure 7.8) have inevitably increased the surface area, which may contribute to the more rapid dissolution of this glass as compared to MW and LBS. The presence of a gel layer was more difficult to identify on the ISG sample (Figure 7.11) at the resolution employed, but "whispy" alteration products were apparent on the surface of the glass that were surrounded by an outer rim.

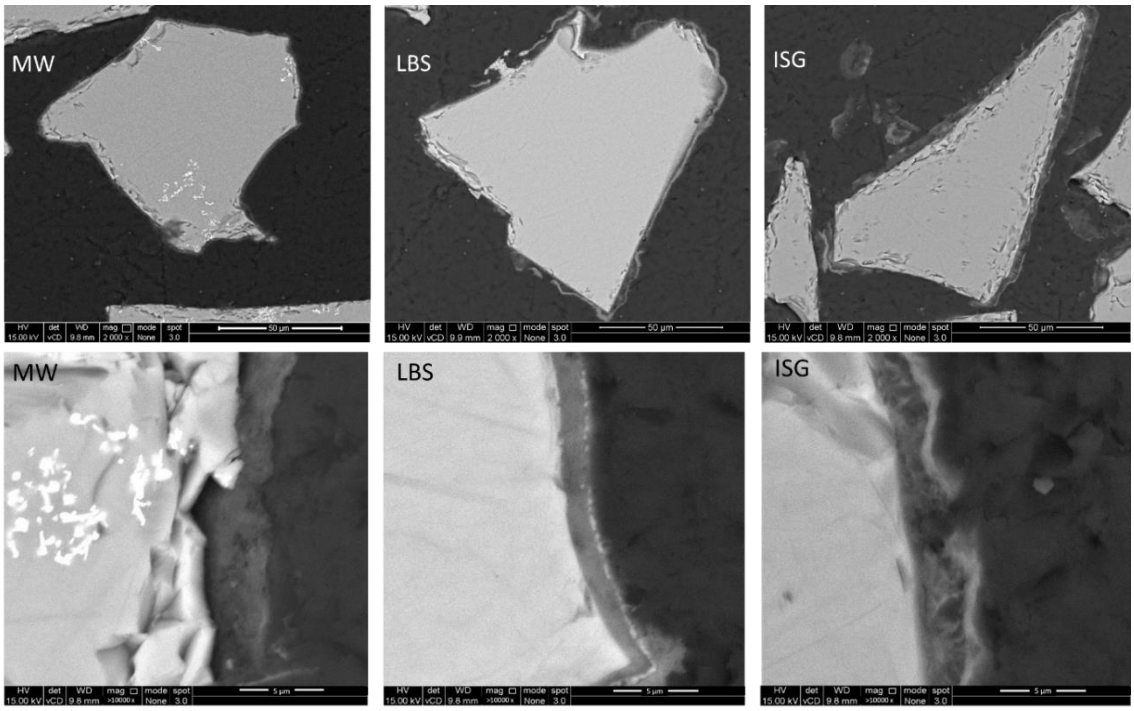

Figure 7.8 Backscattered SEM images of MW25, LBS and ISG glass grains exposed to BFS:PC eq. water for 84 d, bottom row of images are at a higher magnification.

i. MW25 exposed to BFS:PC equilibrated water

MW25 exposed to BFS:PC equilibrated solution for 84 days showed the presence of three distinct alteration layers (see Figure 7.9.a). The elemental information collected using EDS is shown in Table 7.4 and Figure 7.9.b & c. Layer 1 appeared to have a composition similar to the bulk glass, owing to its slightly lower content of soluble glass elements (Si, Fe, Al and Na) with respect to the bulk glass this region could be hydrated glass, however, enrichment of Ca (twice as much Ca when compared to the bulk glass) indicates this is more likely to be a Ca-rich gel phase. Layer 2 was found to be composed of Ca and Si with Ca:Si ratio of 1.1. Finally, an outer rim, labelled in Figure 7.9a, was also found to contain Ca and Si only, but with a slightly lower Ca:Si ratio than Layer 2, of 0.9.

The atomic percent of Ca present in layer 2 was 36 at % compared to the bulk glass with a value of 7 at %, indicating that Ca was removed from the solution to facilitate the formation of alteration products on the surface of the glass (Ca removal from solution can be seen in Figure 7.5).

Table 7.4 SEM F50 EDS spot maps associated with Figure 7.9, average elemental composition of each alteration layer on the surface of MW25 after 84 d exposure to BFS:PC eq. water.

Element At %	Na	Mg	Al	Si	S	K	Ca	Fe	Other
Bulk glass (23)	14.35 ± 0.72	6.79 ± 0.34	13.33 ± 0.67	52.42 ± 2.62	-	-	7.32 ± 0.37	2.25 ± 0.11	3.94 ± 0.20
Layer 1 (24,25)	12.50 ± 4.67	6.26 ± 0.63	11.56 ± 1.19	48.00 ± 1.34	1.87 ± 0.09	0.00 ± 0.23	14.63 ± 6.94	1.70 ± 0.06	1.87 ± 3.02
Layer 2 (28-30)	3.23 ± 1.39	0.60 ± 0.47	4.84 ± 0.59	33.87 ± 2.49	2.87 ± 0.76	0.10 ± 0.58	35.88 ± 2.60	1.66 ± 0.17	5.08 ± 7.02
Rim (26,27)	1.70 ± 0.81	0.64 ± 0.50	5.14 ± 0.64	39.66 ± 5.07	2.63 ± 0.13	-	39.47 ± 1.96	0.40 ± 1.17	4.05 ± 6.61

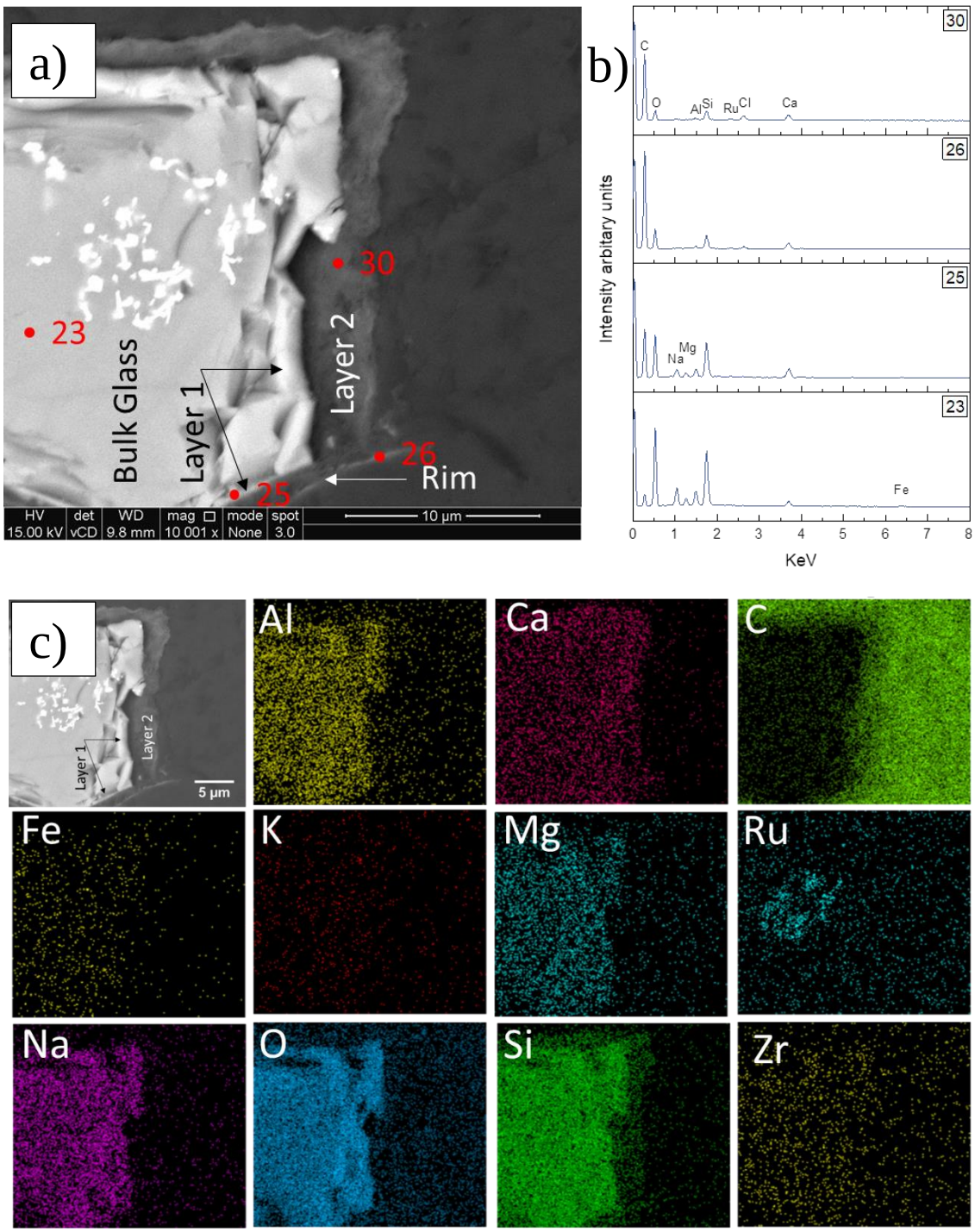

Figure 7.9 SEM analysis on MW25 post exposure to BFS:PC-eq solution for 84 days; a) BSE image, labels indicate alteration products, red spots correspond to the spot analysis in b), c) elemental maps.

ii. LBS exposed to BFS:PC equilibrated water

The alteration layers surrounding the LBS grains in Figure 7.10 were not uniform around the grains; gel, precipitates and nodules were observed in different areas around the grains. Elemental analysis by EDS (Figure 7.10 b & c) show that there is little compositional difference between the bulk glass and Layer 1, suggesting that this layer is likely a broken surface of the pristine glass. However, Layer 2 had a darker Z contrast in the BSE image, confirming a differing composition from the bulk glass. EDS analysis indicated a reduction in the quantity of Al, Na and Mg (Table 7.5) compared to the bulk, and an increase in the amount of Ca, signalling that Ca was removed from solution and utilised in the formation of a Ca-rich silica gel with a Ca:Si ratio of 0.34. The rim encasing the majority of the alteration products exhibited brighter Z contrast compared to the gel (Layer 2) and was composed of nodules clumped together in a chain-like formation. Compositionally, the rim had a greater amount of Mg compared to the gel layer (2) and the bulk glass but was relatively depleted in all other elements compared to Layer 2. The outer precipitate (Layer 3) had a wispy appearance and exhibited a greater Ca:Si ratio, of 0.71, confirming the presence of a Ca-silica precipitate, given the wispy nature it is likely to be C-S-H.

Table 7.5 SEM F50 EDS spot maps associated with Figure 7.10, average elemental composition of each alteration layer on the surface of LBS after 84 d exposure to BFS:PC eq. water.

Element At %	Na	Mg	Al	Si	S	K	Ca	Fe	Other
Bulk glass (1)	20.14 ± 1.01	4.87 ± 0.24	15.00 ± 0.75	50.17 ± 2.51	-	0.42 ± 0.02	0.45 ± 0.02	8.09 ± 0.40	0.86 ± 0.04
Layer 1 (2,3)	19.79 ± 0.45	4.65 ± 0.36	15.30 ± 0.19	50.16 ± 1.03	0.39 ± 0.06	0.25 ± 0.10	1.96 ± 0.13	6.42 ± 0.19	1.10 ± 0.35
Layer 2(4,5)	8.63 ± 0.26	3.98 ± 1.07	11.82 ± 0.09	45.28 ± 0.98	1.79 ± 0.46	0.33 ± 0.14	15.44 ± 0.64	8.65 ± 0.53	2.60 ± 0.46
Rim (6,7)	5.01 ± 0.74	10.95 ± 3.88	12.13 ± 1.26	40.37 ± 2.63	1.09 ± 0.93	0.44 - 0.05	17.78 ± 1.97	8.34 ± 0.71	0.81 ± 0.65
Precipitate (8-10)	2.32 ± 0.93	2.09 ± 0.23	7.13 ± 0.04	46.08 ± 1.32	0.54 ± 0.59	0.02 ± 0.24	32.68 ± 1.09	6.67 ± 0.42	0.41 ± 0.35

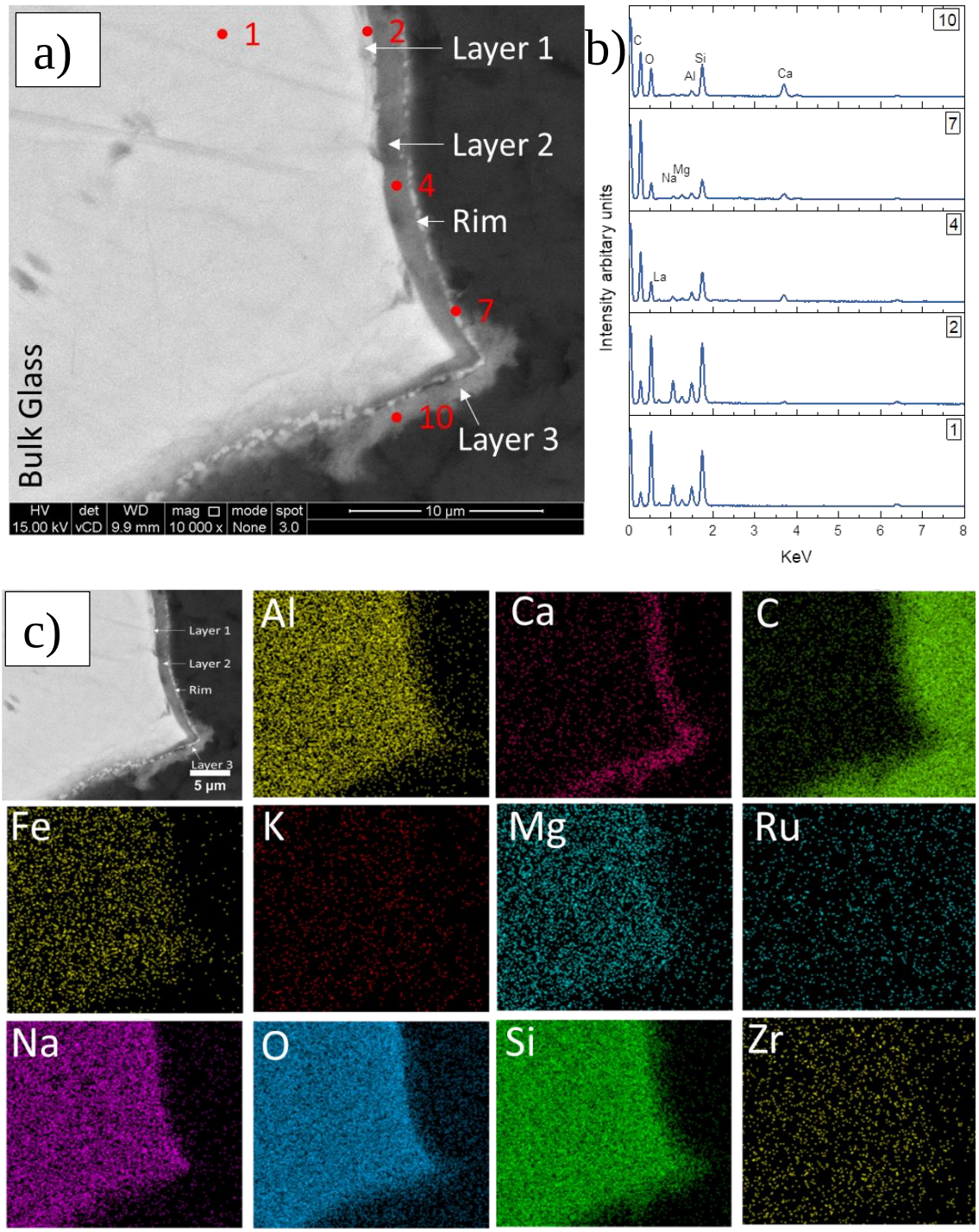

Figure 7.10 SEM analysis of LBS exposed to BFS:PC eq. water for 84 days; a) BSE image, labels indicate alteration products, red spots correspond to the spot analysis in b), c) elemental maps.

iii. ISG exposed to BFS:PC equilibrated water

ISG exposed to BFS:PC eq. water demonstrated three distinct regions (see Figure 7.10). Layer 1, in direct contact with the pristine glass, was found to contain Na, Al, Si, K, Ca and Zr, all in similar at % as that found in the bulk glass. Layer 2 had a fibrous morphology with needle-like precipitates that appeared to have originated close to the pristine glass and grown outwards. This layer exhibited a reduction in the amount of Na, Al and Si present compared to the bulk glass, with an enrichment of Ca (from 6 at % in the bulk to 28 at % Table 7.6) sourced from the BFS:PC eq. water and also contained traces of Fe and K. Sodium, which is highly soluble under the high pH environment of this solution, was depleted in Layer 2 compared to the pristine glass, and the Ca:Si ratio of this layer was 0.54. On the outside of this layer (i.e. in direct contact with the solution during dissolution) was a smooth-edged outer rim without the presence of nodules (as observed on LBS, Figure 7.10), which was composed of Na, Mg, Al, Si, K, Ca, Fe. The dominant elements in this region were Ca and Si and the layer had a Ca:Si ratio of 0.8.

Table 7.6 SEM F50 EDS spot maps associated with Figure 7.11, average elemental composition of each alteration layer on the surface of ISG after 84 d exposure to BFS:PC eq. water.

Element At %	Na	Mg	Al	Si	S	K	Ca	Fe	Other
Bulk glass (11)	18.93 ± 0.95	0.44 ± 0.02	7.68 ± 0.38	64.31 ± 3.22	-	0.03 ± 0.01	6.61 ± 0.33	-	2.18 ± 0.11
Layer 1 (12,13)	18.49 ± 0.59	-	8.06 ± 0.20	63.85 ± 0.74	-	0.15 ± 0.01	7.09 ± 0.21	-	2.60 ± 0.27
Layer 2(17-22)	7.13 ± 1.81	-	6.17 ± 0.42	52.58 ± 2.90	-	0.39 ± 0.38	28.32 ± 4.01	0.23 ± 0.45	5.32 ± 1.03
Rim (14-16)	1.95 ± 0.64	0.07 ± 0.82	6.37 ± 0.37	47.51 ± 0.96	-	0.40 - 0.42	39.22 ± 1.45	0.24 ± 0.28	4.24 ± 0.97

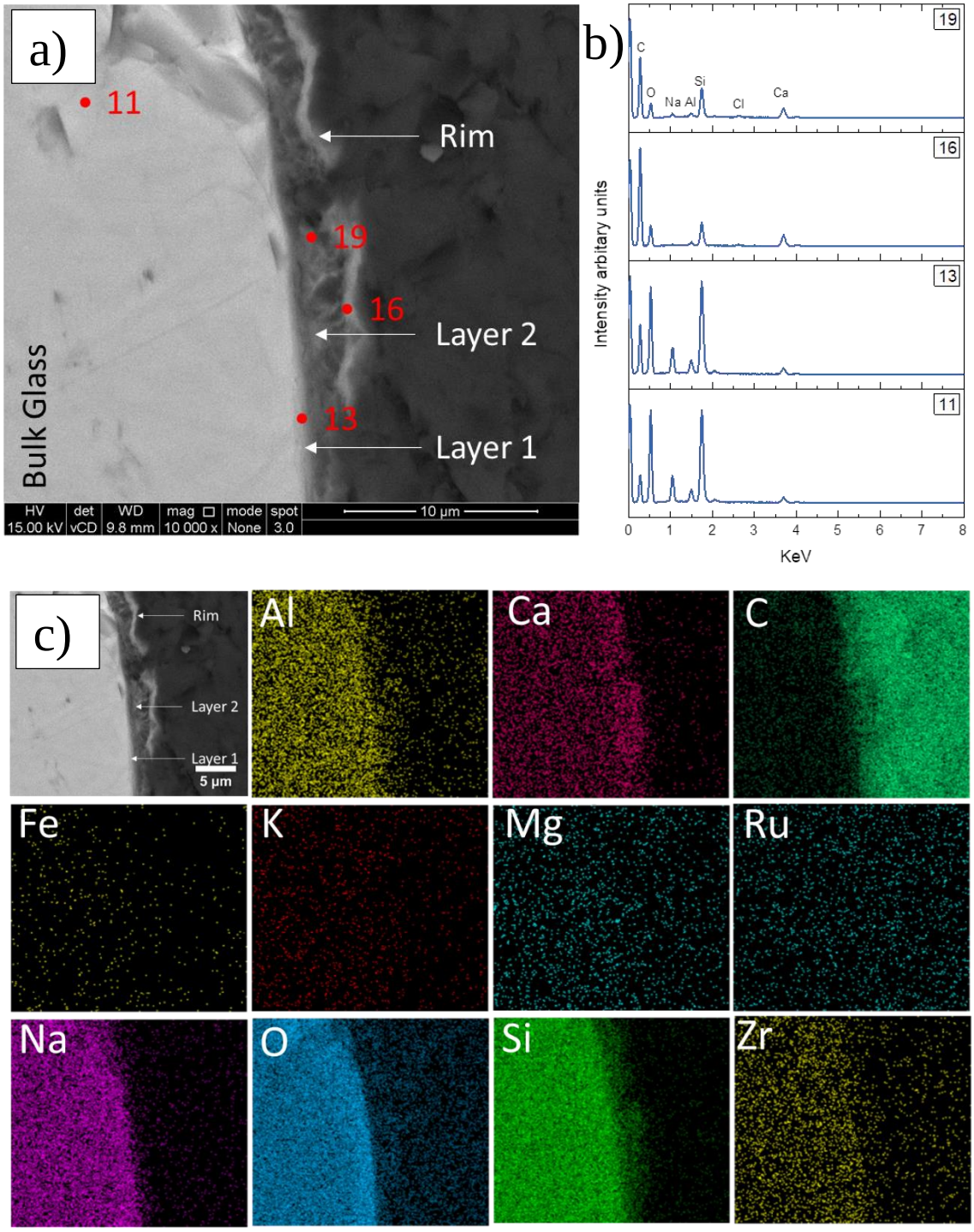

Figure 7.11 SEM analysis from ISG exposed to BFS:PC eq. water for 84 days; a) BSE image, labels indicate alteration products, red spots correspond to the spot analysis in b), c) elemental maps.

7.2.5. Normalised Mass Loss of MW25, LBS & ISG in NRVB-equilibrated water

The normalised mass loss of elements from each of the glass compositions leached in NRVB-eq. water is shown in Figure 7.12. Generally, there was a greater accumulation of elements in solution released from LBS compared to MW25, as the experiment progressed. The initial rates (Section 7.2.2, Table 7.2) for MW25, LBS and ISG were $(1.17 \pm 0.09)\ x10^{-2}\ g\ m^{-2}$, $(1.42 \pm 0.30)\ x\ 10^{-2}\ g\ m^{-2}\ d^{-1}$ and $(2.21 \pm 0.38)\ x\ 10^{-2}\ g\ m^{-2}\ d^{-1}$, respectively.

Boron was continually leached from all glass compositions; ISG exhibited the greatest release with a maximum NL_B of $(74.28 \pm 1.34)\ x10^{-2}\ g\ m^{-2}$ obtained after 112 d. The LBS glass showed an "induction period" where the NL_B was at a steady low level for the first 7 days, after which time it increased to $(66.88 \pm 8.67)\ x10^{-2}\ g\ m^{-2}$ after 84 d. MW25 had the lowest NL_B of all three glass compositions, with a maximum NL_B value of $(52.14 \pm 3.93)\ x10^{-2}\ g\ m^{-2}$ after 112 d. The normalised mass loss of Li from MW25 and LBS (no Li in ISG) followed the same trend as NL_B; for LBS, a maximum NL_{Li} of $(707.7 \pm 4.39)\ x10^{-2}\ g\ m^{-2}$ was observed after 112 d, and MW25 exhibited a maximum NL_{Li} of $(350.3 \pm 9.52)\ x10^{-2}\ g\ m^{-2}$ after 112 d.

The MW25 glass composition had the lowest NL_{Si} values, which remained close to zero throughout the experiment; the maximum value measured was $(0.47 \pm 0.18)\ x10^{-2}\ g\ m^{-2}$ on day 21. The NL_{Si} of the LBS glass composition was twice that of MW25, with a maximum value of $(0.78 \pm 0.90)\ x10^{-2}\ g\ m^{-2}$ after 28 d, and the ISG exhibited the greatest NL_{Si}, with a maximum of $(2.52 \pm 0.19)\ x10^{-2}\ g\ m^{-2}$ after 35 d.

A definitive trend for NL_{Al} was not elucidated since most solution measurements were below the detection limit of the instrument (as evidenced by the large error bars in Figure 7.12). The NL_{Mg} data were likewise below the detection limit for the first 42 days. After that time, the NL_{Mg} averaged at $(25 \pm 4)\ x10^{-2}\ g\ m^{-2}$ for MW25 and $(55 \pm 4)\ x10^{-2}\ g\ m^{-2}$ for LBS glass between 42 - 112 d.

The normalised mass loss of Na, however, did not follow that of boron. The release of Na gradually increased until 35 d for all glass compositions, after which time the values decreased to zero. SEM EDS showed that Na was depleted in the alteration layers compared to the bulk glass for all three glass compositions, confirming that Na was not incorporated into the alteration layer. This anomalous result for all glass compositions, which is in direct contradiction to the surface analysis is likely to be an ICP-OES analysis issue.

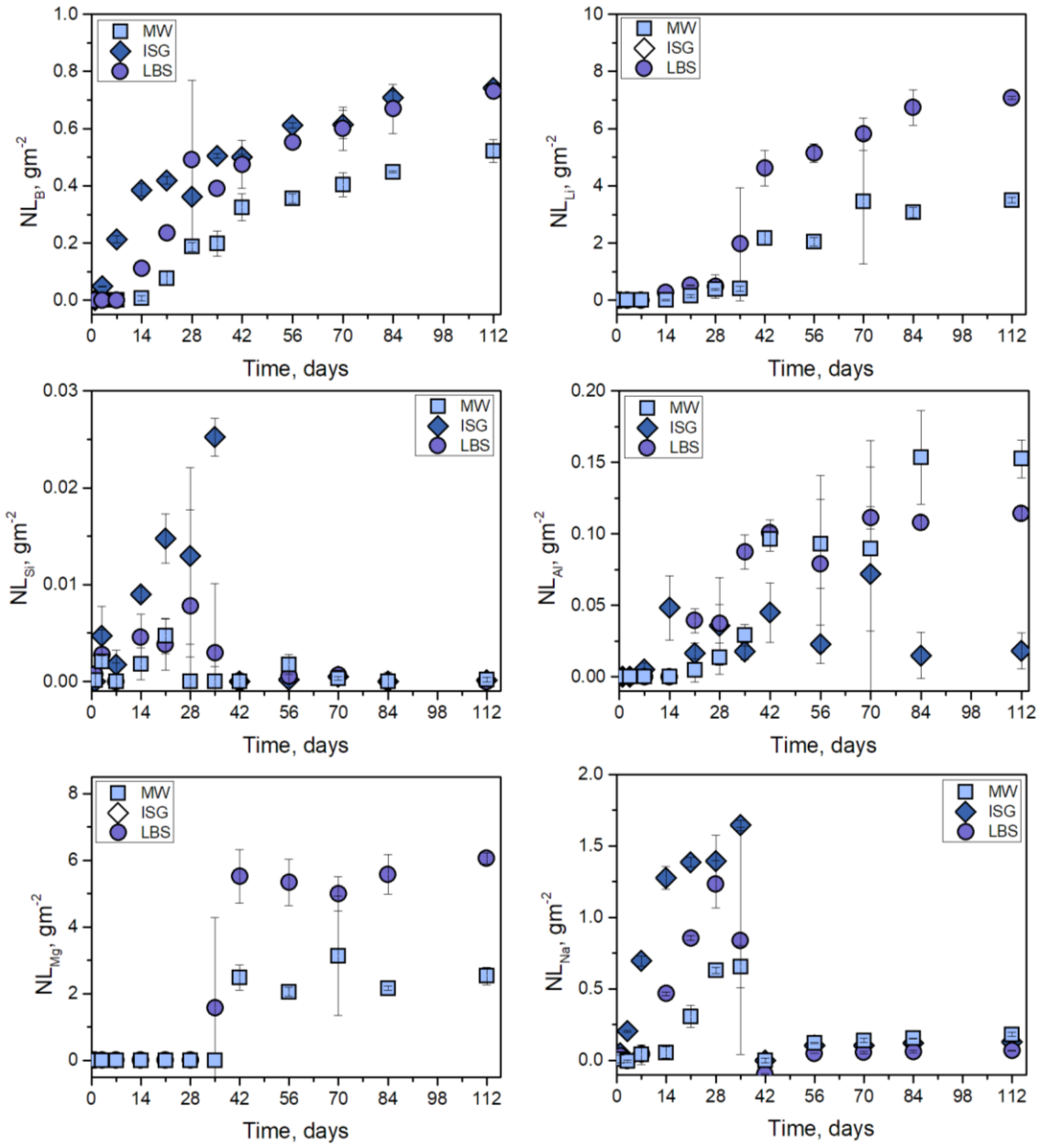

Figure 7.12 Normalised mass loss of elements from MW25, LBS and ISG exposed to NRVB eq. water

Figure 7.13 shows the concentration of Ca and K from NRVB eq. water over the duration of the experiment. The concentration of Ca in the blank solutions was between 800 to 900 mg L^{-1} and, in the presence of glass powder, the concentration of Ca diminished. This correlates with the formation of a Ca-silica gel surrounding the glass grains (Section 7.2.6). Calcium was removed from solution most rapidly for ISG and the other glasses showed the same trend in Ca removal from solution as for BFS:PC-eq. water: ISG > LBS > MW25. The concentration of K in solution did not differ from the blank within error.

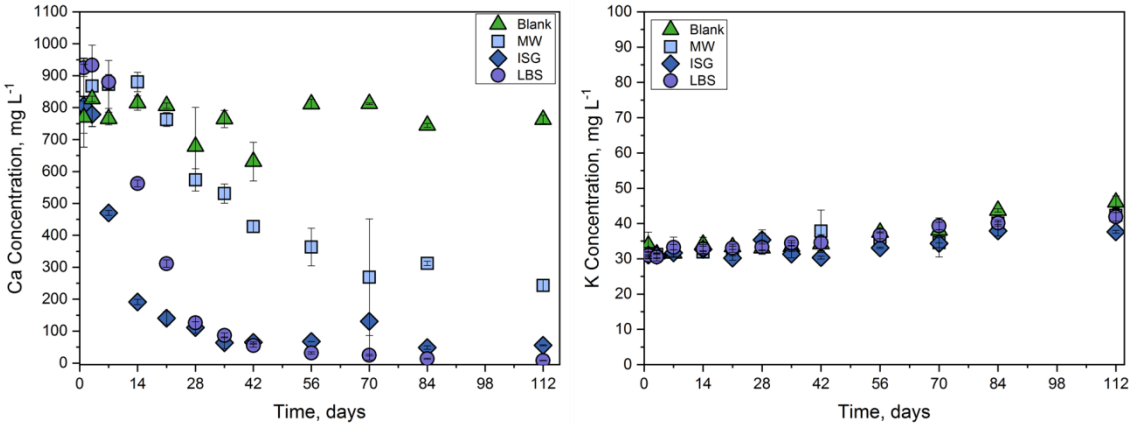

Figure 7.13 Concentration of Ca and K in NRVB eq. water over the duration of the experiment

7.2.6. Alteration Layer Formation in NRVB equilibrated water for MW25, LBS & ISG

X-ray diffraction patterns for the three unreacted glass compositions are displayed on the left hand side of Figure 7.14, and the corresponding patterns obtained after 84 days of exposure to NRVB eq. water are on the right hand side. Small peaks were identified in the MW25 glass sample post-dissolution that were supressed by the background diffraction pattern. In addition to the clearly identifiable RuO_2 peaks, hydrotalcite ($Mg_6Al_2CO_3(OH)_6.4(H_2O)$; PDF 00-014- 0191) and calcite ($CaCO_3$; PDF 00-001-0837) peaks have been identified. The Mg and Al used to form hydrotalcite comes from glasses (because there should be very little Mg and Al leaching from hardened PC, 0.08 mg $L^{-1}$of Al was measured in the blank NRVB solution), MW25 and LBS. It is unlikely that, due to the high pH of the blank solutions, the source of the carbonate was atmospheric CO_2, and since X-ray diffraction of the initial NRVB material (Chapter 3, Section 3.1.4)) confirms the presence of carbonate in the form of calcite, monocarboaluminate ($3CaO{\cdot}Al_2O_3{\cdot}CaCO_3{\cdot}xH_2O$) and hemicarboaluminate ($Ca_8Al_4CO_{16}{:}xH_2O$), it can be concluded that carbonate leached into the cement equilibrated solution and supported formation of the layered double hydroxide (LDH) phase, hydrotalcite.

The broad peaks at 29.35 ° 2θ and 50.07 ° 2θ are attributed to the presence of poorly crystalline C-S-H ($CaOSiO_2H_2O$; PDF 00-033-0306), which is present on both LBS and ISG glass, but not MW25.

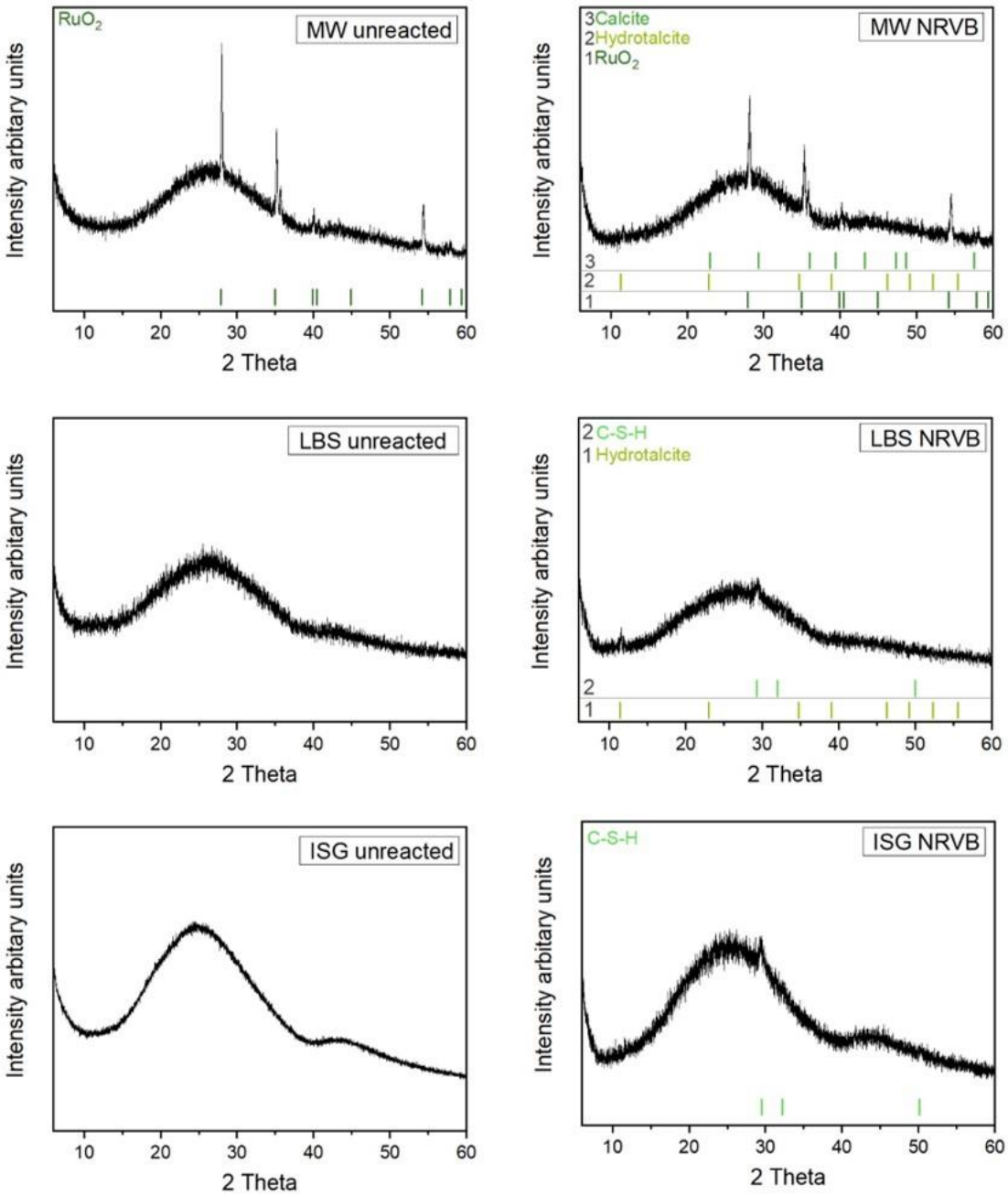

Figure 7.14 Diffraction patterns of MW25, LBS and ISG glass powders before dissolution (LHS) and after 84 days of dissolution in NRVB-eq. water (RHS)

The measured alteration layer thicknesses are shown in Figure 7.15 and Table 7.7. More than 40 line measurements were made on SEM images of glass grains (a minimum of 5 grains) using image J. Additionally, the thickness was calculated using the initial rate based on the NL_B (Section 3.4). There is a significant difference between the measured and calculated values, it is likely that the measured values over estimate the total thickness because a small proportion of grains are selected for analysis, and is evidence that elements from the solution have been incorporated in the formation of gel and precipitate phases as observed in the SEM EDS measurements for each glass (see Figure 7.17). Of the alteration layers formed after 84 days in NRVB eq. water, ISG exhibited a measured average thickness of 4.31 ± 0.56 µm, LBS grains had layers that were on average 1 µm thinner than those on ISG (3.24 ± 0.64 µm) and MW25 displayed the thinnest alteration layers averaging a total thickness of 2.13 ± 0.35 µm.

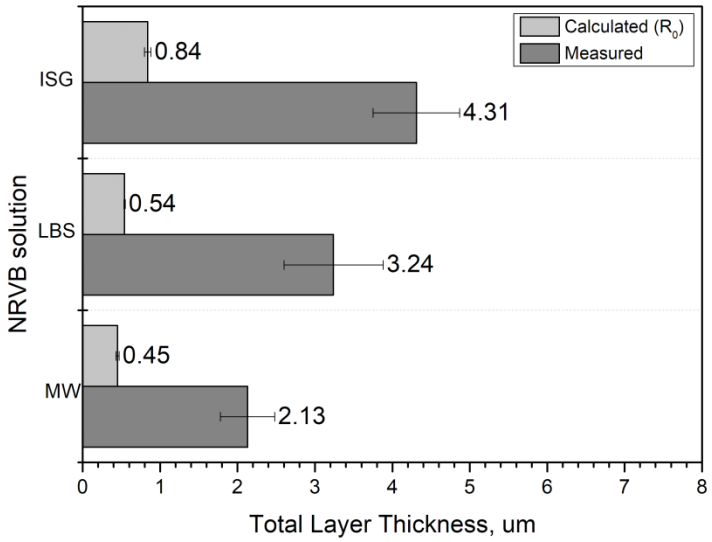

Figure 7.15 Altered layer thickness, measured using SEM line measurements and calculated using the initial dissolution rate (error calculated based on the standard deviation of all measurements ~300 measurements for each glass)

Table 7.7 Total altered layer thickness; measured by image processing electron micrographs, calculated using the initial dissolution rate, and calculated using equivalent boron thickness

NRVB Thickness ,µm after 84 d in NRVB eq. water			
	Measured, µm	Calculated (R_0), µm	Equivalent B thickness, µm
ISG	4.31 ± 0.56	0.84 ± 0.04	0.403 ± 0.05
LBS	3.24 ± 0.64	0.54 ± 0.01	0.698 ± 0.02
MW25	2.13 ± 0.35	0.45 ± 0.02	0.00003 ± 0.00

Powders of each glass, subjected to NRVB eq. water for 84 d were examined by SEM/EDX. Alteration products present on each of the three glasses were distinct, as shown in Figure 7.16. An alteration layer can be seen surrounding each glass grain (Figure 7.16). On the MW25 glass, the layer was always in direct contact with the pristine glass and the thickness did not vary significantly across the outside of the grains. The layers surrounding the LBS grain were not as uniform in thickness and a more complex variety of altered layers were observed, including a gel layer close to the pristine glass, nodules, and randomly distributed crystal growth and, finally, a reaction rim on the outermost surface. ISG exhibited alteration products that were perpendicular to the gel and reaction rim (‘ladder rungs’) discussed in Section 7.2.6 iii.

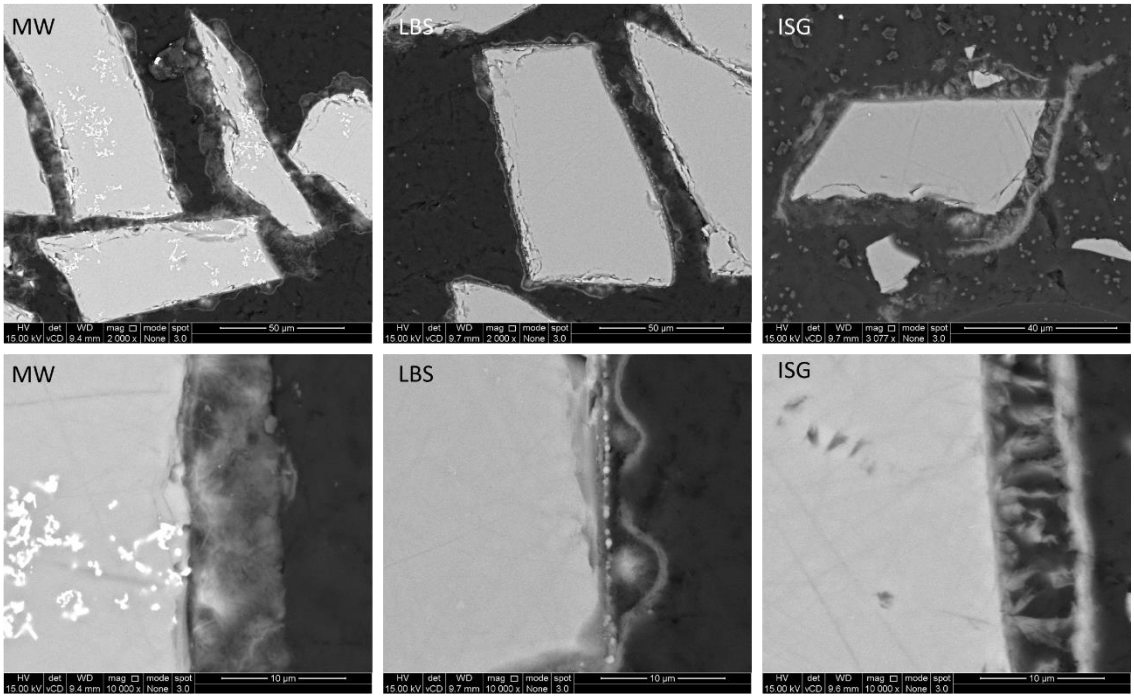

Figure 7.16 Backscattered SEM micrographs of a glass exposed to NRVB eq. water for 84 days, far left = MW25 glass, middle = LBS and right = ISG, bottom row of images are at higher magnification

i. MW25 exposed to NRVB equilibrated water

The MW25 glass grains exposed to NRVB eq. water for 84 days show the existance of two distinct alteration layers (see Figure 7.17a). Layer 1 appeared to have a composition similar to the bulk glass. Owing to its slightly lower content of soluble glass elements (Si, Fe, Al and Na) with respect to the bulk glass, this region could be hydrated glass however, enrichment of Ca (more than twice as much Ca compared to the bulk glass (Table 7.8)) indicates this is more likely to be a Ca-rich gel-like phase. The backscattered electron micrograph shows that Layer 2 is a Ca-Si precipitate comprised of two morphologically distinct phases: the brighter region is formed of clustered needles that reside close to the hydrated glass and are composed of Ca and Si with a Ca:Si ratio of 1.16, with trace amounts of Na, Mg, Al and Fe. The darker phase within Layer 2 had a simlar composition to the needles, however, contained considerably less Mg; a reduction from 5 at % in the needles to 0.3 at % in the dark region (Table 7.8). A decrease in the Ca:Si ratio to 0.92 was also observed in the darker region. Backhouse[70] observed alteration products with an acicular (needle like) morphology on the surface of MW25 glass exposed to $Ca(OH)_2$, and attributed them to clusters of C-S-H based on EDS analysis. C-S-H is a complex phase with a vast range of compositions, the Ca:Si ratios of Layer 2 fall within the given range of 0.5 to 2.5 according to Grandia et al. [128]. C-S-H is often an x-ray amorphous phase owing to its nanocrystalline nature, thus its presence was not confirmed in the XRD conducted on the MW25 glass grains. Analysis of the XRD data could also have been hampered by the presence of intense RuO_2 peaks and the diffuse scattering of the bulk glass.

Table 7.8 SEM F50 EDS spot maps associated with Figure 7.17, average elemental composition of each alteration layer on the surface of MW25 after 84 d exposure to NRVB eq. water.

Element At %	Na	Mg	Al	Si	S	K	Ca	Fe	Other
Bulk glass (30, 31)	14.69 ± 0.12	7.40 ± 0.22	13.31 ± 0.03	50.43 ± 0.74	1.06 ± 0.05	0.10 - 0.14	6.42 ± 0.09	2.27 ± 0.25	5.35 ± 1.30
Layer 1 (32-34)	13.37 ± 3.61	7.12 ± 1.13	12.16 ± 2.28	45.39 ± 2.20	-	0.08 ± 0.11	14.38 ± 9.78	1.87 ± 0.12	5.71 ± 1.59
Layer 2, needles, bright region(35-38)	2.42 ± 0.97	5.58 ± 6.54	7.26 ± 2.92	36.07 ± 2.43	-	0.08 ± 0.08	41.87 ± 8.96	1.66 ± 0.38	6.65 ± 3.06
Layer 2, C-S-H, dark region (39-42)	2.10 ± 0.56	0.27 ± 0.41	6.24 ± 0.34	42.50 ± 2.56	1.52 ± 0.08	0.27 ± 0.13	38.96 ± 5.97	1.36 ± 0.61	5.92 ± 2.56

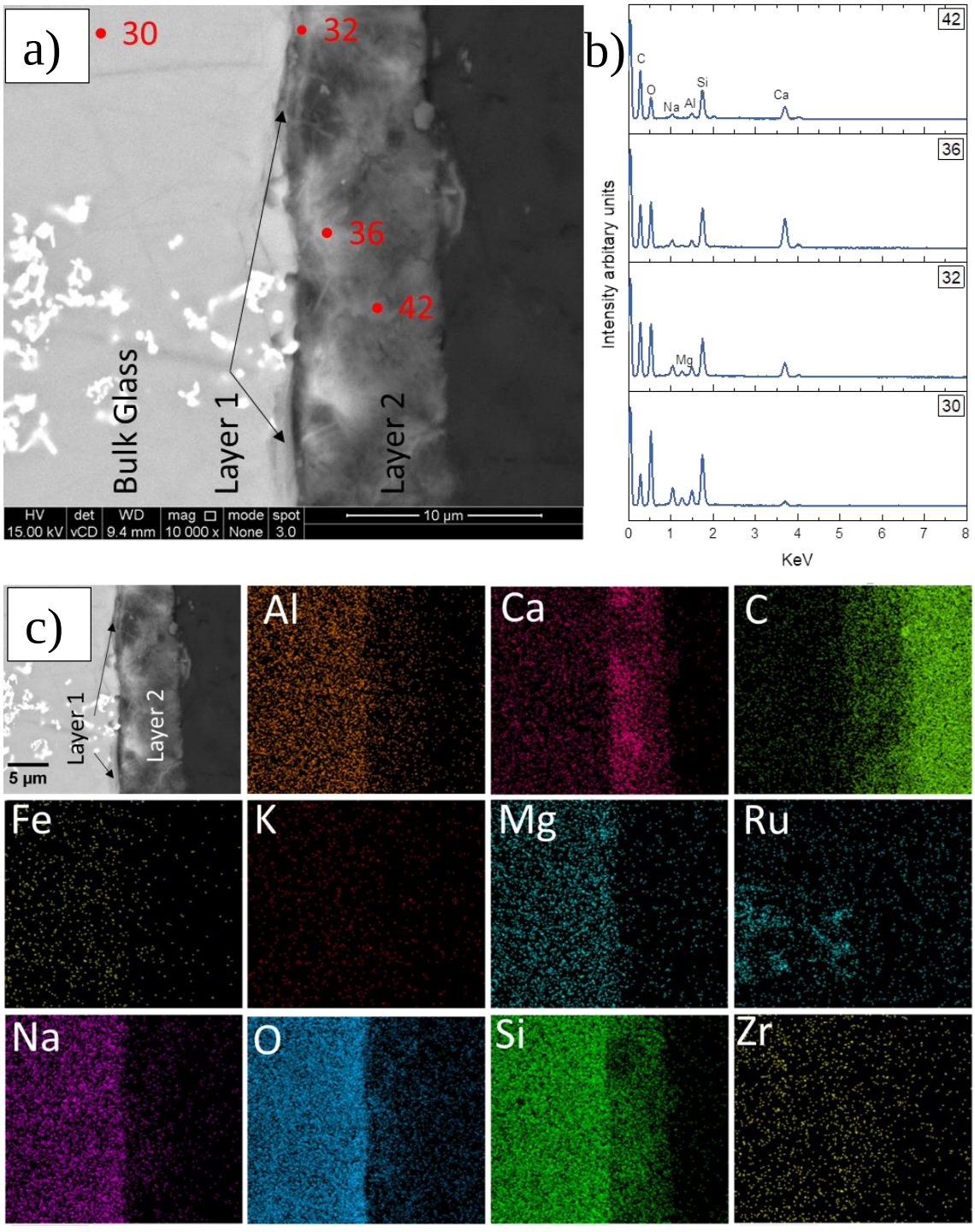

Figure 7.17 SEM analysis from MW25 exposed to NRVB eq. water for 84 days; a) BSE image, labels indicate alteration products, red spots correspond to the spot analysis in b), c) elemental maps.

ii. LBS exposed to NRVB equilibrated water

The alteration layers surrounding LBS glass grains in Figure 7.18 demonstrate the complexity of layer formation on this glass composition; three distinct layers have been identified. A region of broken glass was identified at the edge of the particle (Spot 14, Figure 7.18a) and a gel layer (Layer 1) was observed to form on top of this region. Layer 1 exhibited a reduction in the at % of Na compared to the bulk glass (Table 7.9), but an enrichment in Ca (from 0.95 at % in the bulk glass to 11.8 at % in Layer 1), indicating that Ca removed from solution aided the formation of a Ca-rich silica gel. Layer 2 comprised Ca-rich nodules (~ 25.9 at% Ca) with traces of Na, Mg, Al, Si, S, K and Fe, with a Ca:Si ratio of 0.62. This was the only layer observed to contain S.

Located sparsely, and unevenly distributed on top of the nodules, were radiating crystals composed of Ca and Si with a Ca:Si ratio of 0.72. The outer reaction rim (Layer 3) traced all of the irregular shapes that were formed on the surface of the glass sample as a result of the radiating crystals, and was composed mainly of Ca and Si (Ca:Si ratio of 0.75), with traces of Na, Mg, Al, K and Fe.

Table 7.9 SEM F50 EDS spot maps associated with Figure 7.18, average elemental composition of each alteration layer on the surface of LBS after 84 d exposure to NRVB eq. water.

Element At %	Na	Mg	Al	Si	S	K	Ca	Fe	Other
Bulk glass (1, 2)	19.06 ± 0.31	5.67 ± 0.20	9.55 ± 0.27	55.56 ± 0.12	-	0.04 ± 0.27	0.47 ± 0.21	8.84 ± 0.27	0.82 ± 0.06
Broken glass surface (14,15)	20.30 ± 0.84	6.16 ± 0.06	10.00 ± 0.37	53.97 ± 0.16	-	0.32 ± 0.01	0.95 ± 0.29	7.44 ± 0.49	1.17 ± 0.65
Layer 1, gel (8, 9,10)	11.45 ± 4.28	5.96 ± 1.42	9.77 ± 0.41	50.93 ± 3.55	-	0.22 ± 0.23	11.80 ± 6.21	9.29 ± 1.04	0.56 ± 0.55
Layer 2, nodules (11, 12,13)	5.45 ± 0.20	4.75 ± 0.43	8.44 ± 0.29	41.10 ± 2.26	2.73 ± 0.66	0.32 ± 0.29	25.88 ± 1.80	9.35 ± 1.18	2.90 ± 0.65
Large nodule (6, 7)	1.54 ± 0.23	0.63 ± 0.46	6.10 ± 0.59	49.38 ± 0.09	-	0.27 ± 0.08	35.31 ± 1.26	5.78 ± 0.67	1.67 ± 1.40
Layer 3, Rim (3,4, 5)	1.64 ± 0.45	1.09 ± 0.76	4.48 ± 0.40	45.98 ± 1.74	-	0.14 ± 0.40	34.49 ± 2.17	6.58 ± 1.45	5.59 ± 2.03

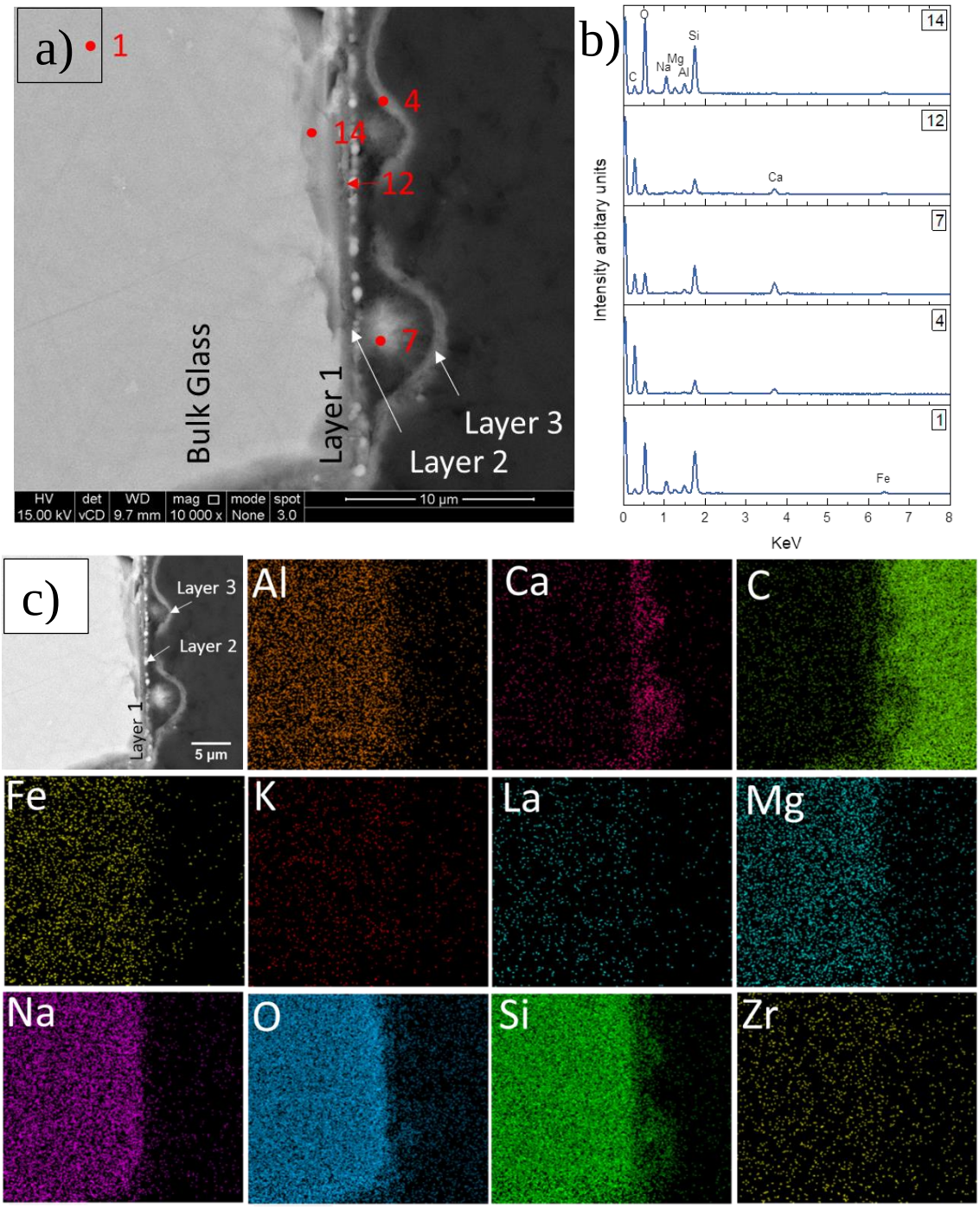

Figure 7.18 SEM analysis from LBS exposed to NRVB eq. water for 84 days; a) BSE image, labels indicate alteration products, red spots correspond to the spot analysis in b), c) elemental maps.

iii. ISG exposed to NRVB equilibrated water

The alteration products surrounding grains of ISG after exposure to NRVB eq. water for 84 d are shown in Figure 7.19. These had a distinctly different morphology to those observed for MW25 or LBS (see above). The alteration products surrounding many of the other ISG grains were not quite as pronounced as shown in Figure 7.17, but the morphology was the same; loosely packed needle-like material was found to reside between the glass and outer reaction rim. The electron micrograph reveals three alteration layers on the surface of the ISG glass, the first (Layer 1) is a region of Si-gel containing Ca, which was depleted in Na, with minor depletion of Al, Si and Fe compared to the bulk glass (Table 7.10). This layer exhibited a significant increase in the at % of Ca compared to the bulk glass (+12.7 at%) and had trace amounts of Mg. Magnesium is not present in ISG glass however a small quantity of Mg is present in hardened NRVB cement paste, thus it must have been incorporated into the layer from the solution.

Layer 2 was composed of products that were orientated perpendicular to, and in between, the glass and the reaction rim. It is not possible to ascertain from the images acquired here whether the phases originated at the bulk glass and branched out, or if they were formed from the reaction-rim inwards. It may be possible that the products filled the entire space between the rim and the glass, and that subsequent drying during imaging (i.e. vacuum desiccation) occurred. The 'ladder rungs' were composed mainly of Ca and Si with a ratio of 0.65, and contained a lower amount of Na, Al, K than the gel, with slightly more Mg and S (1.44 at %).

The reaction rim was observed to encase the alteration products that had grown on the surface of the glass. It also traced the outer perimeter of the glass grain. It was composed of Na, Al, K and Fe in addition to significant amounts of Ca and Si, with a Ca:Si ratio of 0.79. The Ca concentration was observed to increase from the inner to the outer alteration layers, from 7 at % in the glass to 19.7 at % in the gel, 33.8 at % in the ladder rungs and 40.4 at % in the reaction rim.

Table 7.10 SEM F50 EDS spot maps associated with Figure 7.19, average elemental composition of each alteration layer on the surface of ISG after 84 d exposure to NRVB eq. water.

Element At %	Na	Mg	Al	Si	S	K	Ca	Fe	Other
Bulk glass (16,17)	16.31 ± 0.60	-	7.74 ± 0.11	66.88 ± 0.12	-	-	7.01 ± 0.51	0.05 ± 0.21	2.20 ± 0.18
Layer 1, gel (18, 19,20)	10.17 ± 2.26	0.07 ± 0.23	7.62 ± 0.41	60.37 ± 3.11	±	0.21 ± 0.10	19.72 ± 5.59	-	1.93 ± 0.18
Layer 2, ladder rungs (21-26)	4.62 ± 2.91	0.10 ± 0.23	5.88 ± 1.45	52.27 ± 3.96	1.44 ± 0.20	0.11 ± 0.24	33.86 ± 7.21	-	3.27 ± 1.53
Layer 3, rim (27-29)	1.27 ± 0.38	-	5.34 ± 0.09	51.07 ± 0.17	±	0.17 ± 0.11	40.42 ± 0.50	0.07 ± 0.06	1.70 ± 0.28

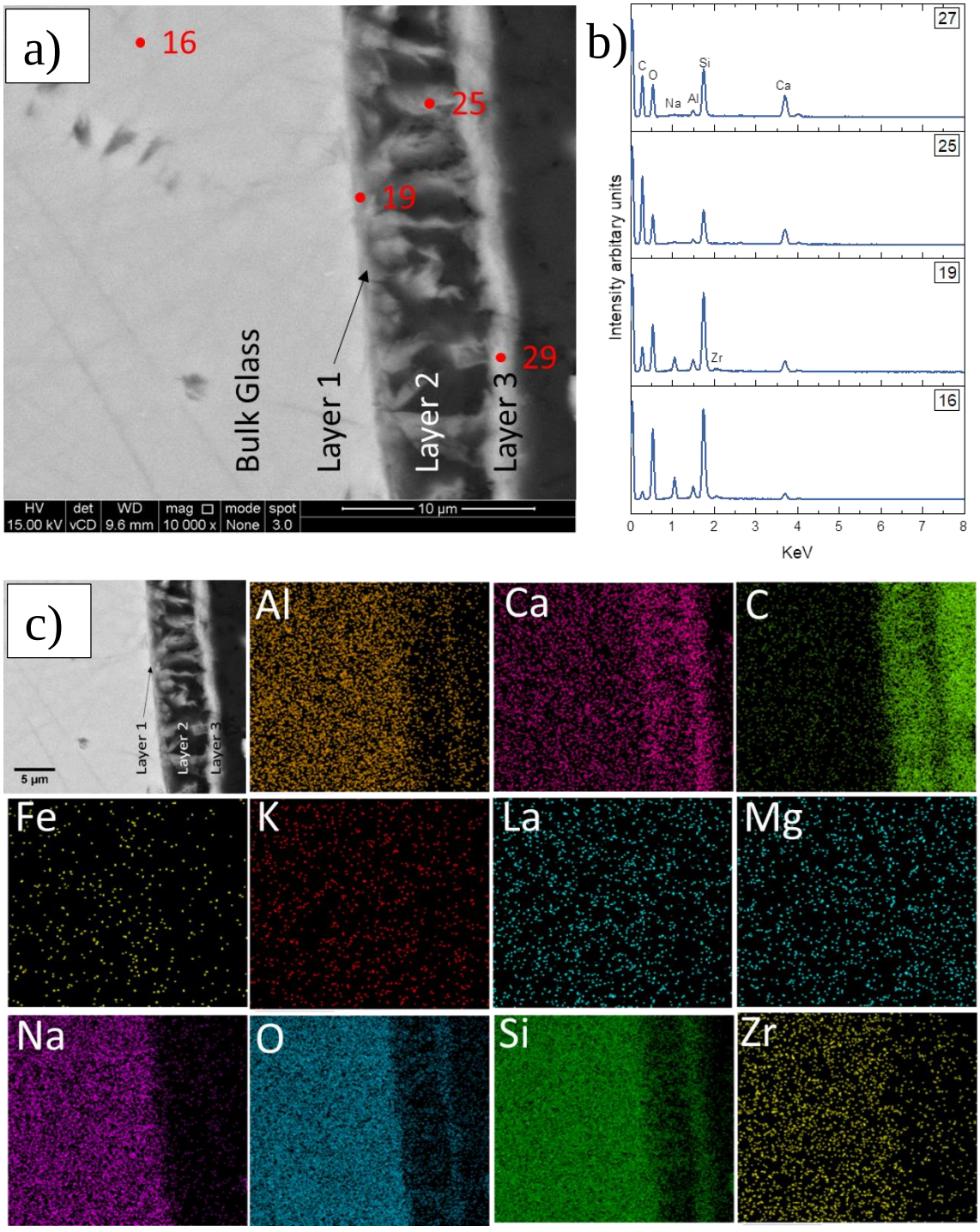

Figure 7.19 SEM analysis from ISG exposed to NRVB eq. water for 84 days; a) BSE image, labels indicate alteration products, red spots correspond to the spot analysis in b), c) elemental maps.

7.2.7. Geochemical Modelling of BFS:PC and NRVB equilibrated cement water systems

The geochemical modelling package PHREEQC was used to provide an indication of the saturation index of mineral phases that are likely to precipitate in the cement-equilibrated water systems investigated here, using the Hatches thermodynamic database developed by Wood Plc. (formally known as AMEC Foster Wheeler) for the NDA. These calculations should be considered as a qualitative indication of alteration layer mineral phase solubility, since the data available in the database are for studies at 25 ºC, and not at the temperature of the experiments performed in this study (50 °C).

The experimental parameters input to the model included solution concentration data (corrected for dilution and the internal gold standard used in the ICP-OES analysis) for the static powder dissolution tests, the temperature set to 50 ºC and the pH values were the measured values at a given time point.

The major limitation of geochemical modelling for high pH systems are the availability of thermodynamic data at highly alkaline values; the rationale for obtaining such data is only relevant to a small selection of disposal facility concepts and for those researchers interested in the evolution of cement materials, thus there has been little effort to extend thermodynamic databases to high pH. Utilising the available data and, where necessary extrapolating lower pH value data (e.g. pH 9 – 10), the solubility of the mineral phases present in the experiments studied in this Chapter are given in Table 7.11. Phases that were under-saturated (i.e., not thermodynamically favourable to precipitate as alteration layer phases) included: calcium borate ($(CaO)_2B_2O_3$), calcite ($CaCO_3$), gypsum $CaSO_4{:}2H_2O$, Na-P zeolite ($Na_2Al_2Si_{2.6}O_{12}{\cdot}4H_{6.4}$), phillipsite-Ca/K/Na ($X_xAl_2Si_5O_{14}{\cdot}5H_2O$) and Fe-Mg-smectite $Ca_{0.025}Na_{0.1}K_{0.2}{}^{2+}Fe_{0.5}{}^{3+}Fe_{0.2}$-$Mg_{1.15}Al_{1.25}Si_{3.5}H_2O_{12}$). Calcite was identified in the XRD (Figure 7.6 and 7.14), however the thermodynamic model did not predict it to be saturated because the input data was taken from the blank ICP-OES results which do not include carbonate concentrations. Retrospectively the carbonate content was calculated using TGA-MS of the hardened cement pastes (giving values of 6.4 wt% $CaCO_3$ in NRVB and 2.5 wt% in BFS:PC). Solution concentrations were estimated from these values, by calculating the dissolution of calcite in pure water using PHREEQC, the results indicate that 0.88 mg L^{-1} (0.012 moles) of $CaCO_3$ dissolved in both NRVB and BFS:PC eq. water., (as little as $x10^{-4}$ mmol L^{-1} of CO_3^{2-} is required to precipitate mono- and hemi-carboaluminate[189,190]). Considering the above carbonate concentration in the equilibrated cement

waters, calcite would be in equilibrium (NRVB- and BFS:PC-eq. water systems saturation indices of 0.62 and 0.57 respectively).

Table 7.11 Mineral phases identified by Phreeqc to be saturated in solution for both NRVB and BFS:PC eq. solutions, results are from Hatches database.

Phases Identified from Hatches Database	
Portlandite	$Ca(OH)_2$
C-S-H (1.1)	$Ca_{1.1}SiO_7H_{7.8}$
C-S-H (1.8)	$Ca_{1.8}SiO_9H_{10.4}$
Ettringite	$Ca_6Al_{12}(SO_4)_3(OH)_2 \cdot 26H_2O$
Gibbsite	$Al(OH)_3$
Hydrotalcite-OH	$Mg_4Al_2(OH)_{17}H_2O$
Brucite	$Mg(OH)_2$
Monosulfoaluminate	$Ca_4Al_2(SO_4)O_{18}H_{24}$
Quartz	SiO_2
Saponite (Ca, K, Mg, Na)	$X\ Mg_3Al_{0.33}Si_{3.67}O_{10}(OH)_2$
Sepiolite	$Mg_2Si_3O_{7.5}\ OH \cdot 3H_2O$
Talc	$Mg_3Si_4O_{10}(OH)_2$
Tobermorite (14A, 11A, 9 A)	$Ca_5Si_6H_{21}O_{27.5}$
Goethite	FeOOH
*The saturation indices for Saponite Ca, K, Mg and Na were all very similar or identical the same was true for Tobermorite 14A, 11A and 9A.	

i. BFS:PC equilibrated water

Blank concentration data was collected at each time point from duplicate PCT vessels exposed to the same conditions as vessels containing glass powder. As such there are small variations in elemental concentration throughout. PHREEQC analysis (Figure 7.20) indicated that hydrotalcite, ettringite, portlandite, brucite and goethite were saturated in the blank solutions throughout the experiment as shown in Figure 7.20.

The geochemical modelling data for MW25 (Figure 7.20) indicated that, in addition to the phases saturated in the blank, tobermorite was predicted to be supersaturated, but only on days 28, 84 and 112; the remaining time points exhibited under saturation. Monosulfoaluminate and C-S-H were predicted to be in equilibrium until day 84 and 112, respectively, when these phases became saturated in solution.

For the LBS glass composition, the saturated phases that could not be attributed to the BFS:PC equilibrated solution (i.e. the blank) were saponite (a Mg-bearing clay), talc (a Mg-bearing LDH) and tobermorite. Portlandite was predicted to gradually move from saturated towards equilibrium; this correlates with removal from solution to form a Ca-silica gel and a C-S-H precipitate, as identified by SEM EDS (Figure 7.10). C-S-H was predicted to be in equilibrium until day 84 when it became saturated. The rim of nodules observed in SEM contain significant quantities of Na, Mg, Al, Si and Ca however the ratios of these elements do not match any of the minerals suggested by PHREEQC.

For ISG, saturated phases that were not predicted to form in the blank solution included tobermorite, talc and saponite. The Mg required for these Mg-bearing phases must have originated from the BFS:PC-eq. water, although it should be noted that no Mg-bearing phases were identified in SEM EDS measurements. As for LBS, the solutions were initially saturated with respect to portlandite, but as Ca was removed from solution, Portlandite moved towards equilibrium and quickly became under saturated by day 56. C-S-H remained at equilibrium throughout.

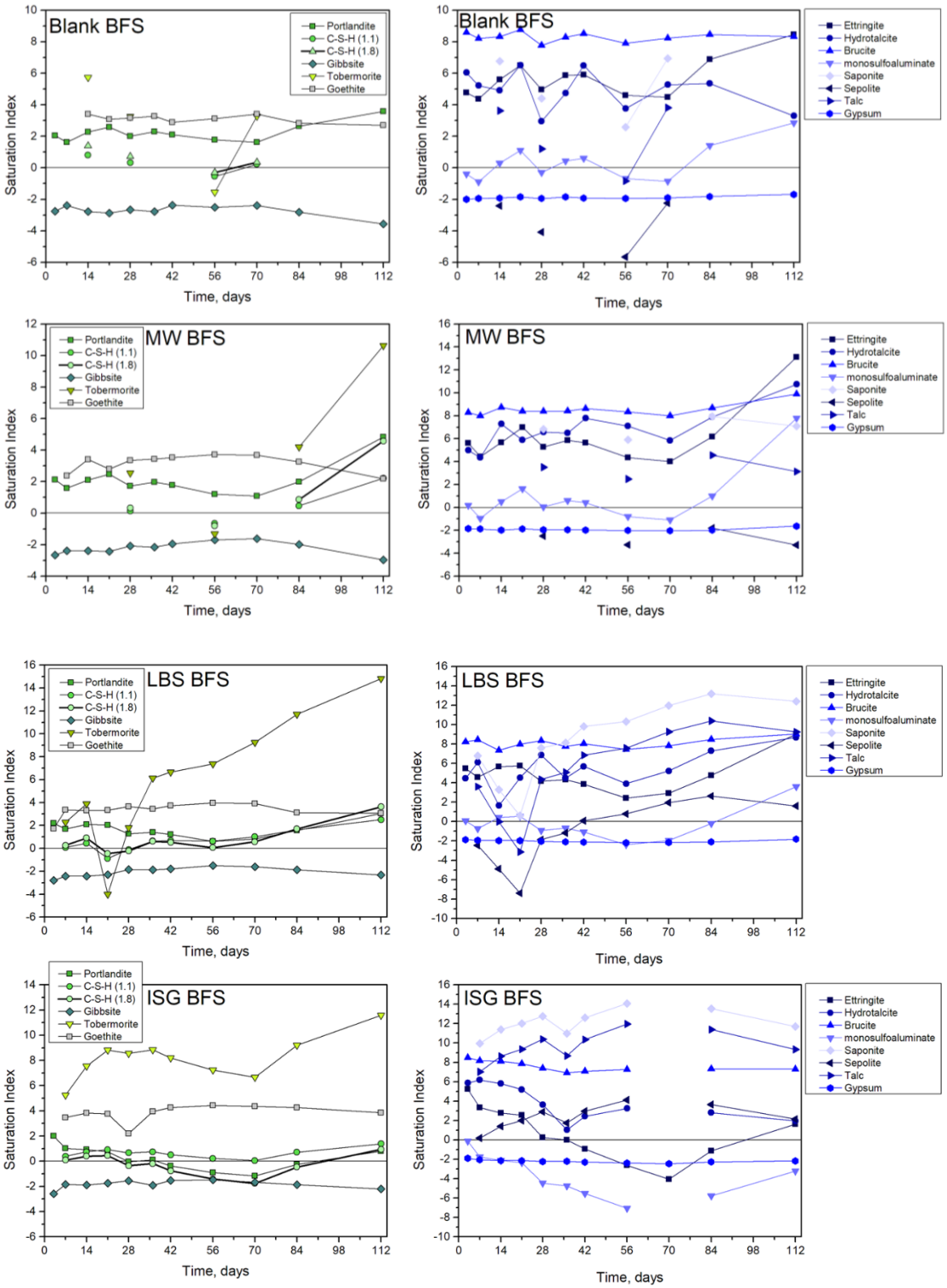

Figure 7.20 Geochemical modelling results for BFS:PC eq. water solution chemistry. Graphs depict phases that are saturated in solution (values > 1), in equilibrium (values between 0-1) and under saturated (values < 0).

ii. NRVB equilibrated water

The geochemical modelling data for the blank NRVB eq. water (Figure 7.21) indicated that goethite, portlandite, C-S-H (1.8) and tobermorite were saturated and C-S-H (1.1) remained in equilibrium. The Mg-containing phases hydrotalcite, brucite, saponite, talc were calculated to be saturated from day 42 onwards, the ICP samples analysed for the first 35 days were close to the detection limits of the ICP, this impacted the Mg, Li and Na data.

The addition of MW25 glass to the NRVB eq. water lead to saturation of two additional phases to those observed in solution compared to the blank: ettringite was predicted to be saturated in solution from day 21-112 (Figure 7.21), and the Mg-silicate phase, sepiolite, from day 42-112. XRD (Figure 7.14) of the corroded glass sample on day 84 identified calcite and hydrotalcite as crystalline phases on the surface of the glass; geochemical modelling predicted hydrotalcite to be saturated in solution from day 42 onwards. Calcite was under saturated throughout (in contrast to observations from XRD), however portlandite was predicted to be saturated in solution for the duration of the experiment and C-S-H was calculated to be at equilibrium, SEM analysis identified a Ca-silica gel in addition to a C-S-H phase that contained traces of Na, Mg, Al and Fe, and was packed with Ca-Si needles.

Geochemical modelling of LBS glass dissolution also predicted the saturation of solution with respect to ettringite, from day 21 -112 (Figure 7.21). Tobermorite saturation indices dropped after day 35, suggesting that Si may be used for the formation of alternative phases, for example, sepiolite which became saturated on day 42. Monosulfoaluminate was predicted to be saturated in solution under these experimental conditions. SEM images identified S and Al in the Ca-rich nodules that formed around the glass grains, suggesting that these may comprise monosulfoaluminate, however since they were also found to contain Mg, Na, Si, K and Fe (which are not required in monosulfoaluminate formation) this SEM phase remains unidentified. The XRD data (Figure 7.14) highlight the presence of hydrotalcite and C-S-H on the surface of the glass sample; this is also predicted by the geochemical modelling, which calculated the mineral hydrotalcite to be saturated throughout the experiment, and C-S-H to be in equilibrium. As little as 40 mg L^{-1} is required to cause precipitation of portlandite[191,192]; the concentration of Ca in solution was measured as 100 mg L^{-1} on day 112, and the geochemical model confirmed portlandite saturation throughout the experiment.

In the presence of ISG, tobermorite saturation indices fell from saturated to undersaturated, which could facilitate the precipitation of sepiolite, predicted to be saturated from day 42 onwards. The

Ca containing phases portlandite, C-S-H and ettringite were close to equilibrium from day 28 to 42, after which time they were calculated to be undersaturated. C-S-H was identified in the XRD and the SEM EDS gives evidence for Ca-silica gel and a precipitate that was termed “ladder rungs”. This precipitate had an enrichment of Mg and Si (supported by the geochemical modelling prediction of saturation of Mg-bearing phases) and also S. The presence of S seems difficult to attribute since, according to the geochemical modelling, both ettringite and monosulfoaluminate were undersaturated in solution. Since ISG does not contain any Mg, the source of Mg must be from the NRVB solution. The Ca-Si rim contained traces of Na, Al, K and Fe, geochemical modelling does not provide any clarity as to what this phase may be.

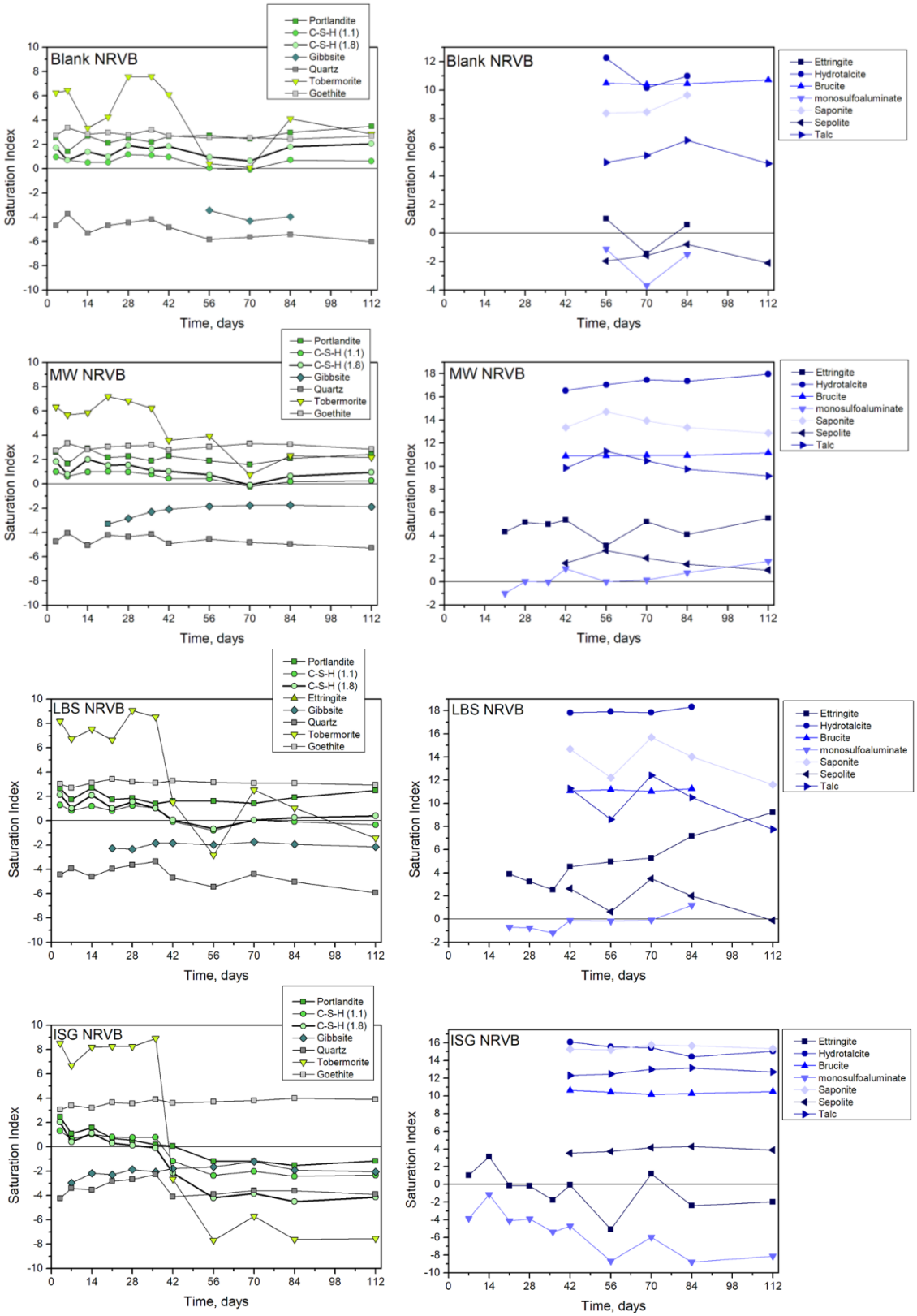

Figure 7.21 Geochemical modelling results for NRVB eq.water solution chemistry. Graphs depict phases that are saturated in solution (values > 1), in equilibrium (values between 0-1) and under saturated (values < 0).

7.3. Discussion

The aim of this study was to compare the influence two different types of cement on glass dissolution mechanisms and kinetic. The cements selected where NRVB and BFS:PC both of which are likely to be implemented in a geological disposal facility. This was achieved by conducting static leaching at 50 ^{o}C on two UK relevant glasses for HLW (MW25) and ILW (LBS) in addition to an internationally studied material (ISG). The kinetics and mechanisms of glass dissolution in BFS:PC- and NRVB-eq. water was investigated.

7.3.1. Effect of cement leachate composition on dissolution of International Simple Glass (ISG)

ISG is used by many nations studying the behaviour of borosilicate glasses in disposal environments. The current study is a significant contribution to the international scientific collaboration, as this is the first glass dissolution experiment utilising real cement-equilibrated solutions, and will aid understanding of how dissolution mechanisms and kinetics change in complex leachate solutions.

The compositions of the two solutions were noticeably different: NRVB is a simplistic cement paste composed of Portland cement, $Ca(OH)_2$,$CaCO_3$ and water. The dissolution of NRVB formed a solution rich in Ca with a minor amount of K and Si from dissolution of the clinker phases. Notable is the absence of any Na (Portland cement does not contain Na^{193}) and the presence of a significant quantity of Mg. Portland cement contains 2 % MgO, therefore it is somewhat surprising that the Mg concentrations were so high (up to 200 mg L^{-1}), especially since solutions with a pH > 10 tend to precipitate as Mg brucite. The reason for such elevated concentrations of Mg in the blank is unknown (a pure $CaCO_3$ reagent was used in this study), however its effects were observed through the precipitation of Mg-bearing phases, particularly on the surface of ISG, which does not contain any Mg. Further work is required to confirm this unexpected presence of Mg, however it should be noted that NRVB will be prepared using limestone flour[7] (as will be the case for the disposal facility) which contains a significant proportion of Mg. Although the solution concentration of carbonate was not measured, it can be assumed that if there is approximately 6.4 wt % $CaCO_3$ in NRVB cement paste, then 46 mg L^{-1} is present in solution. This is expected to influence the mineral phases formed significantly, as described further below.

In contrast, the BFS:PC material comprises one part Portland cement to three parts of blast furnace slag from the industrial processing of iron ore. It thus contains a wider range of elements including S, which readily leached to solution when the cement underwent equilibration with deaerated water (Table 7.12). The solution concentrations of Na and K were significantly higher in this solution than in the NRVB, due to the presence of three parts slag, and owing to the absence of lime and limestone flour used in NRVB, the Ca concentration was considerably lower (Table 7.12).

Table 7.12 Composition of NRVB and BFS:PC eq. water, mg L^{-1}, measured by ICP-OES. The values listed below are the average of all the blank samples throughout the 112 day experiment, errors are the standard deviation taken across each time point. Carbonate content was calculated from TG-MS data outlined in Chapter 2.

Element	Concentration, mg L^{-1}	
	NRVB pH(RT) 12.65 ± 0.2	BFS:PC pH(RT) 12.53 ± 0.2
Ca	766 ± 59	487 ± 28
Na	13 ± 10	43 ± 6
K	36 ± 5	74 ± 7
Al	0.08 ± 0.2	1.96 ± 0.7
Si	1.79 ± 1.4	0.34 ± 1.4
*Mg	16 ± 9. *	0.30 ± 0.2
Fe	1.57 ± 0.7	1.67 ± 1.4
S	10 ± 7	13.5 ± 1.5
*$CaCO_3$	0.88	0.88

*Mg conc = 0 day 1-42, day 56 onwards ~ 20 mg L^{-1}
*$CaCO_3$ conc= calculated based on the dissolution of calcite in the hardened cement pastes using PHREEQC

It was found that BFS:PC-eq. water was 1.4 times less corrosive towards ISG than NRVB-eq. water based on the initial rates, which were measured as (1.61 ± 0.03) $x10^{-2}$ g m^{-2} d^{-1} and (2.21 ± 0.38) $x10^{-2}$ g m^{-2} d^{-1}, respectively. This trend is also reflected in the residual rates, with rates of (0.33 ± 0.05) $x10^{-2}$ g m^{-2} d^{-1} in BFS-eq. water and (2.21 ± 0.03) $x10^{-2}$ g m^{-2} d^{-1} in NRVB-eq. water. The average pH(RT) of the blank solutions was similar 12.5 ± 0.2 (BFS:PC eq. water) and 12.7 ± 0.2 (NRVB eq. water) (Table 7.12), therefore, this cannot explain the differences in behaviour between the two solutions. The addition of crushed ISG to the cement equilibrated solutions reduced the pH over the duration of the experiment (pH <12 after 21 d), indicating the consumption of hydroxide ions[75].

Mercado-Depierre et al. [23] concluded that in high pH, Ca-rich solutions, Ca has dual effects determined by its availability. If the amount of Ca present is limited then a passivating layer can

form on the surface of the glass, thus reducing the dissolution rate. This has been observed by a number of previous studies including Corkhill et al.[61], Utton et al.[75, 55, 59] and Maraghechi et al.[30]. However if Ca is freely available, the conversion of portlandite to C-S-H will be unrestricted and the glass dissolution rates will remain high[23,54] due to the continued dissolution of Si from the glass, the initial rate being proportional to Ca concentration in solution above a certain, not fully defined threshold[54]. This threshold has been reported by several authors, for example, Corkhill et al.[61] and Utton et al.[59] observed an incubation period while Ca concentrations remained above 200 mg L^{-1}, and once the Ca concentration dropped below this threshold, Si was detected in solution[61]. Similarly, Chave et al.[57] showed for the French SON68 glass leached in saturated $Ca(OH)_2$ that when the Ca concentration was below 100 mg L^{-1} Ca was consumed, which aided the formation of a passivating layer, reducing alteration rates. As the Ca concentration continued to drop below 100 mg L^{-1} the alteration layer thickness increased[57].

There was a limited supply of Ca in both NRVB and BFS:PC eq. water, but NRVB eq. water contains twice as much Ca. Solution analysis found that Ca was readily removed from solution, which resulted in the consumption of Si from the glass to facilitate the formation of a C-S-H phase precipitate. This phase was apparently not passivating, explaining the accelerated the rate of dissolution in NRVB eq. water compared to BFS:PC eq. water. Not all of the Ca in BFS:PC eq. water was consumed, suggesting competition for Si by other mineral phases. Indeed, geochemical modelling identified Mg-silicates as phases that are thermodynamically favourable to precipitate (both talc and sepiolite were predicted), however, the formation of these phases were not identified by SEM/EDS or XRD.

The morphology of alteration products also provides an indication as to why NRVB eq. water continued to dissolve ISG at a higher rate than BFS:PC eq. water. Figure 7.22 shows that, on average, the measured thicknesses of the alteration products that formed in both solutions were similar (BFS:PC, 5.31± 0.6 μm and NRVB, 4.31 ± 0.56 μm). However, the morphology was significantly different; BFS:PC eq. water generated a uniform layer surrounding the grains, and NRVB eq. water led to the formation of ladder rungs with a significant fraction of void space. It is hypothesised that the ladder rungs are in fact small crystal-like phases, which nucleate from the surface of the glass and grow outwards towards the rim (based on alternative micrographs). It is possible that when the sample was exposed to the vacuum for SEM analysis some of the precipitates collapsed, leaving the unusual morphology, however this was not observed for any other samples that were prepared with the same methodology. The presence of these "ladder rungs" and their associated void spaces may act to facilitate continued transportation of dissolved

elements from the glass, to the solution, hence, increasing dissolution rate. Further analysis is required to ascertain the porosity of the alteration layers to confirm this hypothesis.

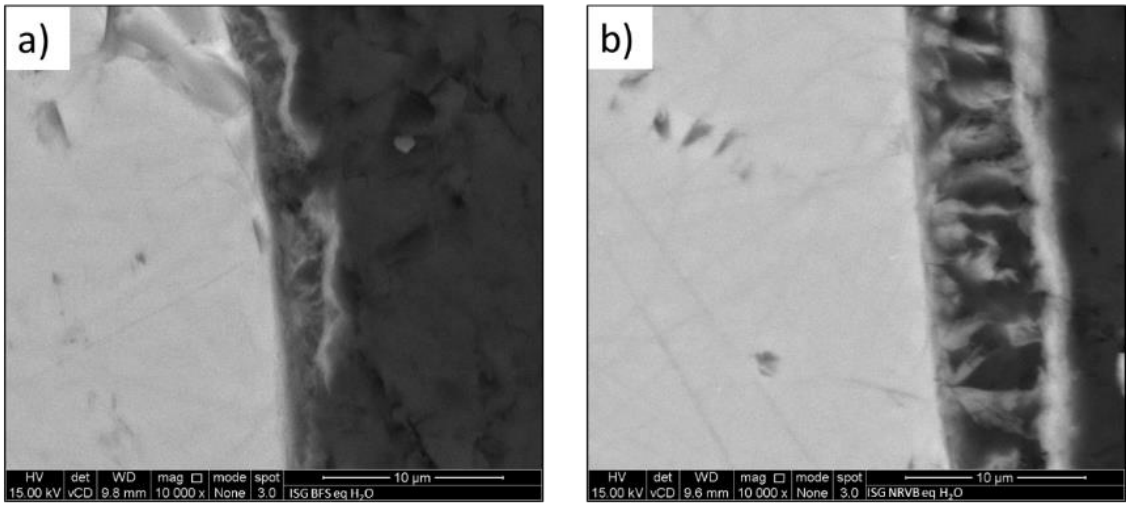

Figure 7.22 BSE SEM a) ISG after dissolution for 84 days in BFS:PC eq. water, b) ISG after dissolution for 84 days in NRVB eq. water.

The rate of ISG dissolution in cement eq. water, as reported in this Chapter, is lower than for previous literature dissolution rate measurements made for ISG reacted in $Ca(OH)_2$, KCl, KOH and YCWCa (Table 7.13). Fournier et al[26] correlated rate resumption with pH, under Na-rich conditions, Ribet and Gin[52] and Inagaki[89] observed greater resumption in the presence of NaOH compared to KOH, Liu et al.[194] postulate that Na^+ plays a "structure-forming" role during precipitation of zeolites. In the current study, ISG shows no signs of entering the rate resumption regime of dissolution, despite the high pH solutions and the availability of Na and other alkali and alkali earth cations.

Table 7.13 Comparison rates for experiments conducted on ISG in high pH solutions

	Rate g m^{-2} d^{-1}	R_x Time	Glass	Experiment details
Present Study	0.016 ± 0.0003	R_0 1-56	ISG	50ºC, pH(RT) 12.53, BFS:PC-eq.water
	0.001 ± 0.0004	R_a 56-112	ISG	50ºC, pH(RT) 12.53, BFS:PC-eq.water
	0.022 ± 0.0004	R_0 1-21	ISG	50ºC, pH(RT) 12.65, NRVB:PC-eq.water
	0.003 ± 0.0001	R_a 21-112	ISG	50ºC, pH(RT) 12.65, NRVB-eq.water
Backhouse[70]	0.051 ± 0.008	R_0 1-3	ISG	50ºC, pH(RT) 12.5, $Ca(OH)_2$ sat.soln.
	0.003 ± 0.001	R_a 3-112	ISG	50ºC, pH(RT) 12.5, $Ca(OH)_2$ sat.soln.
Inagaki[38]	0.378 ± 0.03	R_0 2-5	ISG	50ºC, pH 10 KCl
	1.96 ± 0.03	R_0 2-5	ISG	70ºC, pH 10 KCl
Elia[39]	0.067 ± 0.02	Fwd	ISG	30ºC, pH 11.5, KOH
	0.112 ± 0.04	Fwd	ISG	30ºC, pH 13.0, KOH
	0.204 ± 0.1	Fwd	ISG	30ºC, pH 14.0, KOH
	0.041 ± 0.03	Fwd	ISG	30ºC, pH 13.5, YCWCa
Mann[87]	0.004 ± 0.01	R 1-721	ISG	30ºC, pH(RT) 13.5, YCWCa
	0.171 ± 0.03	R_0 0-56	ISG	70ºC, pH(RT) 13.5, YCWCa
	0.001 ± 0.01	R_a 56-721	ISG	
Fournier[26]	-	R_a	ISG	90ºC, pH 11.7, NaOH ($2.5x10^{-1}$ M)
	1.43	R_{RA} 1-2	ISG	
	0.005	R_a 6-15	ISG	90ºC, pH 11.2, NaOH ($7.9x10^{-1}$ M)
	0.85	R_{RA} 15-21	ISG	
	0.004	R_a 6-29	ISG	90ºC, pH 10.8, NaOH ($2.5x10^{-2}$ M)
	0.33	R_{RA} 29-40	ISG	

R_0= initial rate, R_a= rate drop/transition rate, R_{RA}= rate of resumption of alteration

7.3.2. Comparison of MW25 and LBS dissolution as a function of cement leachate composition

If co-disposal of HLW and ILW is implemented in the UK, it is possible that HLW (MW25 glass) would come into contact with BFS:PC-eq. water from cement used to line the disposal tunnels, while ILW (LBS glass) vaults could be backfilled with NRVB. The interactions of these materials are discussed herein.

Table 7.14 compares the dissolution rates of MW25 and LBS glasses reported in this Chapter compared with other alkaline solutions. The residual rate for LBS was six times faster than MW25 in BFS:PC eq. water ((0.41 ± 0.03) x10^{-2} g m^{-2} d^{-1} and (0.06 ± 0.01) x10^{-2} g m^{-2} d^{-1}, respectively). Utton et al.[55] reported the initial rate of LBS dissolution in $Ca(OH)_2$ at 50 °C to be, 0.012 g m^{-2} d^{-1} which is three times greater than the residual rate reported in the current study for BFS:PC-eq. water. MW25 dissolved ~ 20 times slower in BFS:PC-eq. water compared to $Ca(OH)_2$, as reported by Backhouse[70] (Table 7.14).

Table 7.14 Comparison rates for experiments conducted at SA/V 1200 m^{-1} on MW25 and LBS glass, in high pH solutions.

Reference		Time, days	Rates, g m^{-2} d^{-1}	Glass	Experimental conditions
Present study	Initial		-	LBS	50 °C, pH(RT) 12.7, BFS:PC eq. water
	Residual	1-112	0.0041 ± 0.0003	LBS	
	Initial	1-42	0.0142 ± 0.003	LBS	50 °C, pH(RT) 12.7, NRVB eq. water
	Residual	42-112	0.0032 ± 0.0001	LBS	
Utton[55]	Initial	1-7	0.012 ± 0.001	LBS	50 °C, pH 12.5, $Ca(OH)_2$ sat. soln.
	Residual	14-42	0.0066 ± 0.0016		
	Resumption	42-112	0.027 ± 0.002		
Present study	Initial	1-56	0.0031 ± 0.0001	MW25	50 °C, pH(RT) 12.7, BFS:PC eq. water
	Residual	56-112	0.0006 ± 0.0001		
	Initial	1-42	0.0117 ± 0.0009	MW25	50 °C, pH(RT) 12.7, NRVB eq. water
	Residual	42-112	0.0038 ± 0.0002		
Backhouse[70]	Initial	1-14	0.062 ± 0.009	MW	50 °C, pH(RT) 12.5, Ca(OH)2 sat. soln.
	Residual	14-112	0.017 ± 0.002		
Cassingham[28]	Forward	n/a	0.106 ± 0.032	MW	40 °C, pH 10
Abraitis[41]	Forward	n/a	0.139 ± 0.032		40 °C, pH 10

As for ISG, in NRVB-eq. water the rate of MW25 and LBS glass dissolution was accelerated compared to BFS:PC-eq. water; MW25 dissolved four times faster in NRVB-eq. water than BFS:PC-eq. water and LBS experienced a 10 fold increase. Possible explanations for the magnitude of the difference between the two glasses are discussed later in this Section.

The alteration products that formed on the surface of the glasses were different under each test condition (Figure 7.22 and 7.23), re-enforcing the argument that solution chemistry has a consequential impact on the durability of the glass wasteform. A gel alteration product on the surface of the pristine glass was formed in both solutions (Table 7.15). For MW25 glass, crystalline phases identified as hydrotalcite and calcite were formed, in addition to C-S-H (as identified by SEM/EDS). The measured alteration thickness of MW25 exposed to NRVB-eq. water was twice that of MW25 exposed to BFS:PC-eq. water and the Ca/Si ratio of C-S-H leached in NRVB-eq. water was somewhat higher than that of MW25 leached in BFS:PC-eq. water (1.2, compared to 1.0, respectively). The high Ca concentration in NRVB-eq. water is reflected by the high Ca/Si ratio of the gel layer, which facilitates the continual conversion of portlandite to C-S-H, is in agreement with the PHREEQC modelling. Ferrand et al.[54] stated that the dissolution rate would remain high as long as portlandite was available in solution and could be converted to C-S-H. This is observed for both MW25 and LBS glass in NRVB-eq. water.

In contrast to MW25, the types of phases formed on the surface of LBS glass varied significantly in each solution; in BFS:PC-eq. water, C-S-H was identified, however, in NRVB-eq. water, hydrotalcite was additionally observed and large crystal structures of C-S-H were present with an outer reaction rim. These large, radiating crystal structures formed only on LBS leached in NRVB-eq. water (and not BFS:PC-eq. water), appear to have formed according to a series of dissolution-re-precipitation reactions, according to the model proposed by Geisler et al.[24]. During polymerisation, condensation of Si(OH) units may generate larger units, through two processes: first, enlarging the size of the spherical particles, second, by increasing the number of particles comprising the aggregate[195]. Figure 7.23 depicts small Si-rich aggregates which are chain-like on the outer rim of LBS alteration products in BFS eq. water. Conversely, in the presence of NRVB eq. water, these Si-rich aggregates are much larger, hence, a greater porosity is expected compared with the smaller (less pore space) chain-like aggregates in BFS:PC eq. water (i.e., the alteration layer for BFS:PC eq. water was more protective). It is hypothesised that, as described above, the precipitation of these phases enhances the dissolution rate through the consumption of Si from the glass. This may be enhanced by the presence of the outer rim (also seen in BFS:PC-eq. water for this glass, see Table 7.15), composed of Ca and Si (with minor Al and Zr), which effectively created an enclosed reaction cell, where dissolution-precipitation reactions could take place.

Table 7.15 Summary of findings regarding alteration products on the surface of MW25, LBS and ISG in both NRVB- and BFS:PC-eq. water after 84 days.

	Phases (XRD)	Morphology (SEM)	Thickness, µm	Initial rates, $gm^{-2}d^{-1}$
BFS:PC				
MW25	hydrotalcite, calcite	gel Ca:Si 0.3, precip 1.05, rim 0.99	4.63 ± 0.46	(0.31 ± 0.01) $x10^{-2}$
LBS	C-S-H	Si-gel , nodules 0.7, rim 0.4	3.96 ± 0.06	(0.41 ± 0.03) $x10^{-2}$ *
NRVB				
MW25	hydrotalcite, calcite	gel Ca:Si 0.3, precip 1.16/ 0.99	2.13 ± 0.35	(1.17 ± 0.09) $x10^{-2}$
LBS	hydrotalcite, C-S-H	gel Ca:Si 0.2 , nodules 0.6, rim 0.8	3.24 ± 0.64	(1.42 ± 0.3) $x10^{-2}$

* Residual rate

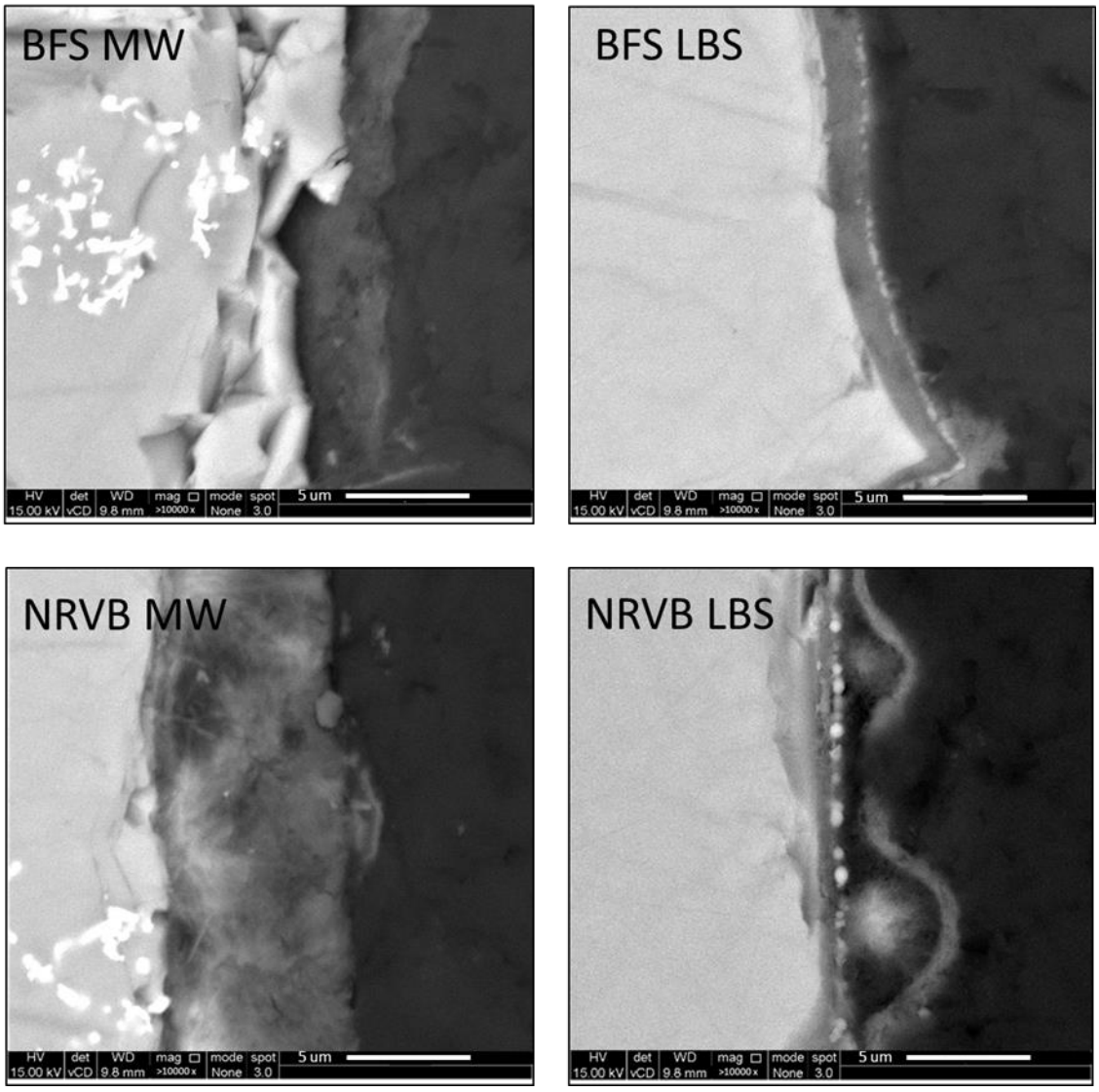

Figure 7.23 Micrographs of glasses exposed to BFS:PC eq. water (TOP) and NRVB eq. water (BOTTOM) for 84 days for comparison.

MW25 exhibited a lower rate of dissolution compared to LBS in both cement water solutions, which is due to variations in the glass compositions. The ratio of network formers to modifiers is similar in both glasses; assuming Si, B, Al and Zr are network formers and Mg, Li, Zn, Ca, K and Na are modifiers, the ratio for MW25 is 67:29 mol % and for LBS 66:29 mol %. Generally,

glasses with a high Si content are more durable than low silica glasses[196], however, since MW25 glass contains 8.8 mol % less Si than LBS, this argument is clearly not sufficient to explain the lower dissolution rate of MW25. Nogues et al.[197] stated that less durable glasses had a (Na+Li)/(B/Al) ratio far from 1.0; the ratio for MW25 was 0.36 and LBS was 1.02. Again, this does not seem to provide a satisfactory explanation for the observed difference in dissolution rates. Hermansson et al.[198] found that the glass composition 'ABS 118', with a low Si concentration, outperformed glasses containing more Si due to elevated concentrations of Al_2O_3, CaO and ZrO_2; Ca has been shown to improve durability[197] and addition of Zr in small quantities (1-2 wt %)[199] also confers enhanced durability. Table 7.16 shows that MW25 contained more Al, Ca, and Zr than LBS, which may have acted to improve the durability. It also contains Zn which has been shown to supress dissolution (at least in the short term)[200,201] and Na, which is known to significantly decrease the durability of soda-lime silicate glasses[202]. These factors can be considered important for the greater durability of MW25 glass compared to LBS, having a lower Si concentration.

Table 7.16 Comparison of key elements, mol % that control the durability of nuclear waste glass

mol %	SiO_2	Al_2O_3	CaO	ZrO_2	ZnO	Na_2O	Other	Total
MW25	43.32	5.30	5.36	0.63	3.43	7.34	34.62	100
LBS	52.12	4.39	0.52	0.41	0.01	13.65	28.9	100

7.4. Conclusion

Since its development in 1994, research has been conducted on NRVB as a backfill material for a cementitious disposal facility containing cement waste forms, where it is also envisaged that vitrified ILW will be disposed. This study considered simulant vitrified wastes being leached by water that has contacted hardened cement pastes. The results presented indicate that dissolution in NRVB eq. water leads to accelerated rates compared to BFS:PC cement material, due to the precipitation of C-S-H phases arising from high concentrations of Ca present in the cement. The initial rate obtained for MW25 glass in NRVB-eq. water was a factor of 10 lower than the forward rate of the glass calculated in alkaline pH-buffered pure water[28], suggesting that the presence of NRVB does confer "protective" properties when compared to dissolution in pure water. However, due to the relatively short duration of these experiments it is not possible to predict how the glass will behave over much longer time scales, especially considering the negative effects of C-S-H precipitation on dissolution rate. After 720 days, Backhouse[70] reported that MW25 monoliths

continued to dissolve, with a linearly increasing NL_B at a rate that was lower than the forward rate, but could not be said to be residual. This "pseudo-Stage III" behaviour, where the continual dissolution and re-precipitation of silica-bearing phases promotes dissolution, indefinitely, requires further investigation. It is also necessary to ascertain whether true Stage-III behaviour (i.e. where the silica gel itself is consumed, leading to a resumption in glass dissolution) can be promoted by the precipitation of C-S-H.

C-S-H phases and hydrotalcite were identified by geochemical modelling and confirmed by XRD to have formed on the surface of LBS and MW25 respectively. These two phases demonstrated the ability to act in a passivating manner. Layered double hydroxides (LDH) are highly versatile and may remove anionic species from solution via two key mechanisms, 1) surface adsorption, and 2) interlayer anion-exchange. In addition to anionic species, some metal cations can also be removed by adsorption processes and furthermore it is possible for radioactive cations to exchange with the $M^{2+}$and M^{3+} ions in the structure [203,204]. Iodine, Tc and U have been reported to successfully incorporate into, or onto, the LDH structure[205,206]. C-S-H is also excellent at trapping elements from solution, as seen in the current study for Al and Zr; it is also possible for radionuclides to be immobilised by C-S-H, for example, Tits et al. [207] investigated the sorption of U(VI) and Th(IV), and found that they sorb to the silanol groups at the surface.

Layered double hydroxides and C-S-H phases tend to improve their adsorption ability with decreasing pH[205], therefore starting with a lower pH cement system that contains silica fume[208] would be desirable and as the cement ages a decrease in the pH would be observed, providing favourable conditions for hydrotalcite and C-S-H to act as a radionuclide sieve/trap. If conditions in the post closure environment alter i.e. pH and solution chemistry, radionuclides retained in these hydrated clays and gels could be mobilised.

BFS:PC-eq. water exhibits more favourable initial and residual rates compared to NRVB eq. water, therefore would be a desired option for plugs and seals. SKB and Posiva are considering the use of low pH cements (pH <11, containing PC plus silica fume) to overcome undesirable effects of hyperalkaline cement pore fluids on the host rock and engineered barriers (notably bentonite)[183] but have ruled out BFS:PC as a potential material due to high quantities of sulphide that leach and heighten copper canister corrosion[208,209].

This study has highlighted that the utilisation of simplified solutions to mimic the geological disposal conditions is not sufficient to understand the behaviour of glass durability. For example, BFS:PC- and NRVB-eq. water were found to be less corrosive than simple $Ca(OH)_2$ solutions

(Table 7.14); $Ca(OH)_2$ is more corrosive due to the availability of Ca in solution, facilitating continual conversion of portlandite to C-S-H. Chapter 4 investigated the impact of synthetic cement waters on glass dissolution, again these solutions exhibited higher dissolution rates than those reported in the presence of real cement leachates. Further work is required, on a range of relevant cement compositions, in equilibrium with relevant groundwater compositions to reduce uncertainty in dissolution rates fed into models for post-closure safety assessment.

Chapter 8. Concluding Remarks

The objective of this thesis was to investigate the durability of simulant vitrified wasteforms in leachates that were representative of an evolving geological disposal facility containing cementitious materials. For this reason, HLW and ILW glasses relevant to the UK disposal scenario were used (MW25 and LBS respectively) in addition to the ISG, for comparison with other, international, studies of glass dissolution.

This thesis has shown that the rate of glass dissolution in synthetic cement waters (Chapter 4) increased in the order OCW ≈ ECW >YCWCa ≈ YCW; the different rates of dissolution were found to be the result of the compositional and morphological differences of the alteration layers, which are strongly dependent on alkali/alkaline earth composition of the leachate solution, and also the pH. Synthetic cement waters contained varying amounts of alkali/alkaline earth ions and the tendency for exchange of hydrated cations with silica indicated that a K-silica gel layer formed preferentially over Na- or Ca-silica gel, although only a low concentration of Ca and Mg need to be present to form Ca- or Mg- containing silica gels. This highlights the requirement to use mixed alkali / alkaline earth solutions to understand glass dissolution in a cementitious disposal facility.

Chapter 5 brought to light the mechanisms and kinetics affecting ISG dissolution in YCWCa; the high pH and leachate composition had a significant influence on the dissolution behaviour. High pH (pH(RT) 13.5) caused repulsion among negatively charged silica particles during the formation of the alteration gel layer, which in turn adversely influenced the polymerisation of silica anions. This resulted in the formation of large interstitial pores between silica gel particles: the evidence for this was observed in TEM measurements where the pore radii were twice as big as those reported for ISG at near neutral pH.

Cations (K, Ca, Na) and anions (Zr, Al) were incorporated into the silica gel, indicating that the alteration layer was in equilibrium with the solution. Evidence from Chapter 4 suggests that Mg may be incorporated by the same mechanism. This is evidence that solution cations are readily transported into the open pore network of the gel layer under these high pH cementitious solution conditions. The driving force for alkali/alkaline earth cation incorporation into the gel is postulated to be charge compensation for anionic species in the silica gel. In agreement with Dove[139], the presence of these cations seemed to have a detrimental effect on glass alteration: because Na and K have a higher frequency of solvent exchange, they have a tendency to increase the frequency of silica hydrolysis and thus the rate of dissolution.

In the ISG study (Chapter 5) at 30 ºC, the glass dissolution mechanism was modelled initially with a diffusion term. The consumption of all Al from solution on day 160 resulted in a mechanistic change, this required an affinity-type model with the affinity term removed (saturation of Si). Two possible explanations were given: 1) Incorporation of alkali/alkaline earth cations into the gel (to charge compensate negative species of Si, Al and Zr) gave rise to a diffusion controlled dissolution rate until the gel layer became positively charged; at this time (160 d) dissolved $[AlO_4]^-$ species in solution were attracted to the gel layer, but since there was no further Ca^{2+} in solution the less effective charge balancing cations K^+ and Na^+ provided the charge balance. 2) The change in dissolution rate was the result of precipitation of poorly charge-balanced aluminosilicate species, which, due to their granular nature, gave rise to the presence of large voids in the gel allowing for rapid dissolution.

The effects of an aging cement leachate were investigated in Chapter 6; as the pH decreased with an increase in leachate age, the rate of ISG dissolution decreased. However, the same was not true for MW25 and LBS glasses when granitic ground water was introduced: the dilute nature of the granitic ground water enhanced the dissolution of MW25 and LBS. It was postulated that the C-S-H alteration layer that encased the ISG glass, that was developed in the ECW and OCW solutions, restricted dissolution of the glass in the groundwater by preferentially dissolving. The alteration layers that formed on the surface of the MW25 and LBS glasses during exposure to ECW for 28 days did not significantly alter the dissolution behaviour in OCW. The presence of hydrotalcite (as identified by XRD, in OCW and GW), a double layered hydroxide, and Fe-rich secondary precipitates (LBS SEM EDS data), have the potential to facilitate continued dissolution, or to cause the glass dissolution rate to enter Stage III (resumption).

The effects of 'real' cement waters were investigated in Chapter 7. Dissolution of MW25, LBS and ISG in NRVB- and BFS:PC-equilibrated water showed that Ca-rich NRVB eq. water led to alteration products with a high Ca:Si ratio, facilitating the continued dissolution of the glass matrix by removing Si to form C-S-H. There was evidence for dissolution re-precipitation; large crystals formed within C-S-H were observed in the outer rim, and spherical Si-aggregates were embedded in the alteration products. It was shown that the rate of dissolution was greater in NRVB eq. water when compared to BFS:PC eq. water, and that cement eq. water was less corrosive than young synthetic cement waters, simple hydroxide solutions and water, as summarised in Table 8.1. The same trends were observed in the simplified solutions (Chapter 4) and cement equilibrated water (Chapter 7), however the alteration layers formed in cement eq. waters exhibited a higher Ca:Si ratio in the gel compared to simplified solutions. Importantly, the

lower rates of dissolution observed for glasses in cement eq. water indicate that glass dissolution rates have been over estimated in much of the literature that utilised simplified saturated alkali leachates (e.g. NaOH, KOH, $Ca(OH)_2$).

Table 8.1 Comparison table of glass dissolution rates, in various leachates for MW25 and LBS glass.

Experiment details	Ref	Rate g m^{-2} d^{-1}	R_0 Time	Glass
Water				
40ºC, pH , deionised H_2O	AMEC[132]	0.033 ± 0.003	0-56	MW
40ºC, pH 9.8, demineralised H_2O	Utton[75]	0.024 ± 0.004	0-21	MW
90ºC, pH ? , deionised H_2O	Zwicky[133]	0.15	0-28	MW
Simplified high pH solutions				
40ºC, pH 12-11.7, $Ca(OH)_2$	Utton[75]	0.029 ± 0.003	0-21	MW
40ºC, pH 12-10.7, 0.03M NaOH	Utton[75]	0.156 ± 0.010	0-21	MW
50ºC, pH 12.5, $Ca(OH)_2$ sat.soln.	Backhouse[70]	0.062 ± 0.0009	0-14	MW
60ºC, pH 9.6, $NaHCO_3$/KOH soln.	Abraitis[131]	0.358 ± 0.39	0-28	MW
30ºC, pH 13.0, KOH	Elia[39]	0.112 ± 0.004	Fwd	ISG
50ºC, pH 12.5, $Ca(OH)_2$ sat.soln.	Backhouse[70]	0.051 ± 0.008	0-3	ISG
50ºC, pH 10, KCl	Inagaki[38]	0.378 ± 0.03	2-5	ISG
Synthetic cement waters				
50ºC, pH(RT) 13.01, YCWCa soln.	Present Study	0.067 ± 0.011	0-28	MW25
50ºC, pH(RT) 13.5, YCW soln.		0.051 ± 0.001	0-32	MW25
50ºC, pH(RT) 12.3 , ECW soln.		0.006 ± 0.0001	0-42	MW25
50ºC, pH(RT) 11.56, OCW soln.		0.007 ± 0.0006	0-112	MW25
50ºC, pH(RT) 13.01, YCWCa soln.	Present Study	0.078 ± 0.007	0-28	LBS
50ºC, pH(RT) 13.5, YCW soln.		0.045 ± 0.003	0-32	LBS
50ºC, pH(RT) 12.3, ECW soln.		0.018 ± 0.001	3-28	LBS
50ºC, pH(RT) 11.56, OCW soln.		0.004 ± 0.0001	0-112	LBS
30ºC, pH(RT) 13.01, YCWCa soln.	Present Study	0.004 ± 0.0001	0-600	ISG
70ºC, pH(RT) 13.5, YCWCa soln.		0.044 ± 0.01	0-112	ISG
Cement eq. water				
50 ºC, pH 12.7, BFS:PC eq. water	Present study	0.0031 ± 0.0001	1-56	MW25
50 ºC, pH 12.7, NRVB eq. water		0.0117 ± 0.0009	1-42	MW25
50 ºC, pH 12.7, BFS:PC eq. water	Present study	0.0041 ± 0.0003	1-112	LBS
50 ºC, pH 12.7, NRVB eq. water		0.0142 ± 0.003	1-42	LBS
50 ºC, pH 12.7, BFS:PC eq. water	Present study	0.0161 ± 0.0003	1-56	ISG
50 ºC, pH 12.7, NRVB eq. water		0.0221 ± 0.004	1-21	ISG

The mechanism for glass dissolution in cement leachates differs slightly from the mechanism proposed by Geisler et al.[25] proposed mechanism. Cement water will contain significant amounts of Ca in addition to Na, K, Mg and Al, and the solution will quickly buffer towards an alkaline pH due to the presence of hydroxyl ions in the cement matrix. When glass contacts the alkaline cement water Si readily dissolves from the glass (due to the high solubility of Si at high pH, see Chapter 2) to form an amorphous silica gel. At this time, alkali /alkaline earth cations in solution are able to move into the gel through the open pore network (which is promoted by negative electrostatic forces acting on silica spheres, due to the high pH[51]) to charge compensate the negative species such as $[SiOH]^{3}$, $[Si(OH)_2]^{2-}$ and $[AlO_4]^{-}$. There is a preferential order for the cations moving into the gel based on the hydration sphere and charge of the ion: $K^+ > Na^+ > Ca^{2+} > Mg^{2+}$ (Figure 8.1) as discussed in Chapter 4. Geisler's model identifies Si aggregation resulting in the formation of a reaction rim, which restricts transport of soluble species.

Finally, in cement waters, due to the availability of Ca or alternative alkali/alkaline earth species, the precipitation of secondary phases like C-S-H or alkali-silicate hydrates, phyllosilicates and smectite clays are likely. The presence of Mg and Al can facilitate the development of zeolitic phases i.e. double layered hydroxides observed in this work.

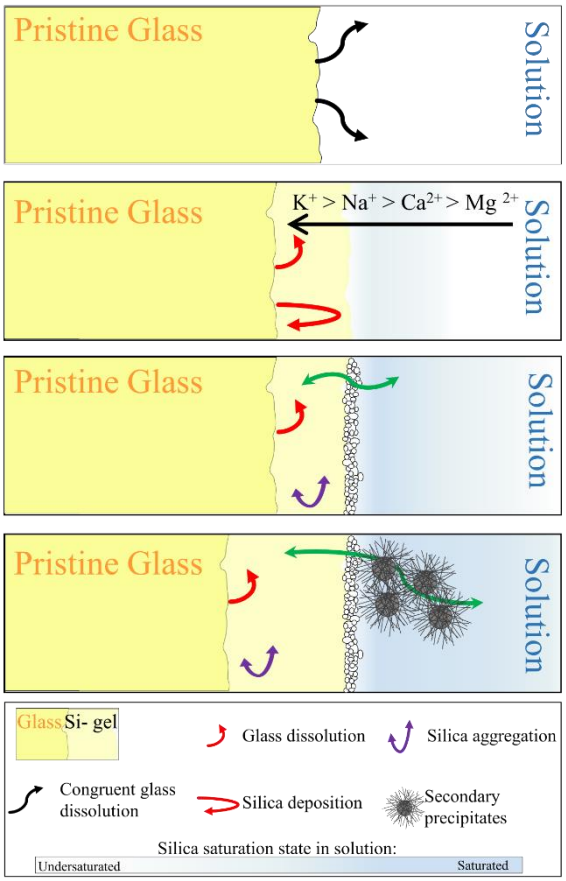

Figure 8.1 Schematic outline of a proposed glass dissolution-silica reprecipitation process in hyper-alkaline solutions based on Geisler's model (2015).

Natural analogues are used by many researchers investigating the long term durability of waste glasses for geological disposal, because the glasses found in nature have been exposed to varying chemical conditions and weathering for extended periods of time. Such studies can aid predictions of the durability of waste glasses. The Peak District has a long history of calcite mining[210], and as such the ground water passing through limestone results in high pH Ca-rich effluents[211]. Working in collaboration with the British Geological Survey, a disused railway tunnel in the Peak District is home to a natural analogue study designed to investigate how simulant nuclear waste glasses will react over a 10- year period. More information on this study can be found in Appendix I.

Although this work has sought to add to the knowledge of glass dissolution in high pH environments, there are still many questions to be answered, as detailed below.

8.1. Future Work

The nature of cement leachates gives rise to mixed alkali/alkaline earth solutions that buffer to high pH. In this thesis, it has not been possible to discern the individual effects of high pH and cation incorporation in the silica gel layer on the development of porosity and the enhancement of the dissolution rate, but it is evident from the work presented in Chapters 4 and 5 that both play a significant role in maintaining an open pore network through which solution and glass species can be transported. Additionally the effects that mixed alkali and alkaline earth cations have on glass dissolution could be investigated more thoroughly to understand the influence that a certain cation may have on the rate of dissolution and durability of alteration layers. A simple experiment whereby the cation in solution is changed to determine its effect on gel density using high resolution TEM and spectroscopic ellipsometry would be feasible.

Numerous authors in the literature (Backhouse[70] and Utton[59]) allude to boron incorporation in the alteration layer: in Chapters 4, 6, and 7 the NL_B and NL_{Li} followed similar trends; however Li was released more rapidly into solution than B, again alluding that B is being incorporated into alteration layers. A systematic study into B retention in alteration layers in hyper-alkaline solutions could provide evidence that suggests B is not a suitable tracer element in hyper-alkaline solutions.

Chapter 6 investigated the impact of an evolving leachate on the alteration layer formation. Greater information could be gained by conducting the experiment with a greater number of time points, to observe the potential retreat of alteration layers when fresh leachate was added and the gradual growth as the solution became saturated (does this process result in rate resumption followed by a rate drop when the solution becomes saturated again?). Additionally, with a greater number of time points, information on the rate of dissolution could be obtained.

Appendix I.

Introduction

A collaboration between the University of Sheffield and the British Geological Survey began in 2015, the aim of the collaboration was to study glass samples that had been exposed to Ca-rich leachate in a cave in the Peak District (known as Peak Dale Tunnel) for approximately 50 years, these samples have the potential to provide information on how glass behaves in a high pH Ca-rich environment over much longer time scales than laboratory experiments. In addition to studying glasses found in the tunnel, a natural analogue study was prepared, the experimental set up is outlined in MRS Advances 2017 paper. Supplementary information has been provided on the glass samples for implementation.

The MRS Advances 2018 paper outlines a study conducted on soda lime silicate glass of the same composition as a glass found in the Peak Dale tunnel comparing synthetic young cement water with added Ca and saturated $Ca(OH)_2$, these solutions are used to mimic a high pH Ca-rich geological disposal environment for long term nuclear waste storage.

MRS Advances 2017: Interactions between Simulant Vitrified Nuclear Wastes and high pH solutions: A Natural Analogue Approach

MRS Advances, 2(12), 669-674. https://doi.org/10.1557/adv.2017.59

Published online 20th January 2017

Interactions between Simulant Vitrified Nuclear Wastes and high pH solutions: A Natural Analogue Approach

Colleen Mann[1], Clare Thorpe[1], Antoni E. Milodowski[2], Lorraine P. Field[2], Richard P. Shaw[2], Luke Boast[1], Russell Hand[1], Neil C. Hyatt[1], John L. Provis[1] and Claire L.Corkhill[1]

[1]*NucleUS Immobilisation Science Laboratory, Department of Materials Science and Engineering, The University of Sheffield, Mappin Street, Sheffield S1 3JD, UK*

[2]*British Geological Survey, Environmental Science Centre, Nicker Hill, Keyworth, Nottingham, NG12 5GG, UK*

Abstract

This study details the characterization of a glass sample exposed to hyperalkaline water and calcium-rich sediment for an extended time period (estimated as 2 - 70 years) at a lime (CaO) waste site in the UK. We introduce this site, known as Peak Dale, in reference to its use as a natural analogue for nuclear waste glass dissolution in the high pH environment of a cementitious engineered barrier of a geological disposal facility. In particular, a preliminary assessment of alteration layer chemistry and morphology is described and the initiation of a long-term durability assessment is outlined.

Introduction

Owing to a long history of encapsulation of radioactive wastes in cementitious materials, the proposed geological disposal facility (GDF) of the UK will most likely incorporate a significant volume of cement. In addition to 450,000 m^3 of cement-encapsulated waste [1], the facility may also use a cementitious backfill as part of the engineered barrier, which will be optimised to physically and chemically impede the transport of radionuclides to the biosphere [2]. Over geological time scales, groundwater will interact with the cementitious components of the facility resulting in high pH conditions in the repository [3]. Should vitrified intermediate level waste be

placed in this environment, an understanding of the effect of cement leachates on the longevity of glass is required.

We describe a new natural analogue site for long-term glass durability assessment in high pH, cement-like leachates, including a preliminary assessment of the physical and chemical conditions and their effects on glass samples recovered from the site.

Methodology

Site and sample description

The Peak Dale Tunnel site is a disused railway tunnel, constructed in the early 20th century, to link the Peak Dale limestone quarry to its associated limekilns. The waste produced from the limekilns is distributed in a thick layer (1 – 2 m) of lime (CaO) over the soil and bedrock of the surrounding area [4]. This has seeped through to the tunnel below, creating a naturally hyperalkaline ground water and Ca-rich sediment. Access to the tunnel was restricted to the public when a locked gate barred the entrance. A number of glass bottles were found to be exposed to these high pH conditions for an estimated period of time between 2 and 70 years, four samples are being examined due to their varying compositions and large proportions of the bottle remains intact.

Site characterization

The tunnel has a stable temperature ranging from 8 – 9 ± 0.5 ^{o}C [4]. A sample of sediment was taken from a depth of 1 - 4 cm and dried in air prior to sieving to a particle size of < 75 μm for X-ray diffraction (XRD) analysis. XRD data were acquired using a Bruker D2 Phaser, with Cu Kα radiation, from $5^{\circ} < 2\theta < 70^{\circ}$ with a step size of 0.01°. The X-ray tube settings were 30 kV and 10 mA.

The water level in the tunnel varies throughout the year, but the back of the tunnel is flooded permanently to a depth of 1-1.5 m^2. Alkaline ground water was sampled from standing water at two locations in the tunnel; the first is periodically subject to complete evaporation (referred to herein as the “beach”), and the second is a deep central pond. Samples were filtered (0.22 μm), acidified with nitric acid and analysed for major elemental content using Inductively Coupled Plasma-Optical Emission Spectroscopy (ICP-OES) analysis (Thermofisher, iCAP Duo).

Glass sampling, preparation and analysis

The glass samples found at the site were removed from beneath the sediment. In the laboratory, glass samples were air dried then sectioned using a diamond slow saw. Compositional analysis via acid digest and ICP will be determined for all glass samples found at the site, samples were prepared for Scanning Electron Microscopy (SEM) by mounting in epoxy resin and grinding the cross-sectional surface on silicon carbide paper (P600, 800 and 1200, respectively), followed by polishing using diamond suspension 6, 3 and 1 µm. The sample was carbon coated prior to inspection on the SEM. Imaging was performed using an FEI Quanta 200 F SEM with EDX using an accelerating voltage of 20 kV and a working distance of 10 mm.

Results and discussion

Figure 1 shows the location of the Peak dale site in the UK (Fig 1a), and the tunnel is shown in Fig. 1b. The stalactites and stalagmites demonstrate the propensity for lime waste leaching into the tunnel from above.

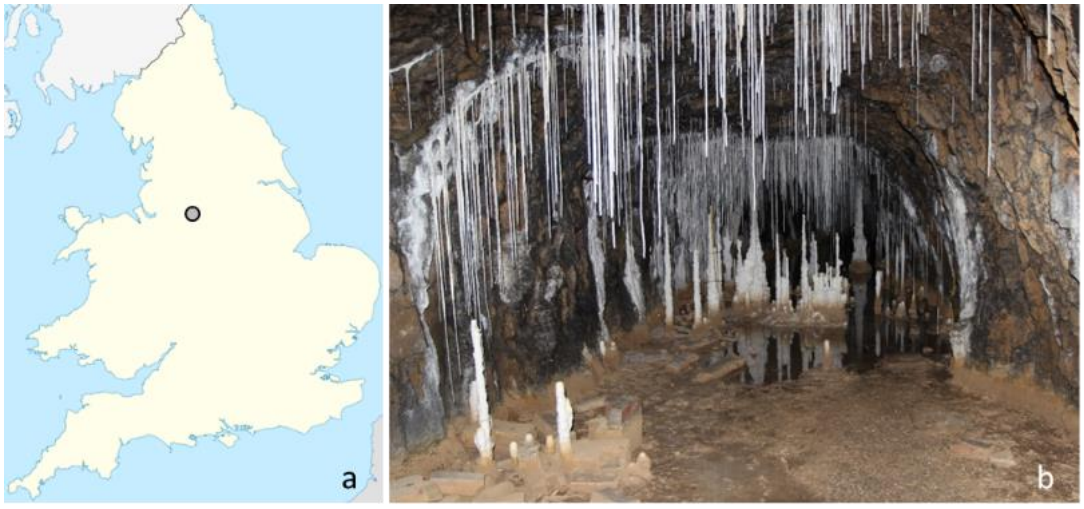

Figure 1 (a) Map of the UK with the location of the Peak Dale Tunnel; (b) photograph of the Peak Dale tunnel.

Analysis of the tunnel sediment by XRD (Figure 2) revealed a composition of calcite ($CaCO_3$), which is formed when the hydrated limewaste ($Ca(OH)_2$) is in equilibrium with atmospheric $CO_{2(g)}$. This is a major difference between this natural analogue site and a GDF, as there will be no atmospheric CO_2. However, low concentrations of $CO_{3(aq)}$ will be present in the GDF ground water[5], albeit at a much lower concentration than at the Peak Dale site.

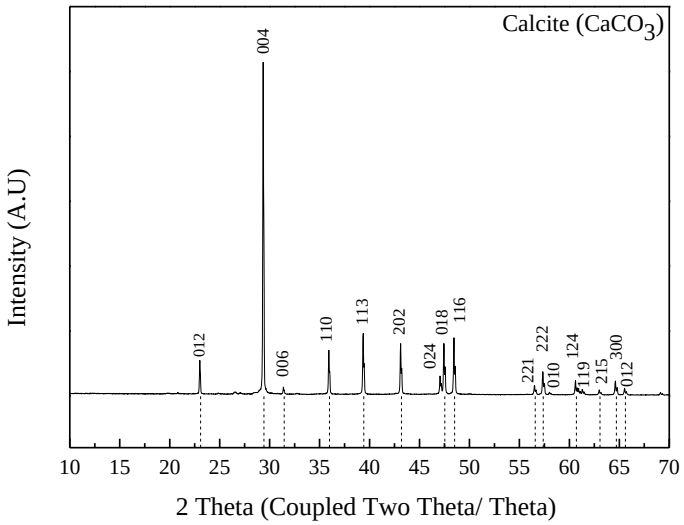

Figure 2. X-ray diffraction pattern of sediment from the central pond in the Peak Dale tunnel.

The pH of the water was measured as pH 12.79 ± 0.5. Table I. shows the analysed concentration of major elements in the two sample locations within the tunnel. For comparison, the composition of three synthetic cement waters are shown. Hyperalkaline cement water will evolve, from an initial potassium rich leachate (pH~13) represented here by young cement water, to a Ca-OH fluid (pH 10 - 12.5) buffered by the dissolution of portlandite ($Ca(OH_2)$). Subsequent dissolution of calcium silicate hydrate phases, represented here by the evolved cement water, will occur and finally an old cement water, with a similar composition to ground water will be present in the GDF [6,7]. The Na value from the central pond at Peak Dale is anomalously high when compared to the value from the beach, which is attributed to grit salt on the nearby roads. The water sample from the beach is comparable to the synthetic evolved cement water, given its low K concentrations and alkalinity being governed by Ca and Na hydroxides.

Table I. Elemental concentration (mg L^{-1}) of standing water from the Peak Dale site, compared with synthetic formulations of cementitious ground waters. Errors stated are based on the standard deviation across the range of measurements.

Element	**Peak Dale Central Pond**	**Peak Dale Beach**	Synthetic Young Cement Water + Ca	Synthetic Evolved Cement Water	Synthetic Old Cement Water
Al	**0.76 ± 0.02**	**0.06 ± 0.02**	-	0.09 ± 0.06	0.01 ± 0.04
Ca	**34.82 ± 0.09**	**332.50 ± 0.76**	15.24 ± 0.74	503.53 ± 3.48	33.58 ± 3.41
K	**22.61 ± 0.08**	**19.93 ± 0.03**	9415.67 ± 18.50	6.72 ± 0.29	0.44 ± 0.75
Na	**1027.31 ± 0.72**	**421.80 ± 0.47**	1595.33 ± 6.85	373.47 ± 10.90	105.67 ± 3.47
S	**35.23 ± 0.08**	**286.20 ± 0.47**	35.88 ± 0.49	0.14 ± 0.015	2.75 ± 0.32
Si	**8.53 ± 0.04**	**8.61 ± 0.05**	0.05 ± 0.02	0.19 ± 0.07	0.02 ± 0.01

The sediment layers and surface morphology of one of the glass samples recovered from the Peak Dale tunnel are shown in Figure 3. A thick (1.0 ± 0.1 mm) layer was observed on the surface of the glass (Fig. 3a), which was banded; this is postulated to be due to repeated wetting and drying as the water level in the tunnel fluctuates throughout the year. The elemental map shown in Figure 3b indicates that these layers are rich in calcium, which is in good agreement with the presence of high quantities of calcite in the sediment (Fig. 2). It is therefore likely that the mineral phase present in the alteration layer is also calcite ($CaCO_3$).

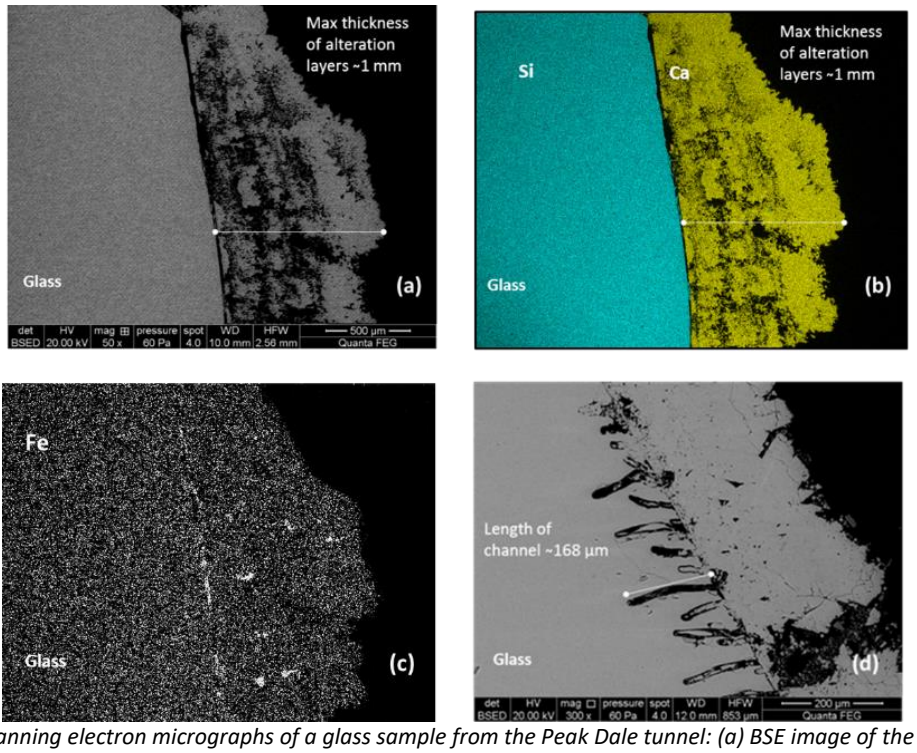

Figure 3. Scanning electron micrographs of a glass sample from the Peak Dale tunnel: (a) BSE image of the alteration layer; (b) elemental mapping showing distribution of Ca and Si and (c), iron (d) BSE image, showing chemiturbation channels at the interface between the sediment on the surface and bulk of the glass.

The main source of iron in the Peak Dale tunnel is from the remnants of steel cables that are now severely corroded. This has been sequestered at the interface between the glass and the alteration layer, as shown in Figure 3d. It is also observed in pores in the banded regions of the alteration layer. Canister corrosion will result in the accumulation of iron in a GDF; it has been shown that the presence of iron corrosion products can affect the initial stage of glass alteration. Silica can sorb to iron corrosion products, retarding the formation of a silica gel layer on the surface of the glass [8]. It is also been shown that silica precipitates on magnetite (Fe_3O_4) and Fe-silicates in the surroundings or within the porous gel layer if iron rich compounds are present [9]. The presence

of iron in the tunnel allows investigation into how iron will affect the dissolution of simulant UK nuclear waste glasses.

Figure 3d shows chemiturbation channels < 200 μm in length. This inward corrosion originates from the surface of the glass and proceeds towards the bulk. The origin of these channels is not yet understood, however, potential causes may be: damage to the glass surface, exposing regions of tensile stress that corrode more rapidly than the surrounding areas; repeat wetting and drying resulting from seasonal changes in the water levels; and morphological features that are, in essence, high energy sites that promote dissolution. Further work is underway to determine the origin of these features.

Future use of the Peak Dale tunnel as a natural analogue for understanding long-term glass dissolution

The conditions at the Peak Dale site are suitable for conducting a long term natural analogue study; a hyperalkaline environment with ground water that is comparable in composition to an evolved cement leachate. In addition, a steady all year round temperature and sufficient water levels will allow the submersion of glass samples for an extended time period of up to 10 years.

The following vitrified waste simulants will be placed within a bespoke sample holder (Figure 4a-c) and immersed within the tunnel water: the International Simple Glass (ISG); UK Magnox waste glass (MW25); vitrified UK plutonium contaminated material (PCM); prototype vitrified ion exchange resin waste; a laboratory borosilicate waste simulant (LBS); SON68 and a re-melted composition of one of the glass bottles originally found in the tunnel.

Samples will be removed at 1, 3, 5 and 10 years, and alteration layers will be characterized by SEM/EDX, glancing incidence XRD, Time of Flight Secondary Ion Mass Spectrometry (TOF-SIMS) and Transmission Electron Microscopy (TEM). This will develop our current knowledge of the chemical composition of alteration layers within this hyperalkaline environment and aid our understanding of the long-term durability of nuclear waste glass.

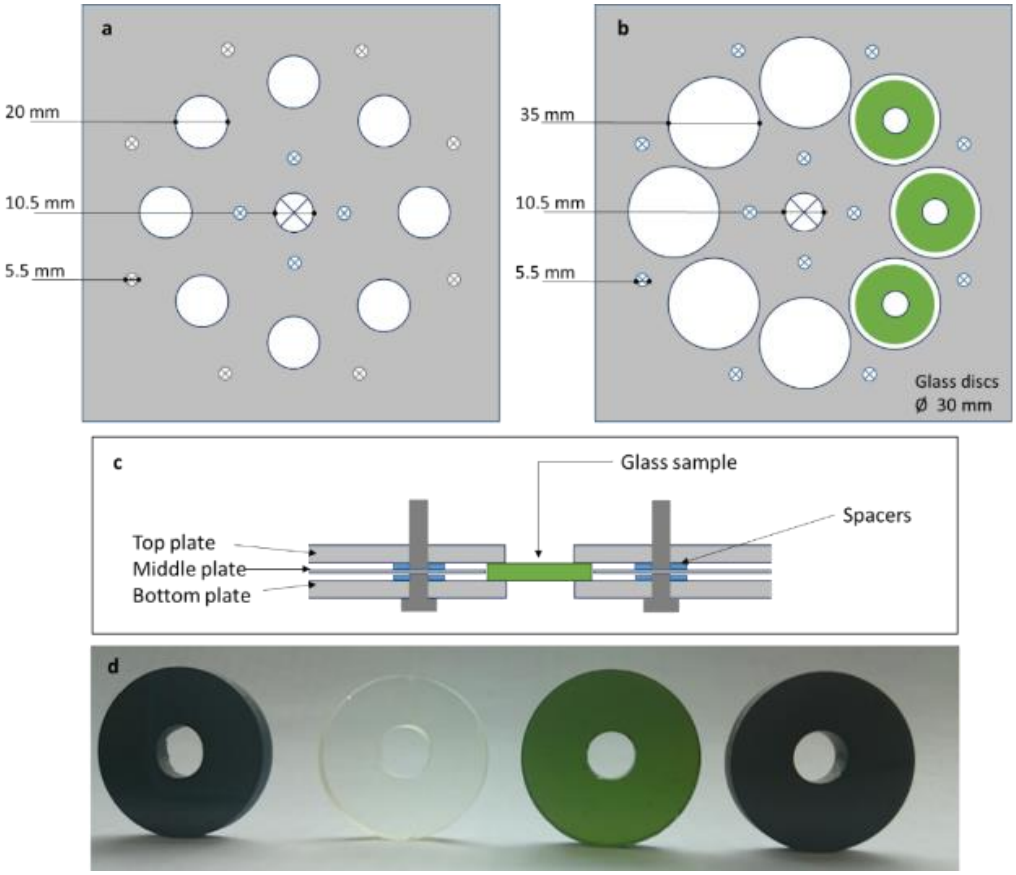

Figure 4. Schematic of sample holder (a) top and bottom plate 5mm thick PTFE used to sandwich glass samples (b) middle plate 1mm thick PTFE, holds glass samples in position (c) side view of the sample holder (d) glass samples left to right PCM, ISG, MW25, LBS.

Conclusion

The Peak Dale site has provided glass samples with significant alteration layers due to an extended exposure in hyperalkaline ground water and Ca-rich sediment, the composition of which is similar to evolved cement water that will occur within a GDF over geological time scales. The presence of chemiturbation channels at the surface of the glass sample require further research to understand how they develop, and to quantify their effect on the long term durability of glass wasteforms. The site is suitable for a long term durability study investigating simulant nuclear waste glasses relevant to the UK disposal scenario in the natural environment despite the presence of air and a temperature of ~ 9 ^{o}C. The results generated from this study will provide information on the long-term behaviour of vitrified waste materials within a cementitious geological disposal facility.

Acknowledgments

The authors wish to acknowledge Martina Klinkenberg at FZ Jülich for assistance with SEM. We acknowledge Coke Turner and Co., Land Agents for the Duchy of Lancaster for permission to work and sample within the tunnel, Mr D. Abraham of Natural England for permission to access the tunnel via the SSSI area. We are grateful to EPRSC for funding through the Nuclear First DTC programme (EP/G037140/1) and for an Early Career Research Fellowship awarded to CLC (EP/N017374/1). This research was performed, in part, at the MIDAS Facility, at the University of Sheffield, which was established with support from the Department of Energy and Climate Change.

References

1. NDA DECC, 2013 UK Radioactive Waste Inventory (2014).

2. Department of Energy & Climate Change, Implementing Geological Disposal, (2014)

3. T.W. Hicks, T.D. Baldwin, P.J. Hooker, P.J. Richardson, N.A. Chapman1, I.G. McKinley1, and F.B. Neall, Galson Services Limited Report (2008).

4. L. P. Field, A. E. Milodowski, R. P. Shaw, L. A. Stevens, A. Kilpatrick, J. Gunn and S. J. Kemp, Min Mag. **080**, 111 (2016).

5. L.O. Werme, R.S. Forsyth, SKB technical report 89-14 (1989)

6. C.D. Coumes, Cement and Concrete Research. **36**, 2152-2163 (2006).

7. U.R. Berner, Waste Management. **12,** 201–219 (1992).

8. D. Rébiscoul, V. Tormos, N. Godon, J.P. Mestre, M. Cabie, G. Amiard, E. Foy, P. Frugier, S. Gin, Applied Geochemistry. **58,** 26-37 (2015).

9. P.Dillmann, S. Gin, D. Neff, L. Gentaz, D. Rebiscoul, Geochimica et Cosmochimica Acta. **172,** 287–305 (2016).

Supplementary Glass Information Prior to Implementation

Materials and Methods

Vitrification

Glass compositions taken from the literature for UK simulant nuclear wastes glasses are outlined below:

MW-25%: this glass was developed as a simulant for the UK's vitrified HLW. It consists of an alkali borosilicate bass glass (MW) containing Zr and loaded with 25 wt % simulant waste rich in Mg and Al from the historic Magnox reactors. The frit (H0023/1 Ca/Zn ½ Li) and calcine (WRW17, contains Ru & Li)) was provided by NLL (Mike Harrison) and mixed prior to melting at the University of Sheffield.

LBS: Laboratory borosilicate glass was developed at the University of Sheffield to simulate ILW waste generated from the SIXSEP plant at Sellafield, the composition was developed by Bingham et al (2009) [212] and used by Utton et al [75].

The oxide precursors for LBS were mixed in a plastic bag prior to the melt, it is worth noting that the melting glass rose and bubbled significantly (don't over fill the crucible), the melt was fluid at 1000 ^{o}C.

Clino: Cs exchanged clinoptilolite-sand was mixed with glass forming reagents to make a glass with a reduced melting temperature to diminish the volatilisation of Cs from the wasteform. The formulation was developed by Jack Clarke at the University of Sheffield.

Clinoptilolite-sand was washed 3 times with de-ionised water and dried overnight at 90 ^{o}C. A 0.25M solution of CsCl was prepared and the dry clinoptilolite added, the mixture was agitated overnight, after filtration, the clinoptilolite was dried overnight at 90 ^{o}C, and the final product was a Cs-exchanged clinoptilolite-sand. 56.22 wt% Cs-exchanges clino was mixed with 43.78 wt% Borax anhydrous to make the glass batch.

PCM: Plutonium contaminated material was mixed with plastic, mortar and metal in addition to glass forming reagents and melted to produce a phase separated glass, the original glass was made my Luke Boast[213,214] in an alumna crucible of which the glass was smashed out of. The fragments of PCM glass were re-melted and cast into a block.

Bottle glass (BGS-1): A fragment of glass bottle found in the Peak Dale tunnel was crushed for elemental analysis by acid digest and ICP-OES. The composition was utilised to re-make the historic glass, for dissolution experiments and implementation in the Peak Dale tunnel.

The oxide and carbonate precursors were mixed in a plastic sample bag by hand for ~ 10 minutes, prior to filling on the preheated crucible.

Table 3. 18 Melt conditions for vitrified glasses

Glass	MW-25%	LBS	Clino	PCM	BGS-1
Melt Temp, ^{o}C	1050	1200	1150	1050	1200
Melt Duration, hrs	4	4	4	4	3
Cooling Rate, ^{o}C min^{-1}	1	1	1	1	1
Anneal. Temp, ^{o}C	500	450	515	500	515
Anneal. Duration, h	1	1	1	1	1
Furnace Type	Electric	Electric	Electric	Electric	Electric
Stirred	Yes	Yes	Yes	Yes	Yes
Crucible Material	Alumina	Alumina	Platinum	Alumina	Platinum

Table 2. Glass compositions wt% values taken from ICP-OES analysis of original samples

	MW	LBS	ISG	Clino	PCM	BGS-1
SiO_2	39.12	47.92	56.2	42.74	54.85	71.37
B_2O_3	19.4	9.62	17.3	43.78	?	-
Na_2O	6.84	12.94	12.2	1.74	6.02	17.49
Li_2O	3.2	3.9	-	-	-	-
GdO_3	-	-	-	-	-	-
ZrO_2	1.02	0.67	3.3	-	<0.05	0.03
MoO_3	0.89	0.52	-	-	-	-
Al_2O_3	8.13	6.85	6.1	7.36	11.7	0.49
Fe_2O_3	2.38	10.24	-	0.67	17.65	0.12
Nd_2O_3	1.38	-	-	-	-	-
Cs_2O	0.88	0.69	-	0.56	-	-
MgO	3.57	3.71	-	0.39	0.86	0.06
CeO_2	1.01	0.36	-	-	-	0.55
BaO	0.27	0.11	-	0.06	0.31	0.01
La_2O_3	0.52	1.53	-	-	-	-
RuO_2	0.63	-	-	-	-	-
Pr_2O_3	0.24	-	-	-	-	-
SrO	0.22	0.13	-	0.28	<0.05	-
NiO	0.4	0.05	-	-	-	-
Sm_2O_3	0.25	-	-	-	-	-
Y_2O_3	0.14	-	-	-	-	0.02
CaO	4.52	0.45	5	1.18	7.07	9.08
K_2O	0.01	0.15	-	1.07	0.48	0.34
V_2O_5	-	-	-	-	<0.05	-
Cr_2O_3	0.41	0.01	-	-	0.13	0.01
SO_3	0.08	0.13	-	0.06	-	0.22
TiO_2	0.01	0.01	-	0.11	-	0.04
Cu_2O	0.02	0.02	-	-	-	0.04
ZnO	4.2	0.01	-	-	-	0.03
As_2O_3	-	-	-	-	-	0.1
Total	99.74	100.02	100.1	100	99.07	100

MRS Advances 2018: Dissolution of glass in cementitious solutions: An analogue study for vitrified waste disposal

MRS Advances, 3(21), 1147-1154. https://doi.org/10.1557/adv.2018.227

Published online: 27 February 2018,

Dissolution of glass in cementitious solutions: An analogue study for vitrified waste disposal

Colleen Mann1, Tjin Le Hoh1, Clare L. Thorpe1, and Claire L. Corkhill1

1NucleUS Immobilisation Science Laboratory, Department of Materials Science and Engineering, The University of Sheffield, Sheffield, United Kingdom, S1 3JD.

The dissolution of a soda-lime silicate glass in two cement leachate compositions, Young Cement Water (YCW) and $Ca(OH)_2$, was investigated, as an analogue for dissolution of vitrified nuclear waste in a cementitious geological disposal facility. Dissolution was performed at repository temperatures (50 °C) and under CO_2-exclusion. Dissolution rates were observed to be a factor of 20 times higher in YCW than in $Ca(OH)_2$, as result of the high potassium content of YCW solutions. The precipitation of the zeolite phase, K-phillipsite ($K(Si,Al)_8O_{16}·6H_2O$), is thought to be responsible for elevated dissolution rates. Conversely, in $Ca(OH)_2$ solutions, the precipitation of calcium- and silica-containing phases, such as tobermorite (Ca5Si6O16(OH)·4H2O), acted to reduce rates of dissolution by forming a barrier to diffusion. These results show that dissolution of vitrified nuclear waste materials in a cementitious repository may be significant during the early stages of cement leaching in groundwater.

Introduction

In the designs of several geological disposal facilities for nuclear waste, cement will feature as a key material in construction. In the UK and Belgium, it may also be used as a layer of containment within the engineered barrier; in the UK this may be as a backfill to surround canisters of cementitious and vitrified intermediate level waste [1], and in Belgium, cement will be used in the supercontainer concept for vitrified high level waste [2]. When groundwater interacts with these cementitious materials, it will be buffered to high pH values; initially these values will be > pH 13 due to the dissolution of alkali elements (Na, K), but the pH will continue to fall with the subsequent dissolution of portlandite ($Ca(OH)_2$, pH ~ 12) and, eventually, calcium silicate hydrates (C-S-H, pH ~ 10) [1]. The key mechanisms of glass corrosion are known to be influenced

by high pH environments due to enhanced solubility of Si and other sparingly soluble elements such as Al and Zr [3 - 5]; the result is enhanced dissolution rates, undesirable for the disposal of vitrified radioactive wastes in a geological disposal facility. However, the presence of elevated concentrations of Ca, resulting from the dissolution of $Ca(OH)_2$ in cement by groundwater, have been shown to improve the durability of vitrified nuclear waste, through the formation of a thick Ca-silicate gel and precipitates of C-S-H, which act as a barrier to diffusion of water and glass elements during dissolution [e.g.4, 6-9].

Despite detailed investigations of simulant nuclear waste glass at high pH in simplified solutions, e.g. KOH and NaOH, few investigations have focused on the effect of cement leachates, which are more complex in chemistry than these simplified solutions [10, 11]. Using a simplified soda-lime-silicate glass, we present results from a comparative study of glass dissolution in solutions representative of early cement leaching (Young Cement Water (YCW)) and intermediate timescales of cement leaching ($Ca(OH)_2$).

Methodology

Samples of glass have been retrieved from the Peak Dale Tunnel (UK, Fig. 1a). Owing to its high pH and $Ca(OH)_2$-dominated groundwater, this site is being utilised as a natural analogue site for dissolution of glass in high pH, Ca-rich solutions [12]. In this study, we replicated the glass composition of one of the soda-lime-silicate glasses thought to have been present in the tunnel for >50 years, to develop an understanding of its dissolution in cementitious leachates. Further investigation of the dissolution of this glass in the tunnel environment is discussed elsewhere [13].

A portion of a soda-lime silicate glass bottle retrieved from the Peak Dale Tunnel (Figure 1) was cleaned using 6% acetic acid for 7 hours to remove the $CaCO_3$ mud on the surface, and analysed by X-ray Fluorescence Spectroscopy (PANalytical Zetium with a Rh Xray source). Based on this analysis (Table 1), a glass was batched for use in dissolution experiments. The glass was melted at 1200 °C for 4 h in a platinum crucible, cast into a block and annealed at 515 °C for 1 h. Analysis of the resultant glass by XRF gave excellent agreement with the original glass.

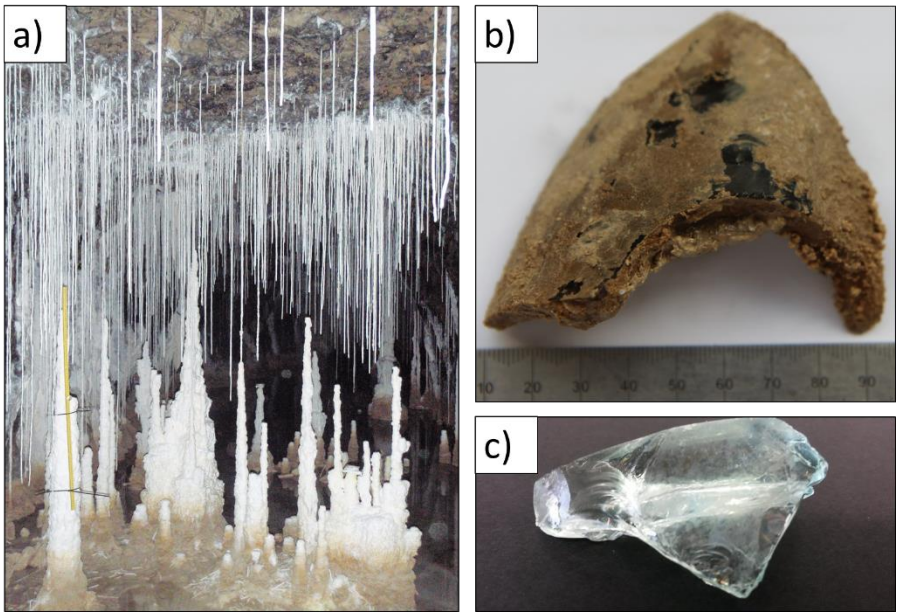

Figure 1. Peak Dale Tunnel (UK) is used as a natural analogue location for high pH, Ca-mediated glass dissolution [12], (a) the stalactites and stalagmites formed by seepage of water through lime waste above the tunnel; (b) glass bottle retrieved from tunnel, coated in $CaCO_3$ mud after >50 years exposure to high pH conditions; (c) cleaned bottle

Table 1. Composition of the Peak Dale Tunnel glass (mol%), as measured by XRF.

Oxide	Al_2O_3	As_2O_3	CaO	CeO_2	CuO	Fe_2O_3	Na_2O	SO_3	SiO_2	Total
mol %	0.82	0.29	12.72	3.06	0.10	0.26	43.22	0.25	39.28	100 %

The glass was crushed and sieved to a 75 – 150 μm particle size, prior to washing according to ASTM C1285 (the Product Consistency Test, PCT [14]). The density of the powders was determined using helium pycnometry (Micromeritics AccuPyc II 1340) to be 2.64 ± 0.001 g cm^{-3}. Dissolution experiments were performed according to the PCT-B methodology [14], using 10 mL of either Young Cement Water (YCW) or $Ca(OH)_2$. YCW with added Ca was prepared according to Ferrand et al. [10], with a target composition stated in Table 2. A solution of 0.1 M $Ca(OH)_2$ was prepared by suspending $Ca(OH)_2$ (99.9%, Sigma Aldrich) in de-aerated ultra-high quality water (18 MK) and agitating vigorously. Both solutions were prepared in an inert gas glove box to prevent carbonation.

Table 2. Target composition of Young Cement Water, representative of the early stages of cement dissolution

Element	Na	K	Ca	Al	Si	So_4^{2-}	CO_3^{2-}
Conc, mol L^{-1}	1.4 $x10^{-1}$	3.7 x 10^{-1}	7 x 10^{-4}	6 x 10^{-3}	3 x 10^{-4}	2 x 10^{-3}	3 x 10^{-4}

Solutions were filtered (0.22 μm) and placed in Teflon vessels, prior to the addition of crushed glass powder, at a SA geo/V ratio of 1200 m-1. Vessels were placed in an oven at 50 ± 2 °C under flowing nitrogen gas (to prevent carbonation) and sacrificially removed at 1, 3, 7, 14, 21 and 28 days. Each time point was performed in triplicate, with duplicate blanks. At each sampling interval, solutions were removed (within an inert atmosphere glove box), filtered using a 0.22 μm filter, and the pH was measured. Acidification with 10 μL of concentrated, ultrapure nitric acid (69%) was performed prior to analysis by Inductively Coupled Plasma-Optical Emission Spectroscopy (ICP-OES, Thermofisher iCAPduo6300) to determine the concentration of dissolved elements. The resulting solution chemistry was modelled with the PHREEQC geochemical modelling package, using the LLNL database.

The normalised mass loss of element *i*, NL_i (g m-2), was calculated according to Eqn. 1, where C_i is the concentration of element, *i*, in solution (g cm-3), C_i,*b* is the concentration of element, *i*, in the blank (g cm^{-3}), f_i is the mass fraction of element, *i*, in the glass (unitless), and SA/V is the surface area to volume ratio (m^{-1}).

$$NL_i = \frac{C_i - C_{i,b}}{f_i \times {SA}/{V}} \qquad \text{Eqn. 1}$$

After dissolution, glass powders were dried and analysed by X-Ray Diffraction (XRD, Bruker D2 Phaser), utilising a Cu Kα source, between 10° > 2θ < 70° at a step size of 0.02 ° per second, to identify any crystalline alteration layer phases. Powders were then mounted in epoxy resin, ground and polished to a 1 μm finish and examined by Scanning Electron Microscopy (SEM, Hitachi TM3030) equipped with Energy Dispersive Spectroscopy (EDS, Bruker Quantax).

Results

Dissolution results

The measured pH of each solution did not significantly deviate throughout the course of the experiments; the starting and finishing pH for $Ca(OH)_2$ experiments was 13.0 ± 0.1, while the starting and finishing pH for YCW experiments was 13.7 ± 0.1 and 13.5 ± 0.1, respectively. The normalised mass loss (NL_i) of major detectable elements is shown in Figure 2. Despite its presence in the glass, it was not possible to calculate the NL_{Ca}, due to a rapid uptake of Ca by the glass; the resulting calculation gave negative values, therefore, data are presented as concentration only.

Despite the similarity in pH of the solutions, for all elements analysed, the NL_i was greater in the YCW solution than in the presence of $Ca(OH)_2$; for example, the NL_i at 28 d was 3.5 times greater for Na, and ~20 times greater for Si, Al and S, in YCW than $Ca(OH)_2$. The corresponding dissolution rate of Si, measured between 1 d and 28 d, was 0.092 ± 0.002 g m-2 d-1 in $Ca(OH)_2$ and 1.862 ± 0.500 g m^{-2} d^{-1} in YCW. In both solutions, the concentration of Ca rapidly decreased (Fig. 2e) and, in the YCW solution, the concentration of K also decreased significantly between 0 and 3 days of dissolution (Fig. 2f). The concentration of these elements in the blank solutions did not decrease (data not shown), indicating that in the presence of glass, formation of Ca- or K-containing alteration layers occurred.

Alteration layer analysis

Glass samples exposed to solutions of YCW for 28 days demonstrated a thick (~20 μm) alteration layer, with a complex, layered morphology (Figure 3a). The inner layer (closest to the glass surface) was rich in K and Si, with some Al present, while the outer layer was rich in Si, K and Ca, with a minor quantity of Al. The presence of K is concurrent with the rapid decrease of this element in solution (Fig. 2f). XRD analysis (Figure 3b) shows that the composition of the alteration layer changed with time. A large region of diffuse scattering was observed, with a number of diffraction peaks. Due to the pseudo-crystalline nature of the material, it was difficult to identify these peaks with confidence, however at earlier time points (3 and 7 days), the peaks were consistent with the presence of phillipsite-K, a zeolite with nominal composition $K(Si,Al)_8O_{16}6H_2O$ (labelled P, Fig. 3b), and tobermorite (nominal formula of $Ca_5Si_6O_{16}(OH)\cdot 4H_2O$, labelled T, Fig. 3b). At 21 days, the peak relating to tobermorite was observed to increase in intensity, concurrent with the outer layer of Ca and Si-rich precipitates observed on the surface of the glass by SEM / EDS. These phases were also identified as being saturated in solution by geochemical modelling, in addition to amorphous silica.

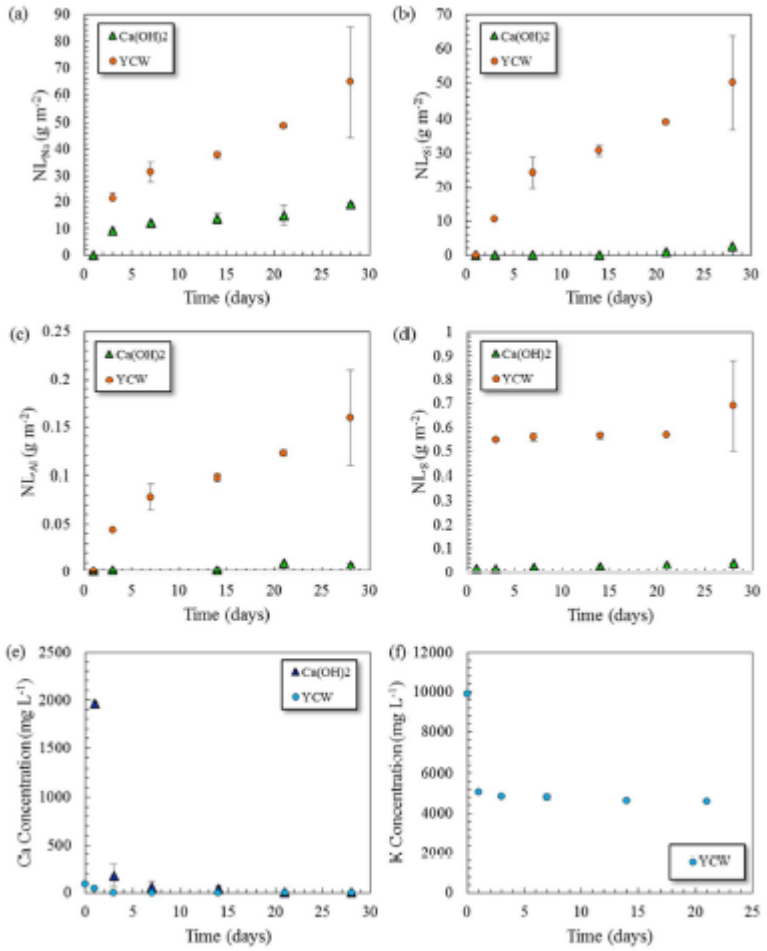

Figure 2. Normalised mass loss of (a) Na; (b) Si; (c) Al and (d) S; and solution concentrations of (e) Ca; and (f) K.

Figure 3c shows the SEM / EDS images for particles of glass exposed to $Ca(OH)_2$ solution for 28 days. These demonstrated a thin alteration layer, less than 1 μm thick, composed of Si and Ca only. In addition to this layer, there were several Ca- and Si containing precipitates observed, which may have become detached from the particles during drying and preparation for imaging. XRD analysis performed after 3, 7 and 21 days of dissolution revealed the presence of a two regions of diffuse scattering (Figure 3d); based on XRD of the pristine material (data not shown) one of these regions may be attributed to the glass, while the other may result from a Ca-Si gel, formed as a result of silica-gel reorganisation upon dissolution, as observed in previous studies [e.g. 4, 9]. Intense diffraction peaks were indexed as tobermorite (labelled T); this phase was also identified as being saturated in solution by geochemical modelling with PHREEQC.

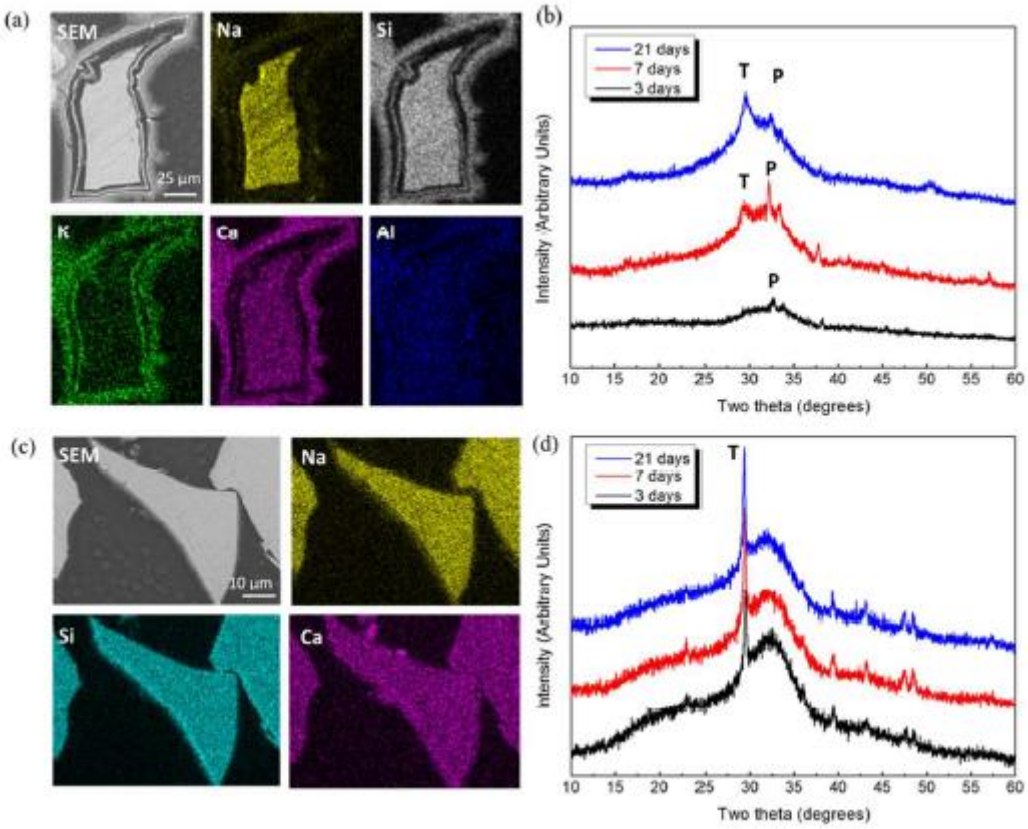

Figure 3. Analysis of glass powders leached in YCW was performed by (a) SEM / EDS after 28 days; and (b) XRD at three time points. Analysis of glass powders leached in $Ca(OH)_2$ was performed by (c) SEM / EDS after 28 days; and (d) XRD at three time points. Major peaks only are indexed on XRD figures, where P = K-phillipsite, and T = tobermorite.

Discussion

Comparison of the dissolution of the analogue glass originating from the Peak Dale Tunnel in $Ca(OH)_2$ and YCW solutions, revealed that dissolution was more rapid in YCW, despite both solutions having similar pH throughout the experiment. Young Cement Water, representative of the initial leaching of cement by groundwater, contains high concentrations of alkali elements. Most notably, the presence of elevated concentrations of K seemed to underpin the large difference in dissolution between the two solutions, as evidenced by the precipitation of phillipsite-K. The dissolution rate was an order of magnitude greater in the presence of YCW than $Ca(OH)_2$. The difference in dissolution is likely to arise from the following processes: i) in the initial stages of dissolution, the removal of Si from solution to form phillipsite-K results in local under saturation of Si in the solution at the glass surface; this drives further Si release to maintain

thermodynamic (quasi-) equilibrium, thus increasing the dissolution rate; and ii) despite no further removal of K from solution, the dissolution rate of the glass remains high. We hypothesise that the alkali-silica gel layer formed on the surface of the glass (e.g. Fig. 3a) must be porous, in accordance with the known behaviour of silica gels [15], and other borosilicate glass alteration layers [10] at high pH, thus allowing the free diffusion of species from the glass to the solution (and *vice versa*). Conversely in $Ca(OH)_2$ solution, the presence of a Ca-Si rich layer on the surface of the glass leached in Ca(OH)2, including precipitates of crystalline tobermorite, acts as a diffusion barrier to dissolution, thus lowering the dissolution rate.

The presence of zeolite phases, like K-phillipsite, has been postulated as being a pre-cursor for the resumption of glass dissolution in the so-called "Stage III" of glass dissolution [16, 17]. Further work, of longer time duration, is required to ascertain the role of this phase in the long-term dissolution of vitrified materials.

Conclusions

The dissolution of glass was found to occur up to 20 times faster in cement solutions representative of early cement leaching, compared with solutions representative of cement leaching at intermediate timescales. Due to the presence of high concentrations of alkali elements, particularly K, a K-bearing zeolite was precipitated, which may significantly influence the long-term behaviour of glass in a cementitious repository. Further work is currently underway, using nuclear waste simulant glasses representative of the UK high level waste inventory, to ascertain the dissolution mechanisms when a glass is transferred in a sequence of 'evolved' and 'old' cement waters, and then to groundwater. Further work on the dissolution of >50 year old samples of soda-lime-silicate glass in the Peak Dale Tunnel will be presented in a forthcoming publication.

Acknowledgements

The authors wish to acknowledge Coke Turner and Co., Land Agents for the Duchy of Lancaster for permission to work and sample within the Peak Dale Tunnel, Mr D. Abraham of Natural England for permission to access the tunnel via the SSSI area, and Dr. Richard Shaw, Dr. Tony Milodowski and Dr. Lorraine Field from the British Geological Survey for continuing support with Peak Dale Tunnel research. We are grateful to EPRSC for funding through the Nuclear First DTC programme (EP/G037140/1) and for an Early Career Research Fellowship awarded to CLC (EP/N017374/1). This research was performed, in part, at the MIDAS Facility, at the University of Sheffield, which was established with support from the Department of Energy and Climate Change.

References

[1] R. G. W. Vasconcelos, N. Beaudoin, A. Hamilton, N. C. Hyatt, J. L. Provis and C. L. Corkhill. Applied Geochemistry, 89, 180 – 189 (2018).

[2] J. J. P. Bel, S. M. Wickham and R. M. F. Gens. Materials Research Society Symposium Proceedings, **932,** 23 – 32 (2006).

[3] S. Gin and J. P. Mestre. Journal of Nuclear Materials, **295**, 83–96 (2001).

[4] S. Mercado-Depierre, F. Angeli, F. Frizon and S. Gin Journal of Nuclear Materials, **441**, 402 – 410 (2013).

[5] S. Gin, P. Jollivet, M. Fournier, C. Berthon, Z. Wang, A. Mitroshkov, A. Zhu & J. V. Ryan. Geochimica et Cosmochimica Acta, **151**, 68 – 85 (2015).

[6] C. A. Utton, S. W. Swanton, S. J. Schofield, R. J. Hand, A. Clacher and N. C. Hyatt. Mineralogical Magazine, **76**, 2919 – 2930 (2012).

[7] C. A. Utton, R. J. Hand, N. C. Hyatt, S. W. Swanton and S. J. Williams. Journal of Nuclear Materials, **442**, 33 – 45 (2013).

[8] C. A. Utton, R. J. Hand, P. A. Bingham, N. C. Hyatt, S. W. Swanton and S. J. Williams. Journal of Nuclear Materials, **435**, 112–122 (2013).

[9] C. L. Corkhill, N. Cassingham, P. G. Heath and N. C. Hyatt. International Journal of Applied Glass Science, **4**, 341 – 356 (2013).

[10] K. Ferrand, S. Liu and K. Lemmens. International Journal of Applied Glass Science, **4**, 328 – 340 (2013).

[11] Z. Andriambololona, N. Godon and E. Vernaz. Materials Research Society Symposium Proceedings, 151–158 (1992).

[12] C. Mann, C. L. Thorpe, A. Milodowski, L. P. Field, R. P. Shaw, L. Boast, R. J. Hand, N. C. Hyatt, J. L. Provis and C. L. Corkhill. MRS Advances, **2**, 669 - 674 (2017).

[13] C. Mann. PhD Thesis, University of Sheffield (2018).

[14] ASTM International, Standard test Methods for Determining Chemical Durability of Nuclear, Hazardous, and Mixed Waste Glasses and Multiphase Glass Ceramics: The Product Consistency Test (PCT). ASTM C1285 (2014).

[15] M. K. Titulaer, M. J. den Exter, H. Talsma, H., J. B. H. Jansen and J. W. Geus. Journal of Non- Crystalline Solids, **170**, 113 – 127 (1994).

[16] I. Ribet, and S. Gin. Journal of Nuclear Materials, **324**, 152–164 (2004).

[17] M. Fournier, S. Gin, P. Frugier, and S. Mercado-Depierre. Materials Degradation, **1**, 17 (2017).

Appendix II.

Concentration of elements as determined by ICP-OES in synthetic cement waters used in Chapters 4, 5 and 6

Table 3.7

Element	Young Cement Water	Young Cement Water + Ca	Evolved Cement Water	Old Cement Water
	Concentration, mg L^{-1} as determined by ICP-OES			
	pH(RT) 13.50 ± 0.43	pH(RT) 13.01 ± 0.48	pH(RT) 12.30 ± 0.50	pH(RT) 11.56± 0.26
Ca	-	1.81 ± 1.11	290 ± 37	3.66 ± 0.18
Na	2900 ± 850	2900 ± 500	212 ± 22	65 ± 14
K	9000 ± 3000	9000± 600	-	-
Al	-	-	0.60 ± 0.48	0.24 ± 0.01
Si	-	-	4.35 ± 2.63	-
Mg	-	-	0.15 ± 0.05	-
Fe	-	3.26 ± 1.36	-	-
S	63 ± 12	67.19 ± 6.17	4.34 ± 1.10	5.28 ± 1.40

Concentration of elements as determine by ICP-OES in cement equilibrated waters used in Chapter 7

Table 3.14

Element	NRVB	BFS:PC
	Concentration, mg L^{-1}	
	pH(RT) 12.65 ± 0.2	pH(RT) 12.59 ± 0.2
Ca	766 ± 59	487 ± 28
Na	13 ± 10	43 ± 6
K	36 ± 5	74 ± 7
Al	0.08 ± 0.2	1.96 ± 0.7
Si	1.79 ± 1.4	0.34 ± 1.4
Mg	16 ± 9. *	0.30 ± 0.2
Fe	1.57 ± 0.7	1.67 ± 1.4
S	10 ± 7	13.5 ± 1.5
*$CaCO_3$	0.88	0.88

*Mg conc = 0 day 1-42, day 56 onwards ~ 20 mg L^{-1}

*$CaCO_3$ conc= calculated based on the dissolution of calcite in the hardened cement pastes using PHREEQC

Concentration of elements as determined by ICP-OES in granitic groundwater used in Chapter 6

Table 3.9

Element	Granitic Ground Water
	Concentration, mg L^{-1}
	pH(RT) 8.83 ± 0.34
Ca	24.12 ± 0 .08
Na	63.67 ± 2.56
K	12.90 ± 0.54
Al	-
Si	5.17 ± 0.94
Mg	6.00 ± 0.19
Fe	1.14 ± 0.05
S	3.90 ± 0.05

Glass compositions of MW25, LBS and ISG used throughout this thesis as determined by ICP-OES/MS

Table 3.2

	MW25		LBS		ISG	
	wt%	mol%	wt%	mol%	wt%	mol%
SiO_2	39.12	43.08	47.92	52.14	56.20	60.10
B_2O_3	19.40	18.43	9.62	9.03	17.30	15.97
Na_2O	6.84	7.31	12.94	13.65	12.20	12.65
Li_2O	3.20	7.08	3.90	8.54	-	-
ZrO_2	1.02	0.55	0.67	0.35	3.30	1.72
MoO_3	0.90	0.41	0.52	0.24	-	-
Al_2O_3	8.13	5.28	6.85	4.39	6.10	3.84
Fe_2O_3	2.38	0.99	10.25	4.20	-	-
Nd_2O_3	1.38	0.27	-	-	-	-
Cs_2O	0.88	0.21	0.69	0.16	-	-
MgO	3.57	5.86	3.71	6.02	-	-
CeO_2	1.01	0.20	0.36	0.07	-	-
BaO	0.27	0.12	0.11	0.05	-	-
La_2O_3	0.52	0.11	1.53	0.31	-	-
RuO_2	0.63	0.36	0.00	0.00	-	-
Pr_2O_3	0.24	0.05	-	-	-	-
SrO	0.23	0.15	0.13	0.08	-	-
NiO	0.40	0.36	0.05	0.05	-	-
Sm_2O_3	0.25	0.05	-	-	-	-
Y_2O_3	0.14	0.04	-	-	-	-
CaO	4.52	5.33	0.45	0.52	5.00	5.73
K_2O	0.01	0.00	0.15	0.10	-	-
Cr_2O_3	0.41	0.18	0.01	0.01	-	-
SO_3	0.08	0.07	0.02	0.02	-	-
TiO_2	0.01	0.01	0.01	0.01	-	-
Cu_2O	0.02	0.02	0.02	0.01	-	-
ZnO	4.20	3.42	0.01	0.01	-	-
Total	99.74	99.89	99.95	99.96	100.10	100.00

References

1. Department of Energy & Climate Change. *2014 White Paper: Implementing Geological Disposal*. (2014).
2. UK GOV. Geological Disposal Facility (GDF) for higher-activity radioactive waste (accessed 13/7/2018). Available at: https://www.gov.uk/government/collections/geological-disposal-facility-gdf-for-high-activity-radioactive-waste. (Accessed: 13th July 2018)
3. PoyryEnergyLimited & AmecFosterWheeler. *2016 UK Radioactive Waste and Materials Inventory: UK Radioactive Waste Inventory Report*. (2017).
4. National Nuclear Laboratory. Position Paper: Thermal Processes for Immobilising Intermediate Level Wastes.
5. Francis, A. J., Cather, R. & Crossland, I. G. *Development of the Nirex Reference Vault Backfill; Report on Current Statur in 1994*. (1996).
6. RWM & NDA. *Part B : Technical Specification Geological Disposal*. (2016).
7. Vasconcelos, R. G. W. *et al.* Characterisation of a high pH cement backfill for the geological disposal of nuclear waste: The Nirex Reference Vault Backfill. *Appl. Geochemistry* **89**, 180–189 (2018).
8. Hyatt, N. C. & James, M. Thermal treatment of ILW. *Nuclear Engineering International* (2013). Available at: http://www.neimagazine.com/features/featurethermal-treatment-of-ilw/. (Accessed: 6th June 2018)
9. Corkhill, C. & Hyatt, N. Nuclear Waste Management. *Phys. World Discov.* 399–404 (2018). doi:10.1088/978-0-7503-1638-5
10. ONDRAF/NIRAS. Research, Development and Demonstration (RD&D) Plan for the geological disposal of high-level and/or long-lived radioactive waste including irradiated fuel of considered as waste, State-of-the-art report as of December 2012. *ONDRAF/NIRAS, Rep. NIROND-TR 2013-12 E* 413 (2013).
11. Poyet, S. The Belgian supercontainer concept : Study of the concrete buffer behaviour in service life. *J. Phys. 4, EDP Sci.* **136**, 167–175 (2006).
12. Smart, N. R. *et al.* Summary of studies on the anaerobic corrosion of carbon steel in alkaline media in support of the Belgian supercontainer concept. *Corros. Eng. Sci. Technol.* **52**, 217–226 (2017).
13. Van Geet, M. & Weetjens, E. *Strategic choices in the Belgian supercontainer design and its treatment in the safety case - NEA/RWM/R(2012)3/REV*. (2012).
14. Ferrand, K., Liu, S. & Lemmens, K. *International technical evaluation of alteration mechanisms relevant to glass corrosion*. **SCK.CEN-ER**, (2015).
15. Wang, L. *Near-field chemistry of a HLW/SF repository in Boom Clay - scoping calculations relevant to the supercontainer design (SCK.CEN-ER-17, 09/LWa/P-140)*. (2009).

16. Lothenbach, B., Le Saout, G., Gallucci, E. & Scrivener, K. *Influence of limestone on the hydration of Portland cements*. *Cement and Concrete Research* **38**, (Cement and Concrete Research, 2008).

17. Lothenbach, B. & Winnefeld, F. Thermodynamic modelling of the hydration of Portland cement. *Cem. Concr. Res.* **36**, 209–226 (2006).

18. Coumes, C. dit. Low pH cements for waste repositories: A review. (2008). Available at: http://cement08.in2p3.fr/Presentation Workshop pour site web/Monday13/PM/Cau_Dit_Coumes.pdf. (Accessed: 13th August 2014)

19. Grambow, B. Nuclear waste glasses - How durable? *Elements* **2**, 357–364 (2006).

20. Frugier, P. *et al.* SON68 nuclear glass dissolution kinetics: Current state of knowledge and basis of the new GRAAL model. *J. Nucl. Mater.* **380**, 8–21 (2008).

21. Gin, S. Open Scientific Questions about Nuclear Glass Corrosion. *Procedia Mater. Sci.* **7**, 163–171 (2014).

22. Gin, S., Ribet, I. & Couillard, M. Role and properties of the gel formed during nuclear glass alteration: Importance of gel formation conditions. *J. Nucl. Mater.* **298**, 1–10 (2001).

23. Mercado-Depierre, S., Angeli, F., Frizon, F. & Gin, S. Antagonist effects of calcium on borosilicate glass alteration. *J. Nucl. Mater.* **441**, 402–410 (2013).

24. Geisler, T. *et al.* Aqueous corrosion of borosilicate glass under acidic conditions: A new corrosion mechanism. *J. Non. Cryst. Solids* **356**, 1458–1465 (2010).

25. Geisler, T. *et al.* The mechanism of borosilicate glass corrosion revisited. *Geochim. Cosmochim. Acta* **158**, 112–129 (2015).

26. Fournier, M., Frugier, P. & Gin, S. Resumption of Alteration at High Temperature and pH: Rates Measurements and Comparison with Initial Rates. *Procedia Mater. Sci.* **7**, 202–208 (2014).

27. Utton, C., Hand, R. J., Hyatt, N. C. & Swanton, S. W. *Glass durability in high pH environments: A review of the literature*. *Serco Report* (2011).

28. Cassingham, N. *et al.* The initial dissolution rates of simulated UK Magnox–ThORP blend nuclear waste glass as a function of pH, temperature and waste loading. *Mineral. Mag.* **79**, 1529–1541 (2015).

29. Paul, A. *Chemistry of glasses, Second Edition*. *Chapman and Hall Ltd* (1990). doi:10.1016/0025-5408(91)90074-V

30. Maraghechi, H., Rajabipour, F., Pantano, C. G. & Burgos, W. D. Effect of calcium on dissolution and precipitation reactions of amorphous silica at high alkalinity. *Cem. Concr. Res.* **87**, 1–13 (2016).

31. Reiser, J. T. G. Structural Investigations of Nuclear Waste Glass Alteration Layers. (2018).

32. Iler, R. K. *The Chemistry of Silica*. (John Wiley & Sons, Inc., 1979).

33. Gin, S. *et al. An international initiative on long-term behavior of high-level nuclear waste glass*. **16**, (Materials Today, 2013).

34. Grambow, B. General Rate Equation for Nuclear Waste Glass Corrosion. *Mater. Res. Soc. Symp. Proc.* **44**, 15–27 (1985).

35. Strachan, D. Glass dissolution as a function of pH and its implications for understanding mechanisms and future experiments. *Geochim. Cosmochim. Acta* **219**, 111–123 (2017).

36. Neeway, J. J., Rieke, P. C., Parruzot, B. P., Ryan, J. V. & Asmussen, R. M. The dissolution behavior of borosilicate glasses in far-from equilibrium conditions. *Geochim. Cosmochim. Acta* **226**, 132–148 (2018).

37. Harrison, M. T. *Review of Glass Dissolution Rates for use in the Disposal System Safety Case Performance Assessment Models, NNL (10)10734, Issue 3*. (2010).

38. Inagaki, Y., Kikunaga, T., Idemitsu, K. & Arima, T. *Initial Dissolution Rate of the International Simple Glass as a Function of pH and Temperature Measured Using Microchannel Flow-Through Test Method*. *International Journal of Applied Glass Science* **4**, (International Journal of Applied Glass Science, 2013).

39. Elia, A., Ferrand, K. & Lemmens, K. Determination of the Forward Dissolution Rate for International Simple Glass in Alkaline Solutions. *MRS Adv.* **2**, 661–667 (2017).

40. Jollivet, P., Gin, S. & Schumacher, S. Forward dissolution rate of silicate glasses of nuclear interest in clay-equilibrated groundwater. *Chem. Geol.* **330**–**331**, 207–217 (2012).

41. Abraitis, P. K., McGrail, B. P., Trivedi, D. P., Livens, F. R. & Vaughan, D. J. Single-pass flow-through experiments on a simulated waste glass in alkaline media at 40°C. *J. Nucl. Mater.* **280**, 196–205 (2000).

42. Fournier, M., Gin, S. & Frugier, P. Resumption of nuclear glass alteration: State of the art. *J. Nucl. Mater.* **448**, 348–363 (2014).

43. Rajabipour, F., Giannini, E., Dunant, C., Ideker, J. H. & Thomas, M. D. A. Alkali-silica reaction: Current understanding of the reaction mechanisms and the knowledge gaps. *Cem. Concr. Res.* **76**, 130–146 (2015).

44. Gin, S., Jollivet, P., Fournier, M., Frugier, P. & Charpentier, T. Origin and consequences of silicate glass passivation by surface layers. (2015). doi:10.1038/ncomms7360

45. Collin, M. & Fournier, M. Impact of alkali on the passivation of silicate glass. *npj Mater. Degrad.* 1–10 (2018). doi:10.1038/s41529-018-0036-3

46. Rébiscoul, D., Bruguier, F., Magnin, V. & Gin, S. Impact of soda-lime borosilicate glass composition on water penetration and water structure at the first time of alteration. *J. Non. Cryst. Solids* **358**, 2951–2960 (2012).

47. Rajmohan, N., Frugier, P. & Gin, S. Composition effects on synthetic glass alteration mechanisms: Part 1. Experiments. *Chem. Geol.* **279**, 106–119 (2010).

48. Abdelouas, A., Crovisier, J. L., Lutze, W., Muller, R. & Bernotat, W. Structure and chemical properties of surface layers developed on R7I7 simulated nuclear waste glass altered in brine at 190°C. *Eur. J. Mineral.* **7**, 1101–1113 (1995).

49. Gougar, M. L. D., Scheetz, B. E. & Roy, D. M. Ettringite and C-S-H Portland

cement phases for waste ion immobilization: A review. *Waste Manag.* **16**, 295–303 (1996).

50. Gin, S., Beaudoux, X., Angéli, F., Jégou, C. & Godon, N. Effect of composition on the short-term and long-term dissolution rates of ten borosilicate glasses of increasing complexity from 3 to 30 oxides. *J. Non. Cryst. Solids* **358**, 2559–2570 (2012).

51. Kaspar, T. C., Reiser, J. T., Ryan, J. V. & Wall, N. A. Non-destructive characterization of corroded glass surfaces by spectroscopic ellipsometry. *J. Non. Cryst. Solids* **481**, 260–266 (2018).

52. Ribet, S. & Gin, S. Role of neoformed phases on the mechanisms controlling the resumption of SON68 glass alteration in alkaline media. *J. Nucl. Mater.* **324**, 152–164 (2004).

53. Andriambololona, Z., Godon, N. & Vemaz, E. R7T7 glass alteration in the presence of mortat:effect of the cement grade. in *CEA-Conference-10993*

54. Ferrand, K., Liu, S. & Lemmens, K. The Interaction Between Nuclear Waste Glass and Ordinary Portland Cement. *Int. J. Appl. Glas. Sci.* **4**, 328–340 (2013).

55. Utton, C. A., Hand, R. J., Hyatt, N. C., Swanton, S. W. & Williams, S. J. *Formation of alteration products during dissolution of vitrified ILW in a high-pH calcium-rich solution*. *Journal of Nuclear Materials* **442**, (Journal of Nuclear Materials, 2013).

56. S.Depierre, F. Frizon, S. G. and F. A. *Cement-Based Materials for Nuclear Waste Storage, Chapter 15: Leaching of Nuclear Waste Glass in Cement Pore Water: Effect of Calcium in Solution*. (Springer, 2013).

57. Chave, T., Frugier, P., Gin, S. & Ayral, A. Glass-water interphase reactivity with calcium rich solutions. *Geochim. Cosmochim. Acta* **75**, 4125–4139 (2011).

58. Chen, J. J., Thomas, J. J., Taylor, H. F. W. & Jennings, H. M. Solubility and structure of calcium silicate hydrate. *Cem. Concr. Res.* **34**, 1499–1519 (2004).

59. Utton, C. A. *et al.* Dissolution of vitrified wastes in a high-pH calcium-rich solution. *J. Nucl. Mater.* **435**, 112–122 (2013).

60. Richardson, I. G. The calcium silicate hydrates. *Cem. Concr. Res.* **38**, 137–158 (2008).

61. Corkhill, C. L., Cassingham, N. J., Heath, P. G. & Hyatt, N. C. Dissolution of UK High-Level Waste Glass Under Simulated Hyperalkaline Conditions of a Colocated Geological Disposal Facility. *Int. J. Appl. Glas. Sci.* **4**, 341–356 (2013).

62. Sugiyama, D. & Fujita, T. A thermodynamic model of dissolution and precipitation of calcium silicate hydrates. *Cem. Concr. Res.* **36**, 227–237 (2006).

63. Atkinson, A., Hearne, J. A. & Knights, C. F. Aqueous Chemistry and Thermodynamic Modelling of CaO-SiO2-H2O Gels. *J.Chem.Soc Dalt. Trans* (1989).

64. Greenberg, S. A. & Chang, T. N. Investigation of the colloidal hydrated calcium silicates. II. Solubility relationships in the calcium oxide-silica-water system at

25°. *J. Phys. Chem.* **69**, 182–188 (1965).

65. Fujii, K. & Kondo, W. Estimation of Thermochemical Data for Calcium Silicate Hydrate (C-S-H). *Commun. Am. Ceram. Soc.* 3–4 (1983).

66. Nieto, P. & Zanni, H. Polymerization of alkaline-calcium-silicate hydrates obtained by interaction between alkali–silica solutions and calcium compounds. A 29Si nuclear magnetic resonance study. *J. Mater. Sci.* **2**, 3419–3425 (1997).

67. Jennings, H. M. Aqueous Solubility Relationships for lhvo Types of Calcium Silicate Hydrate. *J. Am. Ceram. Soc* **69**, 614–618 (1986).

68. Taylor, H. F. W. *Cement Chemistry 2nd edition*. (Thomas Telford, 1997).

69. Van Eijk, R. J. & Brouwers, H. J. H. Modelling the effects of waste components on cement hydration. *Waste Manag. Ser.* **21**, 279–284 (2001).

70. Backhouse, D. J. A Study of the Dissolution of Nuclear Waste Glasses in Highly-Alkaline Conditions. (2016).

71. Cox, G. A. & Ford, B. A. The long-term corrosion of glass by ground-water. *J. Mater. Sci.* **28**, 5637–5647 (1993).

72. Curti, E., Crovisier, J. L., Morvan, G. & Karpoff, A. M. Long-term corrosion of two nuclear waste reference glasses (MW and SON68): A kinetic and mineral alteration study. *Appl. Geochemistry* **21**, 1152–1168 (2006).

73. Burger, E. *et al.* Impact of iron on nuclear glass alteration in geological repository conditions: A multiscale approach. *Appl. Geochemistry* **31**, 159–170 (2013).

74. Abrajano, T. A., Bates, J. K., Woodi-and, A. B. & Bourcier, W. L. Secondary phase formation during nuclear waste-glass dissolution. *Clays Clay Miner.* **38**, 537–548 (1990).

75. Utton, C. A. *et al.* Chemical durability of vitrified wasteforms: effects of pH and solution composition. *Mineral. Mag.* **76**, 2919–2930 (2012).

76. Schofield, J. M. *et al. Experimental studies of the chemical durability of UK HLW and ILW glasses . Interim progress report (RWM005105)*. (2016).

77. Bunker, B. C. Molecular mechanisms for corrosion of silica and silicate glasses. *J. Non. Cryst. Solids* **179**, 300–308 (1994).

78. Railsback, Bruce (Department of Geology, U. of G. Variation in hydrated radius of ions. *Teaching resources 'Fundamentals of Mineralogy and Geochemistry'* Available at: http://www.gly.uga.edu/railsback/FundamentalsIndex.html. (Accessed: 23rd May 2018)

79. Schofield, J. . *et al. Experimental studies of the chemical durability of UK HLW and ILW glasses. First interim progress report (RWM005105)*. (2013).

80. Harrison, M. T. The Effect of Composition on Short- and Long-term Durability of UK HLW Glass. *Procedia Mater. Sci.* **7**, 186–192 (2014).

81. Fleury, B., Godon, N., Ayral, A. & Gin, S. SON68 glass dissolution driven by magnesium silicate precipitation. *J. Nucl. Mater.* **442**, (2013).

82. Thien, B. M. J., Godon, N., Ballestero, A., Gin, S. & Ayral, A. The dual effect of Mg on the long-term alteration rate of AVM nuclear waste glasses. *J. Nucl. Mater.* **427**, 297–310 (2012).

83. Liu, S., Ferrand, K. & Lemmens, K. Transport- and surface reaction-controlled SON68 glass dissolution at 30°C and 70°C and pH=13.7. *Appl. Geochemistry* **61**, 302–311 (2015).

84. Ebert, W. L., Bates, J. K. & Bourcier, W. L. The hydration of borosilicate waste glass in liquid water and steam at 200 °C. *Waste Manag.* **11**, 205–221 (1991).

85. Gin, S. & Mestre, J. P. SON 68 nuclear glass alteration kinetics between pH 7 and pH 11.5. *J. Nucl. Mater.* **295**, 83–96 (2001).

86. Caurel, J. Alteration Hydrothermale Du Verre R7T7 Cinétiques de dissolution du verre à 150 et à 25O oC, rôle des phases néoformées (De L'Universite de Poitiers). (L'Universite de Poitiers, 1990).

87. Mann, C. *et al. Influence of Young Cement Water on the dissolution mechanisms and kinetics of the International Simple Glass*.

88. Grambow, B. *Uhling's Corrosion Handbook, Chapter 24 Corrosion of Glass*. (2000).

89. Inagaki, Y. *et al.* Aqueous alteration of Japanese simulated waste glass P0798: Effects of alteration-phase formation on alteration rate and cesium retention. *J. Nucl. Mater.* **354**, 171–184 (2006).

90. Olszowka, S. A., Sousanpour, W., Adiga, R., Marbury, G. S. & Li, S. Leach rate excursions in borosilicate glasses: effects of glass and leachant composition. *Mater. Res. Soc. Symp. Proc.* **212**, 65–76 (1990).

91. Depierre, S. Study of glass alteration mechanisms in cement waters. (University of Montpellier II, 2012).

92. Vernaz, É. & Bruezière, J. History of Nuclear Waste Glass in France. *Procedia Mater. Sci.* **7**, 3–9 (2014).

93. Poinssot, C. & Gin, S. Long-term Behavior Science: The cornerstone approach for reliably assessing the long-term performance of nuclear waste. *J. Nucl. Mater.* **420**, 182–192 (2012).

94. Van Iseghem, P. *et al.* Glamor- or How we achieved a common understanding on the decrease of glass dissolution kinetics. *J. South Carolina Acad. Sci.* **9**, 115–126 (2013).

95. Ferrand, K. *Topical report on tests on vitrified (V)HLW waste in Supercontainer disposal conditions. (SCK.CEN ER 0286, Version 2.0)*. (2016).

96. Cailleteau, C. *et al.* Insight into silicate-glass corrosion mechanisms. *Nat. Mater.* **7**, 978–983 (2008).

97. C A Utton, NC Hyatt, S. S. *Interactions of vitrified wastes with NRVB A report to NDA RWMD*. *SERCO* (2012).

98. Kaspar, T. C. *et al. DRAFT Physical and optical properties of the International Simple Glass*.

99. Atkins, M. & Glasser, F. P. Application of Portland cement-based materials to radioactive waste immobilization. *Waste Manag.* **12**, 105–131 (1992).

100. Berner, U. R. Evolution of pore water chemistry during degradation of cement in a radioactive waste repository environment. *Waste Manag.* **12**, 201–219 (1992).

101. Reardon, E. J. Problems and Approaches to the Prediction of the Chemical Composition in Cement/Water systems. *Waste Manag.* **12**, 221–239 (1992).

102. Nielsen, E. P., Herfort, D. & Geiker, M. R. Phase equilibria of hydrated Portland cement. *Cem. Concr. Res.* **35**, 109–115 (2005).

103. Cau Dit Coumes, C., Courtois, S., Nectoux, D., Leclercq, S. & Bourbon, X. Formulating a low-alkalinity, high-resistance and low-heat concrete for radioactive waste repositories. *Cem. Concr. Res.* **36**, 2152–2163 (2006).

104. Lagerblad, B. & Trägårdh, J. *Conceptual model for concrete long time degradation in a deep nuclear waste*. (1994).

105. Gascoyne, M. *Influence of grout and cement on groundwater composition*. (2002).

106. Crossland, I. . & Vines, S. . *Why a cementitious repository? (Nirex Report No:N/034)*. (2001).

107. Corkhill, C. L. *et al.* Technetium-99m Traansport and Immobilisation in Porous Media: Development of a Novel Nuclear Imaging Technique. **1518**, (2013).

108. Moranville-Regourd, M. *Cements Made From Blastfurnace Slag. Lea's Chemistry of Cement and Concrete*. (Elsevier, 2003). doi:10.1016/B978-075066256-7/50023-0

109. NDA. *Geological disposal A review of cement powder security of supply, specification and disposability issues*. *NDA Report* **NDA/RWMD/0**, (2010).

110. Standard Test Methods for Determining Chemical Durability of Nuclear , Hazardous , and Mixed Waste Glasses and Multiphase Glass Ceramics : The Product Consistency Test (PCT) (ASTM C1285-14). 1–26 (2002). doi:10.1520/C1285-14.2

111. NDA/RWMD. *Geological Disposal: Generic specification for waste packages containing low heat generating waste*. (2012).

112. *Standard Test Method for Static Leaching of Monolithic Waste Forms for Disposal of Radioactive Waste (ASTM C1220-10)*. (2014). doi:10.1520/C1220-10.Copyright

113. Ermrich, M. & Detlef, O. *X-Ray Powder Diffraction. XRD for the analyst.* (PANalytical, 2011).

114. West, A. R. *Solid State Chemistry and its Applications*. (Wiley, 2013).

115. Bragg, W. . & Bragg, W. . . The Reflection of X-rays by Crystals. *Phys. R. Soc. London As R. Soc. London Ser. A, Contain. Pap. a Math. Phys. Character* **88**, 428–438 (1913).

116. Fawcett, T. G., Faber, J., Kabbekodu, S., Mcclune, F. & Rafaja, D. PDF-4+, the material identification database. *Microstruct. Anal. Mater. Sci.* 1–3 (2005).

117. Goldstein, J. *et al. Scanning Electron Microscopy and X-Ray Microanalysis*. (Springer New York, 2012).

118. Mader Sebatien (The Pennsylvania State University, N. centre N. A. & C. K. Advance Field Emission Scanning Electron Microscopy. (2010). Available at: https://www.youtube.com/watch?v=OAYezQP31dw. (Accessed: 20th February 2018)

119. Mader Sebatien (The Pennsylvania State University, N. centre N. A. & C. K. RAIN: Introduction to Scanning Electron Microscopy. (2010). Available at: https://www.youtube.com/watch?v=TFUi4Q6Llxo. (Accessed: 20th February 2018)

120. DeCraen, M., Wang, L., Van Geet, M. & Moors, H. *Geochemistry of Boom Clay pore water at the Mol site*. *Scientific Report SCK·CEN-BLG-990* (2004).

121. Hill, S. J. *Inductively Coupled Plasma Spectrometry and its Applications*. *Inductively Coupled Plasma Spectrometry and its Applications* (Blackwell Publishing, 2007). doi:10.1002/9780470988794

122. Thermo Fisher Scientific. *iCAP 6000 Series ICP-OES Spectrometer User Guide V3.1*. (2012).

123. Evans Norris, S. . CRM Solutions Improve your ICP-OES Performance by using an Internal Standard. 1–10 (2018). Available at: https://www.armi.com/blog/how-an-internal-standard-can-improve-your-icp-oes-performance. (Accessed: 18th August 2018)

124. Bearcock, J. . & Smedley, P. . *Baseline groundwater chemistry: the Palaeogene of the Thames Basin*. *British Geological Survey, Open Report OR/10/057* **OR/10/057**, (2010).

125. Scheetz, B. *et al.* The Role of Boron in Monitoring the Leaching of Borosilicate Glass Waste Forms. *MRS.Res.Sco.Symp.Proc* **44**, 129–134 (1985).

126. Alexander, G. B., Heston, W. M. & Iler, R. K. The solubility of amorphous silica in water. *J. Phys. Chem.* **58**, 453–455 (1954).

127. Boucetta, H. *et al.* Mechanism of RuO 2 crystallization in borosilicate glass: An original in situ ESEM approach. *Inorg. Chem.* **51**, 3478–3489 (2012).

128. Grandia, F., Galíndez, J., Arcos, D. & Molinero, J. *Quantitative modelling of the degradation processes of cement grout*. *SKB Report: TR-10-25* (2010).

129. Dohmen, L. *et al.* Pattern formation in silicate glass corrosion zones. *Int. J. Appl. Glas. Sci.* **4**, 357–370 (2013).

130. Davies, G. & Oberholster, R. E. Alkali-silica reaction products and their development. *Cem. Concr. Res.* **18**, 621–635 (1988).

131. Abraitis, P. K. *et al.* The kinetics and mechanisms of simulated British Magnox waste glass dissolution as a function of pH, silicic acid activity and time in low temperature aqueous systems. *Appl. Geochemistry* **15**, 1399–1416 (2000).

132. Schofield, J. M. *et al. DRAFT Experimental studies of the chemical durability of UK HLW and ILW glasses . Second interim progress report (RWM005105)*. (2015).

133. Zwicky, H. . *et al.* Corrosion behaviour of British magnox waste glass in pure water. *Mat. Res. Soc. Sci. basis Nucl. waste Manag. XII* **127**, 129–136 (1989).

134. Hou, X., Struble, L. J. & Kirkpatrick, R. J. Formation of ASR gel and the roles of C-S-H and portlandite. *Cem. Concr. Res.* **34**, 1683–1696 (2004).

135. Struble & Diamond, S. Swelling properties of synthetic alkali silica gels. *J. Am. Ceram. Soc.* **64**, 652–655 (1981).

136. Odom, I. E. Smectite clay Minerals: Properties and Uses. *Philos. Trans. R. Soc. A Math. Phys. Eng. Sci.* **311**, 391–409 (1984).

137. Dent Glasser, L. S. & Kataoka, N. The chemistry of 'alkali-aggregate' reaction. *Cem. Concr. Res.* **11**, 1–9 (1981).

138. Knudsen, T. & Thaulow, N. Quantitative microanalyses of alkali-silica gel in concrete. *Cem. Concr. Res.* **5**, 443–454 (1975).

139. Dove, P. M. The dissolution kinetics of quartz in aqueous mixed cation solutions. *Geochim. Cosmochim. Acta* **63**, 3715–3727 (1999).

140. Dove, P. M. & Nix, C. J. The influence of the alkaline earth cations, magnesium, calcium, and barium on the dissolution kinetics of quartz. *Geochim. Cosmochim. Acta* **61**, 3329–3340 (1997).

141. Icenhower, J. P. & Dove, P. M. The dissolution kinetics of amorphous silica into sodium chloride solutions : Effects of temperature and ionic strength. *Geochim. Cosmochim. Acta* **64**, 4193–4203 (2000).

142. Dove, P. M. & Nix, C. J. The influence of the alkaline earth cations, magnesium, calcium and barium on the dissolution kinetics of quartz. *Geochim. Cosmochim. Acta* **61**, 3329–3340 (1997).

143. Atkins, W. . *Atkins' Physical Chemistry*. (Oxford : Oxford University Press, 2002).

144. Conway, B. E. Ion hydration co-sphere interactions in the double layer and ionic solutions. *J. Electroanal.Chem* **123**, 81–94 (1981).

145. Burgess, J. *Ions in Solution: basic principles of chemical interactions*. (Chichester:Horwood Pub., 1999).

146. Kinrade, S. D. Oxygen-17 NMR study of aqueous potassium silicates. *J. Phys. Chem.* **100**, 4760–4764 (1996).

147. Dugger, D. L. *et al.* The Exchange of Twenty Metal Ions with the Weakly Acidic Silanol Group of Silica Gel. *J. Phys. Chem.* **68**, 757–760 (1964).

148. Gimblett, F. G. R. & Monk, C. B. E.M.F. Studies of electrolytic dissociation. *Trans. Faraday Soc.* **50**, 965–972 (1954).

149. Depasse, J. & Watillon, A. The stability of amorphous colloidal silica. *J. Colloid Interface Sci.* **33**, 430–438 (1970).

150. Mähler, J. & Persson, I. A study of the hydration of the alkali metal ions in aqueous solution. *Inorg. Chem.* **51**, 425–438 (2012).

151. Savage, D. A review of analogues of alkaline alteration with regard to long-term

barrier performance. *Mineral. Mag.* **75**, 2401–2418 (2011).

152. Salles, F., Bildstein, O., Douillard, J. M., Jullien, M. & Van Damme, H. Determination of the driving force for the hydration of the swelling clays from computation of the hydration energy of the interlayer cations and the clay layer. *J. Phys. Chem. C* **111**, 13170–13176 (2007).

153. Ngouana W., B. F. & Kalinichev, A. G. Structural arrangements of isomorphic substitutions in smectites: Molecular simulation of the swelling properties, interlayer structure, and dynamics of hydrated cs-montmorillonite revisited with new clay models. *J. Phys. Chem. C* **118**, 12758–12773 (2014).

154. Thien, B. *et al.* Structural identification of a trioctahedral smectite formed by the aqueous alteration of a nuclear glass. *Appl. Clay Sci.* **49**, 135–141 (2010).

155. Curti, E., Dähn, R., Vespa, M., Grolimund, D. & Borca, C. N. Glass Corrosion and Secondary Clay Mineral Formation : The Fate of Ni and Ce as Re- vealed by µ-XRF / XAS Techniques. (2013).

156. Harder, H. The role of magnesium in the formation of smectite minerals. *Chem. Geol.* **10**, 31–39 (1972).

157. Kloprogge, J. T., Komarneni, S. & Amonette, J. E. Synthesis of smectite clay minerals: A critical review. *Clays Clay Miner.* **47**, 529–554 (1999).

158. Gaboriaud, F., Nonat, A., Chaumont, D. & Craievich, A. Aggregation processes and formation of silico-calco-alkaline gels under high ionic strength. *J. Colloid Interface Sci.* **253**, 140–149 (2002).

159. Gaboriaud, F., Nonat, A., Chaumont, D. & Craievich, A. Aggregation and Gel Formation in Basic Silico−Calco−Alkaline Solutions Studied: A SAXS, SANS, and ELS Study. *J. Phys. Chem. B* **103**, 5775–5781 (1999).

160. Gin, S. *et al.* Atom-Probe Tomography, TEM and ToF-SIMS study of borosilicate glass alteration rim: A multiscale approach to investigating rate-limiting mechanisms. *Geochim. Cosmochim. Acta* **202**, 57–76 (2017).

161. Chave, T., Frugier, P., Ayral, A. & Gin, S. Solid state diffusion during nuclear glass residual alteration in solution. *J. Nucl. Mater.* **362**, 466–473 (2007).

162. Sheppard, R. A. & Gude, A. J. Rhodesite from Trinity County. *Am. Mineral.* **54**, 251–256 (1969).

163. Steinfink, H. The Crystal structure of the zeolite, phillipsite. *Acta Crystallogr.* **15**, 644–652 (1962).

164. Boisen, M. B., Gibbs, G. V. & Bukowinski, M. S. T. Framework silica structures generated using simulated annealing with a potential energy function based on an H6Si2O7 molecule. *Phys. Chem. Miner.* **21**, 269–284 (1994).

165. Hopf, J. *et al.* Toward an understanding of surface layer formation, growth, and transformation at the glass – fluid interface q. *Geochim. Cosmochim. Acta* **229**, 65–84 (2018).

166. Ostwald, W. Besprechung der arbeit von Liesegangs “A - Linien”. *Phys. Chem.* **69**, 27–39 (1897).

167. Gin, S. *et al.* The fate of silicon during glass corrosion under alkaline conditions: A mechanistic and kinetic study with the International Simple Glass. *Geochim. Cosmochim. Acta* **151**, 68–85 (2015).

168. North, M. R., Fleischer, M. A. & Swaddle, T. W. Precipitation from alkaline aqueous aluminosilicate solutions. *Can. J. Chem. Can. Chim.* **79**, 75–79 (2001).

169. Cailleteau, C., Devreux, F., Spalla, O., Angeli, F. & Gin, S. Why do certain glasses with a high dissolution rate undergo a low degree of corrosion? *J. Phys. Chem. C* **115**, 5846–5855 (2011).

170. Mercado-Depierre, S., Fournier, M., Gin, S. & Angeli, F. Influence of zeolite precipitation on borosilicate glass alteration under hyperalkaline conditions. *J. Nucl. Mater.* **491**, 67–82 (2017).

171. Fournier, M., Gin, S., Frugier, P. & Mercado-Depierre, S. Contribution of zeolite-seeded experiments to the understanding of resumption of glass alteration. *npj Mater. Degrad.* **1**, 17 (2017).

172. Richardson, I. G. & Groves, G. W. Microstructure and microanalysis of hardened cement pastes involving ground granulated blast-furnace slag. *J. Mater. Sci.* **27**, 6204–6212 (1992).

173. Frost, R. L., Palmer, S. J. & Theiss, F. Synthesis and Raman spectroscopic characterisation of hydrotalcites based on the formula Ca6Al2(CO3)(OH)16. 4H2O. *J. Raman Spectrosc.* **42**, 1163–1167 (2011).

174. Ferrand, K. & Elia, A. HLW-03. (2017).

175. Strachan, D. M. & Neeway, J. J. Effects of alteration product precipitation on glass dissolution. *Appl. Geochemistry* **45**, 144–157 (2014).

176. Wall, N. A. *et al. Coupling of Nuclear Waste Form Corrosion and Radionuclide Transports in Presence of Relevant Repository Sediments (Annual Report-Project 12-3361)*. (2015).

177. Donzel, N., Gin, S., Augereau, F. & Ramonda, M. Study of gel development during SON68 glass alteration using atomic force microscopy. Comparison with two simplified glasses. *J. Nucl. Mater.* **317**, 83–92 (2003).

178. Lobanova, M. *et al.* Effect of ZrO2 on the glass durability. *Mat.Res.Soc.Symp.Proc* **713**, 1–9 (2002).

179. Gin, S., Frugier, P., Jollivet, P., Bruguier, F. & Curti, E. New insight into the residual rate of borosilicate glasses: Effect of s/v and glass composition. *Int. J. Appl. Glas. Sci.* **4**, 371–382 (2013).

180. Trotignon, L., Petit, J. C., Della Mea, G. & Dran, J. C. The compared aqueous corrosion of four simple borosilicate glasses: Influence of Al, Ca and Fe on the formation and nature of secondary phases. *J. Nucl. Mater.* **190**, 228–246 (1992).

181. Michelin, A. *et al.* Silicate glass alteration enhanced by iron: Origin and long-term implications. *Environ. Sci. Technol.* **47**, 750–756 (2013).

182. Rébiscoul, D. *et al.* Glass-iron-clay interactions in a radioactive waste geological disposal: A multiscale approach. *Mater. Res. Soc. Symp. Proc.* **1518**, 185–190 (2013).

183. Savage, D. & Benbow, S. *Low pH cements (Report ISSN 1104-1374)*. (2007).

184. Bamforth, P. . *et al. Cement materials for use as backfill , sealing and structural materials in geological disposal concepts . A review of current status (Report RP0618-252A)*. (2012).

185. *Geological repository systems for safe disposal of spent nuclear fuels and radioactive waste*. (Woodhead publishing series in energy, 2010).

186. United Kingdom Nirex Limited. The Scientific Foundations of Deep Geological Disposal. *Nirex Rep. N/016* 1–116 (2001).

187. RWM. *Geological Disposal Engineered Barrier System Status Report*. **DSSC/452/0**, (2016).

188. Suresh, D. & Nagaraju, K. Ground Granulated Blast Slag (GGBS) In Concrete – A Review " *IOSR J. Mech. Civ. Eng.* **12**, 2278–1684 (2015).

189. Matschei, T., Lothenbach, B. & Glasser, F. P. Thermodynamic properties of Portland cement hydrates in the system CaO-Al2O3-SiO2-CaSO4-CaCO3-H2O. *Cem. Concr. Res.* **37**, 1379–1410 (2007).

190. Matschei, T., Lothenbach, B. & Glasser, F. P. The AFm phase in Portland cement. *Cem. Concr. Res.* **37**, 118–130 (2007).

191. Bullard, J. W., Flatt, R. J. & Ag, S. T. The Role of Calcium Hydroxide Precipitation in the Kinetics of Tricalcium Silicate Hydration. 1–32 (2009).

192. Duchesne, J. & Reardon, E. J. Measurement and prediction of portlandite solubility in alkali solutions. *Cem. Concr. Res.* **25**, 1043–1053 (1995).

193. Ali, M. S., Khan, I. A. & Hossain, M. I. Chemical Analysis of Ordinary Portland Cement of Bangladesh. *Chem. Eng. Res. Bull.* **12**, 7–10 (2008).

194. Liu, C., Gu, W., Kong, D. & Guo, H. The significant effects of the alkali-metal cations on ZSM-5 zeolite synthesis: From mechanism to morphology. *Microporous Mesoporous Mater.* **183**, 30–36 (2014).

195. *Geopolymers; Structure, processing, properties and industrial applications*. (Woodhead publishing, 2009).

196. Ellison, A. J. G., Mazer, J. J. & Ebert, W. L. *Effect of Glass Composition on Waste Form Durability: A Critical Review (Report ANL-94/28)*. (Argonne National Laboratory, 1994).

197. Nogues, J. L., Hench, L. L. & Zarzycki, J. Comparative study of seven glasses for solidification of nuclear wastes. *Mater. Res. Soc. Symp. Proc* **11**, 211–218 (1982).

198. Hermansson, H. P., Christensen, H., Björner, I. K., Werme, L. & Clarkl, D. E. Variables affecting leaching of Swedish nuclear waste glass. *Nucl. Chem. Waste Manag.* **5**, 315–332 (1985).

199. Feng, X., Barkatt, A. & Jiang, T. Systematic Composition Studies on the Durability of Waste Glass WV205. *Mater. Res. Soc. Symp. Proc* **112**, 673–683 (1988).

200. Nogues, W. J. L. & Hench, L. L. Effect of Fe2O3/ZnO on two Glass

Compositions for Solidification of Swedish Nuclear Wastes. *Mater. Res. Soc. Symp. Proc* **11**, 273–278 (1982).

201. Mea, D. G., Gasparotto, A., Betinelli, M., Montenero, A. & Scaglioni, R. Chemical Durability of Zinc-containing Glasses. *J. Non-Crystalline Solidso* **84**, 443–451 (1986).

202. Clark, D. E., Acree, W. A. & Hench, L. L. Electron Microprobe Analysis of Corroded Soda-Lime-Silica Glasses. *J. Am. Ceram. Soc* **59**, 463–464 (1976).

203. Kulyukhin, S. A., Krasavina, E. P., Gredina, I. V. & Mizina, L. V. Sorption of U(VI) from aqueous solutions on layered double hydroxides of Mg, Al, and Nd. *Radiochemistry* **52**, 653–661 (2010).

204. Pshinko, G. N. Layered Double Hydroxides as Effective Adsorbents for U (VI) and Toxic Heavy Metals Removal from Aqueous Media. *J. Chem. Hindawi* **2013**, (2013).

205. Mattigod, S. V, Serne, R. & Fryxell, G. E. *Selection and Testing of 'Getters' for Adsorption of Iodine-129 and Technetium-99: A Review.* (2003). doi:10.2172/15004678

206. Li, F. & Duan, X. *Application of Layered Double Hydroxides. Structure and Bonding, Vol 119*. (Springer, 2000). doi:10.1016/S0047-2727(07)00070-9

207. Tits, J. *et al. Radionuclide uptake by calcium silicate hydrates : Case studies with Th(IV) and U(VI) (PSI Bericht Nr. 14-03)*. (2014).

208. Sievänen, U. *et al. Optimisation of Technical Properties of Low pH Cementitious Injection Grout (POSIVA working report 2006-85)*. (POSIVA, 2006).

209. *Safety functions, performance targets and technical design requirements for a KBS-3V repository (Posiva SKB Report 01)*. (2017).

210. Ford, T. Calcite mining in the peak district. *Min. Hist. Bull. Peak Dist. Mines Hist. Soc.* **15**, 1–9 (2002).

211. Fields, L. *Unpublished Report on the Geological Setting of the Peak Dale Tunnel (British Geological Survey)*. (2015).

212. Bingham, P., Hyatt, N. C. & Hand, R. J. *Glass Formulation Development for Hinkley Point A (HPA) Wet Intermediate Level Waste (WILW). Magnox South Report (MES/EST/HPA/REP/0010/07, Issue 2)* (Magnox South, 2008).

213. Boast, L., Stennett, M. & Hyatt, N. Thermal treatment of plutonium contaminated material (PCM) waste. *MRS Adv.* 1–8 (2017). doi:10.1557/adv.2017.169

214. Hyatt, N. C., Morgan, S., Stennett, M. C., Scales, C. R. & Deegan, D. Characterisation of Plasma Vitrified Simulant Plutonium Contaminated Material Waste. *MRS Proc.* **985**, 6–11 (2006).